DEVELOPMENT OF POLYURETHANES FOR ANALYSIS AND TREATMENT OF CANCER INDUCED BONE DISEASE

By

Jonathan Michael Page

Dissertation

Submitted to the Faculty of the

Graduate School of Vanderbilt University

In partial fulfillment of the requirements

For the degree of

DOCTOR OF PHILOSOPHY

in

Chemical Engineering

May, 2014

Nashville, Tennessee

Approved:

Professor Scott A. Guelcher

Professor Kane Jennings

Professor Matthew Lang

Professor Julie Sterling

To my family and friends

for always supporting me;

and to the memory of my mother,

who always believed in me.

ACKNOWLEDGEMENTS

I would like to acknowledge the funding sources that were utilized to complete this research. Grants from the Orthopaedic Extremity Trauma Research Program, the Armed Forces Institute of Regenerative Medicine, the National Science Foundation, the National Cancer Institute and the National Institutes of Health were instrumental.

I want to thank my research advisor Dr. Scott Guelcher. He took a big chance on me and never looked back. He has been one of my biggest sources of inspiration in both research and in life. His lab provides such a wealth of resources outside of research and allows all of us to grow as entrepreneurs, inventors and professionals. Furthermore he provides us with the room to try new things and not be scared of failing, which ultimately results in innovation and progress. Thanks for believing in me and my crazy ideas. Additionally, I would like to thank my committee members for helping over the course of my time here: Dr. Kane Jennings, Dr. Matthew Lang, and Dr. Julie Sterling. Their support and advice pushed me to complete my goals.

I was extremely fortunate to work with many collaborators on many unique projects and I would like to acknowledge all the help they gave me along the way. The Sterling lab: Alyssa Merkel for go-to advice about anything and everything in the biology lab, Ushashi, Shellese and Denise for all your help. The Sung lab: Angela Zachman for help with all things mice and cell culture. The Duvall lab: Mukesh Gupta for help with synthesis and chemistry, Brian Evans and John Martin for help with interesting problems and new materials. I also want to thank the Vanderbilt Institute of Nanoscale Science and Engineering (VINSE, Dr. Tony Hmelo, Dr. Dmitry Koktysh and Dr. Ben Schmidt) for access to equipment and valuable training.

Thanks to everyone at the Chemical and Biomolecular Engineering department (Mary Gilleran, Rae Uson, Mark Holmes, Julie Canada and Julie James) for helping keep things running. I would also like to thank everyone of the Guelcher lab (past and present) for being so supportive and willing to help at every turn. I have to especially acknowledge Katarzyna Zienkiewicz for all her hard work and dedication. Kasia truly cares about everyone in our lab and without her our lab would fall apart.

I would like to finally acknowledge the support of my family and friends. Thank you to my parents, Barbara and Bill Page for your love and support throughout my life. Although my mother passed away before she could see me graduate I know she is bragging to everyone in heaven that her son graduated from Vanderbilt. Thanks to my grandparents, aunts, uncles, siblings and cousins for always being there for me. In particular I also want to thank my in-laws and their family for being models of faith and love and for accepting me into such a great group. I also want to thank all my friends both in and outside of Vanderbilt for keeping me sane and always making me laugh. I can’t give enough credit or gratitude to my wife, Jessica Page. Jessica has been my rock for nearly 10 years now and none of this would be possible without her love and support. Finally I want to thank my daughter, Lily. She has given me more joy and happiness than I could ever imagine. I can’t wait to see what God has in store for us next.

TABLE OF CONTENTS

Page

LIST OF TABLES

LIST OF FIGURES

CHAPTER I

INTRODUCTION

Overall cancer fatalities have been leveling off for both men and women since the early 1990s, however the prevalence of cancer occurring over a lifetime is still remarkably high for men (45%) and women (38%)[1]. While all of the recent advances in therapies and treatments for cancers have increased the average lifespan of patients, it has opened new doors to metastatic diseases that were not pathologically relevant in the past. One of the most prominent metastatic sites for the most common cancers, e.g. breast, prostate and lung[1], is often the skeletal system[2]. Skeletal metastasis increases mortality significantly[3], and are associated with increased pain, hypercalcemia, and fractures. The growing interest of research in this area is shown in Figure 1.1.

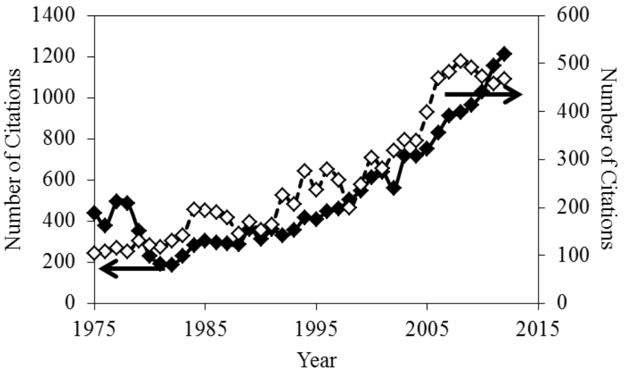

Figure 1.1. Citations per year from Pubmed searches for “cancer metastasis to bone” (♦) and “cancer induced bone disease” (◊).

As in many cases of metastatic disease, the phenotypic and genetic changes that occur when cancers metastasize to bone effectively render the cancer incurable[2a-c, 2e]. One of the many changes that occur upon establishment in the bone microenvironment is the upregulation and secretion of parathyroid related protein (PTHrP)[4]. Parathyroid proteins are utilized by the body to regulate calcium ion concentration in the blood stream, particularly during pregnancy, by stimulating osteoclasts to breakdown bone [5]. This protein has been shown to be an integral part of the vicious cycle of osteolytic cancers[2c]. The vicious cycle is a unique phenomenon in osteolytic tumors where the cancer cells stimulate bone destruction and the bone destruction releases growth factors which further stimulate the tumors.

There has been a large effort to study the mechanisms that drive the vicious cycle, with significant focus being placed on the effects of mechanotransduction. Mechanotransduction is the ability of a cell to react to the local physical environment. Many cells have been shown to sense their local environment by the expression and activation of integrins, a class of transmembrane proteins with specific binding affinity to various extracellular matrices[6]. It has been found that upon exposure to various substrates of similar chemistry but different rigidities, many types of cells will alter their phenotypic and genetic profiles[7]. Specifically, cancerous cells have higher contraction and spreading abilities on substrates with higher rigidity than the native tissue[8]. This can lead to a number of pathological issues, such as increased invasiveness, motility and metastatic possibilities[8-9]. The ability to analyze cellular responses in a physiologically relevant range of rigidity for bone could precipitate the underlying mechanisms of mechanotransduction in cancer induced bone disease and could potentially lead to therapeutic targets.

The goal of this dissertation was to optimize and characterize a polyurethane based cell culture system that could be utilized to study the effects of mechanotransduction in cancer induced bone disease. From these efforts therapeutic targets were identified and methodologies for delivering drug payloads to specific pathological locations were analyzed. Additionally, polyurethane based bone grafts developed in the Guelcher lab were analyzed for biocompatibility and optimized with novel chemistries, paving the way for further studies in the regeneration of bone destroyed by metastatic cancers.

The two-dimensional polyurethane cell culture system, developed in the Guelcher lab and covered in Chapter III, has been previously utilized to determine that there is a correlation between the physiologically relevant rigidity in the bone microenvironment and the expression of osteolytic factors, such as PTHrP, in cancer cells that are known the metastasize to bone[10]. The change in osteolytic gene expression in response to rigidity was associated with TGF-β signaling and Rho-associated kinase (ROCK), a downstream signaling cascade in the mechanotransduction response. In Chapter III this work is expanded by probing the upstream signaling pathways associated with cancer cells that metastasize to bone. In particular, the relationship between integrin and TGF-β signaling is examined by a novel Förster resonance energy transfer (FRET) experiment. The FRET analysis showed that there is a distinct co-localization on the surface of cells cultured on rigid substrates and not on compliant substrates. The ability to limit the expression of integrins, by therapeutics or small hairpin ribonucleic acids (shRNA), prevents this co-localization and lowers osteolytic gene expression *in vitro* and tumor induced bone destruction *in vivo*. From these studies downstream molecular targets are identified for the potential inhibition of osteolytic destruction in cancer induced bone disease.

The downstream targets identified by the previous study can be affected by several classes of small molecule hydrophobic drugs; however, the most effective drugs are insoluble in aqueous environments and have posed significant challenges in both systemic and local delivery to tumors. Additionally, the drugs must be reliably delivered to the cytosol of the cancer cells to achieve the desired affects. Both of these challenges can be overcome with the application of polycationic micellar nanoparticles[11]. Chapter IV screens a library of twelve polycationic polymers that spontaneously form micellar nanoparticles for potential drug delivery vehicles. Some of the twelve polymers in the library tested have been found to be highly effective at encapsulating and delivering small interfering ribonucleic acids (siRNA) *in vitro* and *in vivo*[12]. Furthermore, the polymers have been loaded into injectable polyurethane scaffolds, developed by the Guelcher lab, and shown to be biologically active upon release from implanted scaffolds *in vivo*[13]. However, none of the polymers have been studied for the capacity to encapsulate and deliver small molecule hydrophobic drugs. The synthesis and characterization of the polymer library as well as the ability to encapsulate and delivery a model small molecule hydrophobic drug was completed *in vitro*. Effects of pH and polymer composition on cytotoxicity, membrane disruption, and micellar stability were also analyzed revealing a novel polymer composition for further analysis.

Chapter V describes the analysis of injectable, settable polyurethane biocomposites for use as a regenerative platform for bone defects. Injectable and settable bone grafts offer significant advantages over pre-formed implants due to their ability to be administered using minimally invasive techniques and to conform to the shape of irregular and complex defects. However, injectable biomaterials present biocompatibility challenges due to the potential toxicity and ultimate fate of reactive components that are not incorporated in the final cured product. In this study the effects of stoichiometry and triethylenediamine (TEDA) catalyst concentration on the reactivity, injectability, and biocompatibility of two component lysine-derived polyurethane (PUR) biocomposites were investigated. Rate constants were measured for the complex reactive mixture using an in situ attenuated total reflection Fourier transform infrared spectroscopy technique. Based on the measured rate constants, a kinetic model predicting the conversion of each component with time was developed. The kinetic model successfully predicted the composition of leached material over time and proved that only non-cytotoxic materials could extravasate into the wound bed. The PUR biocomposite supported cellular infiltration and remodeling in femoral condyle defects in rabbits at 8 weeks, and there was no evidence of an adverse inflammatory response induced by unreacted components from the biocomposite or degradation products from the cured polymer. Taken together, these data underscore the utility of the kinetic model in predicting the biocompatibility of reactive biomaterials. The polycationic nanoparticles discussed in Chapter IV and the injectable biocomposites described in Chapter V are prime candidates to be utilized together for patients with cancer induced bone disease. The ability to release specific small molecule hydrophobic drugs from an injectable bone graft could result in reduced margins of resections, localized cancer destruction, and regeneration of tumor destroyed bone.

The injectable, settable polyurethane biocomposites in Chapter V are designed with a polyester component that degrades primarily by hydrolysis of the ester bond[14]. The hydrolytic degradation has also been shown to be autocatalytic[15], which is difficult to control and can create a mismatch between the degradation of the polymer scaffold and regeneration of new tissue *in vivo*[16]. In order to overcome this hurdle, a novel polymer with covalent linkages that are highly susceptible to reactive oxygen species (ROS) called polythioketals (PTKs) were developed and optimized[17]. Since ROS is mainly secreted locally by cells *in vivo*, replacing the polyester component in polyurethane composites with a PTK polymer results in degradation rates that are related directly to the degree of cell infiltration. Chapter VI describes the development of PTKs and Chapter VIII discusses work to add another level of specificity to the degradation mechanism of PTK polymers by incorporating enzymatically labile amino acid sequences. The reaction to form PTKs results from the acid catalyzed step polymerization of a di-functional thiol component with a di-functional hydroxyl analog. Nearly any di-functional thiol compound can be employed for this reaction, including thiolated amino acids. Thiolated amino acid sequences were designed with sensitivity to Cathepsin K, an enzyme secreted by osteoclasts during bone remodeling[18], and added to the PTK reaction. Up to 10% of the amino acid could be integrated into the PTK while still remaining a viscous liquid. Chapter VI discusses the PTK-amino acid (PTK-AA) synthesis and characterization upon incorporated into polyurethanes. The degradation rates and specificity were also analyzed and compared with two different isocyanates and polyester controls. The PTK-AA polymers were found to have both enzymatic and ROS degradable functionality *in vitro*.

Chapter VII concludes the dissertation by summarizing the main results and Chapter VIII presents a cumulative discussion of future studies. Overall this dissertation presents a path to develop polyurethanes to study and ultimately treat cancer induced bone disease.

References

1. Siegel, R.; Naishadham, D.; Jemal, A., Cancer statistics, 2013. *CA: A Cancer Journal for Clinicians* **2013,** *63* (1), 11-30.

2. (a) Chambers, A. F.; Groom, A. C.; MacDonald, I. C., Metastasis: dissemination and growth of cancer cells in metastatic sites. *Nat. Rev. Cancer* **2002,** *2* (8), 563-572; (b) Coleman, R., Metastatic bone disease: clinical features, pathophysiology and treatment strategies. *Cancer Treatment Reviews* **2001,** *27* (3), 165-176; (c) Mundy, G. R., Metastasis: Metastasis to bone: causes, consequences and therapeutic opportunities. *Nat. Rev. Cancer* **2002,** *2* (8), 584-593; (d) Sommerfeldt, D.; Rubin, C., Biology of bone and how it orchestrates the form and function of the skeleton. *European Spine Journal* **2001,** *10* (2), S86-S95; (e) Weilbaecher, K. N.; Guise, T. A.; McCauley, L. K., Cancer to bone: a fatal attraction. *Nat. Rev. Cancer* **2011,** *11* (6), 411-425.

3. (a) Sathiakumar, N.; Delzell, E.; Morrisey, M.; Falkson, C.; Yong, M.; Chia, V.; Blackburn, J.; Arora, T.; Brill, I.; Kilgore, M., Mortality following bone metastasis and skeletal-related events among women with breast cancer: a population-based analysis of U.S. Medicare beneficiaries, 1999–2006. *Breast Cancer Res Tr* **2012,** *131* (1), 231-238; (b) Sathiakumar, N.; Delzell, E.; Morrisey, M. A.; Falkson, C.; Yong, M.; Chia, V.; Blackburn, J.; Arora, T.; Kilgore, M., Mortality following bone metastasis and skeletal-related events among men with prostate cancer: a population-based analysis of US Medicare beneficiaries, 1999–2006. *Prostate cancer and prostatic diseases* **2011,** *14* (2), 177-183.

4. Yoneda, T.; Sasaki, A.; Mundy, G., Osteolytic bone metastasis in breast cancer. *Breast Cancer Res Tr* **1994,** *32* (1), 73-84.

5. Wysolmerski, J. J., Parathyroid hormone-related protein: an update. *The Journal of Clinical Endocrinology & Metabolism* **2012,** *97* (9), 2947-2956.

6. Katsumi, A.; Orr, A. W.; Tzima, E.; Schwartz, M. A., Integrins in mechanotransduction. *Journal of Biological Chemistry* **2004,** *279* (13), 12001-12004.

7. (a) Breuls, R. G. M.; Klumpers, D. D.; Everts, V.; Smit, T. H., Collagen type V modulates fibroblast behavior dependent on substrate stiffness. *Biochemical and Biophysical Research Communications* **2009,** *380* (2), 425-429; (b) Boyan, B. D.; Hummert, T. W.; Dean, D. D.; Schwartz, Z., Role of material surfaces in regulating bone and cartilage cell response. *Biomaterials* **1996,** *17* (2), 137-146; (c) Califano, J. P.; Reinhart-King, C. A., Substrate Stiffness and Cell Area Predict Cellular Traction Stresses in Single Cells and Cells in Contact. *Cellular and Molecular Bioengineering* **2010,** *3* (1), 68-75; (d) Dokukina, I. V.; Gracheva, M. E., A Model of Fibroblast Motility on Substrates with Different Rigidities. *Biophysical Journal* **2010,** *98* (12), 2794-2803; (e) Freyman, T. M.; Yannas, I. V.; Yokoo, R.; Gibson, L. J., Fibroblast contraction of a collagen-GAG matrix. *Biomaterials* **2001,** *22* (21), 2883-2891; (f) Ghosh, K.; Pan, Z.; Guan, E.; Ge, S. R.; Liu, Y. J.; Nakamura, T.; Ren, X. D.; Rafailovich, M.; Clark, R. A. F., Cell adaptation to a physiologically relevant ECM mimic with different viscoelastic properties. *Biomaterials* **2007,** *28* (4), 671-679.

8. (a) Butcher, D. T.; Alliston, T.; Weaver, V. M., A tense situation: forcing tumour progression. *Nat. Rev. Cancer* **2009,** *9* (2), 108-122; (b) Weaver, V. M.; Petersen, O. W.; Wang, F.; Larabell, C. A.; Briand, P.; Damsky, C.; Bissell, M. J., Reversion of the

malignant phenotype of human breast cells in three-dimensional culture and in vivo by integrin blocking antibodies. *Journal of Cell Biology* **1997,** *137* (1), 231-245.

9. Mueller, M. M.; Fusenig, N. E., Friends or foes - Bipolar effects of the tumour stroma in cancer. *Nat. Rev. Cancer* **2004,** *4* (11), 839-849.

10. Ruppender, N. S.; Merkel, A. R.; Martin, T. J.; Mundy, G. R.; Sterling, J. A.; Guelcher, S. A., Matrix Rigidity Induces Osteolytic Gene Expression of Metastatic Breast Cancer Cells. *Plos One* **2010,** *5* (11).

11. Brannon-Peppas, L.; Blanchette, J. O., Nanoparticle and targeted systems for cancer therapy. *Advanced Drug Delivery Reviews* **2012,** *64, Supplement* (0), 206-212.

12. Nelson, C. E.; Kintzing, J. R.; Hanna, A.; Shannon, J. M.; Gupta, M. K.; Duvall, C. L., Balancing Cationic and Hydrophobic Content of PEGylated siRNA Polyplexes Enhances Endosome Escape, Stability, Blood Circulation Time, and Bioactivity In Vivo. *ACS nano* **2013**.

13. Nelson, C. E.; Gupta, M. K.; Adolph, E. J.; Guelcher, S. A.; Duvall, C. L., siRNA Delivery from an Injectable Scaffold for Wound Therapy. *Advances in Wound Care* **2013,** *2* (3), 93-99.

14. Hafeman, A. E.; Zienkiewicz, K. J.; Zachman, A. L.; Sung, H. J.; Nanney, L. B.; Davidson, J. M.; Guelcher, S. A., Characterization of the degradation mechanisms of lysine-derived aliphatic poly(ester urethane) scaffolds. *Biomaterials* **2011,** *32* (2), 419-429.

15. (a) Antheunis, H.; van der Meer, J.-C.; de Geus, M.; Heise, A.; Koning, C. E., Autocatalytic Equation Describing the Change in Molecular Weight during Hydrolytic Degradation of Aliphatic Polyesters. *Biomacromolecules* **2010,** *11* (4), 1118-1124; (b) Li, S., Hydrolytic degradation characteristics of aliphatic polyesters derived from lactic and glycolic acids. *Journal of Biomedical Materials Research* **1999,** *48* (3), 342-353; (c) Pitt, C. G.; Chasalow, F. I.; Hibionada, Y. M.; Klimas, D. M.; Schindler, A., Aliphatic polyesters. I. The degradation of poly(ϵ-caprolactone) in vivo. *Journal of Applied Polymer Science* **1981,** *26* (11), 3779-3787.

16. Dumas, J. E.; Prieto, E. M.; Zienkiewicz, K. J.; Guda, T.; Wenke, J. C.; Bible, J. E.; Holt, G. E.; Guelcher, S., Balancing the Rates of New Bone formation and Polymer Degradation Enhances Healing of Weight-Bearing Allograft/Polyurethane Composites in Rabbit Femoral Defects. *Tissue Engineering* **2013,** (ja).

17. (a) Wilson, D. S.; Dalmasso, G.; Wang, L.; Sitaraman, S. V.; Merlin, D.; Murthy, N., Orally delivered thioketal nanoparticles loaded with TNF-α–siRNA target inflammation and inhibit gene expression in the intestines. *Nature materials* **2010,** *9* (11), 923-928; (b) Martin, J. R.; Gupta, M. K.; Page, J. M.; Yu, F.; Davidson, J. M.; Guelcher, S. A.; Duvall, C. L., A porous tissue engineering scaffold selectively degraded by cell-generated reactive oxygen species. *Biomaterials* **2014,** *35* (12), 3766-3776.

18. (a) Lecaille, F.; Choe, Y.; Brandt, W.; Li, Z.; Craik, C. S.; Brömme, D., Selective Inhibition of the Collagenolytic Activity of Human Cathepsin K by Altering Its S2 Subsite Specificity†. *Biochemistry* **2002,** *41* (26), 8447-8454; (b) Lecaille, F.; Weidauer, E.; Juliano, M. A.; Bromme, D.; Lalmanach, G., Probing cathepsin K activity with a selective substrate spanning its active site. *Biochemical Journal* **2003,** *375*, 307-312.

CHAPTER II

BACKGROUND

Cancer Induced Bone Disease: Biology, Pathology, and Cellular Mechanisms

The skeletal system is an important reserve for minerals, immune cells, proteins, and growth factors[1]. The bone microenvironment is in a constant state of remodeling with the entire skeleton being replaced on average of 7-10 years. Bone turnover, in healthy individuals, is a tightly controlled process with strain and biochemical signals influencing the rate of new bone formation[2]. This process is generally controlled by three cell populations: osteoblasts, osteoclasts and osteocytes[1b, c, 2]. Osteoblasts are the bone building cells. They begin the bone forming process by excreting tropocollagen, which polymerizes extracellularly into collagen. New mineralized bone is formed by reinforcing the collagen fibers with precipitated hydroxyapatite (HA). Some osteoblasts envelop themselves in mineralized matrix and differentiate to osteocytes. The osteocytes regulate bone turnover and aid in maintaining ion equilibrium in the plasma. Osteocytes are stimulated to induce bone resorption by many factors, including constant strain, injury, electrochemical interactions and biochemical markers from the endocrine system[2]. The resorption process of bone is completed by the osteoclasts. These cells are formed by a merger of bone progenitor cells and result in a large multinucleated single cell. The osteoclasts form sealed resorption areas by integrin activated attachment to extracellular proteins like vitronectin (Vn) and fibronectin (Fn)[3]. The resorption areas directly underneath the cells are then exposed to excreted proteases, reactive oxygen species (ROS), and high concentrations of acidic species. This results in dissolution of both the mineral structure of bone and the underlying collagen reinforcements. This in turn releases ions and growth factors such as transforming growth factor β (TGF-β), bone morphogenetic proteins (BMP), insulin-like growth factors (IGF) and many more.

There are several pathologies, such as osteoporosis, hyperthyroidism, arthritis, and metastatic cancers, that result in unbalanced bone formation and a majority of these diseases are caused in part by a disruption or hijacking of the endocrine system[4]. The endocrine system is comprised of many glands that secrete regulatory hormones which act on nearly every system in the body. In regards to bone remodeling, the parathyroid has been isolated as a primary driver of bone resorption. During pregnancy the parathyroid releases a large dose of parathyroid related protein (PTHrP), which acts to increase levels of Ca^{2+} ions in the blood for fetal development and lactation[4d]. PTHrP indirectly acts to enhance bone resorption by binding to receptors in osteoblasts which induces the production of receptor activator of nuclear factor κ-B ligand (RANKL) and prevents the formation of osteoprotogerin (OPG) which acts as an inhibitor to RANKL. RANKL binds to RANK receptors on osteoclasts and stimulates bone resorption. While this process is tightly controlled in healthy individuals, many forms of cancer that are known to metastasize to bone show the ability to locally produce PTHrP and in turn this generates what is known as the "vicious cycle" of cancer induced bone disease[4c].

In some of the most common forms of cancer, e.g. breast, lung and prostate, late stage diagnosis often includes metastatic sites in bone. Once these tumors establish in the bone microenvironment they begin to secrete PTHrP, which has been shown to be regulated through the transcription factor Gli2[5]. PTHrP stimulates the resorption of bone through the RANKL mechanism and this causes the release of growth factors held within the bone like TGF-β. In normal cells, and even in tumors at the primary site in breast cancer, TGF-β results in apoptosis; however, the metastatic cancer cells that establish in bone have an alternative signaling pathway and are stimulated in the presence of TGF-β to produce more PTHrP[6]. The vicious cycle positive feedback loop results in osteolysis and tumor proliferation.

The causes of metastasis to bone have been widely studied and are linked to many factors including chemokine receptors, protease expression, and integrin expression[7]. Integrins are a class of transmembrane proteins that have specific binding domains targeted to various extracellular matrix molecules. They are vastly important to regular cell function as adhesion sites for motility and they initiate differentiation[8]. In cancers, integrins have been found to be overexpressed in many tumors including those that preferentially metastasize to bone. Specifically, overexpression of integrin $\alpha_v\beta_3$, an integrin with binding domains specific to Vn and Fn, is known to result in aggressively bone metastatic phenotypes[7b, 9]. However, if metastatic tumor cells are artificially stimulated to express high levels of $\alpha_v\beta_3$ and directly transplanted into the bone, there is no difference in the osteolytic potential compared to cells that express normal levels of $\alpha_v\beta_3$[9b]. Inhibition of integrin $\alpha_v\beta_3$ by treatment with small molecule antagonists or antibodies results in lower prevalence of metastasis to bone[10]. Systemic inhibition of $\alpha_v\beta_3$ is thought to act synergistically to reduce metastasis by decreasing tumor angiogenesis and preventing osteoclasts form forming resorption pits. However, since $\alpha_v\beta_3$ is prevalent in many normal cells systemic delivery of anti-integrin therapeutics may have adverse side effects[6a].

While the basic mechanism of the vicious cycle and metastasis are well studied, the reason behind the distinctly different gene expression between primary tumors and metastatic bone lesions is more complex (Figure 2.1). The expression of the osteolytic proteins such as PTHrP is nearly 100% prevalent in metastatic tumors that reside in bone, where other metastatic sites (even within the same patient) have significantly less expression of PTHrP[11]. It has been shown that the TGF-β signaling pathway increases gene expression of Gli2, a transcription factor that can regulate PTHrP, however TGF-β is ubiquitously expressed, thus cannot alone explain the bone specific expression. One factor that can aid analysis is studying the rigidity of the bone microenvironment and the utilization of organ specific *in vitro* models.

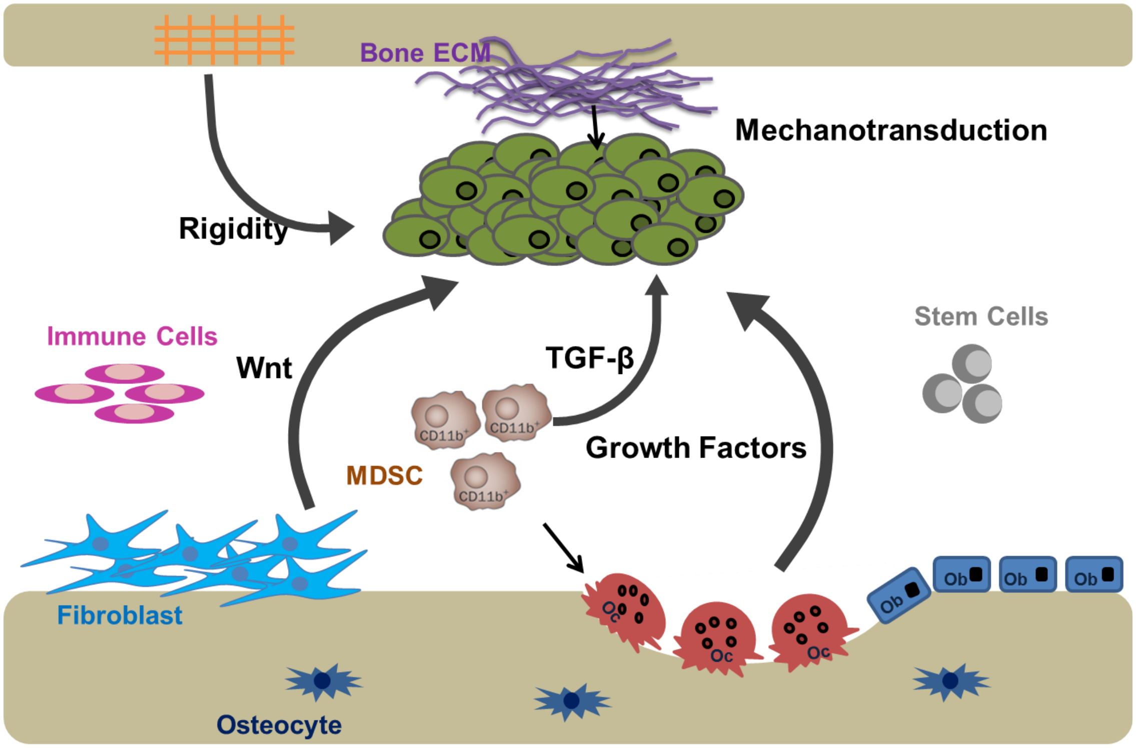

Figure 2.1. Current scheme of the possible factors involved with the vicious cycle.

Organ Specific *In Vitro* Models

The cells ability to sense and respond to the mechanical cues of the surrounding microenvironment is known to play a large role in phenotype and gene expression of many cell populations. In the case of cancers, studies looking at primary breast tumors have shown that there is a slight increase in the rigidity of the extracellular matrix surrounding a tumor[12]. This increase in rigidity is commonly modeled *in vitro* with hydrogels. The organ specific models were able to provide insight on tumor invasiveness and novel molecular pathways that resulted in target therapeutics[12b]. However, a large majority of studies use hydrogels which are limited in modulus to <100kPa. These materials are unable to provide a range of rigidity that is specific to bone.

The bone microenvironment is divided into two types of mineralized matrix cancellous and cortical bone[2]. Cortical bone is the hard outer casing of bones and it has high mineral density and limited vascularity. Cancellous or trabecular bone occurs in the interstitial space of cortical bone, primarily near joints, and is comprised of a network of spindle shaped mineralized trabeculae. The trabecular bone is filled with marrow and blood vessels. Recent mechanical analysis of these two types of bone with nanoindentation has yielded a range of rigidity of 365 ± 223 MPa for trabecular bone and 9.9 ± 1.7 GPa for cortical bone[13]. Other methods of analysis have obtained similar values; however, nanoindentation probes the material on a similar scale to cellar interactions.

In order to better model the rigidity of bone, a polyurethane (PUR) cell culture system was developed. The PUR films were made by melt casting a liquid reactive isocyanate and poly-hydroxyl. The molecular weight of the precursor materials is directly correlated to the modulus of the resulting film. By adjusting the molecular weight, PUR films were generated with rigidity that spanned from 1 MPa - >1GPa (Figure 2.2). Initial studies with the PUR films *in vitro* have shown that PTHrP and Gli2 are stimulated in metastatic breast cancer cells simply by increasing the rigidity from basement membrane levels (~1 MPa) to cortical bone levels (~1 GPa)[14]. It was also found that inhibition of the downstream mechanotransduction regulator Rho associated kinase (ROCK) limited the rigidity mediated stimulation. These experiments showed that modeling the rigidity of the bone microenvironment *in vitro* has a direct correlation to clinically relevant gene expression *in vivo*. Additionally, it is more likely that novel therapeutic targets can be better identified when biologically relevant models are employed. Future studies with bone biomimetic models should aid in elucidation of the complex interplay of cancers that metastasize preferentially to bone.

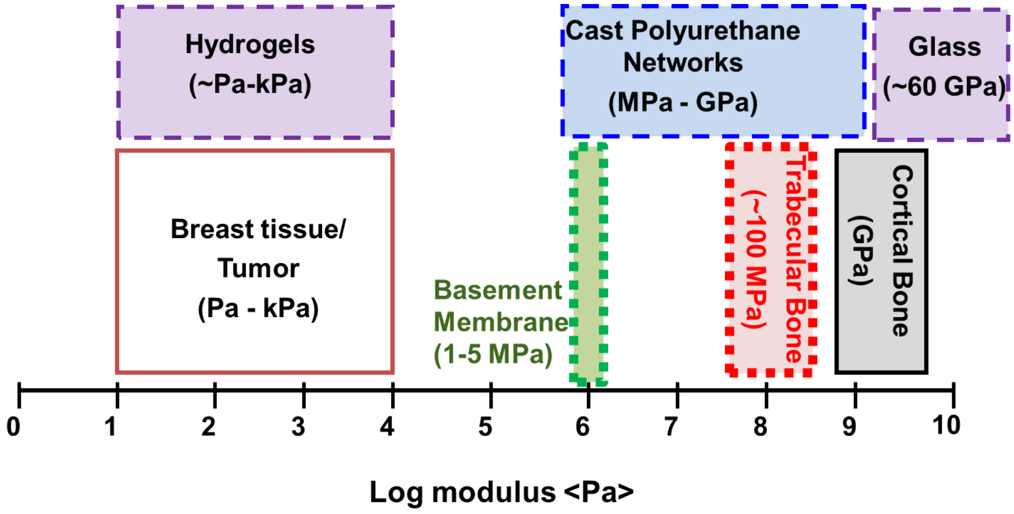

Figure 2.2. Diagram of the range of modulus seen in cancers that metastasize to bone with physiological rigidities boxed in solid lines and model systems in dashed boxes.

Injectable Biomaterials for Tissue Engineering

Biomaterials are generally defined as non-viable materials used in medical devices that are intended to interact with biological systems in order to replace any tissue, organ, or function of the body[15]. While this classification is constantly evolving to encompass new areas of research[15e], the definition of injectable biomaterials exhibits more variability depending on the specific application, reactivity of the material, and interaction with the tissue[15d, 16]. For the purposes of this review, the term injectability will focus on materials that are viscous enough to be extruded through clinically relevant applicators with minimally invasive surgical techniques. Injectable biomaterials offer advantages compared to prefabricated implants due to their ability to be utilized in non-invasive surgical procedures, cure *in situ*, fill complex defects, and easily incorporate cells or therapeutics. Prefabricated biomaterials require implantation through invasive surgical procedures, which increases the risk of complications and recovery time[17]. With the interest in biomaterials for tissue engineering applications presumably rising for the foreseeable future, injectable biomaterials are anticipated to increase in clinical significance[18].

Injectable and settable biomaterials can be classified based on curing mechanisms (non-settable injectable materials are outside the scope of this review). Physically settable biomaterials include environmentally responsive crosslinked (i.e. pH, temperature, micelle formation in water, etc.) and ionically crosslinked polymers[19]. The lack of covalent linkages in physically settable biomaterials produces weak mechanical properties, which limits their use. Chemically settable biomaterials, which form covalent bonds *in situ,* cure by photopolymerization, thermally activated polymerization, catalyzed reactions, click-based reactions, or enzymatically catalyzed reactions[20].

Despite the advantages of settable biomaterials, there are distinct challenges associated with the development of clinically relevant therapies. Strategies for clinical translation must address sterilization procedures, handling properties, biocompatibility, and regenerative capabilities[21]. The toxicity of low molecular weight reactants, catalysts, or other additives released during *in situ* cure is of particular concern for settable biomaterials. Settable biomaterials must be designed as to inject low molecular weight monomers (and optionally catalysts or other additives) that subsequently react *in vivo* without damaging host tissue. The requirements of biocompatibility and biodegradability apply to both the low molecular weight precursors as well as the cured material. The following critical engineering challenges must be addressed when designing settable biomaterials for clinical use.

Sterilization and Infection

Despite meticulous surgical care, the incidence of bacterial infection resulting from implanted biomaterials can be as high as 5%[17, 22]. Infection rates are highly dependent on the type, application, and location of implantation[22a]. Infection of temporary implants, such as catheters, wound dressings and mucosal inserts, can result in pain, discomfort, use of systemic antibiotics and additional re-applications[23]. Orthopedic and cardiovascular implant infections are more serious, and as with many biomaterial infections the bacteria involved are also increasingly resistant to common antibiotics[17a]. Infections associated with these permanent implants can result in tissue damage, excess surgeries, implant failure, or mortality[17].

Sterilization is the first line of defense against bacterial infections. Settable systems are more sensitive to sterilization procedures due to potential polymerization or loss of reactivity of the monomeric components, which would adversely affect their performance. Applications that utilize injectable systems to deliver bioactive molecules, drugs, or cells are particularly sensitive, and consequently sterilization and its effects on the efficacy of these biologics must be analyzed. For most settable biomaterials, ethylene oxide (EtO) or gamma irradiation is the gold standard for sterilization of liquid organic components[24]. Radiation doses below 25 kGy have been reported to have minimal effects on the functionality of most biomedical polymers[24c].

In cases where sterilization and proper surgical technique alone are insufficient for preventing infection, a growing amount of research has been applied to local delivery of antibiotics from an implanted material[25]. Local delivery of antibiotics has the benefit of sustaining effective doses directly at the site of implantation. Although systemic delivery can provide basal levels of protection from infection, its ability to provide bacteriocidal concentrations at the implant site is limited due to ischemic conditions and the inability of the drug to diffuse to the surface of the implant[26]. Since bacterial colonization occurs on the surface of biomaterials, local delivery of antibiotics from the implant allows for a more controlled targeted therapeutic intervention. Settable biomaterials can easily incorporate antibiotics by simple loading during mixing of the precursors[25b, c]. The release of the antibiotics is typically diffusion-controlled, which can be tuned based on material parameters such as crosslink density and porosity[25b, c, 25f]. Alternative carriers, such as microbeads, conjugated pro-drugs, or even materials with known microbial resistance such as chitosan, can be added to further control the release of antibiotics and invasion of microbial species[25a, 25d, e, 25g, 27]. These techniques have proven to reduce infections in animal models of orthopedic trauma for up to 8 weeks[25b, 25f, 25i, 28]. While the incorporation of antibiotics for localized delivery holds much promise, concerns remain about overuse and the occurrence of resistant bacterial strains[17a, 26].

Handling properties

Handling properties of settable biomaterials, such as storage, mixing, and delivery, must be optimized to facilitate ease of use in the clinic[16]. Storage requirements are highly dependent on the composition of the material. Water-soluble materials can be lyophilized to improve shelf life and require re-suspension or solubilization before use[29]. Stabilizers can be added to reactive organic liquids to enhance storage stability. Storage at low temperatures and/or reduced pressures in containers purged with an inert gas can further enhance stability. Regardless of the conditions under which the material is stored, care should be taken to ensure functionality is retained. Depending on the number of precursors required for a given system, the materials might need to be mixed directly prior to injection. Rheological characterization can provide insight into the viscoelastic properties of materials *in situ*, which can directly translate into clinical performance of an injectable system. Suspensions of solid particles in low-viscosity monomeric precursors are typically shear-thinning fluids, which are characterized by a reduction in viscosity with increasing shear rate[30]. Shear-thinning behavior can enhance the injectability of settable biomaterials, due to the consequent reduction in viscosity upon the application of force[31]. When the applied force is removed, the viscosity increases, which can prevent extravasation of material away from the site of injection. In order to determine shear thinning behavior, a shear rate analysis must be performed using a plate-based rheometer. In this test, the viscosity is measured as a function of shear rate, from which the apparent yield stress (e.g., the force required to cause the material to flow) can be calculated.

Many biphasic injectable systems, such as injectable composites or cements, exhibit yield stresses spanning a range from 1 – 1,000 Pa[31]. The yield stress is directly correlated to the injectability of the system, with lower yield stresses resulting in easier injection. There are additional factors required to fully define injectability, such as diameter of the injection device and molecular interactions[32], but the yield stress and shear thinning behavior provide valuable insight on *in situ* viscoelastic properties of injectable systems that can be directly translated into clinical performance.

The time between mixing and chemical gelation, also known as the working time, is a crucial parameter for characterizing settability. Working time can be calculated from the rheological cure profile measured under constant strain conditions[33]. In this experiment, the viscosity, storage, and loss modulus are measured versus time. As the material cures, the storage modulus (corresponding to energy stored elastically) increases, while the loss modulus (corresponding to energy dissipated by flow) decreases. The working time is identified as the point at which the storage modulus equals the loss modulus (i.e., the crossover point). Consequently, the working time is also known as the gel time, at which point the material has formed a network and can no longer flow. Working times of 5 – 15 min are preferred for clinical use[16].

Reaction conditions

Settable biomaterials must undergo rapid setting, exhibit a mild exotherm, comprise non-toxic precursors, and present minimal risk of extravasation. Rapid setting reduces the delay before the surgeon can close the wound, which consequently reduces the risk of infection[34]. Many of the available chemistries cure via an exothermic reaction. Since a rise in temperature of just 5° C for 300 s can cause necrosis[35], controlling the exotherm is important to avoid damaging local native tissue. In extreme cases, such as the exothermic poly methylmethacrylate (PMMA) reaction, temperatures can reach 125° C[35b]. The exotherm can be reduced for many reactions by lowering the concentration of catalyst or initiator, but lower catalyst concentrations can increase the working time. The reaction should also undergo a high conversion of precursors in order to eliminate the possibility of unreacted material leaching from the implant. While the reaction is proceeding, there is a corresponding increase in molecular weight and viscosity, which decreases extravasation of material away from the implantation site. Thus, reaction rates, which can be measured using techniques such as Fourier transform infrared spectroscopy (FTIR), must be optimized to provide for sufficiently rapid cure without generating a harmful exotherm[33a]. Even for reactions that rapidly achieve high conversions, leaching of harmful low molecular weight components is possible. The adverse effects of leaching on healing depend on the toxicity and concentration of the components, as well as the native tissue at the injection site[36]. Thus, biocompatibility testing of the individual components is essential to understand the potential risk of leaching toxic monomers or catalysts into the wound bed during cure. Guidelines for toxicity testing can be found in the ISO-10993 standard[37], which provides established protocols for testing biomedical devices required for regulatory approval. In particular, ISO-10993-5: Cytotoxicity specifies *in vitro* testing methods for assessing biomaterials at very early stages of development. The cytotoxicity protocol assesses the viability of cells treated with extracts obtained by incubating a biomedical device in saline or medium for 72 hours. For injectable systems with multiple reactive components, this analysis is also helpful for determining the toxicity of individual components. Cytotoxicity tests are simple, rapid, inexpensive, and highly sensitive[38]. Thus, they provide an early indication of biocompatibility. *In vivo* testing is required to determine the safety of the device prior to use in patients. ISO 10993-11 Systemic Toxicity, which evaluates the potential adverse effects of the device on the body's organs and tissues, and ISO 10993-6 Implantation Testing, which determines the local pathological effects of the device on surrounding tissue, are useful for assessing the safety of settable biomaterials at later stages of development.

Degradation and tissue regeneration

In regenerative applications, biomaterials must not only support infiltration of cells and ingrowth of new tissue, but also degrade into non-toxic breakdown products[39]. The mechanism and rate of degradation of a settable biomaterial after implantation affects the release of degradation products and the healing of the surrounding tissue. Upon implantation, degradation inevitably results in loss of mechanical strength. Therefore, it is imperative to tune the degradation rate to allow proper cellular infiltration and remodeling, which will return native function and eventually mechanical properties.

Many types of biomaterials are designed to degrade by passive mechanisms (e.g., hydrolysis). Hydrolysis rates are dependent on the type of crosslinking, chemical structure of the precursors, and the anatomic site[40]. The rate of hydrolytic degradation can in many cases be adjusted to match that of remodeling. However, in the case of polyesters, a commonly utilized polymer for injectable biomaterials, hydrolysis occurs faster at low pH and the degradation products of hydrolysis are acids[41]. This can lead to auto-catalytic degradation, which can subsequently increase degradation rates at later time points *in vivo*[42]. Furthermore, the local reduction in pH can cause tissue damage which hinders healing[43].

In recent years, cell-degradable materials have been developed by incorporating proteolytically cleavable peptides in the backbone. Proteolytic degradation can occur by many types of enzymes *in vivo*, with matrix metalloproteinases (MMPs) garnering much interest[44]. Proteolytic degradation is generally achieved via incorporation of small sequences of amino acids that have been identified as highly sensitive to specific enzymatic cleavage, which enables cells to actively degrade the material.

Polyurethane Based Bone Grafts

Polyurethanes (PURs) are a class of biocompatible polymers, derived from the reaction of isocyanates (hard segment) with hydroxyls (soft segment), that have been utilized for biomedical applications for nearly 40 years[45]. The individual segments have inherent physical attributes that make them advantageous when together, as the hard and soft segments provide physical strength and elasticity, respectively. The duality of the final polymer allows for unique and tunable physical and chemical properties. PURs can be further classified by the functionality of the precursors used for synthesis. Precursors with a functionality of 2 generate linear elastomers, where functionality >2 produces crosslinked networks. Both linear and crosslinked PUR materials have been widely utilized in the field of biomaterials. Linear elastomers offer more traditional options in biomaterial design. These polymers can be electrospun[46], solvent cast[47], or molded into various shapes to fit different applications, such as coatings[48], sutures[49], catheters[50], and artificial tissue matrices[20c]. Crosslinked networks can be utilized for injectable formulations that cure *in situ*.

Injectable PURs are a relatively novel attempt to harness the diverse library of biocompatible polymers. Multi-component *liquid* reactive systems are required to form injectable PURs. The components are liquid isocyanates, poly-hydroxyls, water, stabilizers, and catalysts. Common catalysts used in injectable PUR systems are amine or metal based. Amine based catalysts are non-toxic, but they have been found to selectivity catalyze the water reaction in aliphatic isocyanates, which can cause overfoaming[51]. However, the isocyanate-water reaction produces a urea bond, which improves strength of the network via increased hydrogen bonding[52]. Furthermore, the water reaction produces carbon dioxide which acts as a blowing agent to form porous PUR foams in situ that are ideal for enabling cellular infiltration[52]. Metallic catalysts are selectively catalyze the hydroxyl-isocyanate reaction, but are generally more toxic then their amine counterparts[51]. Combinations of catalysts can be utilized to produce many types of PURs.

There are numerous sources for liquid isocyanates, but their application is limited by possible toxicities. Low molecular weight, aliphatic diisocyanates such as 1,4 butane diisocyante and 1,6 hexamethylene diisocyanate are known to have non-toxic degradation products and are widely utilized in biomedical PUR elastomers[43, 53]. However, both these diisocyanates have high vapor pressures and are highly toxic as inhalants, limiting their use as injectable precursors[54]. To combat toxicity issues related to some of these liquid isocyanate sources, prepolymers of isocyanates synthesized from low molecular weight linkers can be used instead[55]. Common aromatic isocyanates, such as toluene diisocyanate and methylene diphenyl diisocyanate, are known to be toxic as monomers[56]. Additionally, upon degradation, aromatic-based diisocyanates form aromatic amines, which are known carcinogens[56c, 57]. Aliphatic isocyanates derived from lysine have a combination of low vapor pressure, low monomeric toxicity, non-toxic degradation products, and low melting point making them ideal for injectable PURs[55]. Lysine methyl ester diisocyanate (LDI) and lysine triisocyanate (LTI) have been utilized for injectable PUR applications in soft and hard tissue regeneration[55, 58]. For applications in soft tissue, lysine based biomaterials undergo significant oxidative degradation which results in implant lifespans of only 4 weeks[58a].

The cellular components of the wound healing and bone regeneration are well known and can be targeted for use in designing degradable biomaterials. The initial response to injury or biomaterial implantation in bone begins by neutrophil and macrophage migration[22a, 59]. This cell population utilizes oxidative species to remove cellular debris and dispose of bacterial threats. Additionally, these cells secrete cytokines that recruit and aid in differentiation of stem cells. If a material does not illicit a foreign body reaction, then the inflammatory cells disperse within days and secondary populations of cells proliferate and induce angiogenesis[22a, 59]. In bone regeneration, osteoblasts progress into the wound, begin laying down cortex material, and ossifying structurally weak areas. The ossified bone is remodeled into native bone by osteoclasts which secrete acids and enzymes, such as cathepsin k and MMPs, to aid matrix degradation[60]. For biomaterials utilized in bone regeneration, osteoclasts are known to be the major cell population that induces degradation and remodeling[31b, 58b, 61].

Degradable mechanisms for PURs *in vivo* can be deemed passive or active depending on cellular involvement. Passive degradation mechanisms occur without cellular intervention (hydrolysis), while active degradation mechanisms respond to cellular cues (enzymatic)[62]. Biodegradable PURs are traditionally formulated with polyester soft segments which hydrolytically degrade *in vitro* and *in vivo* to non-toxic alpha acids[63]. This passive degradation can be adjusted by several factors including, polymer composition, molecular weight, hard segment content, and crystallization[20c]. However, there are issues with autocatalytic degradation with polyesters due to the release of acidic byproducts during degradation[40]. This leads to quicker and less controllable degradation *in vivo*. Active degradation mechanisms allow for the natural wound healing response to remodel the polymer matrix[62]. An additional benefit of active degradation is that the polymer maintains structural integrity until the desired cellular response is achieved. The incorporation of novel polymer chemistries, such as poly(thioketals) (PTKs), and amino acid substrates for specific cell released enzymes can induce active degradation in PURs.

Localized Drug Delivery from Polyurethane Grafts

For soft tissue applications, injectable formulations of lysine-based PUR foams have proven to produce a non-toxic reaction environment during injection, remain non-toxic until complete degradation, exhibit clinically relevant handling properties, and form a simple method for incorporating therapeutics or cells[64]. Recently injectable biodegradable foams composed of LTI and a polyester polyol were shown to promote cellular infiltration and ingrowth in a rat excisional wound model[64a]. These porous scaffolds maintained structural integrity during the 7-day study as they degraded at a similar rate as local tissue regeneration. The regenerated tissue had reduced alignment of collagen, which is indicative of lower scar formation[64a]. In another study, similar LTI-based porous PUR scaffolds were loaded with pH-responsive nanoparticles which encapsulated small interfering ribonucleic acid (siRNA) *in vitro*[64c]. The siRNA nanoparticles were uniformly loaded within the PUR precursors during mixing and remained stable while the PUR foaming reaction completed[64c]. After the foam cured, the siRNA nanoparticles were released and silenced a luciferase reporter gene. The activity was similar to free nanoparticles, indicating the PUR reaction did not interfere with the nanoparticles' properties[64c]. The diffusion-controlled release was hypothesized to be effective for *in vivo* gene silencing over the period of several weeks[64c]. These examples highlight that LTI-based injectable PUR foams can be fabricated into a mechanically stable, porous matrix utilized for drug delivery in soft tissue applications.

Injectable polyurethanes derived from lysine have been utilized in the development of biocomposites intended for tissue regeneration in hard tissue sites as well[31b, 58b, 61, 65]. Injectable formulations for hard tissue applications generally include LDI- or LTI-based prepolymers, amorphous polyester polyol, water, catalyst, solid filler, and therapeutics. Mineralized matrices, such as calcium phosphates[66] or allograft bone particles [31b], can be incorporated in the liquid reacting mixture to increase the mechanical properties of the PUR biocomposite. Therapeutics, such as antibiotics[25f] or growth factors[67] can also be added as labile powders to aid the biological properties. Theoretically, the incorporation of nanoparticle based therapeutics (as discussed above) should also be possible in the PUR biocomposites.

References

1. (a) Alves, R. D. A. M.; Demmers, J. A. A.; Bezstarosti, K.; van der Eerden, B. C. J.; Verhaar, J. A. N.; Eijken, M.; van Leeuwen, J. P. T. M., Unraveling the Human Bone Microenvironment beyond the Classical Extracellular Matrix Proteins: A Human Bone Protein Library. *Journal of Proteome Research* **2011,** *10* (10), 4725-4733; (b) Lord, B. I., The architecture of bone marrow cell populations. *International journal of cell cloning* **1990,** *8* (5), 317-31; (c) Rho, J.-Y.; Kuhn-Spearing, L.; Zioupos, P., Mechanical properties and the hierarchical structure of bone. *Medical Engineering & Physics* **1998,** *20* (2), 92-102.
2. Cowin, S.; Hegedus, D., Bone remodeling I: theory of adaptive elasticity. *Journal of Elasticity* **1976,** *6* (3), 313-326.
3. Teitelbaum, S. L., Bone Resorption by Osteoclasts. *Science* **2000,** *289* (5484), 1504-1508.
4. (a) Chambers, A. F.; Groom, A. C.; MacDonald, I. C., Metastasis: dissemination and growth of cancer cells in metastatic sites. *Nat. Rev. Cancer* **2002,** *2* (8), 563-572; (b) Coleman, R., Metastatic bone disease: clinical features, pathophysiology and treatment strategies. *Cancer Treatment Reviews* **2001,** *27* (3), 165-176; (c) Mundy, G. R., Metastasis: Metastasis to bone: causes, consequences and therapeutic opportunities. *Nat. Rev. Cancer* **2002,** *2* (8), 584-593; (d) Wysolmerski, J. J., Parathyroid hormone-related protein: an update. *The Journal of Clinical Endocrinology & Metabolism* **2012,** *97* (9), 2947-2956.
5. (a) Johnson, R. W.; Nguyen, M. P.; Padalecki, S. S.; Grubbs, B. G.; Merkel, A. R.; Oyajobi, B. O.; Matrisian, L. M.; Mundy, G. R.; Sterling, J. A., TGF-β promotion of Gli2-induced expression of parathyroid hormone-related protein, an important osteolytic factor in bone metastasis, is independent of canonical hedgehog signaling. *Cancer research* **2011,** *71* (3), 822-831; (b) Sterling, J. A.; Oyajobi, B. A., The hedgehog signaling molecule Gli2 induces parathyroid hormone-related peptide expression and osteolysis in metastatic human breast cancer cells. *Cancer Res* **2006,** *66* (15), 7548-7553.
6. (a) Glick, A. B.; Van Waes, C., *Signaling Pathways in Squamous Cancer*. Springer: 2011; (b) Gonterman, R. M., *Parathyroid Hormone-related Protein Gene Expression and Function: Relationship with Oncogenic Pathways in the Skin and Squamous Cell Carcinomas of the Lung*. ProQuest: 2008.
7. (a) TAKAYAMA, S.; ISHII, S.; IKEDA, T.; MASAMURA, S.; DOI, M.; KITAJIMA, M., The Relationship Between Bone Metastasis from Human Breast Cancer and Integrin αvβ3 Expression. *Anticancer Research* **2005,** *25* (1A), 79-83; (b) Wong, N.; Mueller, B.; Barbas, C.; Ruminski, P.; Quaranta, V.; Lin, E. K.; Smith, J., αv Integrins mediate adhesion and migration of breast carcinoma cell lines. *Clin Exp Metastasis* **1998,** *16* (1), 50-61; (c) Zhang, Y.; Ma, B.; Fan, Q., Mechanisms of breast cancer bone metastasis. *Cancer Letters* **2010,** *292* (1), 1-7.
8. Katsumi, A.; Orr, A. W.; Tzima, E.; Schwartz, M. A., Integrins in mechanotransduction. *Journal of Biological Chemistry* **2004,** *279* (13), 12001-12004.
9. (a) Claudia Tanja, M., The integrin alphav beta3 increases cellular stiffness and cytoskeletal remodeling dynamics to facilitate cancer cell invasion. *New Journal of Physics* **2013,** *15* (1), 015003; (b) PÉCHEUR, I.; PEYRUCHAUD, O.; SERRE, C.-M.; GUGLIELMI, J.; VOLAND, C.; BOURRE, F.; MARGUE, C.; COHEN-SOLAL, M.;

BUFFET, A.; KIEFFER, N.; CLÉZARDIN, P., Integrin αvβ3 expression confers on tumor cells a greater propensity to metastasize to bone. *The FASEB Journal* **2002,** *16* (10), 1266-1268; (c) Zhao, Y.; Bachelier, R.; Treilleux, I.; Pujuguet, P.; Peyruchaud, O.; Baron, R.; Clément-Lacroix, P.; Clézardin, P., Tumor αvβ3 Integrin Is a Therapeutic Target for Breast Cancer Bone Metastases. *Cancer research* **2007,** *67* (12), 5821-5830.

10. (a) Cai, W.; Chen, X., Anti-Angiogenic Cancer Therapy Based on Integrin αvβ3 Antagonism. *Anti-Cancer Agents in Medicinal Chemistry- Anti-Cancer Agents)* **2006,** *6* (5), 407-428; (b) Harms, J.; Welch, D.; Samant, R.; Shevde, L.; Miele, M.; Babu, G.; Goldberg, S.; Gilman, V.; Sosnowski, D.; Campo, D.; Gay, C.; Budgeon, L.; Mercer, R.; Jewell, J.; Mastro, A.; Donahue, H.; Erin, N.; Debies, M.; Meehan, W.; Jones, A.; Mbalaviele, G.; Nickols, A.; Christensen, N.; Melly, R.; Beck, L.; Kent, J.; Rader, R.; Kotyk, J.; Pagel, M. D.; Westlin, W.; Griggs, D., A small molecule antagonist of the α v β3 integrin suppresses MDA-MB-435 skeletal metastasis. *Clin Exp Metastasis* **2004,** *21* (2), 119-128; (c) Posey, J. A.; Khazaeli, M.; DelGrosso, A.; Saleh, M. N.; Lin, C. Y.; Huse, W.; LoBuglio, A. F., A pilot trial of Vitaxin, a humanized anti-vitronectin receptor (anti α v β 3) antibody in patients with metastatic cancer. *Cancer Biotherapy and Radiopharmaceuticals* **2001,** *16* (2), 125-132.

11. (a) Linforth, R.; Anderson, N.; Hoey, R.; Nolan, T.; Downey, S.; Brady, G.; Ashcroft, L.; Bundred, N., Coexpression of parathyroid hormone related protein and its receptor in early breast cancer predicts poor patient survival. *Clinical cancer research* **2002,** *8* (10), 3172-3177; (b) Powell, G. J.; Southby, J.; Danks, J. A.; Stillwell, R. G.; Hayman, J. A.; Henderson, M. A.; Bennett, R. C.; Martin, T. J., Localization of parathyroid hormone-related protein in breast cancer metastases: increased incidence in bone compared with other sites. *Cancer research* **1991,** *51* (11), 3059-3061.

12. (a) Paszek, M. J.; Weaver, V. M., The tension mounts: mechanics meets morphogenesis and malignancy. *Journal of mammary gland biology and neoplasia* **2004,** *9* (4), 325-342; (b) PaszeK, M. J.; Zahir, N.; Johnson, K. R.; Lakins, J. N.; Rozenberg, G. I.; Gefen, A.; Reinhart-King, C. A.; Margulies, S. S.; Dembo, M.; Boettiger, D., Tensional homeostasis and the malignant phenotype. *Cancer cell* **2005,** *8* (3), 241-254; (c) Tilghman, R. W.; Cowan, C. R.; Mih, J. D.; Koryakina, Y.; Gioeli, D.; Slack-Davis, J. K.; Blackman, B. R.; Tschumperlin, D. J.; Parsons, J. T., Matrix rigidity regulates cancer cell growth and cellular phenotype. *Plos One* **2010,** *5* (9), e12905; (d) Tilghman, R. W.; Parsons, J. T. In *Focal adhesion kinase as a regulator of cell tension in the progression of cancer,* Seminars in cancer biology, Elsevier: 2008; pp 45-52.

13. Smith, K. E.; Hyzy, S. L.; Sunwoo, M.; Gall, K. A.; Schwartz, Z.; Boyan, B. D., The dependence of MG63 osteoblast responses to (meth)acrylate-based networks on chemical structure and stiffness. *Biomaterials* **2010,** *31* (24), 6131-6141.

14. Ruppender, N. S.; Merkel, A. R.; Martin, T. J.; Mundy, G. R.; Sterling, J. A.; Guelcher, S. A., Matrix Rigidity Induces Osteolytic Gene Expression of Metastatic Breast Cancer Cells. *Plos One* **2010,** *5* (11).

15. (a) Ratner, B. D.; Bryant, S. J., Biomaterials: where we have been and where we are going. *Annu. Rev. Biomed. Eng.* **2004,** *6*, 41-75; (b) Donaruma, L. G., Definitions in biomaterials, D. F. Williams, Ed., Elsevier, Amsterdam, 1987, 72 pp. *Journal of Polymer Science Part C: Polymer Letters* **1988,** *26* (9), 414-414; (c) ASTM F2150-02. In *Standard Guide for Characterization and Testing of Biomaterial Scaffolds Used in Tissue-Engineered Medical Products* ASTM International: West Conshohocken, PA; (d)

Migliaresi, C.; Motta, A.; DiBenedetto, A. T., Injectable Scaffolds for Bone and Cartilage Regeneration. *Engineering of Functional Skeletal Tissues* **2007**, 95-109; (e) Williams, D. F., On the nature of biomaterials. *Biomaterials* **2009,** *30* (30), 5897-5909.

16. Bohner, M., Design of ceramic-based cements and putties for bone graft substitution. *Eur Cells Mater* **2010,** *20*, 1-12.

17. (a) Campoccia, D.; Montanaro, L.; Arciola, C. R., The significance of infection related to orthopedic devices and issues of antibiotic resistance. *Biomaterials* **2006,** *27* (11), 2331-2339; (b) Gristina, A. G., Biomaterial-centered infection: microbial adhesion versus tissue integration. *Science* **1987,** *237* (4822), 1588-1595.

18. Lysaght, M. J.; Jaklenec, A.; Deweerd, E., Great expectations: private sector activity in tissue engineering, regenerative medicine, and stem cell therapeutics. *Tissue Eng. Part A* **2008,** *14* (2), 305-315.

19. (a) Domb, A. J.; Kumar, N., *Biodegradable Polymers in Clinical Use and Clinical Development*. Wiley: 2011; (b) Vernon, B., *Injectable Biomaterials: Science and Applications*. Woodhead Publishing: 2011.

20. (a) Li, Y.; Rodrigues, J.; Tomas, H., Injectable and biodegradable hydrogels: gelation, biodegradation and biomedical applications. *Chemical Society Reviews* **2012,** *41* (6), 2193-2221; (b) Nguyen, M. K.; Lee, D. S., Injectable Biodegradable Hydrogels. *Macromolecular Bioscience* **2010,** *10* (6), 563-579; (c) Guelcher, S. A., Biodegradable polyurethanes: Synthesis and applications in regenerative medicine. *Tissue Engineering Part B-Reviews* **2008,** *14* (1), 3-17; (d) Kolb, H. C.; Finn, M. G.; Sharpless, K. B., Click Chemistry: Diverse Chemical Function from a Few Good Reactions. *Angewandte Chemie International Edition* **2001,** *40* (11), 2004-2021; (e) Moreira Teixeira, L. S.; Feijen, J.; van Blitterswijk, C. A.; Dijkstra, P. J.; Karperien, M., Enzyme-catalyzed crosslinkable hydrogels: Emerging strategies for tissue engineering. *Biomaterials* **2012,** *33* (5), 1281-1290.

21. Omstead, D. R.; Baird, L. G.; Christenson, L.; Moulin, G. D.; Tubo, R.; Maxted, D. D.; Davis, J.; Gentile, F. T., Voluntary guidance for the development of tissue-engineered products. *Tissue Engineering* **1998,** *4* (3), 239-266.

22. (a) Anderson, J. M., Mechanisms of inflammation and infection with implanted devices. *Cardiovascular Pathology* **1993,** *2* (3), 33-41; (b) Belt, H.; Neut, D.; Schenk, W.; Horn, J. R.; Mei, H. C.; Busscher, H. J., Infection of orthopedic implants and the use of antibiotic-loaded bone cements: a review. *Acta Orthopaedica* **2001,** *72* (6), 557-571; (c) Schierholz, J. M.; Beuth, J., Implant infections: a haven for opportunistic bacteria. *Journal of Hospital Infection* **2001,** *49* (2), 87-93; (d) Rimondini, L.; Fini, M.; Giardino, R., The microbial infection of biomaterials: A challenge for clinicians and researchers. A short review. *J Appl Biomater Biomech* **2005,** *3* (1), 1-10.

23. SAFDAR, N.; KLUGER, D. M.; MAKI, D. G., A Review of Risk Factors for Catheter-Related Bloodstream Infection Caused by Percutaneously Inserted, Noncuffed Central Venous Catheters: Implications for Preventive Strategies. *Medicine* **2002,** *81* (6), 466-479.

24. (a) Fray, M. E.; Bartkowiak, A.; Prowans, P.; Slonecki, J., Physical and mechanical behavior of electron-beam irradiated and ethylene oxide sterilized multiblock polyester. *Journal of Materials Science: Materials in Medicine* **2000,** *11* (11), 757-762; (b) Mendes, G. C. C.; Brandão, T. R. S.; Silva, C. L. M., Ethylene oxide sterilization of medical devices: A review. *American Journal of Infection Control* **2007,** *35* (9), 574-581;

(c) Benson, R. S., Use of radiation in biomaterials science. *Nuclear Instruments and Methods in Physics Research Section B: Beam Interactions with Materials and Atoms* **2002,** *191* (1–4), 752-757.
25. (a) Adams Jr, S. B.; Shamji, M. F.; Nettles, D. L.; Hwang, P.; Setton, L. A., Sustained release of antibiotics from injectable and thermally responsive polypeptide depots. *Journal of Biomedical Materials Research Part B: Applied Biomaterials* **2009,** *90* (1), 67-74; (b) Guelcher, S. A.; Brown, K. V.; Li, B.; Guda, T.; Lee, B.-H.; Wenke, J. C., Dual-Purpose Bone Grafts Improve Healing and Reduce Infection. *Journal of Orthopaedic Trauma* **2011,** *25* (8), 477-482 10.1097/BOT.0b013e31821f624c; (c) Hafeman, A. E.; Zienkiewicz, K. J.; Carney, E.; Litzner, B.; Stratton, C.; Wenke, J. C.; Guelcher, S. A., Local delivery of tobramycin from injectable biodegradable polyurethane scaffolds. *Journal of Biomaterials Science, Polymer Edition* **2010,** *21* (1), 95-112; (d) Ji, Q. X.; Chen, X. G.; Zhao, Q. S.; Liu, C. S.; Cheng, X. J.; Wang, L. C., Injectable thermosensitive hydrogel based on chitosan and quaternized chitosan and the biomedical properties. *Journal of Materials Science: Materials in Medicine* **2009,** *20* (8), 1603-1610; (e) Leprêtre, S.; Chai, F.; Hornez, J. C.; Vermet, G.; Neut, C.; Descamps, M.; Hildebrand, H. F.; Martel, B., Prolonged local antibiotics delivery from hydroxyapatite functionalised with cyclodextrin polymers. *Biomaterials* **2009,** *30* (30), 6086-6093; (f) Li, B.; Brown, K. V.; Wenke, J. C.; Guelcher, S. A., Sustained release of vancomycin from polyurethane scaffolds inhibits infection of bone wounds in a rat femoral segmental defect model. *J. Control. Release* **2010,** *145* (3), 221-230; (g) Prestwich, G. D.; Luo, Y., Novel biomaterials for drug delivery. *Expert Opinion on Therapeutic Patents* **2001,** *11* (9), 1395-1410; (h) Shi, M.; Kretlow, J. D.; Spicer, P. P.; Tabata, Y.; Demian, N.; Wong, M. E.; Kasper, F. K.; Mikos, A. G., Antibiotic-releasing porous polymethylmethacrylate/gelatin/antibiotic constructs for craniofacial tissue engineering. *J. Control. Release* **2011**; (i) Wenke, J. C.; Guelcher, S. A., Dual delivery of an antibiotic and a growth factor addresses both the microbiological and biological challenges of contaminated bone fractures. *Expert Opinion on Drug Delivery* **2011,** *8* (12), 1555-1569.
26. Campoccia, D.; Montanaro, L.; Speziale, P.; Arciola, C. R., Antibiotic-loaded biomaterials and the risks for the spread of antibiotic resistance following their prophylactic and therapeutic clinical use. *Biomaterials* **2010,** *31* (25), 6363-6377.
27. (a) Desgranges, S.; Ruddle, C. C.; Burke, L. P.; McFadden, T. M.; O'Brien, J. E.; Fitzgerald-Hughes, D.; Humphreys, H.; Smyth, T. P.; Devocelle, M., β-Lactam-host defence peptide conjugates as antibiotic prodrug candidates targeting resistant bacteria. *RSC Adv.* **2012**; (b) Suzuki, Y.; Tanihara, M.; Nishimura, Y.; Suzuki, K.; Kakimaru, Y.; Shimizu, Y., A new drug delivery system with controlled release of antibiotic only in the presence of infection. *Journal of Biomedical Materials Research* **1998,** *42* (1), 112-116.
28. (a) Zheng, Z.; Yin, W.; Zara, J. N.; Li, W.; Kwak, J.; Mamidi, R.; Lee, M.; Siu, R. K.; Ngo, R.; Wang, J., The use of BMP-2 coupled–Nanosilver-PLGA composite grafts to induce bone repair in grossly infected segmental defects. *Biomaterials* **2010,** *31* (35), 9293-9300; (b) Stewart, R.; Goldstein, J.; Eberhardt, A.; Gabriel Chu, G. T.-M.; Gilbert, S., Increasing Vascularity to Improve Healing of a Segmental Defect of the Rat Femur. *Journal of Orthopaedic Trauma* **2011,** *25* (8), 472-476 10.1097/BOT.0b013e31822588d8.
29. Martin, J. L.; Norris, B. J.; Murphy, E.; Crowe, J. A., Medical device development: The challenge for ergonomics. *Applied Ergonomics* **2008,** *39* (3), 271-283.

30. Gupta, R. K., *Polymer and composite rheology*. CRC: 2000; Vol. 58.

31. (a) Baroud, G.; Cayer, E.; Bohner, M., Rheological characterization of concentrated aqueous β-tricalcium phosphate suspensions: The effect of liquid-to-powder ratio, milling time, and additives. *Acta Biomaterialia* **2005,** *1* (3), 357-363; (b) Dumas, J. E.; BrownBaer, P. B.; Prieto, E. M.; Guda, T.; Hale, R. G.; Wenke, J. C.; Guelcher, S. A., Injectable reactive biocomposites for bone healing in critical-size rabbit calvarial defects. *Biomedical Materials* **2012,** *7* (2), 024112; (c) Liu, C.; Shao, H.; Chen, F.; Zheng, H., Rheological properties of concentrated aqueous injectable calcium phosphate cement slurry. *Biomaterials* **2006,** *27* (29), 5003-5013.

32. Habib, M.; Baroud, G.; Gitzhofer, F.; Bohner, M., Mechanisms underlying the limited injectability of hydraulic calcium phosphate paste. *Acta Biomaterialia* **2008,** *4* (5), 1465-1471.

33. (a) Page, J. M.; Prieto, E. M.; Dumas, J. E.; Zienkiewicz, K. J.; Wenke, J. C.; Baer, P. B.; Guelcher, S. A., Biocompatibility and Chemical Reaction Kinetics of Injectable, Settable Polyurethane/Allograft Bone Biocomposites. *Acta Biomaterialia* **2012**; (b) Sarvestani, A. S.; He, X.; Jabbari, E., Viscoelastic characterization and modeling of gelation kinetics of injectable in situ cross-linkable poly (lactide-co-ethylene oxide-co-fumarate) hydrogels. *Biomacromolecules* **2007,** *8* (2), 406-415.

34. Småbrekke, A.; Espehaug, B.; Havelin, L.; Furnes, O., Operating time and survival of primary total hip replacements An analysis of 31 745 primary cemented and uncemented total hip replacements from local hospitals reported to the Norwegian Arthroplasty Register 1987–2001. *Acta Orthopaedica* **2004,** *75* (5), 524-532.

35. (a) LEESON, M. C.; LIPPITT, S. B., Thermal aspects of the use of polymethylmethacrylate in large metaphyseal defects in bone: a clinical review and laboratory study. *Clinical orthopaedics and related research* **1993,** *295*, 239; (b) Radev, B. R.; Kase, J. A.; Askew, M. J.; Weiner, S. D., Potential for thermal damage to articular cartilage by PMMA reconstruction of a bone cavity following tumor excision: A finite element study. *Journal of biomechanics* **2009,** *42* (8), 1120-1126.

36. (a) Lador, R.; Dreiangel, N.; Ben-Galim, P. J.; Hipp, J. A., A pictorial classification atlas of cement extravasation with vertebral augmentation. *The Spine Journal* **2010,** *10* (12), 1118-1127; (b) Rodrigues, D.; Gilbert, J.; Hasenwinkel, J., Pseudoplasticity and setting properties of two-solution bone cement containing poly (methyl methacrylate) microspheres and nanospheres for kyphoplasty and vertebroplasty. *Journal of Biomedical Materials Research Part B: Applied Biomaterials* **2009,** *91* (1), 248-256.

37. ISO, Biological evaluations of medical devices. In *Tests for in vitro cytotoxicity*, ISO: Geneva, Switzerland, 2009(E); Vol. 10993-5.

38. Wallin, R.; Arscott, E., A practical guide to ISO 10993-5: Cytotoxicity. *MEDICAL DEVICE AND DIAGNOSTIC INDUSTRY* **1998,** *20*, 96-98.

39. Hubbell, J. A., Biomaterials in tissue engineering. *Nature Biotechnology* **1995,** *13* (6), 565-576.

40. Göpferich, A., Mechanisms of polymer degradation and erosion. *Biomaterials* **1996,** *17* (2), 103-114.

41. Vert, M.; Li, S.; Spenlehauer, G.; Guerin, P., Bioresorbability and biocompatibility of aliphatic polyesters. *Journal of Materials Science: Materials in Medicine* **1992,** *3* (6), 432-446.

42. Antheunis, H.; van der Meer, J.-C.; de Geus, M.; Kingma, W.; Koning, C. E., Improved Mathematical Model for the Hydrolytic Degradation of Aliphatic Polyesters. *Macromolecules* **2009,** *42* (7), 2462-2471.
43. Gunatillake, P. A.; Adhikari, R., Biodegradable synthetic polymers for tissue engineering. *Eur Cell Mater* **2003,** *5* (1), 1-16.
44. (a) Lutolf, M. P.; Hubbell, J. A., Synthetic biomaterials as instructive extracellular microenvironments for morphogenesis in tissue engineering. *Nat Biotech* **2005,** *23* (1), 47-55; (b) Hsu, C. W.; Olabisi, R. M.; Olmsted-Davis, E. A.; Davis, A. R.; West, J. L., Cathepsin K-sensitive poly(ethylene glycol) hydrogels for degradation in response to bone resorption. *Journal of Biomedical Materials Research Part A* **2011,** *98A* (1), 53-62; (c) West, J. L.; Hubbell, J. A., Photopolymerized hydrogel materials for drug delivery applications. *Reactive Polymers* **1995,** *25* (2–3), 139-147.
45. Zdrahala, R. J.; Zdrahala, I. J., Biomedical Applications of Polyurethanes: A Review of Past Promises, Present Realities, and a Vibrant Future. *Journal of Biomaterials Applications* **1999,** *14* (1), 67-90.
46. Bashur, C. A.; Shaffer, R. D.; Dahlgren, L. A.; Guelcher, S. A.; Goldstein, A. S., Effect of fiber diameter and alignment of electrospun polyurethane meshes on mesenchymal progenitor cells. *Tissue Eng. Part A* **2009,** *15* (9), 2435-2445.
47. Murphy, W. L.; Dennis, R. G.; Kileny, J. L.; Mooney, D. J., Salt fusion: an approach to improve pore interconnectivity within tissue engineering scaffolds. *Tissue Engineering* **2002,** *8* (1), 43-52.
48. Park, J. H.; Cho, Y. W.; Kwon, I. C.; Jeong, S. Y.; Bae, Y. H., Assessment of PEO/PTMO multiblock copolymer/segmented polyurethane blends as coating materials for urinary catheters: in vitro bacterial adhesion and encrustation behavior. *Biomaterials* **2002,** *23* (19), 3991-4000.
49. Zia, K. M.; Zuber, M.; Bhatti, I. A.; Barikani, M.; Sheikh, M. A., Evaluation of biocompatibility and mechanical behavior of polyurethane elastomers based on chitin/1,4-butane diol blends. *International Journal of Biological Macromolecules* **2009,** *44* (1), 18-22.
50. Francois, P.; Vaudaux, P.; Nurdin, N.; Mathieu, H.; Descouts, P.; Lew, D. P., Physical and biological effects of a surface coating procedure on polyurethane catheters. *Biomaterials* **1996,** *17* (7), 667-678.
51. Tanzi, M. C.; Verderio, P.; Lampugnani, M. G.; Resnati, M.; Dejana, E.; Sturani, E., Cytotoxicity of some catalysts commonly used in the synthesis of copolymers for biomedical use. *Journal of Materials Science: Materials in Medicine* **1994,** *5* (6), 393-396.
52. Szycher, M., *Szycher's Handbook of Polyurethanes*. CRC Press LLC: Boca Raton, 1999.
53. Skarja, G.; Woodhouse, K., Structure-property relationships of degradable polyurethane elastomers containing an amino acid-based chain extender. *Journal of Applied Polymer Science* **2000,** *75* (12), 1522-1534.
54. (a) Pauluhn, J., Inhalation Toxicity of 1,6-Hexamethylene Diisocyanate Homopolymer (HDI-IC) Aerosol: Results of Single Inhalation Exposure Studies. *Toxicological Sciences* **2000,** *58* (1), 173-181; (b) Karol, M. H.; Dean, J. H., Respiratory effects of inhaled isocyanates. *CRC critical reviews in toxicology* **1986,** *16* (4), 349-379.

55. Guelcher, S. A.; Srinivasan, A.; Dumas, J. E.; Didier, J. E.; McBride, S.; Hollinger, J. O., Synthesis, mechanical properties, biocompatibility, and biodegradation of polyurethane networks from lysine polyisocyanates. *Biomaterials* **2008,** *29* (12), 1762-1775.

56. (a) Butcher, B. T.; Salvaggio, J. E.; Weill, H.; Ziskind, M. M., Toluene diisocyanate (TDI) pulmonary disease: immunologic and inhalation challenge studies. *Journal of allergy and clinical immunology* **1976,** *58* (1), 89-100; (b) Vock, E. H.; Lutz, W. K., Distribution and DNA adduct formation of radiolabeled methylenediphenyl-4, 4'-diisocyanate (MDI) in the rat after topical treatment. *Toxicology letters* **1997,** *92* (2), 93-100; (c) Bolognesi, C.; Baur, X.; Marczynski, B.; Norppa, H.; Sepai, O.; Sabbioni, G., Carcinogenic risk of toluene diisocyanate and 4, 4'-methylenediphenyl diisocyanate: epidemiological and experimental evidence. *CRC critical reviews in toxicology* **2001,** *31* (6), 737-772.

57. (a) Kim, M.-N.; Jang, J.-C.; Lee, I.-M.; Lee, H.-S.; Yoon, J.-S., TOXICITY AND BIODEGRADATION OF DIAMINES. *Journal of Environmental Science and Health, Part B* **2002,** *37* (1), 53-64; (b) Batich, C.; Williams, J.; King, R., Toxic hydrolysis product from a biodegradable foam implant. *Journal of Biomedical Materials Research* **1989,** *23* (S14), 311-319; (c) Schoental, R., Carcinogenic and chronic effects of 4, 4′-diaminodiphenylmethane, an epoxyresin hardener. **1968**.

58. (a) Adolph, E. J.; Hafeman, A. E.; Davidson, J. M.; Nanney, L. B.; Guelcher, S. A., Injectable polyurethane composite scaffolds delay wound contraction and support cellular infiltration and remodeling in rat excisional wounds. *Journal of Biomedical Materials Research Part A* **2012,** *100A* (2), 450-461; (b) Dumas, J. E.; Zienkiewicz, K.; Tanner, S. A.; Prieto, E. M.; Bhattacharyya, S.; Guelcher, S. A., Synthesis and Characterization of an Injectable Allograft Bone/Polymer Composite Bone Void Filler with Tunable Mechanical Properties. *Tissue Eng. Part A* **2010,** *16* (8), 2505-2518; (c) Guelcher, S.; Srinivasan, A.; Hafeman, A.; Gallagher, K.; Doctor, J.; Khetan, S.; McBride, S.; Hollinger, J., Synthesis, In vitro degradation, and mechanical properties of two-component poly(ester urethane)urea scaffolds: Effects of water and polyol composition. *Tissue Engineering* **2007,** *13*, 2321-2333; (d) Guelcher, S. A.; Patel, V.; Gallagher, K. M.; Connolly, S.; Didier, J. E.; Doctor, J. S.; Hollinger, J. O., Synthesis and in vitro biocompatibility of injectable polyurethane foam scaffolds. *Tissue Engineering* **2006,** *12* (5), 1247-1259; (e) Hafeman, A.; Li, B.; Yoshii, T.; Zienkiewicz, K.; Davidson, J.; Guelcher, S., Injectable Biodegradable Polyurethane Scaffolds with Release of Platelet-derived Growth Factor for Tissue Repair and Regeneration. *Pharm. Res.* **2008,** *25* (10), 2387-2399.

59. Anderson, J. M.; Rodriguez, A.; Chang, D. T., Foreign body reaction to biomaterials. *Seminars in Immunology* **2008,** *20* (2), 86-100.

60. Dimitriou, R.; Tsiridis, E.; Giannoudis, P. V., Current concepts of molecular aspects of bone healing. *Injury* **2005,** *36* (12), 1392-1404.

61. Dumas, J. E.; Davis, T.; Holt, G. E.; Yoshii, T.; Perrien, D. S.; Nyman, J. S.; Boyce, T.; Guelcher, S. A., Synthesis, characterization, and remodeling of weight-bearing allograft bone/polyurethane composites in the rabbit. *Acta Biomaterialia* **2010,** *6* (7), 2394-2406.

62. Hubbell, J. A., Bioactive biomaterials. *Current Opinion in Biotechnology* **1999,** *10* (2), 123-129.

63. Hafeman, A. E.; Zienkiewicz, K. J.; Zachman, A. L.; Sung, H. J.; Nanney, L. B.; Davidson, J. M.; Guelcher, S. A., Characterization of the degradation mechanisms of lysine-derived aliphatic poly(ester urethane) scaffolds. *Biomaterials* **2011,** *32* (2), 419-429.

64. (a) Adolph, E. J.; Hafeman, A. E.; Davidson, J. M.; Nanney, L. B.; Guelcher, S. A., Injectable polyurethane composite scaffolds delay wound contraction and support cellular infiltration and remodeling in rat excisional wounds. *Journal of Biomedical Materials Research Part A* **2012**; (b) Hafeman, A. E.; Zienkiewicz, K. J.; Zachman, A. L.; Sung, H. J.; Nanney, L. B.; Davidson, J. M.; Guelcher, S. A., Characterization of the degradation mechanisms of lysine-derived aliphatic poly (ester urethane) scaffolds. *Biomaterials* **2011,** *32* (2), 419-429; (c) Nelson, C. E.; Gupta, M. K.; Adolph, E. J.; Shannon, J. M.; Guelcher, S. A.; Duvall, C. L., Sustained local delivery of siRNA from an injectable scaffold. *Biomaterials* **2012,** *33* (4), 1154-1161.

65. Adhikari, R.; Gunatillake, P. A.; Griffiths, I.; Tatai, L.; Wickramaratna, M.; Houshyar, S.; Moore, T.; Mayadunne, R. T. M.; Field, J.; McGee, M.; Carbone, T., Biodegradable injectable polyurethanes: Synthesis and evaluation for orthopaedic applications. *Biomaterials* **2008,** *29* (28), 3762-3770.

66. Yoshii, T.; Dumas, J. E.; Okawa, A.; Spengler, D. M.; Guelcher, S. A., Synthesis, characterization of calcium phosphates/polyurethane composites for weight-bearing implants. *Journal of Biomedical Materials Research Part B: Applied Biomaterials* **2012,** *100B* (1), 32-40.

67. Jerald, E. D.; Pamela, B. B.; Edna, M. P.; Teja, G.; Robert, G. H.; Joseph, C. W.; Scott, A. G., Injectable reactive biocomposites for bone healing in critical-size rabbit calvarial defects. *Biomedical Materials* **2012,** *7* (2), 024112.

CHAPTER III

POLYURETHANES AS SUBSTRATES FOR ADVANCED ANALYSIS OF MECHANOTRANSDUCTION EFFECTS IN CANCER INDUCED BONE DISEASE

Introduction

The rigidity of the extracellular matrix is of increasing interest in the development of new, effective therapies to prevent cancer induced bone disease. Rigidity has been shown to stimulate Rho-mediated cell contractility to influence a number of cellular outcomes, including motility, morphology and differentiation[1]. When cells are cultured on gels approximating the rigidity of soft tissue, increasing rigidity of the substrate generates larger cellular traction forces that result in activation of integrins, formation of focal adhesions, and consequent activation of SFKs[2]. Up-regulation of SFKs activates Rho/ROCK signaling and subsequent phosphorylation of myosin light chain (MLC), driving increased cell contractility. In soft tissue, forces arising from ROCK-generated contractility can drive cytoskeletal remodeling, resulting in stiffening of the matrix surrounding the tumor[3] that can lead to a 100-fold increase in matrix rigidity[4]. In contrast, in the bone microenvironment, tumor cells interact with a rigid matrix that is at least 100,000,000-fold stiffer than the primary site. Consequently, the rigid mineralized bone matrix is anticipated to drive a feed-forward loop where integrin-dependent signaling is stimulated upon establishment of the tumor cells in the bone microenvironment. Since many common tumors metastasize to bone, it is of the utmost importance to study all aspects of the bone microenvironment.

Decades of research has demonstrated that once these tumor cells establish in the bone they secrete factors like parathyroid hormone related protein (PTHrP), interleukin 6 and 8, or other factors that induce osteoblast expression of Receptor Activator of NF-κβ Ligand (RANKL) that stimulates the osteoclast to resorb bone[5]. This resorption results in release of TGF-β from the bone matrix that continues to drive the expression of PTHrP (or other factors) by the tumor cells[6]. While the mechanisms of TGF-β regulation of PTHrP expression in tumor-induced bone disease have been studied extensively, it is still unclear how the bone microenvironment regulates gene expression in tumor cells or why tumors recur in the bone many years after the primary tumor has been removed. Despite these mechanistic studies, the major clinical treatments for bone metastases focus on inhibiting bone resorption. While effective, these therapies do not directly inhibit tumor burden and do not significantly extend survival, suggesting a need for newer approaches[7].

The physical rigidity of the microenvironment is one component that has been demonstrated to regulate tumor cell invasion in soft tissue. However, until our paper in 2010 it was thought that tumor cells could not respond to rigidities above that of the basement membrane[8]. While we observed that they could respond to the rigidity of bone to alter gene expression, the molecular mechanisms remained unknown. Since mechanotransduction signaling in soft tissue is regulated by integrin based focal adhesions[4, 9] and their ability to regulate contractility and invasion[10], we reasoned that integrins were involved in the response of tumors to high moduli.

While specific integrins, such as $\alpha_v\beta_3$, has been demonstrated to promote metastasis to bone[11], integrins in general have been shown to cross-talk with growth factor receptors in primary tumors, which mediates tumor malignancy and invasiveness[12]. For example, transforming growth factor-beta Receptor type II (TGF-β RII) interacts physically with $\alpha_v\beta_3$ integrin to enhance TGF-β-mediated stimulation of MAP-kinases (MAPKs) and Smad2/3-mediated gene transcription in mammary epithelial cells (MECs) during epithelial-mesenchymal transition (EMT)[13].

In the present study, we hypothesized that integrin $\alpha_v\beta_3$ mediated tumor response to the rigidity of bone and influence tumor-induced bone disease. To test our hypothesis we utilized a 2D polyurethane (PUR) film monoculture system to mimic the viscoelastic properties of the basement membrane and mineralized bone *in vitro*. These studies demonstrated that rigidity increased integrin β_3 expression, which led to a co-localization with TGF-β RII and increased expression of PTHrP, thus stimulating bone destruction. Inhibition of tumor produced integrin β_3 molecular and genetic interference decreased gene expression of PTHrP and Gli2 *in vitro* and reduced bone destruction *in vivo*.

Experimental

Synthesis of 2D Substrates for Cell Culture Experiments

2D films with varying rigidity were prepared for the cell culture experiments. The parameter typically used to quantify the rigidity of tissues and synthetic matrices is the elastic modulus, which is defined by the initial slope of the stress (σ) versus strain (ε) curve and has SI units of N/m^2 or Pascal (Pa). Unlike compliance or stiffness, the modulus is independent of the geometry of the material. Biocompatible poly(ester urethane) (PUR) substrates were synthesized and characterized as described previously[14]. Briefly, an appropriate amount of poly(ε-caprolactone-co-glycolide) triol (Mn = 300, 600, 720 or 3000 Da) was mixed with an LDI prepolymer and COSCAT 83 catalyst (Vertellus) for 20s in a Hauschild SpeedMixerTM DAC 150 FVZ-K vortex mixer

(FlackTek, Inc, Landrum, SC). The targeted index (ratio of NCO to OH equivalents times 100) was 105. The resultant mixture was poured into the wells of a tissue culture plate and allowed to cure for 24h at 60° C. To facilitate cell adhesion and ensure that the surface chemistry was constant for all substrates tested, fibronectin (Fn) was adsorbed to the surface of the substrates by incubation in a 4 μg/mL solution of Fn in PBS at 4^oC overnight.

Fibronectin Characterization

To measure the surface concentration of Fn, coated substrates were incubated in a solution of Fn antibody (1:1000) followed by incubation with a secondary HRP-conjugated antibody. The relative amount of adsorbed antibody was then quantified by reaction with 2'- azino-bis(3-ethylbenzthiazoline-6-sulphonic acid) (ABTS) and subsequent optical density reading at 405nm. All PUR and PAA and were prepared at the same surface concentration of Fn (1.9 μg cm-2).

Mechanical Testing

PUR films and scaffolds were analyzed with an Agilent G200 nanoindenter (Agilent Technologies, Chandler, AZ) to determine the elastic modulus at the cellular interface of the materials. All the samples are probed by a diamond Berkovich indenter tip, which has been calibrated from indents made on fused silica. All the nanoindentation experiments were conducted at a constant strain rate of 0.05. The elastic modulus and hardness values were determined by the method proposed by Oliver and Pharr, shown in equations 1-3[15]. The depth of contact is derived from an empirical equation relating the tip geometry, load, and stiffness of the material, shown in equation 1 and Figure 3.1. The material stiffness, S, is defined as the slope of the unloading curve. Once the depth of contact is obtained, the elastic modulus can be derived from first determining the reduced modulus, equation 2, and then applying equation 3.

$$h_c = h - 0.75\frac{P}{S} \tag{1}$$

Where h_c is the depth of contact of the indenter into the sample, h is the full depth of penetration, P is the load, and S is the material stiffness.

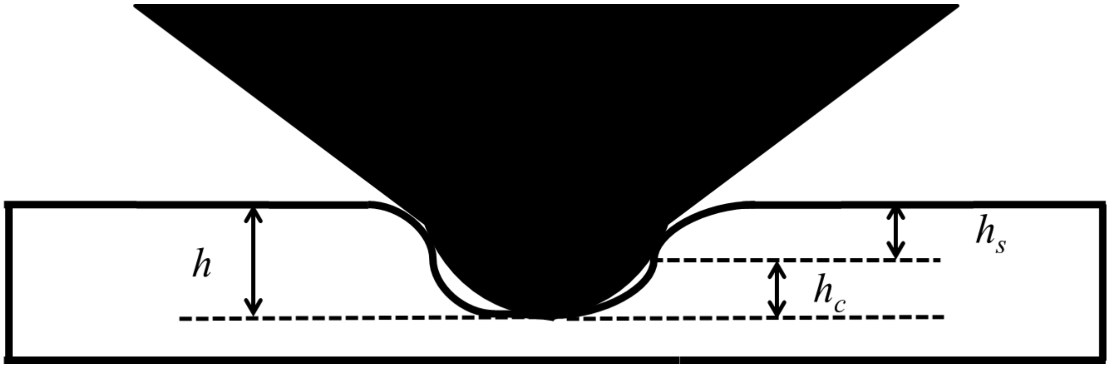

Figure 3.1. Diagram of the interaction between the nanoindenter and the sample.

$$E_r = \frac{\sqrt{\pi}}{2}\frac{S}{\sqrt{A}} \tag{2}$$

Where E_r is the reduced modulus and A is the contact area.

$$E_{IT} = (1 - v_s^2)\left[\frac{2}{S}\sqrt{\frac{A}{\pi}} - \frac{1-v_i^2}{E_i}\right]^{-1} \tag{3}$$

Where E_{IT} is the indentation area, $v_{i,s}$ is the Poisson ratio for either the indenter or the sample, respectively.

Cell Culture

MDA-MB-231 cells were originally derived from ATCC (Manassas, VA) and selected for the ability to metastasize to bone[16]. MDA-MB-231 cells stably expressing a dominant negative (MDA-KDΔ4) form of ROCK were transfected and maintained as described previously[14]. The human squamous cell lung carcinoma cell line RWGT2 was purchased from ATCC (Manassas, VA) and a bone specific clone was generated in our lab. Cells were maintained and cultured at 37^{o}C under 5% CO2 in 1x DMEM (MDA-MB-231) or MEMα (RWGT2) plus 10% heat inactivated FBS and 1% penicillin/streptomycin.

shRNA Transfections

MDA-MB-231 cells were stably transfected with 1 µg of shRNA for either human integrin β_3 subunit or control shRNA plasmid (SantaCruz) according to manufacturer's instructions. Transfected lines, β_3 KD cells, were maintained in DMEM plus 10% heat inactivated FBS, 1% penicillin/streptomycin and 5µg/mL puromycin.

Quantitative Real-Time PCR

To measure changes in gene expression, mRNA reverse transcription was carried out using the Quantitect Reverse Transcription kit (Qiagen) per manufacturer's instructions. Briefly, cells were harvested with trypsin after 24 h in culture and total RNA was extracted using the RNeasy Mini Kit (Qiagen). The Quantitect Reverse Transcription kit was used to synthesize cDNA using 1µg total RNA. The expression of PTHrP, Gli2, integrin-β_3 and TGF-β RII was measured in triplicate by quantitative RT-PCR using validated TaqMan primers with the 7300 Real-Time PCR System (Applied Biosciences) using the following cycling conditions: 95°C for 15 seconds and 60°C for 1 minute, preceded by an initial incubation period of 95°C for 10 minutes. Quantification was performed using the absolute quantitative for human cells method using 18S as an internal control. The expression of osteopontin (OPN), interleukin-11 (IL11), CXCR4, connective tissue growth factor (CTGF), and matrix metalloproteinase-9 (MMP9) was determined using SYBR green primers as described previously[17].

Western Blots

Cells were harvested 48 h after seeding on substrates in a radioimmunoprecipitation buffer containing a cocktail of protease and phosphatase inhibitors (Roche, Basel, Switzerland). Equal protein concentrations were prepared for loading with NuPAGE sample buffer (Invitrogen) and separated on a 12% SDS-PAGE gel (Biorad). Proteins were transferred to a PVDF membrane and blocked with 5% BSA in TBS containing 0.1% Tween-20 for 1h at room temperature, followed by incubation with either phospho-p38MAPK (1:1000, Cell Signalling), p38MAPK (1:1000, Cell Signalling), phospho-Smad2/3 (1:1000, Millipore) or Smad2/3 (1:1000, Millipore) antibodies overnight at 4°C. After washing, membranes were blotted with anti-rabbit IgG (1:2000), and bands were detected by enhanced chemiluminescence. Membranes were then stripped and reprobed using an antibody for β-actin (1:5000, Invitrogen) as a loading control.

Immunoprecipitation

To investigate association of membrane proteins, cells were lysed using a 1% Nonidet-P40 buffer containing a cocktail of protease and phosphatase inhibitors. 400μg total protein lysate per tube was incubated overnight at 4°C under gentle end-over-end mixing with anti-TGF-β RII (1 μg, Santa Cruz). Subsequently, the immune complex was captured with protein A/G agarose resin, thoroughly washed with lysis buffer and eluted with non-reducing sample buffer. Proteins were then separated on an SDS-PAGE gel (7.5%, Biorad) and transferred to a PVDF membrane. Following blocking with 5% milk, membranes were incubated with anti-integrin β_3 (Santa Cruz, 1:1000) at 4°C overnight.

After washing, membranes were blotted with anti-rabbit or anti-mouse IgG (1:5000), and bands were detected by enhanced chemiluminescence.

Förster Resonance Energy Transfer (FRET) Microscopy

To investigate the association of TGF-β and Integrin β_3, we performed Förster Resonance Energy Transfer (FRET) and confocal microscopy. Briefly, the donor antibody: anti-Integrin β_3 (SantaCruz) was labelled with Alexa Fluor® 488 Carboxylic Acid, Succinimidyl Ester (Life Technologies) (ITG-β_3-488) and the acceptor antibody: anti TGF-β receptor type 2 (SantaCruz) was labelled with Alexa Fluor® 546 Carboxylic Acid, Succinimidyl Ester (Life Technologies) (TGF-β RII-546) in a 2.25:1 molar ratio of antibody:dye overnight at 4˚. Labelled antibody was purified with size exclusion chromatography using PD-10 Desalting Columns (GE Healthcare). MDA-MB-231 and RWGT2 cells were grown on discs of rigid and compliant 2D PURs. After 24 hours of culture, cells were fixed with 10% Formaldehyde in PBS and stained overnight at 4˚ with ITG-β_3-488, TGF-β RII-546, ITG-β_3-488 + TGF-β RII-546 or IgG control (1ug/1x10^6 cells). Images were taken with a Zeiss LSM 510 inverted confocal microscope. FRET experiments were performed on a BioTek Synergy 2 using excitation filter 485/20 and emission filter 590/35. Data was normalized to fluorescence of IgG control.

Drug Treatments

Cells were pretreated with the Smad-3 inhibitor, SIS3 (EMD4Biosciences, 10 μM) or the p38 MAPK inhibitor SB202190 (Tocris, 10μM), for one hour and harvested. To stimulate TGF-β signalling, cells were treated with either 5 ng/mL TGF-β or TGF-β vehicle (5% BSA-HCL) in serum-free media for 24 h prior to harvesting.

Animal Experiments and Analysis

Confluent MDA-MB-231 cells, KDΔ4 or β_3 KD human breast cancer cells were trypsinized, washed, and resuspended in PBS for injection into the right tibia of anesthetized 4-week-old female athymic nude mice (Harlan Sprague Dawley, Inc.) at 2.5×10^5 cells per mouse. Contralateral intratibial injections of PBS were used as an internal control for each mouse. Animals were euthanized four weeks after injection. Hind limb specimens (tibia and femora) were removed during autopsy and fixed in 10% neutral-buffered formalin (Fisher Scientific) for 48 hours at room temperature. Bone specimens were decalcified in 10% EDTA for 2 weeks and embedded in paraffin. Bone sections were stained with hematoxylin, eosin, orange G, and phloxine. Histomorphometry was used to analyze tumor burden in the tibia and femurs using Metamorph software (Molecular Devices, Inc.). Specifically, using the drawing tool in Metamorph, the region between the cortices directly below the growth plate was selected and calculated by the software as the total area in squared centimeters. The tumor, as determined by H&E staining, was selected using the same approach. Tumor burden was calculated as a percentage of tumor area over total tissue area. Multiple levels of bone sections were stained and imaged, and all statistical analyses were quantified at the same histomorphometric level.

Radiographs of mice

Animals were anesthetized deeply and laid down in a prone position on the platform of the Faxitron LX-60. Images were acquired at 35 kV(p) for 8 seconds. Lesion area and lesion number were determined using quantitative image analysis software (Metamorph; Molecular Devices).

Ex-vivo μCT analysis

Tibias were analyzed using the Scanco μCT 40. Specifically, 100 slices from the proximal tibia were scanned at 12-μm resolution. Images were analyzed using the Scanco Medical Imaging software to determine the VOX–bone volume.

Statistical analysis

All statistical analyses were performed using InStat version 3.03 software (GraphPad Software, Inc.). Values are presented as mean ± SEM, and *P* values determined using unpaired *t* test, where *, $P < 0.05$; **, $P < 0.01$; ***, $P < 0.001$ unless otherwise stated.

Results

The PUR films were analyzed for rigidity by the slope of the unloading curve of a nanoindentation plot (Figure 3.2). Nano-indentation is utilized to determine the mechanical properties of materials on a highly localized scale that is relevant for cellular traction forces[18]. Table 3.1 displays the elastic modulus in kPa for each PUR film. PUR-3 and PUR-30 films are designated rigid and compliant films respectively.

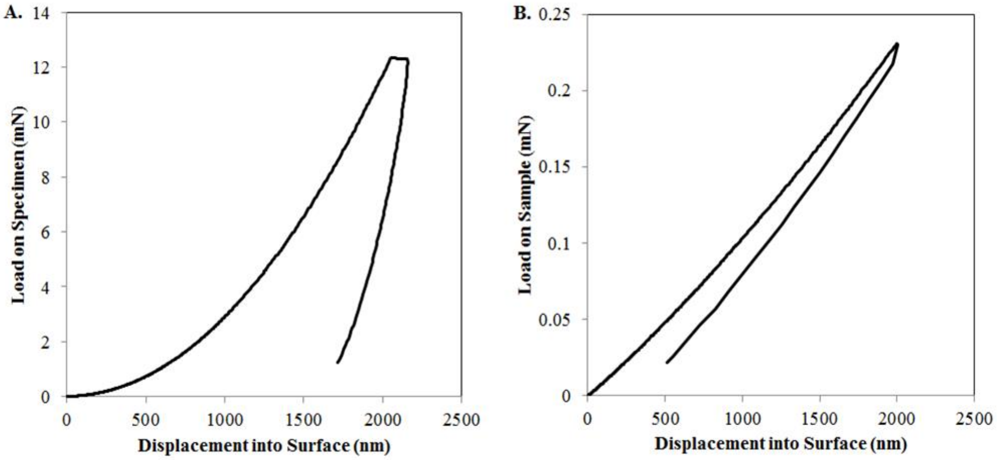

Figure 3.2. Representative nanoindentation curves for rigid (A) and compliant (B) PUR films.

Table 3.1. Elastic modulus in (kPa) of PUR films as measured by nano-indentation.

Sample Designation	Elastic Modulus (kPa)
PUR-3	$3.8*10^6 \pm 1*10^5$
PUR-6	$8*10^4 \pm 7*10^3$
PUR-30	$2.5*10^5 \pm 5*10^3$

We previously reported that PTHrP and Gli2 expression is regulated by ROCK[14], a known downstream effector of integrin signaling. However it remained unknown what regulated the response to rigidity upstream. Integrins are well-established regulators of rigidity mediated responses, specifically, the $\alpha_v\beta_3$ integrin has been shown to regulate migration and early stage invasiveness in metastatic bone cancer cell lines[10]. Since one of the primary binding ligands for $\alpha_v\beta_3$ is fibronectin (Fn), Fn was deposited onto PUR films and cell culture dishes to ensure $\alpha_v\beta_3$ binding was isolated. The effect of Fn concentration was found to be minimal above 0.5 μg/mL. *In vitro* studies with PUR films coated with poly-l-lysine, a positively charged polymer that only would allow for electrostatic binding, or other binding proteins such as vitronectin or type I collagen produced non-significant or reveresed gene expression for PTHrP, Gli2 and integrin β_3 (Figure 3.3).

PUR films, coated with Fn, were utilized to analyze the gene expression of MDA-MB-231 and RWGT2 cells as a function of rigidity. Both cell lines are prone to metastatic invasion of bone which often results in osteolytic tumors. Interestingly, both cell lines expressed significantly increasing ($p<0.001$) amounts of PTHrP, Gli2 and the integrin β_3 subunit as the rigidity is increased from basement membrane levels to that of trabecular bone (Figure 3.3 A-C). Up-regulation of integrins as a function of rigidity has been seen in cancers in the primary site[19], however, the range of rigidity spanned is orders of magnitudes lower than the PUR films utilized in this study. These results reveal that the mechanosensing of rigidity is highly specific to the associated pathological sites. Since it has been shown that integrin $\alpha_v\beta_3$ is highly influential in bone metastatic cancer cells further analysis into the relationship between the expression of osteolytic factors and integrin β_3 was conducted.

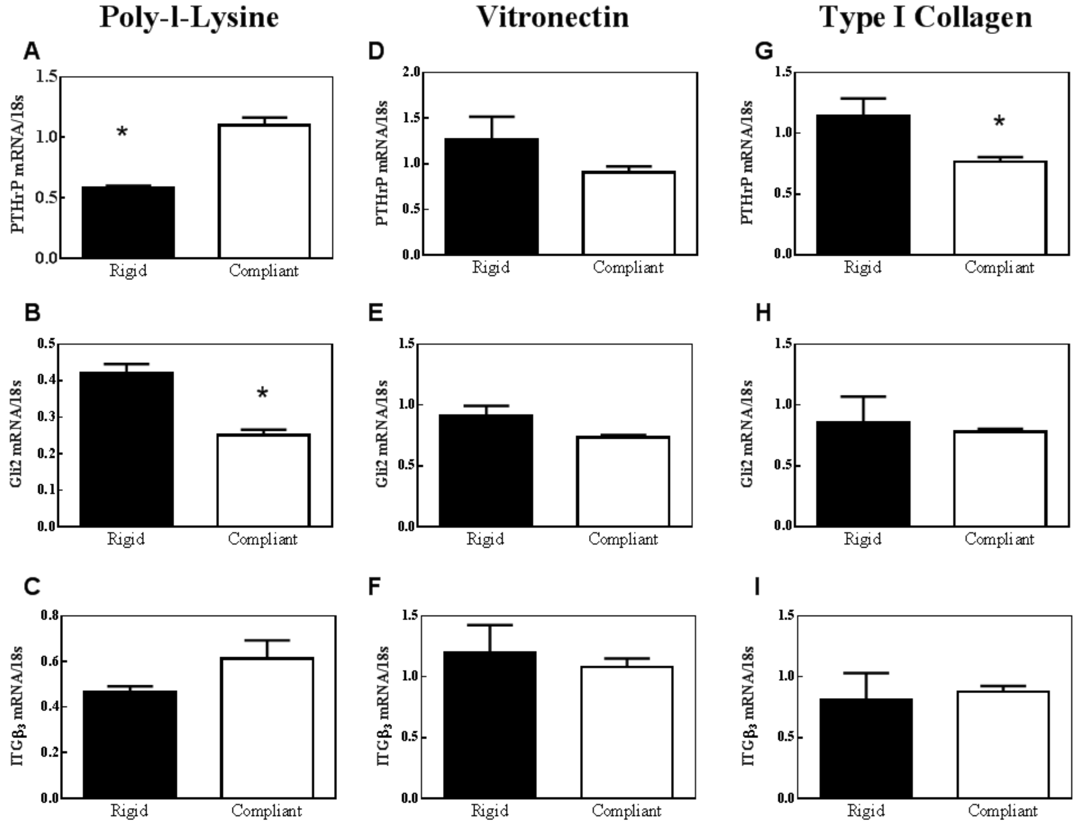

Figure 3.3. PTHrP, Gli2 and integrin β_3 gene expression of MDA-MB-231 cells cultured on rigid and compliant PUR films coated with poly-l-lysine (A-B), vitronectin (D-F) or type I collagen (G-I).

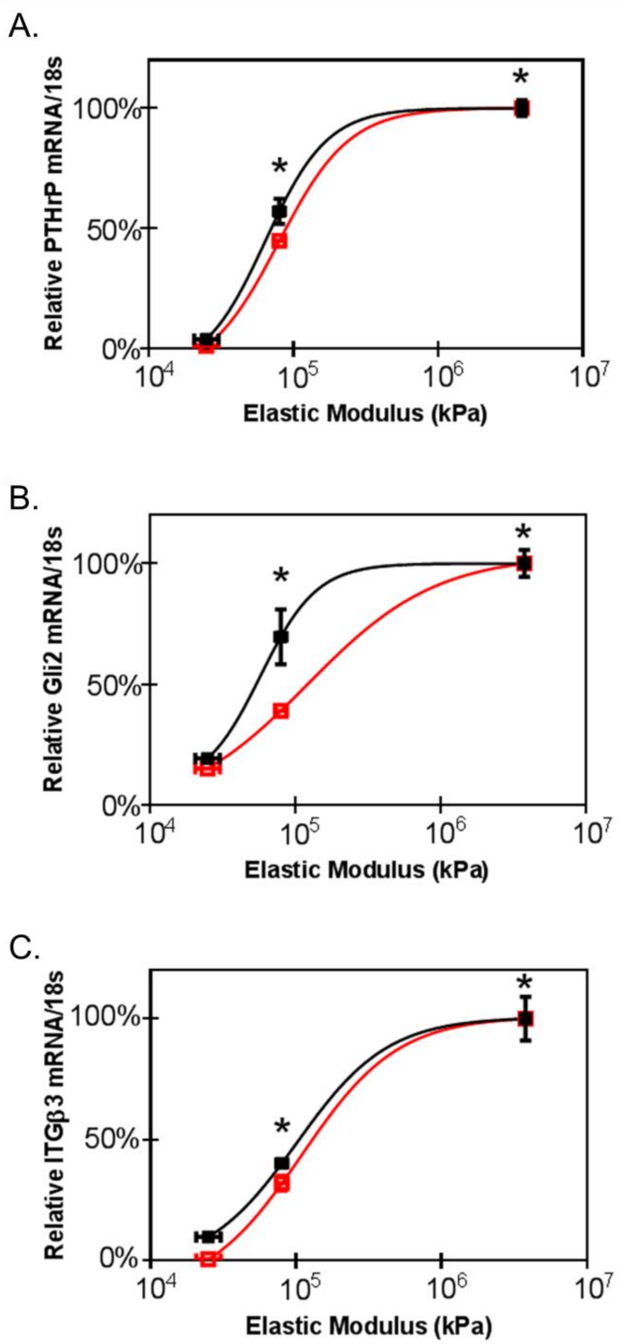

Figure 3.4. Gene expression of osteolytic factors and integrin-β3 as a function of rigidity. Gene expression of PTHrP (A), Gli2 (B) and integrin-β3 (C) for MDA-MB-231 cells (black squares and black lines) and RWGT2 cells (red squares and red lines) seeded on polyurethane scaffolds of increasing rigidity. The fit lines are derived from a sigmoidal fit of the data R^2>0.92 for all curves.

The effect of integrin β_3 on PTHrP and Gli2 expression was investigated by utilizing MDA-MB-231 cells transfected with shRNA for the integrin β_3 subunit (β_3 KD cells, 90% KD, Figure 3.5) and MDA-MB-231 cells treated with an inhibitor of $\alpha_v\beta_3$ integrin (LM609). Both treatments produced a significant decrease ($p<0.01$) in PTHrP mRNA (Figure 3.6 A&E) and Gli2 mRNA (Figure 3.5 B&F) compared to control groups. The effect of integrin concentration on osteolytic gene expression was tested on rigid and compliant substrates with MDA-MB-231 cells transfected to over express integrin β_3. The overexpressed cells resulted in higher levels of osteolytic gene expression on compliant substrates (supplemental information). The increased gene expression on compliant substrates could be due to the increased cell contractility that has been shown to occur in cells overexpressing integrin β_3[10a]. Taken together these results are one of the first to designate the link between osteolytic gene expression and integrin activity.

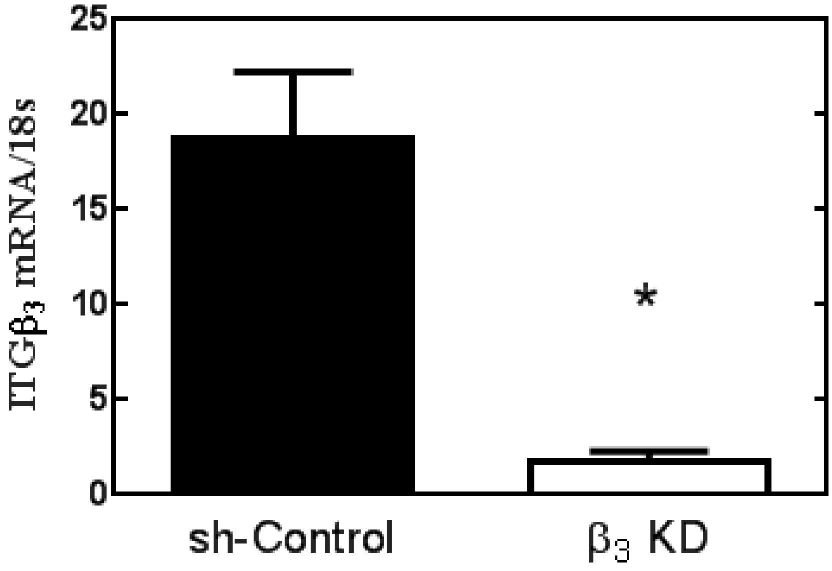

Figure 3.5. Integrin β_3 gene expression of β_3 KD cells compared to mock transfected controls.

It is widely understood that the TGF-β signaling pathway is known to stimulate expression of osteolytic factors such as PTHrP and Gli2[6a]. To test whether this stimulation was affected by integrin β_3, the inhibited MDA-MB-231 cells were treated with exogenous TGF-β. In both cases, inhibition of the β_3 integrin subunit reduced PTHrP and Gli2 mRNA expression significantly ($p<0.01$; Figure 3.6 C-D & G-H). Furthermore, exogenous TGF-β treatment was not able to significantly increase the PTHrP or Gli2 expression in the inhibited cells (Figure 3.6 C-D & G-H). The exogenous TGF-β treatment had no effect on the gene expression of integrin β_3 in control or β_3 KD cells, indicating the regulation of the integrin subunit is not directly related to the TGF-β KD signaling (Figure 3.7). While targeting integrin $\alpha_v\beta_3$ has been widely utilized as a potential anti-cancer therapeutic, with varying degrees of success[20], there is still a debate about its mechanism of action. Inhibition of $\alpha_v\beta_3$ is thought to prevent angiogenesis and adhesion[11b, 20c, 21], however, our data suggests that it affects the gene expression of osteolytic factors as well.

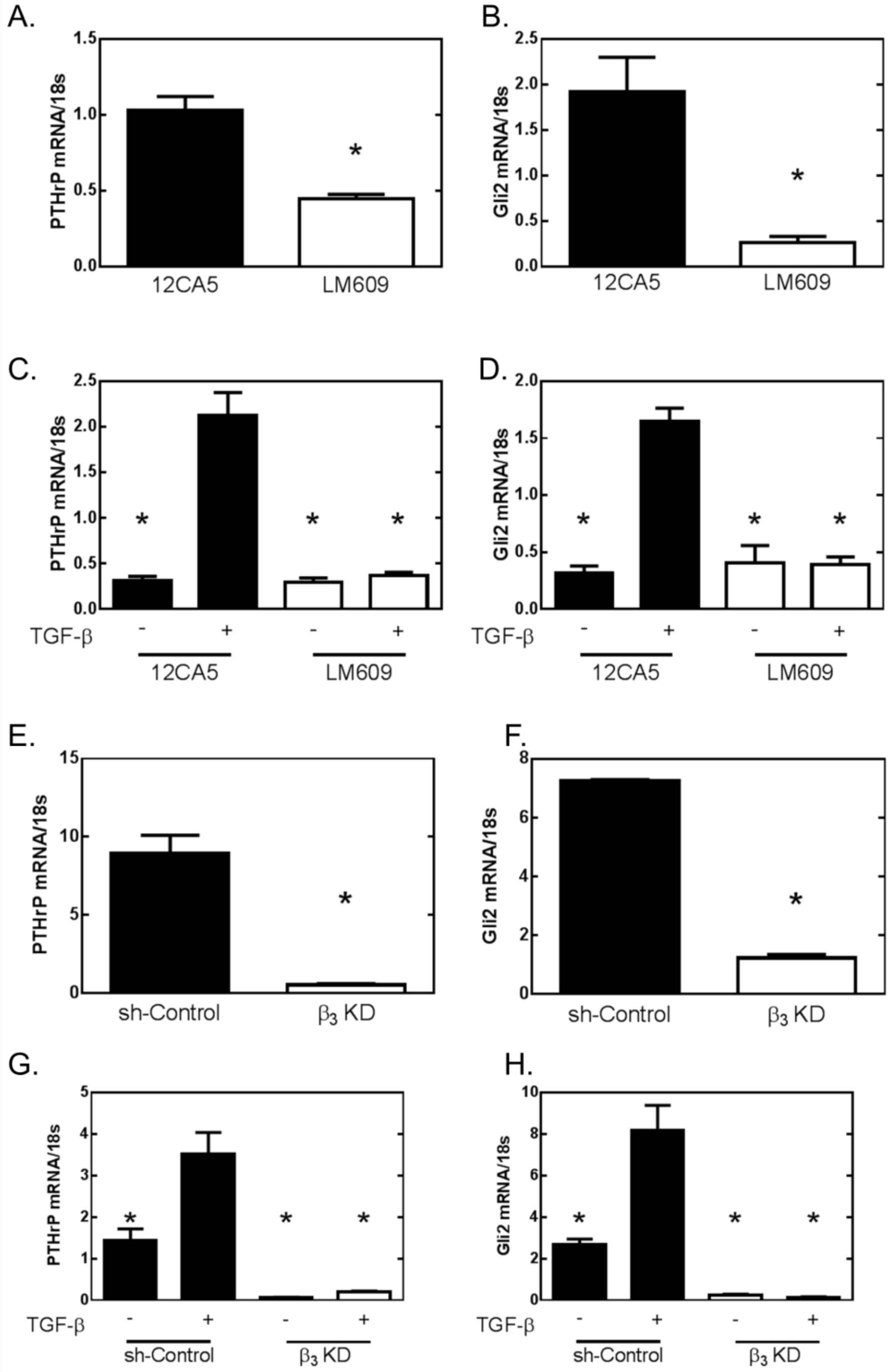

Figure 3.6. TGF-β stimulation is negated by genetic or molecular inhibition of integrin-β_3 subunit. PTHrP and Gli2 levels are significantly reduced when integrin-β_3 subunit is knocked down with the integrin specific antibody, LM609 (A-D) or when a targeted shRNA (E-H) is utilized. The addition of exogenous TGF-β is unable to increase the levels of PTHrP and Gli2 in either case (C-D & G-H).

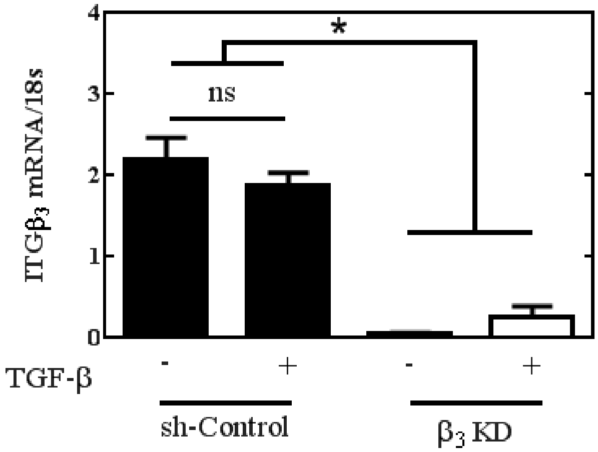

Figure 3.7. Integrin β_3 gene expression of mock transfected MDA-MB-231 and β_3 KD cells with or without exogenous TGF-β.

We have shown that integrin β_3 is activated on a range of modulus that is relevant to the bone microenvironment and that inhibition is enough to limit the osteolytic gene expression of metastatic cancer cells, yet the underlying mechanism for this phenomenon was not explained. It has been previously reported that integrins cluster with various receptors to greatly alter gene expression during EMT[13]. Specifically, it was shown that src phosphorylates TGF-β RII following clustering with β_3 integrin subunit[13]. This led to the analysis of clustering of membrane proteins by immunoprecipitation in response to substrate rigidity, where we found that TGF-β RII associated with the integrin β_3 subunit in MDA-MB-231 cells cultured on rigid, bone-like substrates, but not on compliant substrates approximating basement membrane (Figure 3.8).

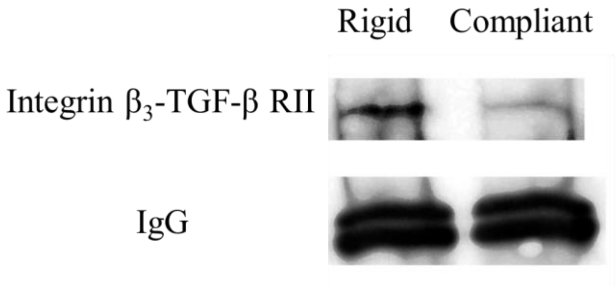

Figure 3.8. Immunoprecipitation of the interaction of integrin β_3 and TGF-β RII with MDA-MB-231 cells cultured on rigid and compliant films.

To further analyze this interaction, Förster resonance energy transfer (FRET) analysis was conducted with MDA-MB-231 and RWGT2 cells cultured on rigid and compliant films. Upon incubation with anti-bodies for integrin β_3 and TGF-β RII that were labeled with a fluorescent FRET pair, both MDA-MB-231 and RWGT2 cells induced a FRET response when cultured on substrates approaching bone rigidity, while there was no FRET signal on compliant substrates (Figure 3.9). The most noticeable difference in the single channel fluorescence is the expression of integrin β_3, which increases significantly on rigid substrates. The fluorescent emission associated with TGF-β RII is not affected by rigidity (Figure 3.9A&D) and this was correlated with gene expression (Figure 3.10). To ensure that the Fn coating was not affecting the expression of either FRET target, a dose response analysis was conducted (Figure 3.9E). It was found that even low levels of Fn coatings (0.5 and 2 μg/mL) produced a significant ($p<0.05$) FRET response and that response was not significantly altered with high levels of Fn coatings (12 and 50 μg/mL). These results show that the increased activation of integrin β_3 on rigidities that mimic the bone microenvironment are inducing crosstalk events with the already overexpressed TGF-β signaling pathway and this interaction is resulting in osteolytic gene expression. Whether the interaction between the integrin and

TGF-β RII is due to the increase in the number of integrins on the surface or a more complex interaction, MDA-MB-231 cells were transfected to overexpress integrin β_3 and cultured on rigid and compliant PUR films. The expression of PTHrP was increased on compliant substrates and there was no significant difference in gene expression on cells cultured on rigid and compliant PUR films (Figure 3.11). This seems to point to the fact that there is an independent, diffusion limited threshold between the integrin β_3 and TGF-β RII interacting and bone like rigidity stimulates the tumor cells to express more integrins pushing over this threshold.

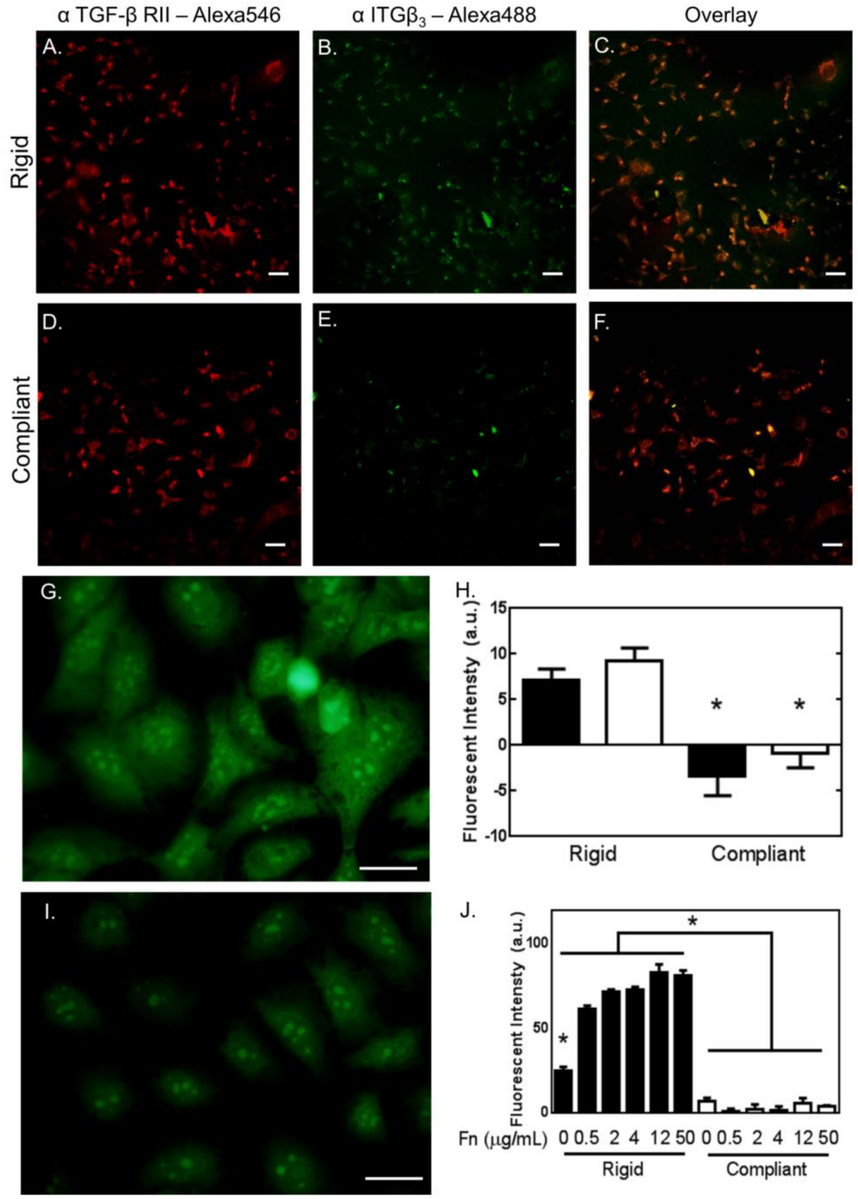

Figure 3.9. Proximity of TGF-β RII and integrin-β_3 subunit in MDA-MB-231 cells point to a potential crosstalk event. Fluorescently labeled antibody staining for TGF-β RII (Alexa 546; A&D) and integrin-β_3 subunit (Alexa 488; B&E) on rigid and compliant PUR surfaces show increases in integrin β_3 subunit, while TGF-β RII remains relatively constant (A-F). Förster energy resonance transfer (FRET) quantification of the fluorescent antibodies reveals a significant difference of FRET expression on rigid PUR surface indicating close proximity of TGF-β RII and integrin-β_3 subunit on the cell membrane for both MDA-MB-231 (black) and RWGT2 cells (white) (B). High magnification fluorescent images of MDA-MB-231 cells cultured on rigid (G) and compliant (I) PUR films show the differences in integrin β_3 expression. Panel J shows the effect of fibronectin concentration on the quantified FRET response with MDA-MB-231 cells.

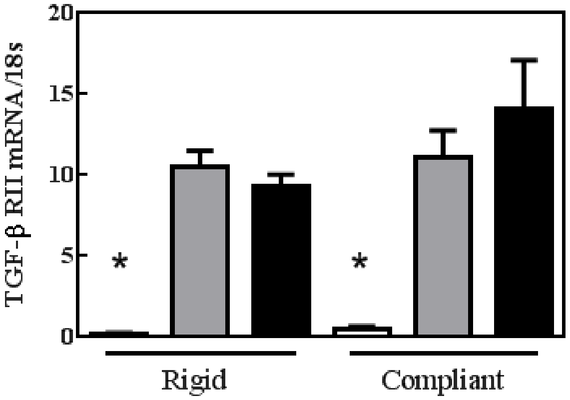

Figure 3.10. TGF-β RII gene expression is not affected by rigidity. TGF-β RII gene expression of MCF-7 (white), RWGT2 (grey), and MDA-MB-231(black) cells cultured on rigid and compliant films.

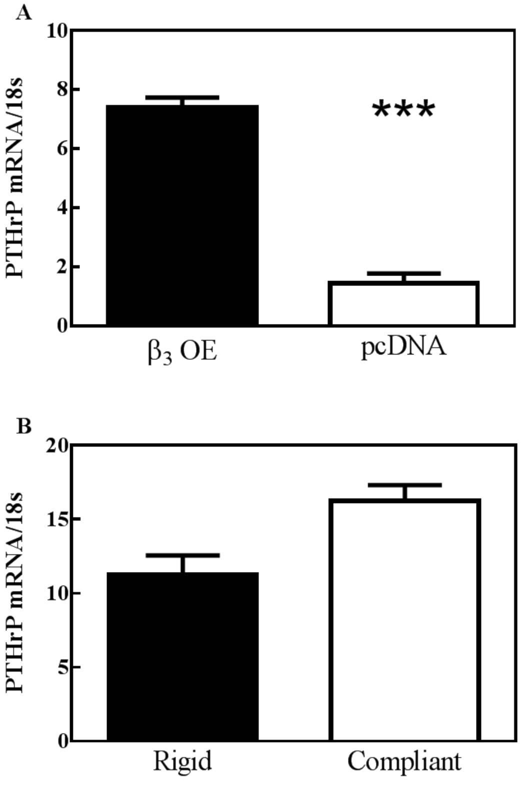

Figure 3.11. PTHrP gene expression is increased when integrin β_3 is overexpressed. PTHrP gene expression of β_3 OE compared to mock treated MDA-MB-231 cells (A) and PTHrP gene expression of β_3 OE cells cultured on rigid and compliant films (B).

Since we TGF-β signaling was involved in the response of tumor cells to rigidity and TGF-β signaling in bone metastases can be mediated through Smad or p38 MAPK-dependent downstream signaling[22], we investigated whether one or both of these pathways was required for tumor cells to respond to bone rigidity. Western blot analysis showed that the phosphorylation of p38-MAPK increased when in MDA-MB-231 cells were cultured on rigid substrates as compared to those grown on compliant substrates (Figure 3.12), suggesting an important role of p38 MAPK in tumor response to bone rigidity. Additionally, SMAD2/3 was also shown to increase with rigidity. Taken together this suggests that both play a role, but that p38MAPK may be the predominant signaling pathway for the response to bone rigidity.

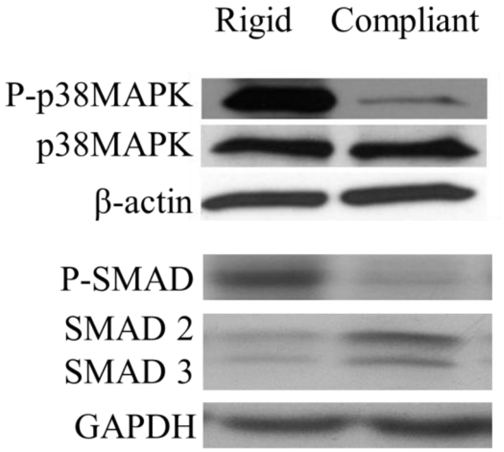

Figure 3.12. Rigidity influences MAPK and SMAD expression and inhibition of these downstream molecules results in decreased osteolytic gene expression.

Since inhibition of integrin β_3 with shRNA reduced the expression of osteolytic factors *in vitro*, we reasoned that this would block tumor-induced bone disease. Therefore, we injected MDA-MB-231 cells stably expressing the β3 shRNA into the tibia of nude mice. Ex vivo analyses using μCT (Figure 3.13A-C) and histomorphometry (Figure 3.13D-F) demonstrated an increase in the BV/TV of β_3 KD cells compared to control cells, but did not have a significant effect on tumor growth. Analysis of x-ray scans of the bone indicate a lower number of osteolytic lesions in β_3 KD inoculated animals (Figure 3.13G-I). There were no differences in growth or expression of common cancer genes by the β_3 KD cells compared to the mock transfected controls (Figure 3.14). This indicates that the differences in osteolysis were a product of the inhibition of integrin β_3.

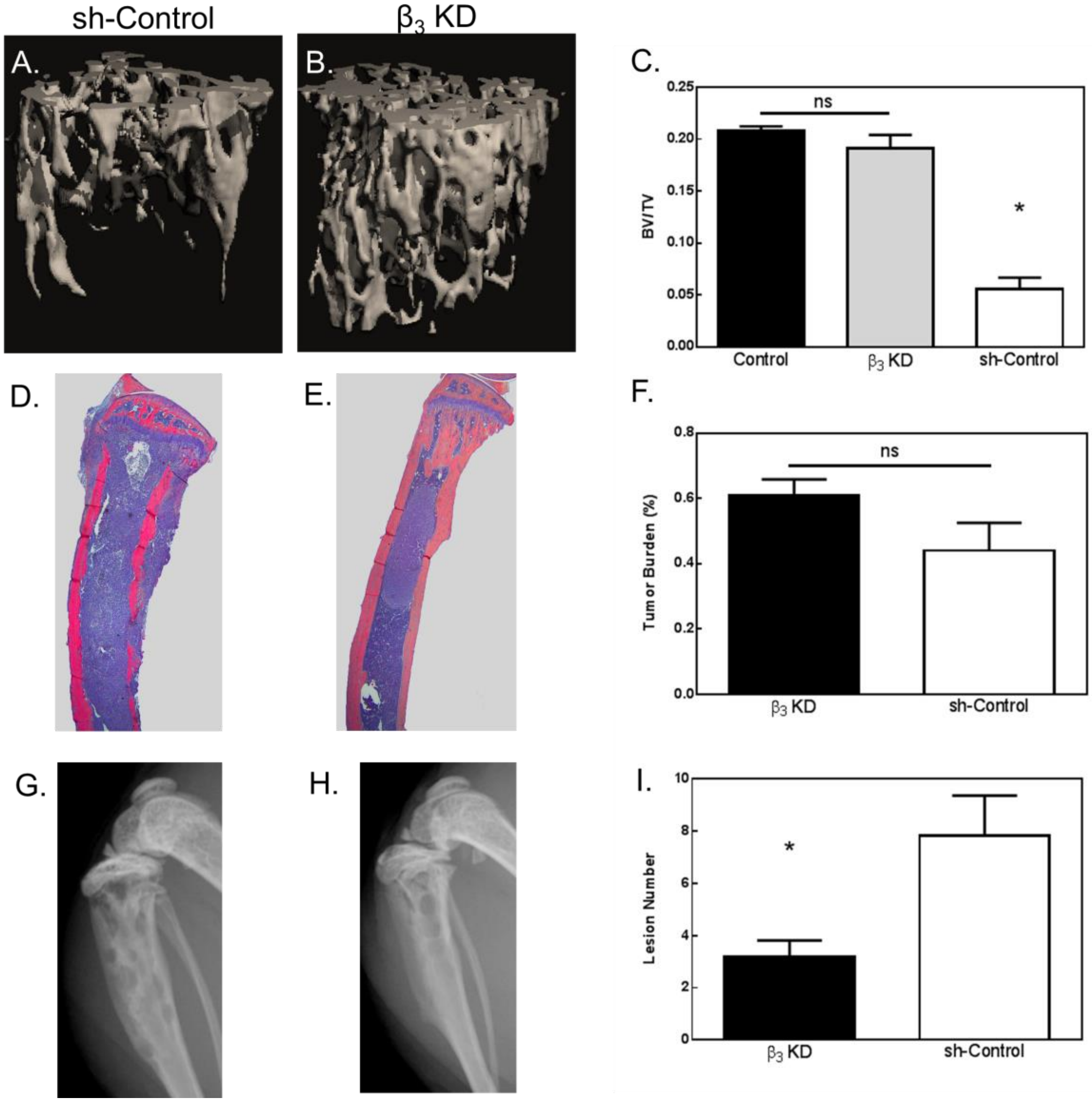

Figure 3.13. Genetic inhibition of integrin-β_3 subunit in MDA-MB-231 cells transplanted into the tibia of immunocompromised mice reduces the osteolytic effects. μCT renderings of control cells and β_3 KD cells significantly decreased bone destruction (A-B), which is mirrored in the quantified bone volumes (C). Histological analysis shows no reduction in tumor burden in the bone, but an odd migration of the tumor into the marrow space (D-F). Additionally, x-ray scans (G-H) and the resulting quantification of lesion numbers show a reduced number of osteolytic lesions in β_3 KD treated animals (I).

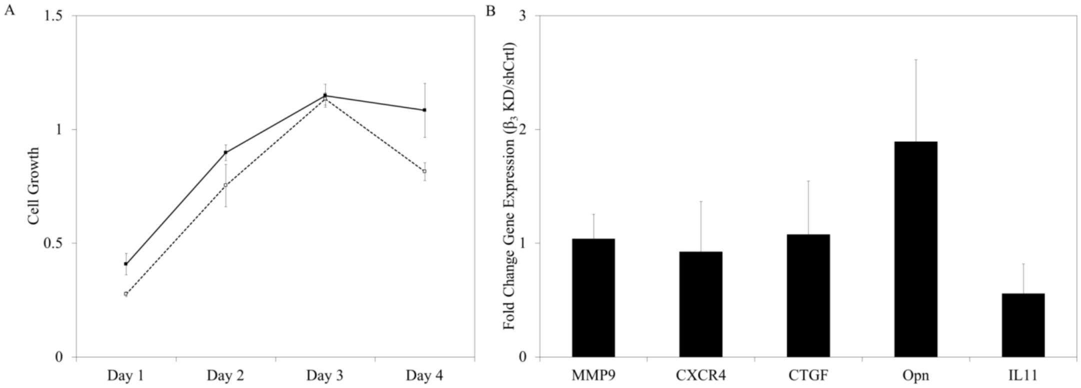

Figure 3.14. Comparison of growth and common markers of cancer cells between β_3 KD and control cells. MTS assays of the β_3 KD (filled squares-solid line) and control cells (empty squares-dashed line) showed no difference in growth patterns (A). Fold change of gene expression of common cancer markers also show no change between β_3 KD cells and controls.

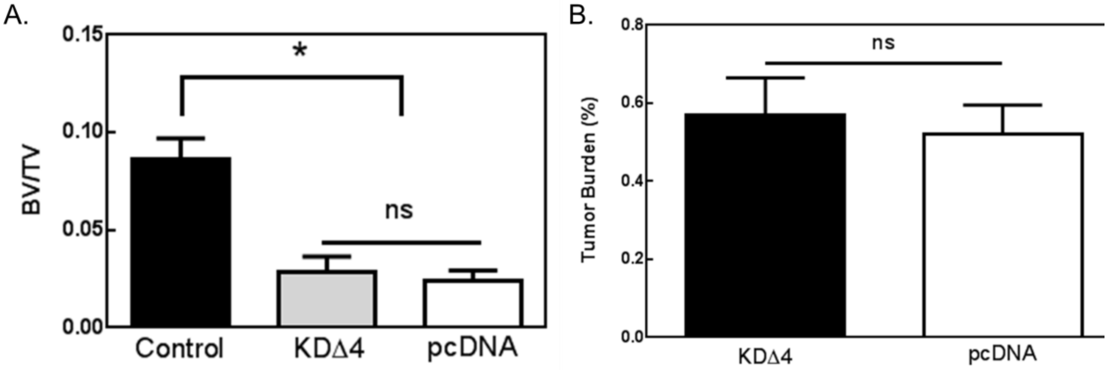

Figure 3.15. Inhibition of ROCK (KDΔ4 cells), a downstream mechanotransduction regulator, does not produce the same effects of reduced osteolysis *in vivo*. μCT quantification of bone volume (A) and histological analysis of tumor burden (B) show no significant differences between KDΔ4 cells and mock transfected controls.

Interestingly, when downstream ROCK signaling (a downstream mediator of mechanotransduction) was blocked using a dominant negative construct, KDΔ4 cells, bone resorption was also inhibited as determined by increased BV/TV by μCT, but to a lesser extent than the β_3 KD cells (Figure 3.15). These data further indicated that integrin β_3 plays an important role for regulating the expression of PTHrP and bone destruction, and that using β_3 inhibitors may reduce tumor induced bone disease, while alternative mechanotransduction inhibitors may not result in the same affect *in vivo*.

Discussion

In this study we show that PTHrP and Gli2 expression is mediated by two synergistic mechanisms (1) mechanotransduction induced integrin clustering on substrates mimicking the rigidity of bone and (2) an altered TGF-β signaling pathway driven by enhanced interaction with clustered integrins and downstream p38 MAPK phosphorylation. We chose to focus our studies on the TGF-β crosstalk with integrin and TGF-β RII pathways, since clustering of $\alpha_v\beta_3$ with TGF-β RII is known to activate MAPK signaling, a known driver of osteolytic gene expression[13]. Interaction between TGF-β RII and $\alpha_v\beta_3$ has also been associated with EMT[13], a process influenced by tissue rigidity[4, 9b]. However, these studies focused only on the effects of rigidity for gels approximating soft tissue (~1–100 kPa). We find that both expression of β_3 integrin subunit as well as its association with TGF-β RII increases on substrates with bone-like mechanical properties (~1,000,000 kPa). Additionally, our study shows that inhibition of integrin $\alpha_v\beta_3$ is sufficient to reduce the expression of PTHrP and the transcription factor Gli2 in MDA-MB-231 tumor cells. Taken together, these data imply that breast cancer cells specifically change their expression of β_3 integrin subunit, which pairs with the overexpressed TGF-β signaling present in bone metastatic cells, in response to bone-like mechanical properties. Furthermore, the increased association of β_3 integrin subunit with TGF-β RII and increased phosphorylation of p38-MAPK on rigid substrates suggest that bone-like mechanical properties activates MAPK signaling in MDA-MB-231 cells.

Integrins are known to play a significant role in cancer tropism and metastasis[12], and integrin $\alpha_v\beta_3$ has been shown to directly facilitate metastasis to bone upon IV injection in mouse models[10a, b, 10d, 11b]. Specifically, stably transfecting MDA-MB-231 cells to overexpress $\alpha_v\beta_3$ results in significantly increased osteolysis upon IV injection compared to non-transfected cells, but the difference is muted with intratibial injections[11b]. The authors note that this is possibly due to the bone targeting effect of $\alpha_v\beta_3$ in the IV injections and more cells make it to the bone microenvironment when $\alpha_v\beta_3$ is overexpressed. Since, previous studies have shown that targeting $\alpha_v\beta_3$ prevented tumor cells from early stage metastasis to bone we chose to isolate the effect of integrin expression on the establishment and osteolytic potential of the tumors by focusing on intratibial injections. The injection of β_3 KD cells directly into the tibia showed that inhibition of $\alpha_v\beta_3$ can reduce ostelysis in tumors that are established in the bone microenvironment. High magnification images of the tumor locations actually point to the migration and establishment of the β_3 KD cells into the marrow space, rather than centered in the injection site within the trabecular bone (Figure 3.16). The control cells establish in the injection site in the trabecular bone and significant osteolysis occurs. This correlates well with the previous studies in which $\alpha_v\beta_3$ aids cells in homing to and attaching within the bone microenvironment. Inhibition of the β_3 integrin may prevent the cells from attaching well in the trabecular bone.

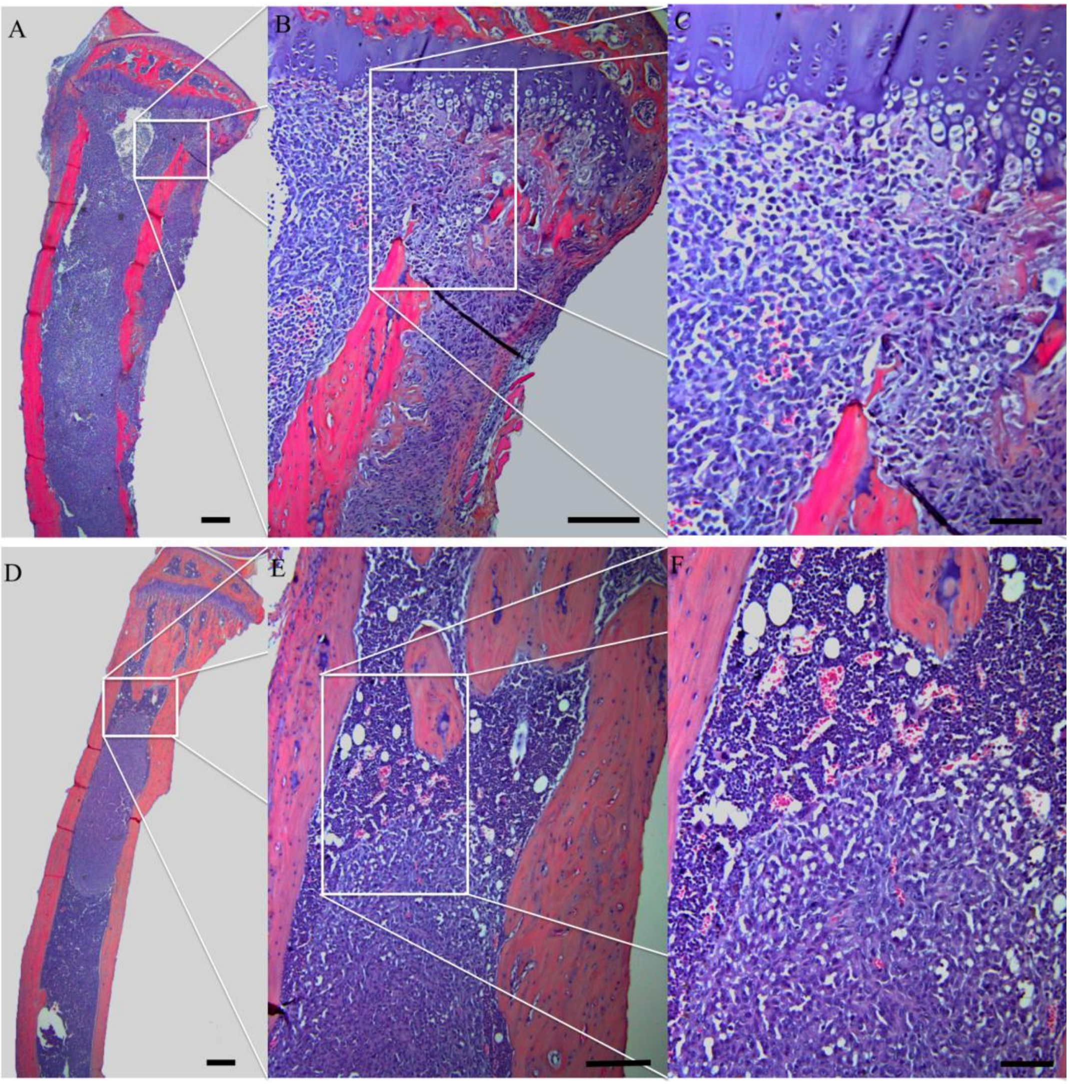

Figure 3.16. High magnification images of histological sections of tumor establishment. Animals inoculated with control cells are highly osteolytic and are even resorbing cortical bone (A-C), while the animals inoculated with β3 KD cells appear to have large tumors in the marrow space with little osteolysis.

Specific inhibitors to $\alpha_v\beta_3$ have shown promise in preclinical studies, reducing both tumor burden and incidence in bone[11b, 23]. Inhibition of $\alpha_v\beta_3$ can reduce osteolysis by blocking the metastasis[10c, d], preventing vascularization[20b], or even affecting osteoclast differentiation and resorption[11b]. Here we show that inhibition of integrin $\alpha_v\beta_3$ specifically reduced the expression of PTHrP and the transcription factor Gli2 in MDA-

MB-231 tumor cells. We also demonstrate that the rigidity of the bone microenvironment is a key driver in integrin $\alpha_v\beta_3$ expression, which has a direct correlation to osteolytic behavior *in vivo*. This points to the fact that alternative mehcanotransduction targets, that are known to affect integrin expression[24], can be added to the potential therapies to treat cancer induced bone disease.

Conclusion

In this study, we have shown that rigid substrates with bone-like mechanical properties stimulate expression of osteolytic factors *in vitro* through β_3 integrin and TGF-β RII complexation, which is known to activate MAPK signaling through Src phosphorylation[13]. This subsequently induces expression of the osteoclastogenic factor PTHrP and its transcription factor Gli2. Specifically, $\alpha_v\beta_3$ appear to be part of a mechano-sensing feed-forward loop that when paired with TGF-β RII drives signaling through MAPK to initiate expression of osteolytic factors (Figure 3.17). Taken together, these data suggest that the rigid mineralized bone matrix is involved in the establishment of osteolytic metastases by stimulating integrin-mediated contractility. This is especially important in breast cancer, as bone metastases are associated with poor patient prognosis. Understanding the mechanisms involved in the establishment of these metastases could ultimately lead to new targeted therapies to improve clinical outcomes.

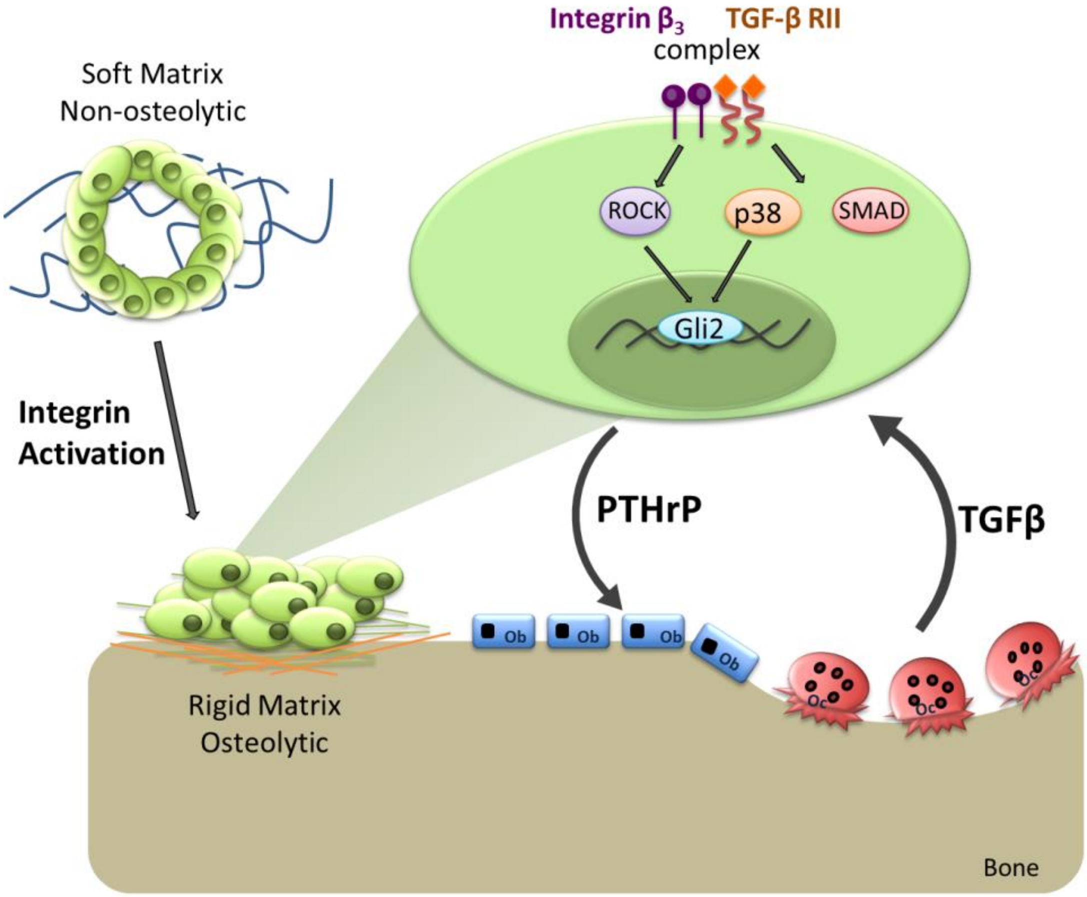

Figure 3.17. Schematic diagram of the potential crosstalk of solid state (integrin) and soluble (TGF-β) signaling pathways that drive osteolytic behavior.

References

1. (a) DE Discher, e. a., Tissue cells feel and respond to the stiffness of their substrate. *Science* **2005,** *310* (5751), 1139-43; (b) Engler, A. J.; Sen, S.; Sweeney, H. L.; Discher, D. E., Matrix Elasticity Directs Stem Cell Lineage Specification. *Cell* **2006,** *126*, 677-689; (c) McBeath, R.; Pirone, D. M.; Nelson, C. M.; Bhadriraju, K.; Chen, C. S., Cell shape, cytoskeletal tension, and RhoA regulate stem cell lineage commitment. *Dev Cell* **2004,** *6*, 483-95; (d) MR Brouns, e. a., p190 RhoGAP is the principal Src substrate in brain and regulates axon outgrowth, guidance and fasiculation. *Nat Cell Biol* **2001,** *3* (4), 361-7; (e) Mulder, J., p116Rip targets myosin phosphatase to the actin cytoskeleton and is essential for RhoA/ROCK-regulated neuritogenesis. *Mol Biol Cell* **2004,** *15*, 5516-5527; (f) Narumiya, S.; Tanji, M.; Ishizaki, T., Rho signaling, ROCK and mDia1, in transformation, metastasis and invasion. *Cancer Metastasis Rev* **2009,** *28* (1-2), 65-76; (g) Nishimura, Y.; Itoh, K.; Yoshioka, K.; Tokuda, K.; Himeno, M., Overexpression of ROCK in human breast cancer cells: evidence that ROCK activity mediates intracellular membrane traffic of lysosomes. *Pathol Oncol Res* **2003,** *9* (2), 83-95; (h) Nobes, H., Rho, rac, and cdc42 GTPases regulate the assembly of multimolecular focal complexes associated witha ctin stress fibers, lamellipodia and filopodia. *Cell* **1995,** *81*, 53-62; (i) Nobes, H., Rho GTPases control polarity, protrusion and adhesion during cell movement. *J Cell Biol* **1999,** *144* (6), 1235-44; (j) Ridley, H., The small GTP-binding protein rho regulates the assembly of focal adhesions and actin stress fibers in response to growth factors. *Cell* **1992,** *70* (3), 389-399; (k) Wells, R. G.; Discher, D. E., Matrix elasticity, cytoskeletal tension, and TGF-beta: the insoluble and soluble meet. *Science Signaling* **2008,** *1* (10).
2. (a) Na, S.; Collin, O.; Chowdhury, F.; Tay, B.; Ouyang, M.; Wang, Y.; Wang, N., Rapid signal transduction in living cells is a unique feature of mechanotransduction. *Proc Natl Acad Sci U S A* **2008,** *105* (18), 6626-31; (b) Sawada, Y.; Tamada, M.; Dubin-Thaler, B. J.; Cherniavskaya, O.; Sakai, R.; Tanaka, S.; Sheetz, M. P., Force sensing by mechanical extension of the Src family kinase substrate p130Cas. *Cell* **2006,** *127* (5), 1015-26; (c) Wang, Y.; Botvinick, E. L.; Zhao, Y.; Berns, M. W.; Usami, S.; Tsien, R. Y.; Chien, S., Visualizing the mechanical activation of Src. *Nature* **2005,** *434* (7036), 1040-5.
3. Butcher, D. T.; Alliston, T.; Weaver, V. M., A tense situation: forcing tumour progression. *Nat. Rev. Cancer* **2009,** *9* (2), 108-122.
4. PaszeK, M. J.; Zahir, N.; Johnson, K. R.; Lakins, J. N.; Rozenberg, G. I.; Gefen, A.; Reinhart-King, C. A.; Margulies, S. S.; Dembo, M.; Boettiger, D., Tensional homeostasis and the malignant phenotype. *Cancer cell* **2005,** *8* (3), 241-254.
5. (a) Powell, G. J.; Southby, J.; Danks, J. A.; Stillwell, R. G.; Hayman, J. A.; Henderson, M. A.; Bennett, R. C.; Martin, T. J., Localization of parathyroid hormone-related protein in breast cancer metastases: increased incidence in bone compared with other sites. *Cancer research* **1991,** *51* (11), 3059-3061; (b) Southby, J.; Kissin, M. W.; Danks, J. A.; Hayman, J. A.; Moseley, J. M.; Henderson, M. A.; Bennett, R. C.; Martin, T. J., Immunohistochemical localization of parathyroid hormone-related protein in human breast cancer. *Cancer research* **1990,** *50* (23), 7710-7716.
6. (a) Sterling, J. A.; Oyajobi, B. O.; Grubbs, B.; Padalecki, S. S.; Munoz, S. A.; Gupta, A.; Story, B.; Zhao, M.; Mundy, G. R., The hedgehog signaling molecule Gli2

induces parathyroid hormone-related peptide expression and osteolysis in metastatic human breast cancer cells. *Cancer research* **2006,** *66* (15), 7548-7553; (b) Yin, J. J.; Selander, K.; Chirgwin, J. M.; Dallas, M.; Grubbs, B. G.; Wieser, R.; Massagué, J.; Mundy, G. R.; Guise, T. A., TGF-beta signaling blockade inhibits PTHrP secretion by breast cancer cells and bone metastases development. *J Clin Invest* **1999,** *103* (2), 197-206.

7. Neville-Webbe, H. L.; Coleman, R. E., Bisphosphonates and RANK ligand inhibitors for the treatment and prevention of metastatic bone disease. *European Journal of Cancer* **2010,** *46* (7), 1211-1222.

8. Ruppender, N. S.; Merkel, A. R.; Martin, T. J.; Mundy, G. R.; Sterling, J. A.; Guelcher, S. A., Matrix rigidity induces osteolytic gene expression of metastatic breast cancer cells. *PloS one* **2010,** *5* (11), e15451.

9. (a) Alexander, N. R.; Branch, K. M.; Parekh, A.; Clark, E. S.; Iwueke, I. C.; Guelcher, S. A.; Weaver, A. M., Extracellular matrix rigidity promotes invadopodia activity. *Current Biology* **2008,** *18* (17), 1295-1299; (b) Paszek, M. J.; Weaver, V. M., The tension mounts: mechanics meets morphogenesis and malignancy. *Journal of mammary gland biology and neoplasia* **2004,** *9* (4), 325-342.

10. (a) Claudia Tanja, M., The integrin alphav beta3 increases cellular stiffness and cytoskeletal remodeling dynamics to facilitate cancer cell invasion. *New Journal of Physics* **2013,** *15* (1), 015003; (b) PÉCHEUR, I.; PEYRUCHAUD, O.; SERRE, C.-M.; GUGLIELMI, J.; VOLAND, C.; BOURRE, F.; MARGUE, C.; COHEN-SOLAL, M.; BUFFET, A.; KIEFFER, N.; CLÉZARDIN, P., Integrin αvβ3 expression confers on tumor cells a greater propensity to metastasize to bone. *The FASEB Journal* **2002,** *16* (10), 1266-1268; (c) TAKAYAMA, S.; ISHII, S.; IKEDA, T.; MASAMURA, S.; DOI, M.; KITAJIMA, M., The Relationship Between Bone Metastasis from Human Breast Cancer and Integrin αvβ3 Expression. *Anticancer Research* **2005,** *25* (1A), 79-83; (d) Wong, N.; Mueller, B.; Barbas, C.; Ruminski, P.; Quaranta, V.; Lin, E. K.; Smith, J., αv Integrins mediate adhesion and migration of breast carcinoma cell lines. *Clin Exp Metastasis* **1998,** *16* (1), 50-61; (e) Zhang, Y.; Ma, B.; Fan, Q., Mechanisms of breast cancer bone metastasis. *Cancer Letters* **2010,** *292* (1), 1-7.

11. (a) Schneider, J. G.; Amend, S. R.; Weilbaecher, K. N., Integrins and bone metastasis: integrating tumor cell and stromal cell interactions. *Bone* **2011,** *48* (1), 54-65; (b) Zhao, Y.; Bachelier, R.; Treilleux, I.; Pujuguet, P.; Peyruchaud, O.; Baron, R.; Clément-Lacroix, P.; Clézardin, P., Tumor αvβ3 integrin is a therapeutic target for breast cancer bone metastases. *Cancer research* **2007,** *67* (12), 5821-5830.

12. Desgrosellier, J. S.; Cheresh, D. A., Integrins in cancer: biological implications and therapeutic opportunities. *Nat. Rev. Cancer* **2010,** *10* (1), 9-22.

13. Galliher, A. J.; Schiemann, W. P., Beta3 integrin and Src facilitate transforming growth factor-beta mediated induction of epithelial-mesenchymal transition in mammary epithelial cells. *Breast Cancer Res* **2006,** *8* (4), R42.

14. Ruppender NS, M. A., Martin TJ, Mundy GR, Sterling JA and Guelcher SA, Matrix Rigidity Induces Osteolytic Gene Expression of Metastatic Breast Cancer Cells. *PLoS One* **2010,** *5* (11), e15451.

15. Oliver, W. C.; Pharr, G. M., Improved technique for determining hardness and elastic modulus using load and displacement sensing indentation experiments. *Journal of materials research* **1992,** *7* (6), 1564-1583.

16. Yoneda, T.; Williams, P.; Hiraga, T.; Niewolna, M.; Nishimura, R., A Bone-Seeking Clone Exhibits Different Biological Properties from the MDA-MB-231 Parental Breast Cancer Cells and a Brain-Seeking Clone In Vivo and In Vitro. *Journal of Bone and Mineral Research* **2001,** *16* (8), 1486-1495.
17. Kang, Y.; Siegel, P. M.; Shu, W.; Drobnjak, M.; Kakonen, S. M.; Cordo´n-Cardo, C.; Guise, T. A.; Massague, J., A multigenic program mediating breast cancer metastasis to bone. *Cancer Cell* **2003,** *3*, 537-49.
18. Thompson, M. T.; Berg, M. C.; Tobias, I. S.; Rubner, M. F.; Van Vliet, K. J., Tuning compliance of nanoscale polyelectrolyte multilayers to modulate cell adhesion. *Biomaterials* **2005,** *26* (34), 6836-6845.
19. Levental, K. R.; Yu, H.; Kass, L.; Lakins, J. N.; Egeblad, M.; Erler, J. T.; Fong, S. F. T.; Csiszar, K.; Giaccia, A.; Weninger, W.; Yamauchi, M.; Gasser, D. L.; Weaver, V. M., Matrix Crosslinking Forces Tumor Progression by Enhancing Integrin Signaling. *Cell* **2009,** *139* (5), 891-906.
20. (a) Harms, J.; Welch, D.; Samant, R.; Shevde, L.; Miele, M.; Babu, G.; Goldberg, S.; Gilman, V.; Sosnowski, D.; Campo, D.; Gay, C.; Budgeon, L.; Mercer, R.; Jewell, J.; Mastro, A.; Donahue, H.; Erin, N.; Debies, M.; Meehan, W.; Jones, A.; Mbalaviele, G.; Nickols, A.; Christensen, N.; Melly, R.; Beck, L.; Kent, J.; Rader, R.; Kotyk, J.; Pagel, M. D.; Westlin, W.; Griggs, D., A small molecule antagonist of the α v β3 integrin suppresses MDA-MB-435 skeletal metastasis. *Clin Exp Metastasis* **2004,** *21* (2), 119-128; (b) Cai, W.; Chen, X., Anti-Angiogenic Cancer Therapy Based on Integrin αvβ3 Antagonism. *Anti-Cancer Agents in Medicinal Chemistry- Anti-Cancer Agents)* **2006,** *6* (5), 407-428; (c) Posey, J. A.; Khazaeli, M.; DelGrosso, A.; Saleh, M. N.; Lin, C. Y.; Huse, W.; LoBuglio, A. F., A pilot trial of Vitaxin, a humanized anti-vitronectin receptor (anti α v β 3) antibody in patients with metastatic cancer. *Cancer Biotherapy and Radiopharmaceuticals* **2001,** *16* (2), 125-132.
21. Brem, S., Angiogenesis and cancer control: from concept to therapeutic trial. *Cancer Control* **1999,** *6* (5), 436-458.
22. Yin, J. J.; Selander, K.; Chirgwin, J. M.; Dallas, M.; Grubbs, B. G.; Wieser, R.; Massague, J.; Mundy, G. R.; Guise, T. A., TGF-beta signaling blockade inhibits PTHrP secretion by breast cancer cells and bone metastases development. *The Journal of clinical investigation* **1999,** *103* (2), 197-206.
23. Harms, e. a., A small molecule antagonist of the alphavbeta3 integrin suppresses MDA-MB-435 skeletal metastasis. *Clin Exp Met* **2004,** *21*, 119-128.
24. (a) Stupp, R.; Ruegg, C., Integrin Inhibitors Reaching the Clinic. *Journal of Clinical Oncology* **2007,** *25* (13), 1637-1638; (b) Moschos, S. J.; Drogowski, L. M.; Reppert, S. L.; Kirkwood, J. M., Integrins and cancer. *Oncology (Williston Park, N.Y.)* **2007,** *21* (9 Suppl 3), 13-20.

CHAPTER IV

SYNTHESIS AND CHARACTERIZATION OF NANOPARTICLES FOR HYDROPHOBIC DRUG DELIVERY FOR THE ULTIMATE GOAL OF DRUG RELEASING POLYURETHANE BIOMATERIALS

Introduction

Self-assembled nanoparticles from amphipathic polymers provide a useful platform for improving pharmacokinetics, solubility, and target site bioavailability of small molecule drugs[1], proteins[2], and nucleic acids[3]. Hydrophobic small molecule therapeutics can be encapsulated by preferential interaction with the hydrophobic core of the polymer micelle, and a "stealth" PEG shell is typically utilized to reduce opsonization and increase in vivo stability of the nanoparticles so that they can leverage the enhanced permeability and retention (EPR) effect to preferentially accumulate within tumors[4]. This approach has recently been paired with receptor ligand targeting to the prostate-specific membrane antigen in order to produce a docetaxel nanomedicine with enhanced circulation time and potentially improved clinical efficacy in humans[5].

A variety of environmentally-responsive polymers have also been utilized in order to tailor micelle drug release mechanisms that are triggered by pathology-specific changes in pH[1a-c], reactive oxygen species[1d, 3b], enzymatic degradation[6], and others. Leveraging pH for drug release is especially relevant because tumor tissues are characterized by a slightly acidic pH in the range of 5.8-6.5[7]. Thus, stable packaging of cargo at physiologic pH of 7.4 and accelerated release at acidic pH is a useful approach for triggering drug release intracellularly and within tumor microenvironments Furthermore, once internalized into endo-lysosomal pathways, nanocarriers are exposed to a gradual decrease in pH as they are trafficked from early endosomes (pH ~ 6.8) to late endosomes and lysosomes (pH ~ 4-6). This acidification can be utilized as an environmental trigger to mediate endosomal disruption, releasing the therapeutic payload into the cytoplasm. Additionally, the ability to release drugs via the early stage endosomal pathway decreases the likelihood of multi-drug resistance from occurring due to the release of the therapeutic into the cytoplasm of the cells[8].

Development of nanoparticles based on basic, amine-containing polymers is a promising approach for achieving pH dependent drug release mechanisms[9]. Lee et al. utilized poly(amino acids) derived from lysine or histidine as the ionic species and created mixed micelles with non-ionic hydrophobic block copolymers to titrate in the ideal amount of ionic charge for optimal drug delivery[9c]. The proper tuning of polymer properties is key to achieving stable drug loading, optimally-tuned triggered drug release, and biocompatibility of pH-responsive polymers[10]. Copolymerization with biocompatible hydrophobic monomers[3a, 11] and incorporation of degradable moieties represent two key approaches to reducing potential toxicity and tuning the nanoparticle stability and drug release profiles of pH-responsive micelles[12]. For example, copolymerization of cationic monomers with the hydrophobic monomer butyl methacrylate (BMA) has been utilized to increase in vivo blood circulation time and stability of siRNA nanocarriers while simultaneously tuning the effective pK_a of the polymer side chains such that they becomes ionized and destabilize the nanoparticle core to trigger drug release and membrane disruption at endosomal pH[11]. Degradable monomers with cationic branches attached via ester groups have the ability to trigger drug release at endosomal pH while simultaneously becoming hydrolyzed in the process, thereby abrogating their potential cytotoxic effects[13].

The goal of this study was to synthesize and screen a library of polymers in order to study the potential synergy between pH- and degradation-dependent release mechanisms in order to identify optimal micelle formulations for pH-triggered intracellular delivery of hydrophobic small molecule drugs. The library of copolymers was synthesized via reverse addition-fragmentation chain transfer (RAFT) polymerization using a poly(ethylene glycol) (PEG) macro-chain transfer agent to enable "grafting from" the 5000 Da hydrophilic polymer block that forms the micelle corona. The resulting pH sensitive ester bond connecting the PEG corona to the core co-polymer is a secondary degradation mechanism that can result in micelle destabilization and a concomitant release of a therapeutic payload. A total of 12 copolymers were RAFT synthesized using 4 different cationic monomers with varied hydrophobicity and degradability. For each cationic monomer, 3 different polymers were synthesized containing approximately 40, 50 or 60 mole percent cationic monomer copolymerized with the neutral hydrophobic monomer BMA. The time-dependent stability of micelles formed from these polymers was studied at a range of pH values mimicking physiological stages of the endosomal pathway and the decreased pH of the tumor microenvironment. Additionally the ability to encapsulate and release a model hydrophobic small molecule was tested, and the effect of polymer composition on cytocompatibility and drug release kinetics was assessed. Degradable cationic monomers were utilized to tune the release of a therapeutic payload based on synergistically acting with pH changes that drive phase changes in the hydrophobic core block of the ampipathic diblock copolymers, resulting in triggered macromolecular disassembly and drug release from the micelle core.

Experimental

Materials

All chemicals and reagents were purchased from Sigma-Aldrich and were of analytical grade unless otherwise stated. Butyl methacrylate (BMA), 2-(dimethylamino ethyl methacrylate) (DMAEMA), 2-(dimethylamino ethyl acrylate) (DMAEA), 2-(diethylamino ethyl acrylate) (DEAEA), and 2-(diethylamino ethyl methacrylate) (DEAMA) were filtered through a basic alumina column to remove inhibitors prior to use. 2,2'-azobis(2-methylpropionitrile) (AIBN) was recrystallized twice from methanol before use. 1,4-Dioxane was distilled prior to use.

Synthesis of 4-cyano-4-(ethylsulfanylthiocarbonyl) sulfanylpentanoic acid (ECT)

The RAFT chain transfer agent ECT was synthesized following protocols previously described by Convertine et al.[3a] and adapted from Moad et al.[14]. Briefly, ethanethiol (76 mmol, 4.72 g) was reacted with carbon disulfide (79 mmol, 6.0 g) in the presence of sodium hydride (79 mmol, 3.15 g) in diethyl ether for 1h. The resulting sodium S-ethyl trithiocarbonate was further reacted with iodine (25 mmol, 6.3 g) to obtain bis(ethylfulfanyl-thiocarbonyl) disulfide, which was further refluxed with 4,4'-azobis(4-cyanopentanoic acid) in ethyl acetate for 18 h. The crude ECT was purified by column chromatography using silica gel as the stationary phase and a gradient of ethyl acetate:hexane (40:60 to 70:30) as the mobile phase. ^{1}H NMR (400MHz, $CDCl_3$): δ 1.36 t ($SCH_2C\mathbf{H}_3$); δ 1.88 s ($CCNC\mathbf{H}_3$); δ 2.3–2.65 m ($C\mathbf{H}_2C\mathbf{H}_2$); δ 3.35 q ($SC\mathbf{H}_2CH_3$).

Synthesis of polyethylene glycol (PEG) macro-chain transfer agent (CTA)

Dicyclohexylcarbodimide (DCC, 8 mmol, 1.64 g) was added to the stirring solution of mono methoxy-poly(ethylene glycol) (M_n = 5000, 2 mmol, 10 g), ECT (4 mmol, 1.045 g) and, DMAP (48 mg, 0.4 mmol) in 250 ml of anhydrous dichloromethane. The reaction mixture was stirred for 48h. The precipitated cyclohexyl urea was removed by filtration, and the dichloromethane layer was concentrated and precipitated into diethyl ether twice. The precipitated polymer was washed three times with diethyl ether and dried under vacuum. ^{1}H NMR spectra of the product showed 84 % of the PEG was conjugation with ECT. ^{1}H NMR($CDCl_3$) δ 1.36 t ($SCH_2\mathbf{CH_3}$); δ 1.88 s ($CCN\mathbf{CH_3}$); δ 2.3–2.65 m ($CH_2\mathbf{CH_2}$); δ 3.35 q ($S\mathbf{CH_2}CH_3$), 3.64 s($\mathbf{CH_2}O$).

Synthesis and characterization of PEG-b-(X-co-BMA) copolymers where X is DMAEMA, DMAEA, DEAEMA, or DEAEA

The PEG-ECT macro-CTA was utilized in the RAFT copolymerization of four different cationic monomers DMAEMA, DMAEA, DEAEMA, DEAEA with BMA, and 3 different copolymers were made from cationic monomer with 40%, 50%, and 60% BMA. All 12 polymerizations were carried out in distilled dioxane under a nitrogen atmosphere at 65°C for 18-24 hours using AIBN as the free radical initiator. The reaction mix was purged with nitrogen for 30 minutes prior to polymerization. The molar ratio of the PEG-ECT macro-CTA to AIBN was 10:1 and the monomer to macro-CTA molar ratio was set to achieve a molecular weight of approximately 20,00 g/mol (molar feed ratios and monomer to macro-CTA molar ratios were adjusted and optimized accordingly to achieve the desired composition and MW). The resulting polymers were precipitated in cold (-20°C) hexane, redissolved in acetone, and precipitated into cold (-20°C) pentane twice, followed by drying overnight *in vacuo*. Gel permeation chromatography (GPC, Agilent) was used to determine molecular weight and polydispersity (M_w/M_n, PDI) of the diblock copolymers using HPLC-grade DMF containing 0.1% LiBr at 60°C as mobile phase. Molecular weight calculations were calculated with ASTRA V software (Wyatt Technology) and were based on experimentally determined dn/dc values. ^1H NMR analysis in $CDCl_3$ was utilized to determine copolymer composition and verify the molecular weights determined by GPC.

Potentiometic Titration

Milli-Q ultra-purified water was utilized to prepare aqueous solutions of each polymer and their corresponding monomers. The solutions were acidified using 1 M HCl. The polymer solutions were titrated with 0.1 M NaOH using a Metrohm 798 MPT Titrino automated titrator[15]. The pKa values were obtained from where the degree of protonation (α) curves for each polymer composition are equal to 0.5.

Formation and characterization of micelles

Stock solutions were generated by dissolving polymers in ultrapure methanol at a concentration of 100 mg/mL. Solutions were stored at -20^o C until further use. Micelle formation was induced by the slow addition of 1 mL PBS (pH 7.4) by syringe pump at a flow rate of 8 mL/hr to 10 uL of polymer stock solution in methanol, producing 1 mg/mL micelle solutions. Dynamic light scattering (DLS) analysis was utilized to determine hydrodynamic radius, polydispersity, ζ-potential, and critical micelle concentration (CMC) of the various micelle formulations. Transmission electron microscopy (TEM) imaging was used to verify micelle size and morphology. ^1H NMR in D_2O was utilized to verify micelle formation evinced by the shielding of resonant peaks associated with the copolymer polymer block that forms the micelle core. Additionally, micelles were loaded with Nile red (NR) and serially diluted with PBS (concentrations of 1, 0.5, 0.1, 0.01, 0.001, 0.0001 mg/mL) to verify CMC values obtained by DLS.

pH-dependent degradation of micelles

Micelle solutions of PEG-*b*-(DMEAE-*co*-BMA) and PEG-*b*-(DEAEA-*co*-BMA) were formulated in pH adjusted PBS (pH 7.4 and 5.6), and micelle degradation and destabilization was analyzed by ^{1}H NMR and GPC analyses. The micelles were incubated at 37^o C for 0 h, 24 h, 2 d, 4 d and 8 days followed by lyophilization and analysis by ^{1}H NMR in $CDCl_3$ to assess degradation as determined by the chemical shift that results from the hydrolysis of the DMAEA and DEAEA polymer subunits into dimethylamino ethanol and diethylamino ethanol degradation products, respectively. GPC traces were also analyzed over time to assess both the loss of the PEG corona and degradable side chains.

Red blood cell hemolysis assay

The ability to disrupt the lipid bilayer of cell membranes was tested for each polymer at physiological and endosomal pH levels. Each polymer group was tested at concentrations of 5, 20 and 40 μg/mL and at pH 7.4 (physiologic), 6.8 (early endosome/tumor microenvironment), 6.2 (late endosome) and 5.6 (lysosome). Red blood cells were incubated at 37^o C with the polymers for 1 hour. The membrane disruption was evaluated by observing the release of hemoglobin ($\lambda = 451$) from the lysed red blood cells.

Nile red encapsulation and pH-dependent release

NR was co-dissolved at 1 mg/mL in ultrapure methanol with polymers at a concentration of 100 mg/mL. 1 mL of PBS was added at a rate of 8 mL/h by syringe pump to 10 μL of the NR/polymer solution in methanol. Non-encapsulated NR was removed by centrifugation and subsequent filtration. Average fluorescent intensity of the loaded NR was utilized to compare drug loading of each polymer micelle. In order to assess pH-dependent release kinetics, micellization was carried out in pH-adjusted PBS (pH 7.4, 6.5, and 5.6). The samples were subsequently incubated in a sealed 96 well plate at 37^{o} C and fluorescence intensity was measured over time for 45 days on a TECAN Infinite M1000 Pro plate reader.

Cell culture

Murine derived fibroblasts (MC3T3-E1), primary rat derived bone marrow mesenchymal stem cells (MSCs), and metastatic breast cancer cells (MDA-MB-231), were cultured separately in Dulbecco's Eagle medium (DMEM) supplemented with 10% fetal bovine serum, 1% L-glutamine, and 1% penicillin/streptomycin. Cells were incubated at 37^{o} C with 5% CO_2.

Micelle cytotoxicity

The CytoTox-ONE Homogenous Membrane Integrity assay (Promega) was used to assess the cytotoxicity of micelle treatments at a range of concentrations according to the manufacturer's instructions. Briefly, MC3T3 cells were plated on a 96 well plate at a cell density of 10,000 cells/well and allowed to attach overnight. Cell culture media was replaced with media containing a range of micelle concentrations (10, 25, 50 and 100 ug/mL) and incubated for 2 hours. After 2 hours of incubation with treatments, cells were washed twice with PBS and cell culture media was replaced for 24 hours. After 24 hours the cells were re-suspended in 100 µL lysis buffer. Each well was then supplemented with 100 µL lactate dehydrogenase (LDH) substrate and incubated at RT for 10 minutes prior to the addition of 50 µL stop solution. LDH-induced fluorescence (excitation 550 nm, emission 600 nm) was then quantified with a TECAN Infinite M1000 Pro plate reader and used to determine relative cell viability compared to untreated control groups.

Uptake and intracellular release of NR loaded micelles in MC3T3, MSCs, and MDA-231 cells

MC3T3, MSCs, and MDA-231 cells were added to a 96-well plate at 10,000 cells per well and allowed to attach for 12 h. Cellular uptake and intracellular release of Nile Red loaded micelles were analyzed by replacing the cell culture media with media containing Nile red-loaded micelles (100 ug/mg polymer), or with free Nile red equivalent to the amount loaded into the micelles (10 ug/ml). After 2 h of incubation cells were washed with PBS twice and supplemented with fresh media and fluorescent images were taken with an Olympus DP71 camera attached to an Olympus CKX41 microscope (Center Valley, PA). All images were analyzed with ImageJ image processing software.

Statistical analysis

Statistical analysis was performed with the PRISM Graphpad software package. Statistical significance was defined with $p<0.05$. All graphs represent mean ±SEM.

Results and Discussion

Polymer synthesis

The library of polymers was synthesized as described in Figure 4.1, and the final composition of the copolymers was calculated from ^{1}H NMR (Figure 4.2). The composition of the synthesized polymers generally matched well with the feed ratio, as shown in Table 4.1. The DEAEA (i.e. EA) series of polymers was the exception, requiring a higher feed ratio of the cationic monomer to attain the desired compositions. The reactivity ratios for each monomer were determined using the Fineman-Ross method[16] as reported in the Figure 4.3A-D. The values of r_1 and r_2 for DMAEMA/BMA, DMAEA/BMA, and DEAMA/BMA were all close to 1 which would result in a random copolymer. However, the reactivity ratios for the DEAEA/BMA system were r_1=0.33 and r_2=0.97 respectively. This indicates the potential for compositional shifting, resulting in slightly longer segments of BMA[17]. However, since the reactivity ratio of BMA is less than 1, the copolymer is still considered a random distribution of DEAEA and BMA. Molecular weights were tightly controlled for all of the methacrylate-based copolymers, but the ethyl acrylate copolymer formulations resulted in increased polydispersity, which is attributable to the difficulty in polymerizing bulky, diethylaminoethyl ester side chains[18]. To our knowledge, this is the first time that DEAEA based polymers have been synthesized by RAFT polymerization or utilized to formulate degradable, pH-responsive micelles.

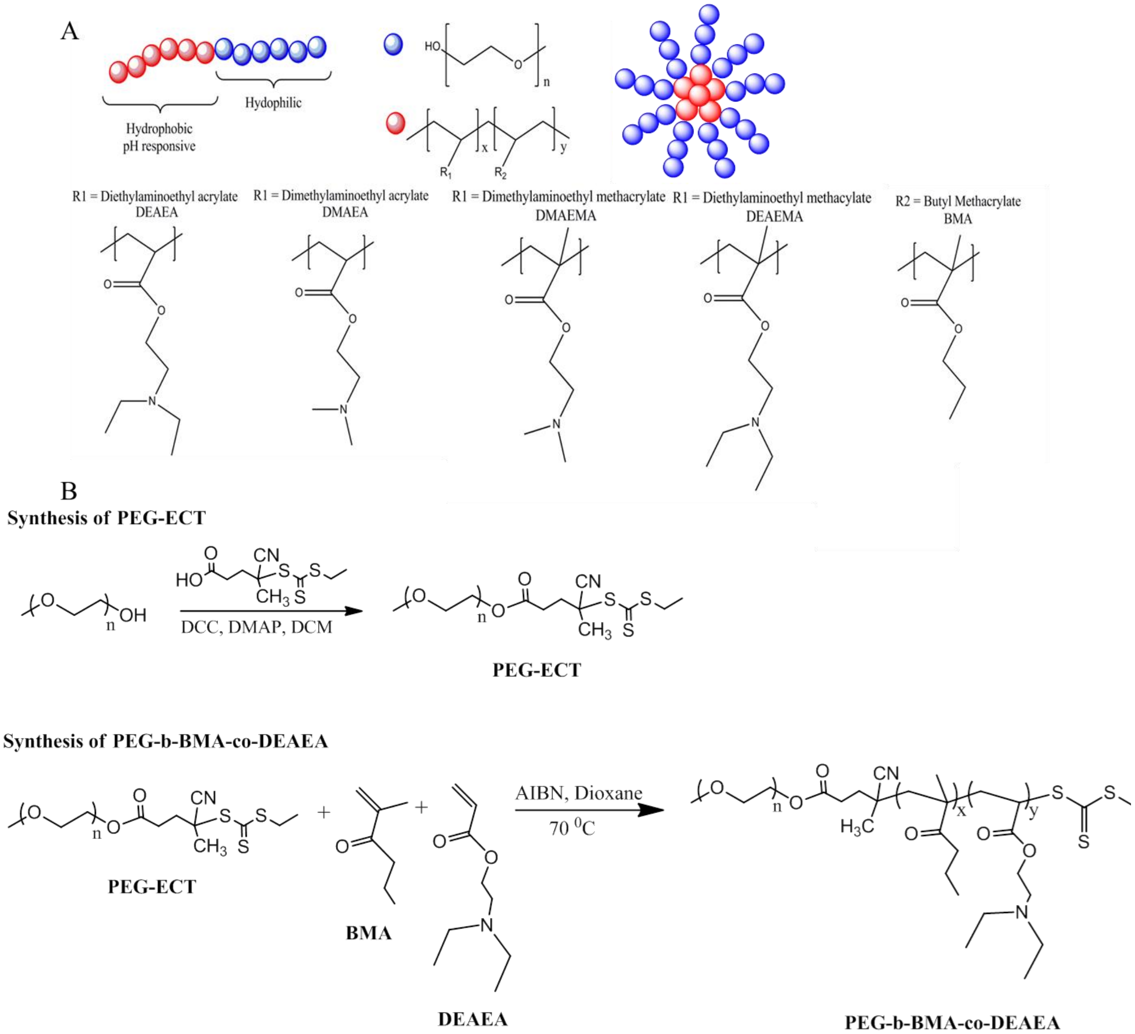

Figure 4.1. Chemical structures and synthesis schemes for copolymers. (A) Diagram of micelle structures; synthesis scheme for generating one of the copolymers (B).

Table 4.1. Results of copolymerization with BMA and cationic monomers.

Polymer	Target BMA %	Target Cationic Monomer %	Target MW	BMA % (NMR)	Cationic Monomer % (NMR)	MW (NMR)	MW (GPC)	PDI (GPC)	D_h (nm; PDI_{DLS})	pKa
PEG_{113}-b-$DEAEMA_{45}$-co-BMA_{36} (MA 6)	40%	60%	18,683	37.50%	62.50%	19,020	18,030	1.091	44 (0.21)	5.9
PEG_{113}-b-$DEAEMA_{39}$-co-BMA_{46} (MA 5)	50%	50%	17,995	46.96%	53.04%	18,775	18,830	1.206	26 (0.21)	5.7
PEG_{113}-b-$DEAEMA_{31}$-co-BMA_{58} (MA 4)	60%	40%	17,996	58.56%	41.44%	18,366	20,850	1.18	28 (0.16)	5.5
PEG_{113}-b-$DMAEMA_{73}$-co-BMA_{53} (MMA 6)	40%	60%	27,231	39.6%	60.4%	25,765	23,690	1.117	24 (0.36)	5.9
PEG_{113}-b-$DMAEMA_{65}$-co-BMA_{68} (MMA 5)	50%	50%	27,456	48.3%	51.7%	23,040	27,410	1.040	22 (0.24)	5.8
PEG_{113}-b-$DMAEMA_{52}$-co-BMA_{82} (MMA 4)	60%	40%	27,681	58.6%	41.4%	24,938	24,650	1.081	31 (0.05)	5.7
PEG_{113}-b-$DEAEA_{50}$-co-BMA_{38} (EA 6)	25%	75%	46,240	39%	61%	18,646	19,210	1.54	39 (0.27)	6.5
PEG_{113}-b-$DEAEA_{38}$-co-BMA_{52} (EA 5)	40%	60%	40,362	53.39%	46.61%	18,636	18,950	1.403	33 (0.16)	5.9
PEG_{113}-b-$DEAEA_{29}$-co-BMA_{69} (EA 4)	60%	40%	30,785	66.7%	33.3%	19,568	19,820	1.368	33 (0.15)	5.8
PEG_{113}-b-$DMAEA_{66}$-co-BMA_{53}(MEA 6)	40%	60%	26,418	44.29%	55.71%	21,125	22,830	1.554	35 (0.29)	6.2
PEG_{113}-b-$DMAEA_{51}$-co-BMA_{65} (MEA 5)	50%	50%	26,504	55.89%	44.11%	21,454	21,690	1.564	35 (0.15)	6
PEG_{113}-b-$DMAEA_{45}$-co-BMA_{82} (MEA 4)	60%	40%	26,388	64.48%	35.52%	23,207	23,150	1.556	32 (0.11)	5.8

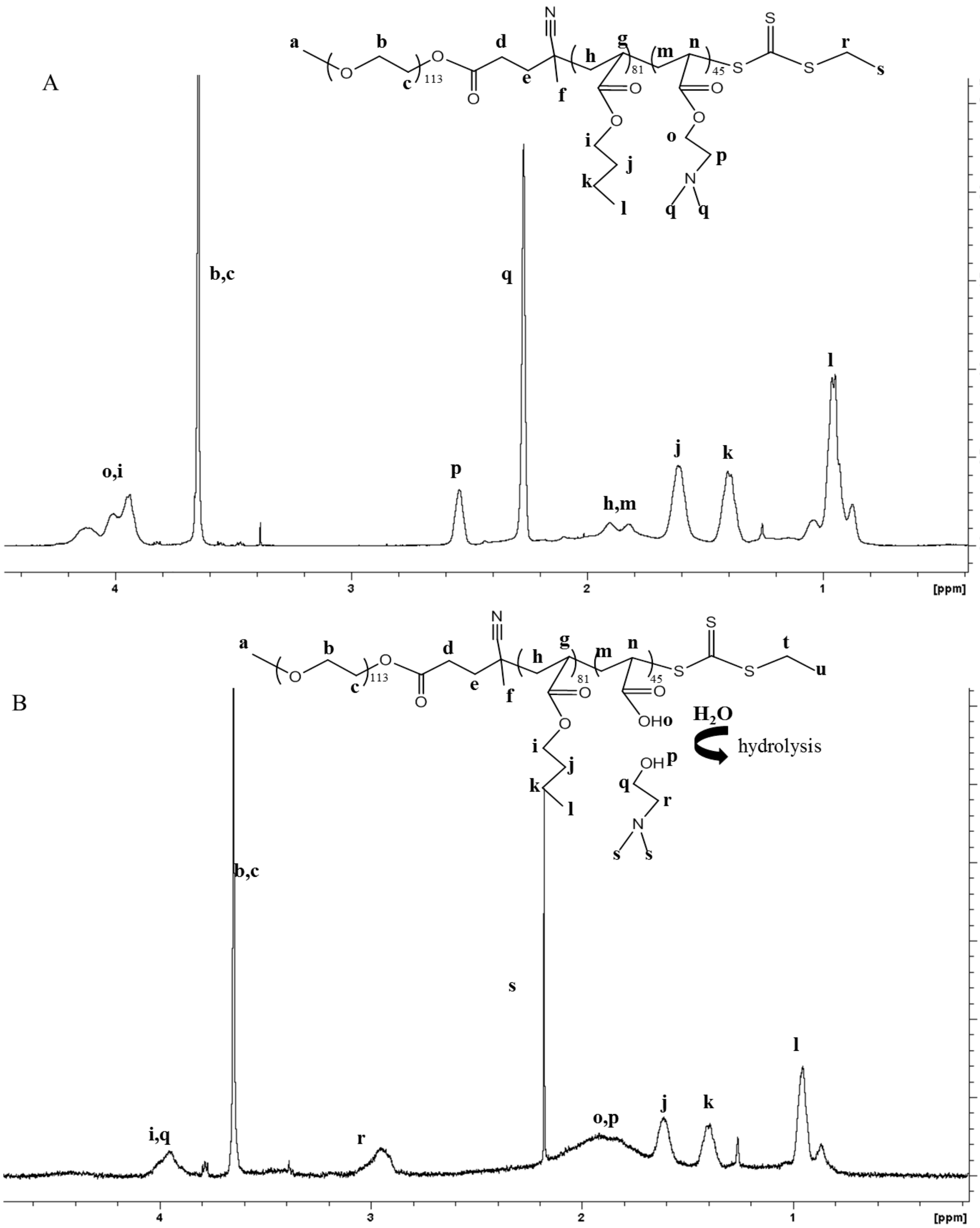

Figure 4.2. ^{1}H NMR spectra of PEG-b-DMAEA-co-BMA in $CDCl_3$ before (A) and after degradation (B).

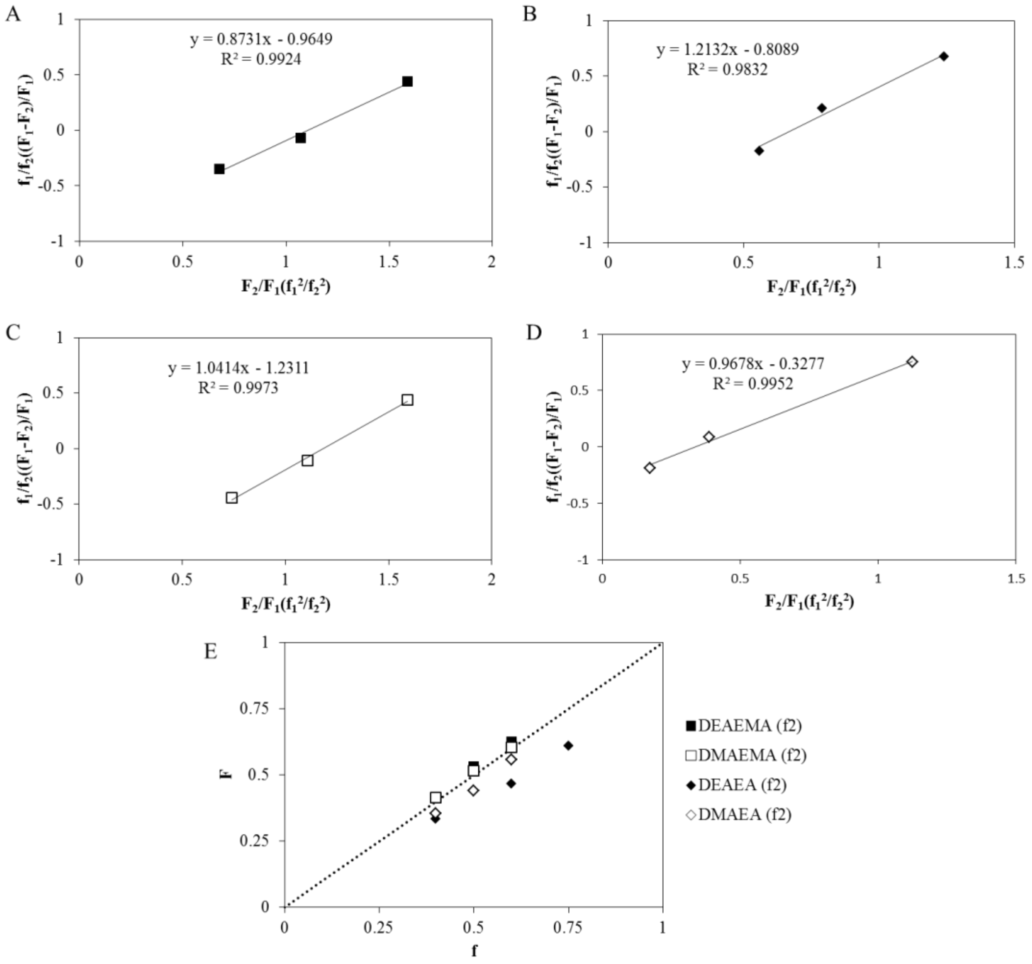

Figure 4.3. Fineman-Ross and feed ratio plots for each copolymer system. The slope (r_{BMA}), intercept ($r_{\text{cationic monomer}}$) and fit for (A) DMAEMA-co-BMA; (B) DMAEA-co-BMA; (C) DEAMA-co-BMA; and (D) DEAEA-co-BMA is shown. Feed ratio (*f*) plotted against molar concentration in the copolymer **(F).**

Micelle formation

The composition-dependent characteristics of the various micelle formulations were determined using ζ-potential, a NR fluorescent molecule assay, DLS, and TEM. The ζ-potential of micelle solutions was obtained at pH 7.4 directly after formulation. Figure 4.4A displays the critical micelle concentrations (CMC) of each polymer determined from plotting the fluorescence intensity of NR versus polymer concentration[1d]. The fluorescent intensity of Nile red is dependent upon being encapsulated in the hydrophobic core of the micelles. Nile red is released at concentrations of polymer below the CMC, and NR fluorescence is quenched when it is released into the polar aqueous phase due to micelle disassembly. As expected, CMC values for all polymers were inversely proportional to hydrophobic content in the core-forming block (i.e. %BMA).

An important aspect of the current study was comparison of degradable and non-degradable polycations. To assess the effect of degradation on polymer CMC, each of the polymers were treated with concentrated acid and elevated temperatures, and their CMC values were subsequently re-measured to assess the effect of PEG shedding and hydrolytic removal of the dimethylamino ethanol and diethylamino ethanol groups. Both DMAEA and DEAEA monomers are hydrolyzed into the smaller, more hydrophilic monomer acrylic acid, and this resulted in an approximately 3-fold increase in the CMC for all of the degradable copolymers. The CMC shift was not nearly as pronounced with the non-degradable polymers, and can be attributed to shedding of the PEG corona through hydrolysis of the ester linkage to the copolymer core block. As expected, following degradation, all micelles still showed the trend of decreasing CMC with increased hydrophobic BMA.

DLS was utilized to obtain the average size and qualitatively assess stability as a function of concentration, Figure 4.4B. The range of sizes for each copolymer was 20-45 nm with no significant trends between groups. DLS measurements resolved aggregation and micelle disassembly into unimers at polymer concentrations below the CMC ranges determined in the NR assay, further corroborating the results from the more quantitative NR method. TEM images verified size and uniformity of the micelles, with a representative image shown in Figure 4.4D. The surface charge of each micelle ranged from neutral to slightly negative upon formation (Figure 4.4C), which demonstrates the charge shielding effect of the hydrophilic PEG corona. The size, polydispersity, and surface charge of the nanoparticles indicates efficient self-assembly and ideal characteristics for administration via the circulatory system[19], especially for tumor targeting via the EPR effect[20].

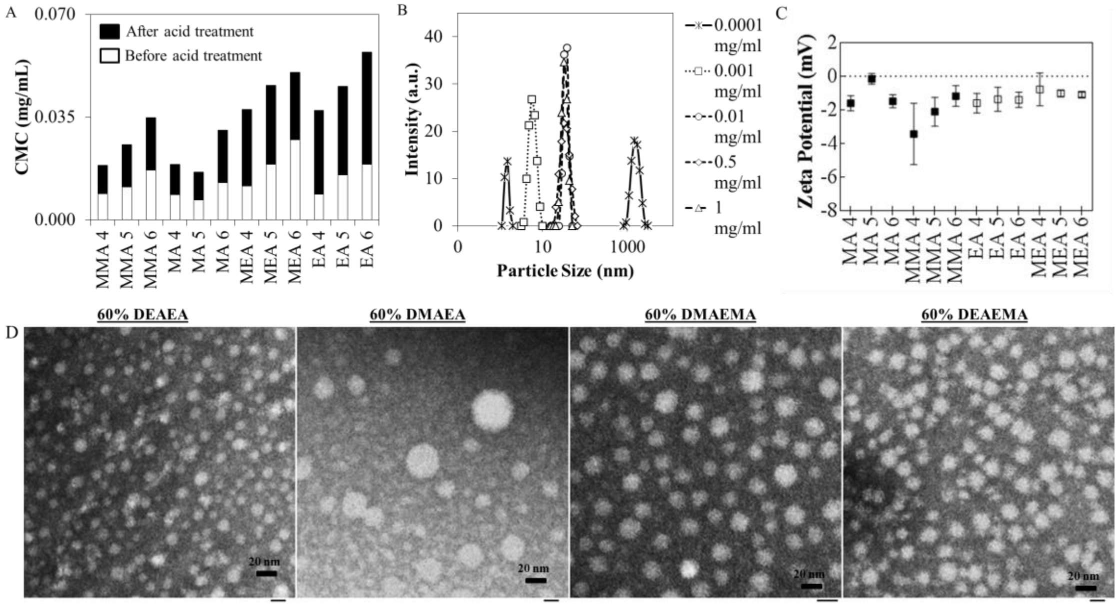

Figure 4.4. Compositional effects on micelle stability, size and surface charge. (A) Critical micelle concentration (CMC) for each polymer composition before and after an acid treatment effectively hydrolyzing both the PEG corona and the hydrolytic side chains. (B) Representative dynamic light scattering (DLS) plot as a function of concentration showing aggregation and unimers at low concentations of polymer. (C) Zeta potential readings for each polymer composition. (D) Representative transmission electron microscopy (TEM) images for the 60% cationic compositions.

Micelle stability and pH degradation

Micelle stability at pH 7.4 was tracked over time by DLS. The degradable micelle compositions began to show signs of aggregation as early as 24 hours (Figure 4.5A), while the non-degradable micelles showed excellent stability with very little aggregation even after 4 days in solution (Figure 4.5B). These data indicate that the increase in CMC due to monomer degradation can be utilized to enhance micelle destabilization, which may be useful for efficient, triggered drug release. This result is in agreement with a recent study that incorporated small quantities of the degradable monomer DMAEA into a diblock copolymer of dimethylacrylamide (DMA), n-isopropylacrylamide (NIPAM) and butyl acrylate (BA)[21]. In this study, the DMA-*b*-

(NIPAM-*co*-DMAEA-*co*-BA) micelles destabilized upon degradation of the DMAEA monomer. The degradation of DMAEA has been deemed to be autocatalytic, occurring over the span of roughly 10 days, and independent of pH, concentration and polymer molecular weight[12-13, 22].

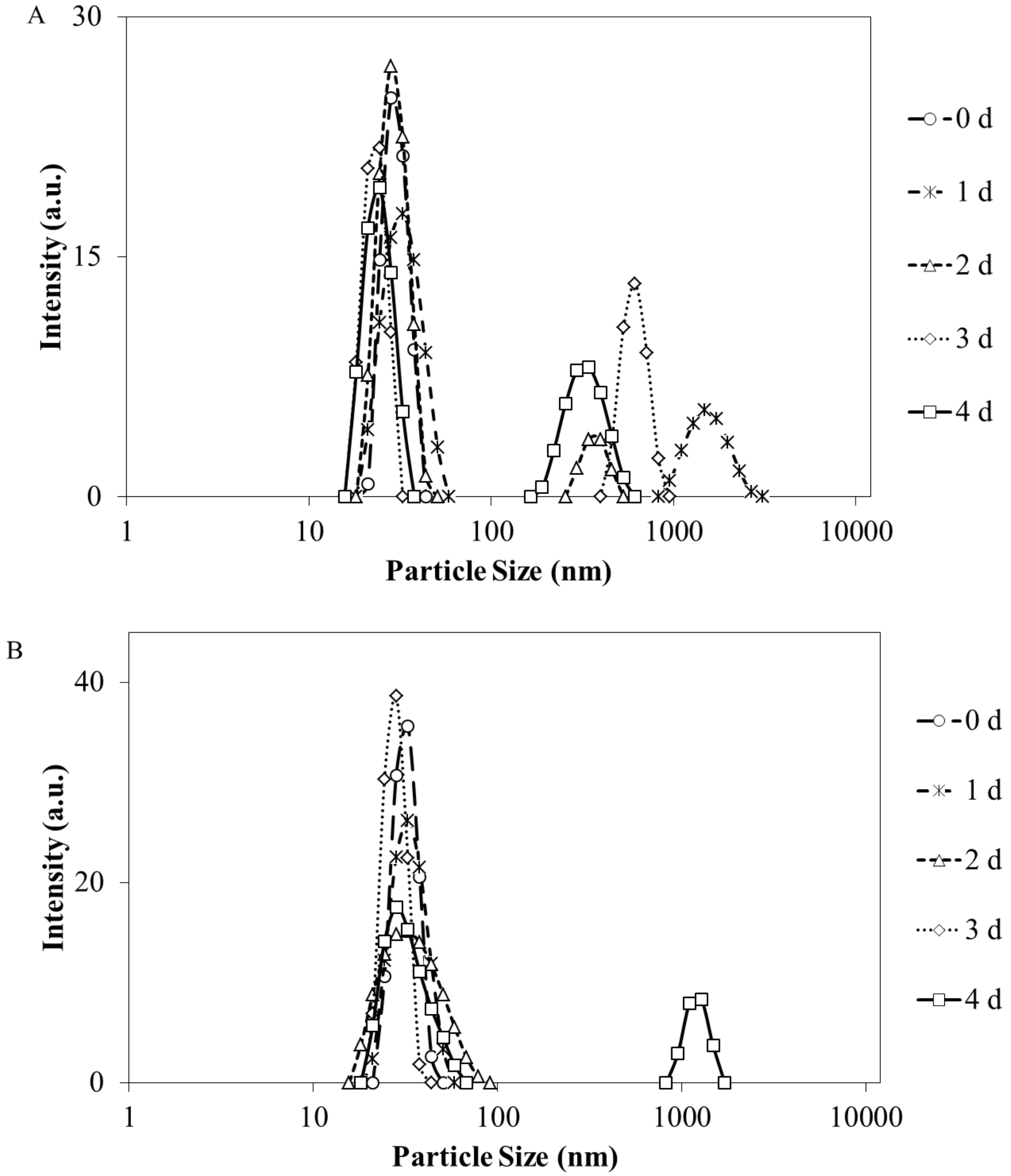

Figure 4.5. Representative DLS plots of a degradable (A) and a non-degradable (B) formulation with 60% cationic monomer incorporation.

To further track hydrodynamic stability, micelles were formulated in pD 7.4 D_2O and analyzed by ^1H NMR. The appearance of peaks associated with the exposure of the cationic core of the micelles was tracked with time, shown in Figure 4.6. The rate of appearance of peaks related to the cationic core is inversely proportional to hydrophobic content. None of the solutions show signs of cationic core exposure for at least 24 hours, but at 6 days the degradable micelles showed characteristic peaks of the hydrophobic core indicating micelle instability (Figure 4.6B Insert).

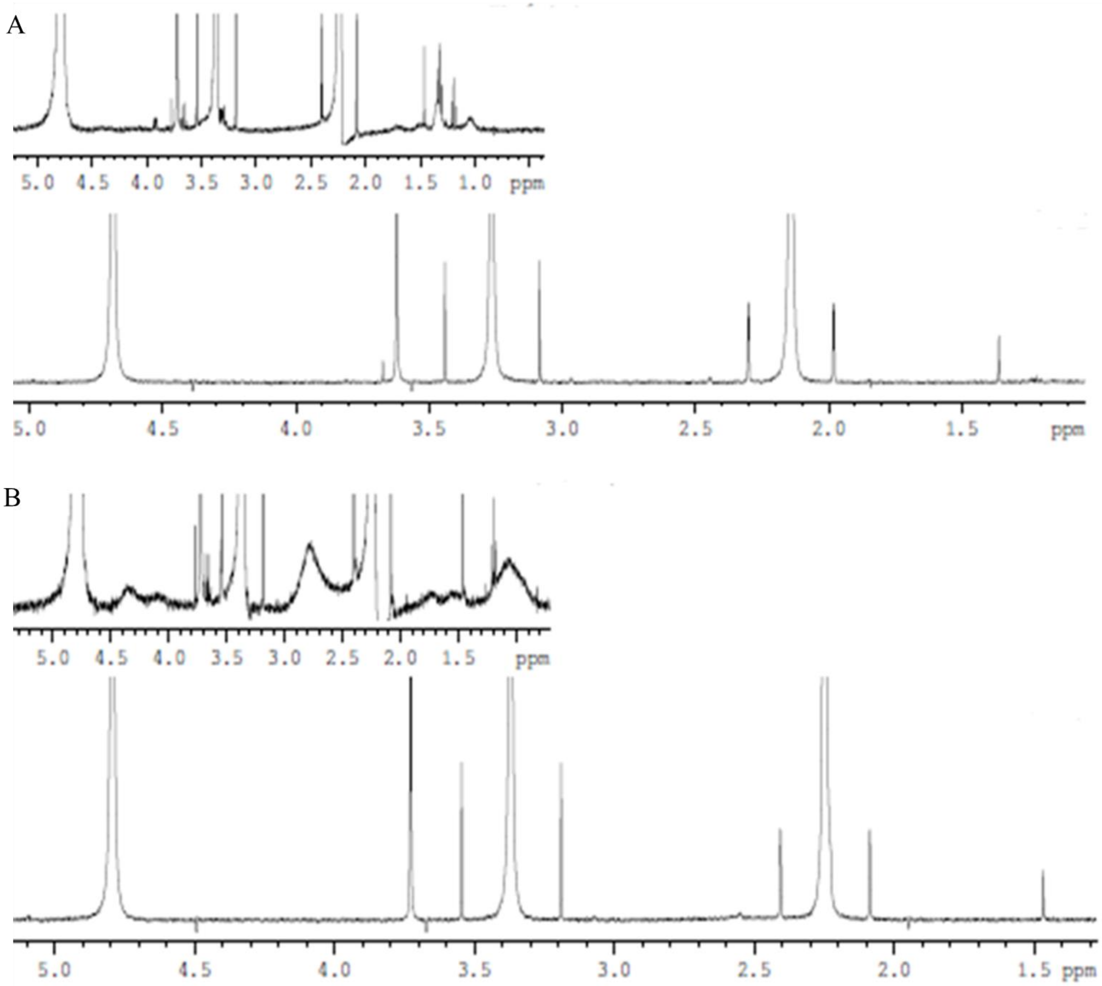

Figure 4.6. ^1H NMR spectra of a non-degradable (A) and degradable (B) polymer with 60% cationic monomer incorporation in buffered D_2O. Main spectral scans are at t=0, while the inserts are after 6 days in solution.

The degradation of the micelles with the highest percentage cationic monomers, which was hypothesized to show the largest difference of degradation effects (i.e. 60% DMAEA and 60% DEAEA) was studied at pH 7.4, 6.5 and 5.6. The polymers were lyophilized and re-dissolved in $CDCl_3$. Interestingly, there is a large change in spectra, which occured faster at lower pH, in the region of 2-4 ppm corresponding to the protons of the cationic branch (Figure 4.7). The downfield shifts in the NMR spectra occur by 6 hours for both DMAEA and DEAEA at pH 5.6 and further shifts downfield occur over the 7 day study. The early shifts can potentially be attributed to the lower pH inducing the cationic branches to protonate, while the slow change over time designates degradation.

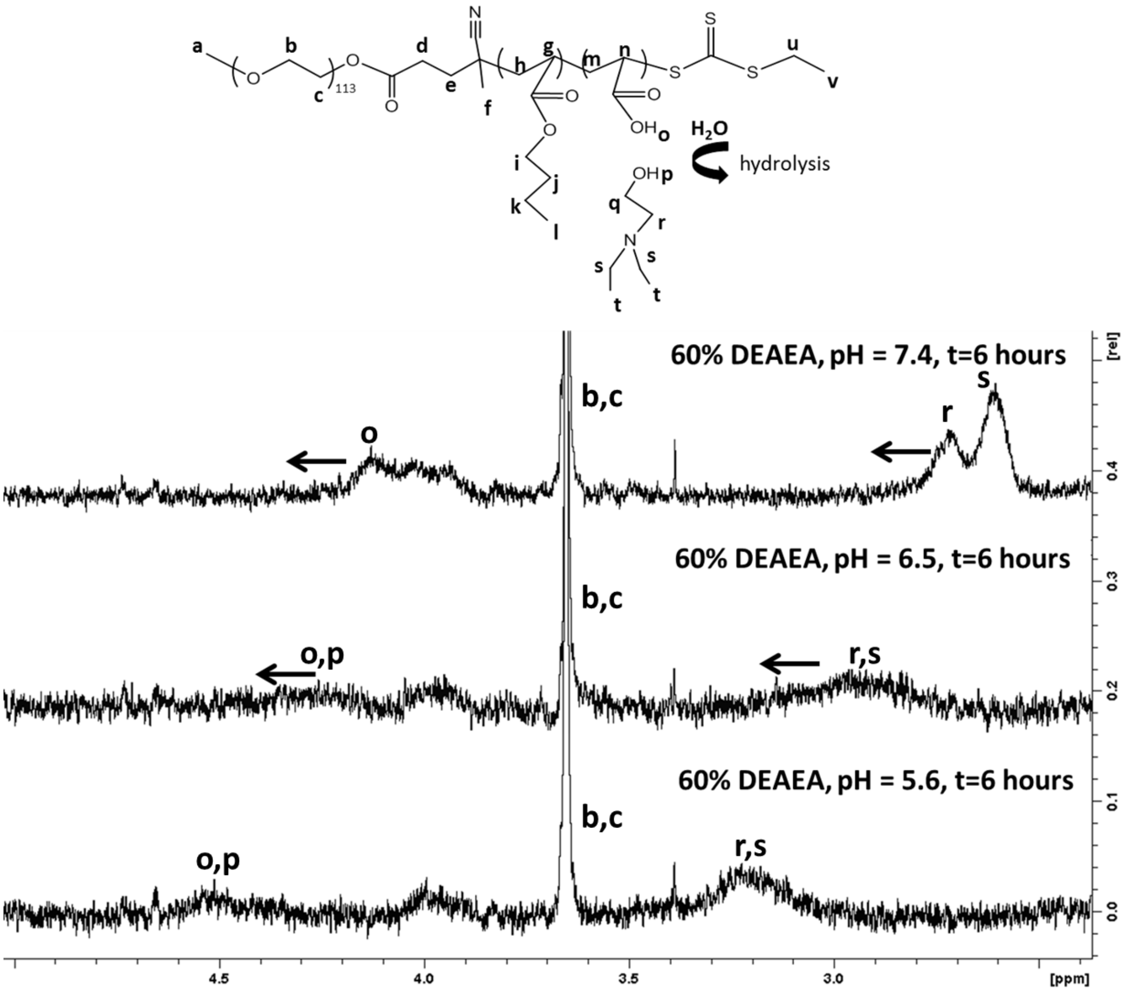

Figure 4.7. ^{1}H NMR spectra of a EA 6 in $CDCl_3$. The polymer was incubated in PBS at a pH of 7.4, 6.5 and 5.6. Downfield shifts could be caused by degradation.

GPC traces showed that the PEG corona degrades only when the cationic content is increased above 40% (Figure 4.8). pH seems to have little effect on the degradation of the micelle. The appearance of a secondary elution peak with the EA 6 polymer matches the elution time of the PEG-ECT starting material. Additional shifts in the primary elution peak could be indicative of backbone degradation. Taken as a whole, the polymers with 60% cationic monomers are less stable micelles, which results in susceptibility to degradation.

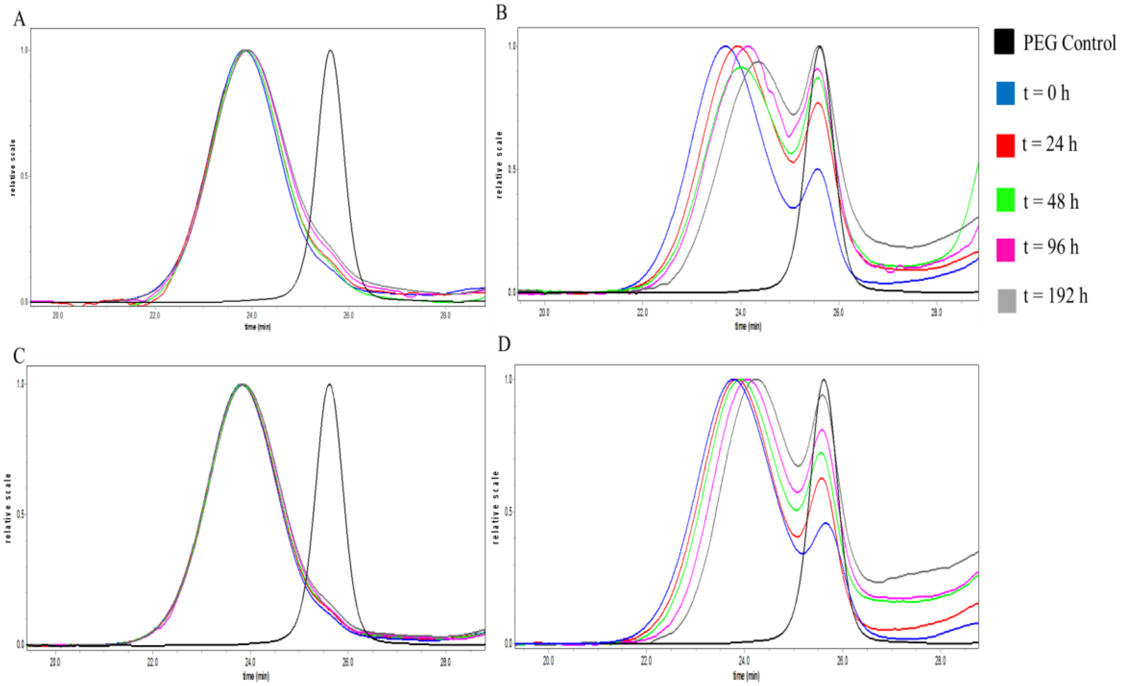

Figure 4.8. Gel permeation chromatography scans of EA 4 (A&C) and EA 6 (B-D) at pH 7.4 (top row) and 5.6 (bottom row).

Hemolysis

The hemolytic behavior of each polymer is shown in Figure 4.9. There is a strong dependence on the relative amounts of cationic and hydrophobic monomers in the hemolytic activity at all concentrations and pH values. Below the CMC, the MEA and MMA subsets show significant hemolysis even at physiological pH, while the degradable EA and MA subsets show no hemolysis at any concentration at physiological pH. The hemolysis begins to occur with most polymers at pH 6.2-6.8, while all polymers show nearly complete hemolysis at pH 5.6. The EA and MA polymer subsets show the most sensitivity in response to slight changes in pH as evinced by the sharp pH-dependent transitions in hemolytic activity in Figure 4.9.

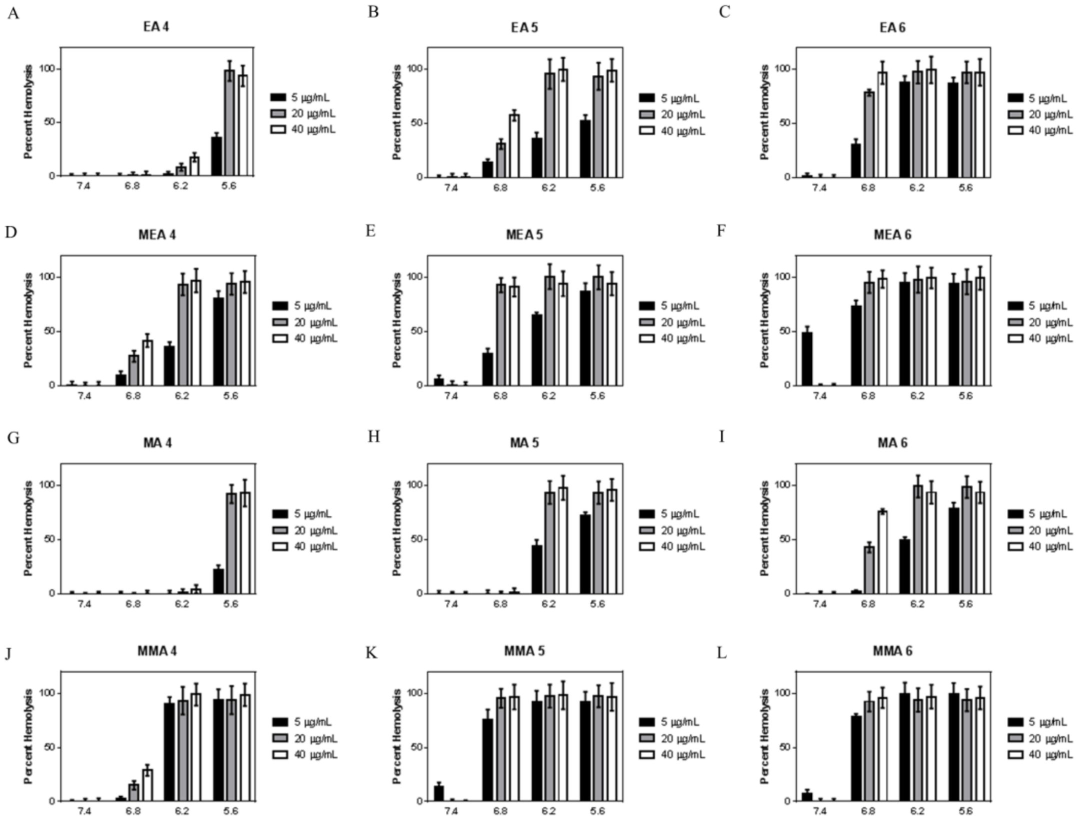

Figure 4.9. Membrane disruptiveness as a function of composition and concentration. Both the degradable (A-F) and the non-degradable (G-L) polymers showed pH responsive membrane disruption. Higher concentration resulted in more hemolytic behavior in a lower range of pH values.

Nile red release

The relationship between pH and micelle destabilization was assessed in the context of release of the model hydrophobic drug NR. Each polymer was tested for encapsulation efficiency and composition dependent release of a model hydrophobic drug was tracked over 4 days at pH 5.6, 6.5 and 7.4, representative of physiological pH, the pH of the early endosomes, and of late endosomes/lysosomes, respectively. At pH 7.4, there was little difference between the polymer groups, as shown in Figure 4.10A-D. Overall there was a slight trend of increased release with increasing amount of cationic monomer incorporation. The EA group showed the most differential release as a function of cationic monomer content with the EA 6 group showing a significant burst release over the first 24 hours. This burst release is likely due to the electrostatic repulsion in the core upon protonation along with the decreased amount of hydrophobic monomer incorporation, which destabilizes the micelles and accelerates drug release.

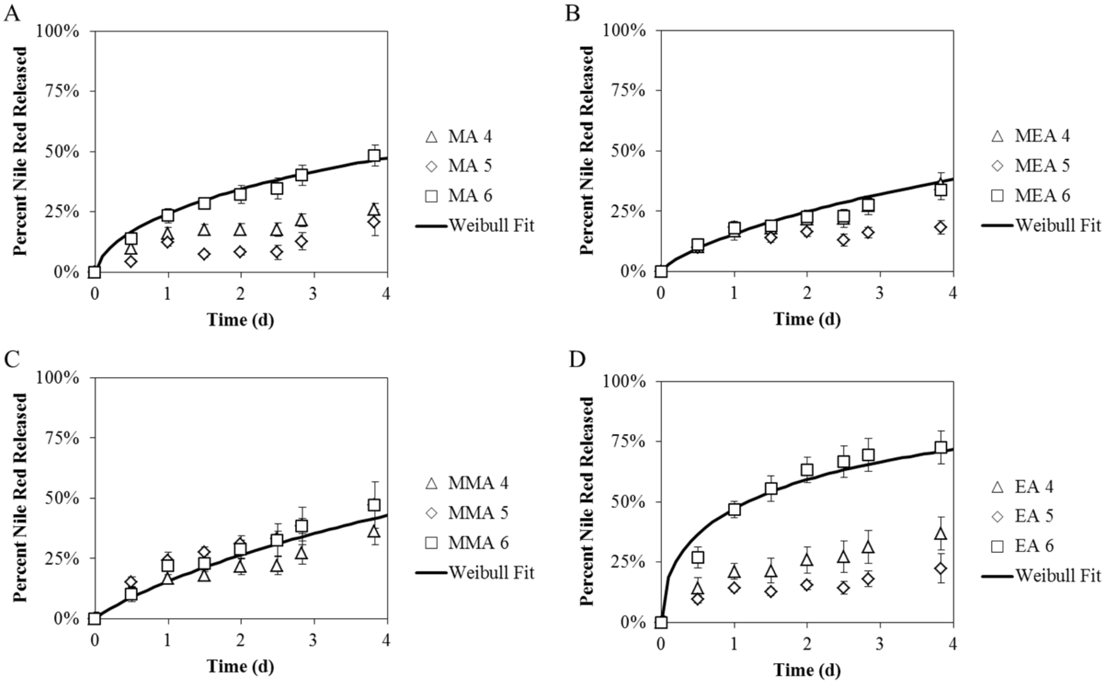

Figure 4.10. Model hydrophobic drug, NR, release at pH 7.4 as a function of time. Nile Red release from non-degradable MMA and MA micelles (A & C, respectively) and degradable MEA and EA micelles (B & D, respectively) over time. Weibull fits are shown for the micelles with highest cationic content (R^2 >= 0.95 for all curves).

The pKa's for each polymer, derived from potentiometric titration, displayed in Table 4.1 shows that EA 6 has the highest value which correlates well with the faster release. The release of drug was modeled by the Weibull function[23], and all polymers could be modeled as diffusion-controlled release (fitting parameters shown in Table 4.2). The lower pH values of 6.5 and 5.6 had minimal effect on the release kinetics of micelles made from the 40% and 50% cationic monomers; however, the 60% cationic monomer groups showed increased burst release behavior (Figure 4.12A-D). The kinetics of release over the first 24 hours showed that the release can be highly accelerated with the pH decreases seen in the early and late stage endosome with the EA 6 formulation demonstrating the fastest release at all pH levels. Additionally, the EA subset of polymers had the most NR loading relative to any of the other groups (Figure 4.13). The release of NR never surpassed 80-85% for all groups indicating that even after degradation there are still hydrophobic aggregates capable of sequestering the NR.

Table 4.2. Weibull fitting parameters for the release of a model hydrophobic drug from each polymer compositoin.

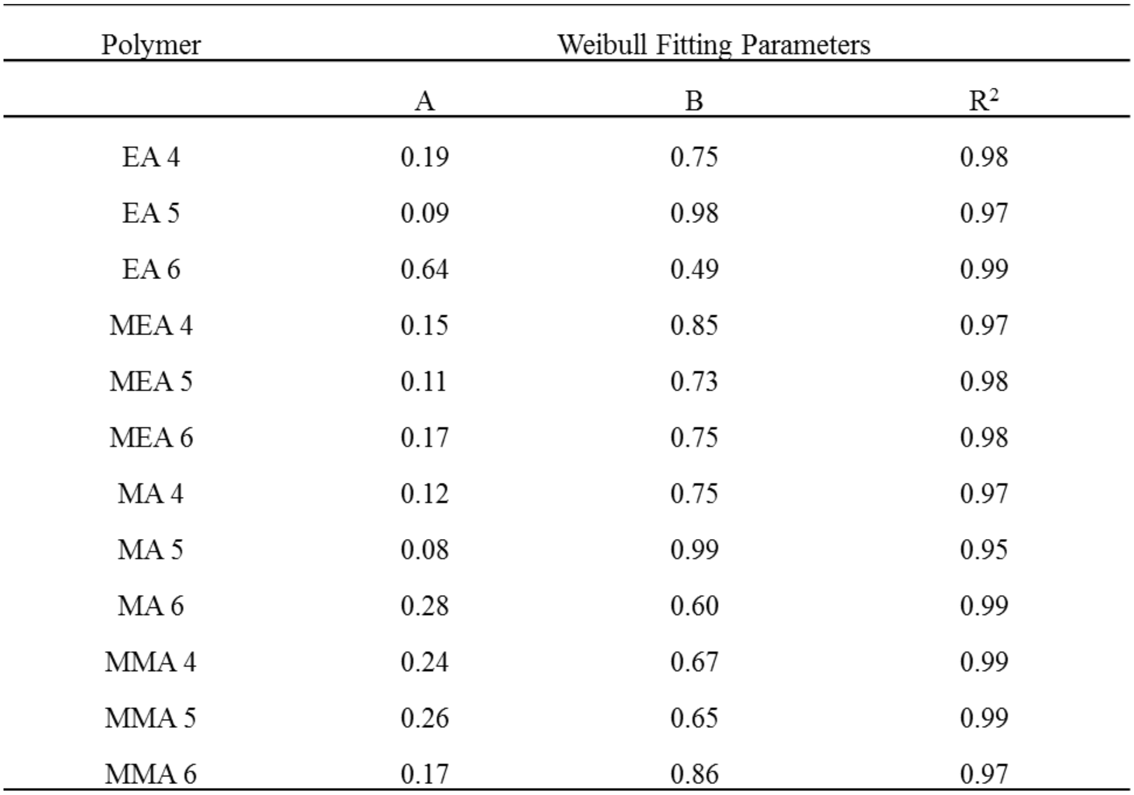

Polymer	Weibull Fitting Parameters		
	A	B	R^2
EA 4	0.19	0.75	0.98
EA 5	0.09	0.98	0.97
EA 6	0.64	0.49	0.99
MEA 4	0.15	0.85	0.97
MEA 5	0.11	0.73	0.98
MEA 6	0.17	0.75	0.98
MA 4	0.12	0.75	0.97
MA 5	0.08	0.99	0.95
MA 6	0.28	0.60	0.99
MMA 4	0.24	0.67	0.99
MMA 5	0.26	0.65	0.99
MMA 6	0.17	0.86	0.97

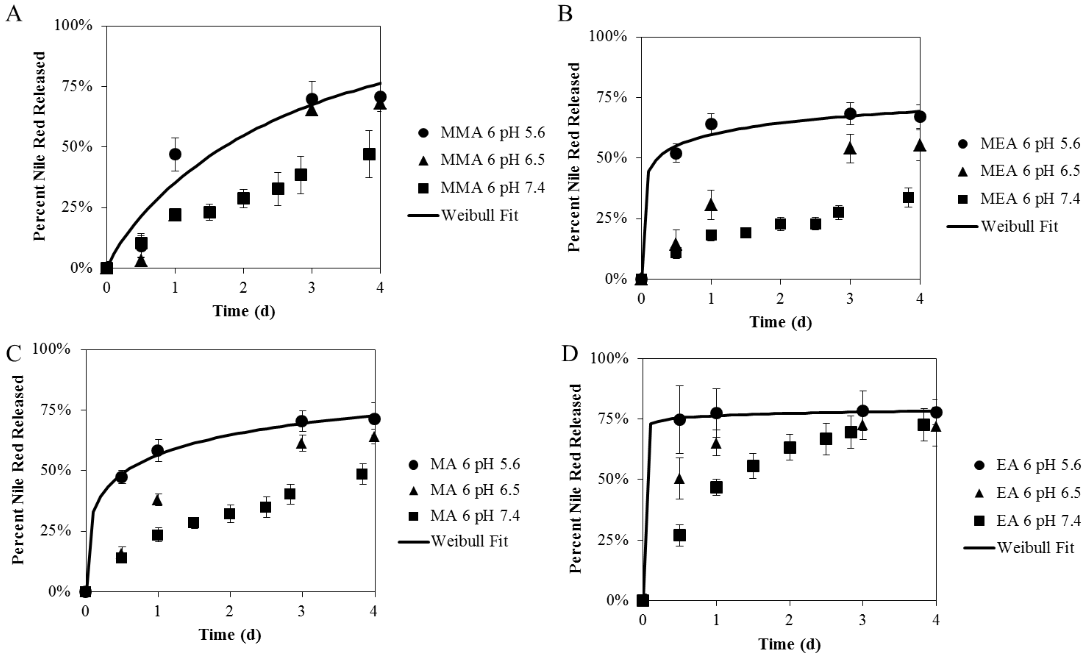

Figure 4.11. Model hydrophobic drug release as a function of pH. Nile Red release from non-degradable (A & C) and degradable (B & D) micelles over time. Weibull fits are shown for the micelles in PBS pH 5.6 (R^2 >= 0.90 for all curves).

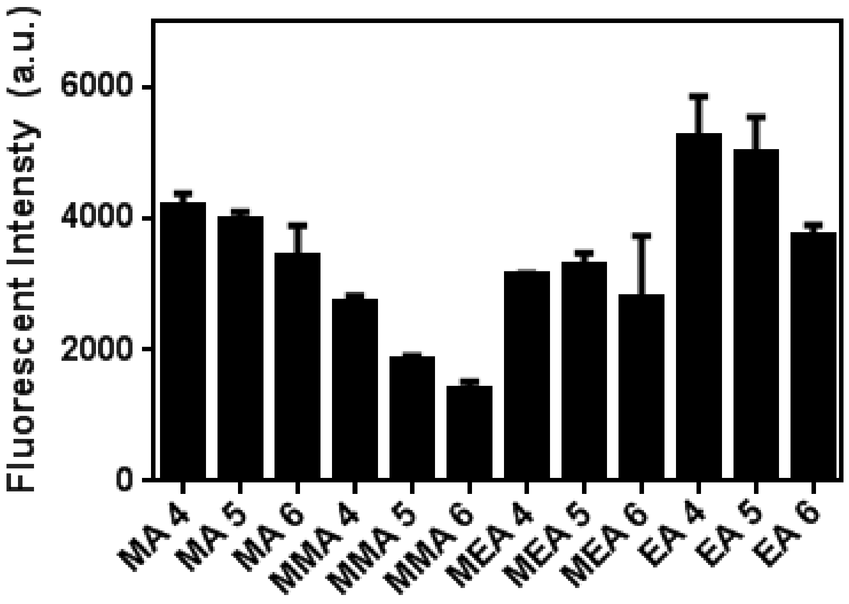

Figure 4.12. Relative Nile Red loading for each polymer composition.

Cytotoxicity

MC3T3 cells were utilized to assess cytotoxicity of each of the polymer groups, shown in Figure 4.13A-B. Not surprisingly, the toxicity increases with increasing cationic content for all of the polymers. At 10 ug/mL concentrations, all micelles exhibit little cytotoxic behavior except for the MEA polymers. The exhibited toxicity of the MEA polymers has been seen in literature for MEA homopolymers above 7 kDa and the toxicity was greatly increased when the polymers were protonated[12]. The total Mw of the MEA segments in the polymer groups analyzed in this study range from 6.5-8.9 kDa. The EA groups exhibited marginal toxicity up to 100 μg/mL, further indicating their potential usefulness. This data matches well with the membrane disruptiveness seen in the hemolysis assay, as the most membrane-disruptive polymers display increased cytotoxicity.

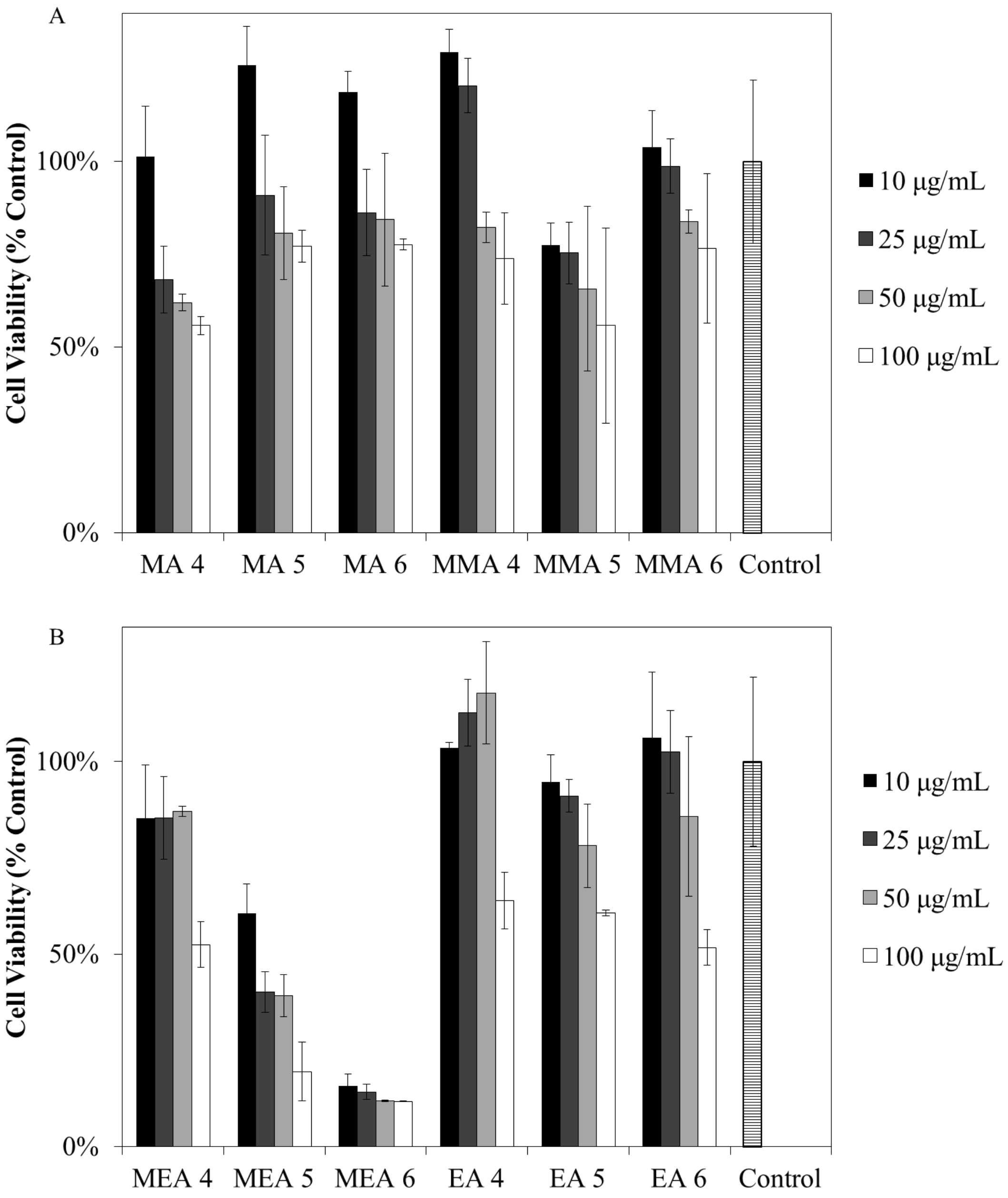

Figure 4.13. Effect of a 2 hour exposure of micelles, followed by 24 hours of incubation, on viability of MC3T3 cells. Viability of MC3T3 cells exposed to varying concentrations of (A) non-degradable and (B) degradable micelles over 24 hours.

Cellular uptake

Cell uptake was visualized by encapsulation of Nile Red in micelles at a concentration of 0.1 mg/mL. The Nile Red loaded micelles were added to cell culture media of MDA-231, MC3T3, and rat derived BMSCs. Pure Nile Red solubilized in methanol (10 ug/mL) was added to control wells. Fluorescent microscopy was used to visually observe the uptake of the Nile Red. The resulting images shown (Figure 4.14) were taken after 2 hours of treatment. The fluorescent signals were higher in all of the nanoparticle treated cells with respect to the pure drug control, regardless of the composition of the micelles or cell type. Cellular uptake was normalized to fluorescent intensity per cell and the average fold increase of fluorescence over the control treatments was 33, 21, and 5 for the MDA, MSCs and MC3T3s, respectively. The increase in uptake may be due to the accelerated rate of growth of the cancerous cell line. There were no significant trends between polymer groups when the uptake was analyzed on a per cell basis for each cell line. The release of Nile Red seems to be distributed throughout the cells cytoplasm suggesting escape from the endo-lysosomal trafficking pathway. The ability to deliver small quantities of Nile Red (10 ug/mL) and produce robust intracellular distribution (compared to the same amount of pure drug) convincingly demonstrates the potential of these particles for tuned delivery of a hydrophobic payload.

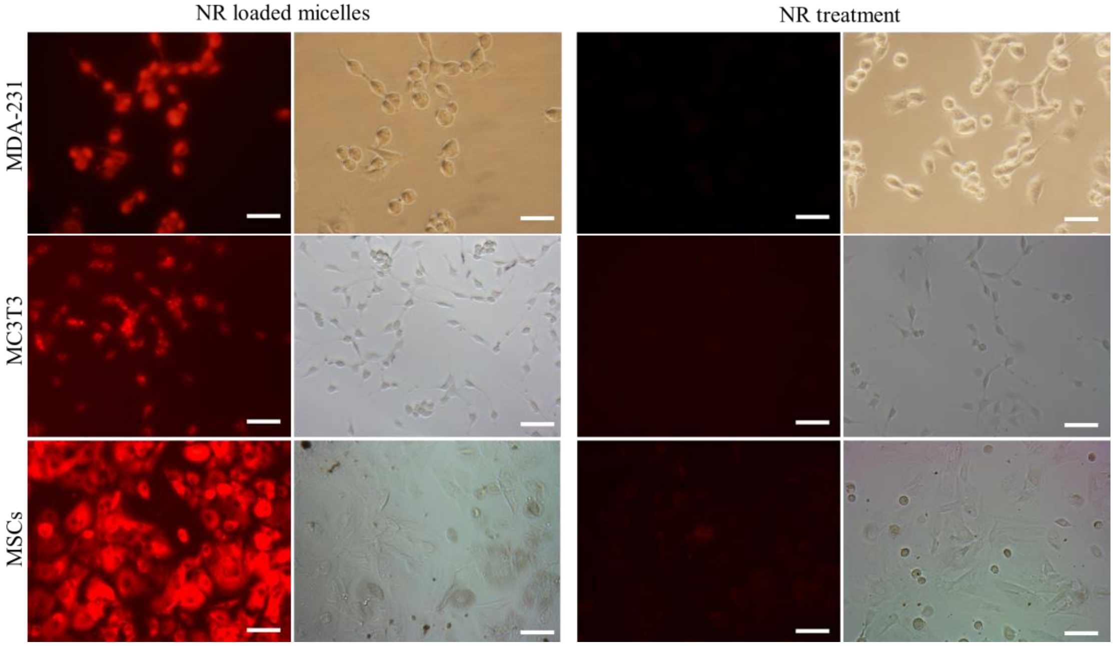

Figure 4.14. Cellular uptake of NR loaded micelles or treatment with NR dissolved in methanol.

Conclusions

A PEG RAFT macro-CTA was utilized to copolymerize degradable or non-degradable cationic monomers with the hydrophobic monomer BMA. The resulting library of polymers produced narrowly dispersed micelles that were able to load and release a model hydrophobic drug upon exposure to pH ranges indicative of the endo-lysosomal trafficking pathway. Polymers containing a higher mole percent of the cationic monomers displayed the most pH-sensitive release kinetics, specifically, the polymers comprised of the degradable DEAEA monomer showed accelerated release relative to the analogous polymers. Finally, the efficient intracellular delivery of NR was shown in three different cell lines representing various targetable populations. Of particular interest is that the cancerous cell lines had increased uptake based on the per cell fluorescent readings, and that cancer microenvironments are typically characterized by a slightly acidic pH which would trigger accelerated drug release from the degradable EA micelle formulations. In conclusion, this work shows that micellar nanoparticles formulated from amphiphilic diblock copolymers consisting of cationic and hydrophobic monomers show promise for the controlled, pH-dependent delivery of hydrophobic therapeutics and allow for endosomal release of the payload into the cytoplasm. These findings highlight the potential of multifunctional, environmentally responsive ‘smart’ drug delivery vehicles for a variety of therapeutic applications and support further study and optimization of this approach to the intracellular delivery of hydrophobic drugs.

References

1. (a) Gaucher, G.; Marchessault, R. H.; Leroux, J.-C., Polyester-based micelles and nanoparticles for the parenteral delivery of taxanes. *J. Control. Release* **2010,** *143* (1), 2-12; (b) Lu, J.; Li, N.; Xu, Q.; Ge, J.; Lu, J.; Xia, X., Acetals moiety contained pH-sensitive amphiphilic copolymer self-assembly used for drug carrier. *Polymer* **2010,** *51* (8), 1709-1715; (c) Chan, J. M.; Zhang, L.; Yuet, K. P.; Liao, G.; Rhee, J.-W.; Langer, R.; Farokhzad, O. C., PLGA–lecithin–PEG core–shell nanoparticles for controlled drug delivery. *Biomaterials* **2009,** *30* (8), 1627-1634; (d) Gupta, M. K.; Meyer, T. A.; Nelson, C. E.; Duvall, C. L., Poly(PS-b-DMA) micelles for reactive oxygen species triggered drug release. *J. Control. Release* **2012,** *162* (3), 591-598.

2. (a) Duvall, C. L.; Convertine, A. J.; Benoit, D. S.; Hoffman, A. S.; Stayton, P. S., Intracellular delivery of a proapoptotic peptide via conjugation to a RAFT synthesized endosomolytic polymer. *Molecular pharmaceutics* **2010,** *7* (2), 468-476; (b) Zhang, J.; Lei, Y.; Dhaliwal, A.; Ng, Q. K. T.; Du, J.; Yan, M.; Lu, Y.; Segura, T., Protein−Polymer Nanoparticles for Nonviral Gene Delivery. *Biomacromolecules* **2011,** *12* (4), 1006-1014.

3. (a) Convertine, A. J.; Benoit, D. S.; Duvall, C. L.; Hoffman, A. S.; Stayton, P. S., Development of a novel endosomolytic diblock copolymer for siRNA delivery. *J. Control. Release* **2009,** *133* (3), 221-229; (b) Wilson, D. S.; Dalmasso, G.; Wang, L.; Sitaraman, S. V.; Merlin, D.; Murthy, N., Orally delivered thioketal nanoparticles loaded with TNF-α–siRNA target inflammation and inhibit gene expression in the intestines. *Nature materials* **2010,** *9* (11), 923-928.

4. Maeda, H.; Wu, J.; Sawa, T.; Matsumura, Y.; Hori, K., Tumor vascular permeability and the EPR effect in macromolecular therapeutics: a review. *J. Control. Release* **2000,** *65* (1), 271-284.

5. Hrkach, J.; Von Hoff, D.; Ali, M. M.; Andrianova, E.; Auer, J.; Campbell, T.; De Witt, D.; Figa, M.; Figueiredo, M.; Horhota, A., Preclinical development and clinical translation of a PSMA-targeted docetaxel nanoparticle with a differentiated pharmacological profile. *Science translational medicine* **2012,** *4* (128), 128ra39-128ra39.

6. (a) Chien, M.-P.; Thompson, M. P.; Barback, C. V.; Ku, T.-H.; Hall, D. J.; Gianneschi, N. C., Enzyme-Directed Assembly of a Nanoparticle Probe in Tumor Tissue. *Advanced Materials* **2013,** *25* (26), 3599-3604; (b) Li, H.; Yu, S. S.; Miteva, M.; Nelson, C. E.; Werfel, T.; Giorgio, T. D.; Duvall, C. L., Matrix Metalloproteinase Responsive, Proximity-Activated Polymeric Nanoparticles for siRNA Delivery. *Advanced Functional Materials* **2013,** *23* (24), 3040-3052.

7. Tannock, I. F.; Rotin, D., Acid pH in Tumors and Its Potential for Therapeutic Exploitation. *Cancer research* **1989,** *49* (16), 4373-4384.

8. (a) Kim, D.; Lee, E. S.; Oh, K. T.; Gao, Z. G.; Bae, Y. H., Doxorubicin-Loaded Polymeric Micelle Overcomes Multidrug Resistance of Cancer by Double-Targeting Folate Receptor and Early Endosomal pH. *Small* **2008,** *4* (11), 2043-2050; (b) Lee, E. S.; Na, K.; Bae, Y. H., Doxorubicin loaded pH-sensitive polymeric micelles for reversal of resistant MCF-7 tumor. *J. Control. Release* **2005,** *103* (2), 405-418.

9. (a) Lee, E. S.; Shin, H. J.; Na, K.; Bae, Y. H., Poly (l-histidine)–PEG block copolymer micelles and pH-induced destabilization. *J. Control. Release* **2003,** *90* (3), 363-374; (b) Lee, E. S.; Oh, K. T.; Kim, D.; Youn, Y. S.; Bae, Y. H., Tumor pH-responsive flower-like micelles of poly (l-lactic acid)-< i> b</i>-poly (ethylene glycol)-<

i> b</i>-poly (l-histidine). *J. Control. Release* **2007,** *123* (1), 19-26; (c) Lee, E. S.; Na, K.; Bae, Y. H., Polymeric micelle for tumor pH and folate-mediated targeting. *J. Control. Release* **2003,** *91* (1), 103-113.

10. Cai, J.; Yue, Y.; Rui, D.; Zhang, Y.; Liu, S.; Wu, C., Effect of Chain Length on Cytotoxicity and Endocytosis of Cationic Polymers. *Macromolecules* **2011,** *44* (7), 2050-2057.

11. Nelson, C. E.; Kintzing, J. R.; Hanna, A.; Shannon, J. M.; Gupta, M. K.; Duvall, C. L., Balancing Cationic and Hydrophobic Content of PEGylated siRNA Polyplexes Enhances Endosome Escape, Stability, Blood Circulation Time, and Bioactivity in Vivo. *ACS Nano* **2013,** *7* (10), 8870-8880.

12. Truong, N. P.; Jia, Z.; Burges, M.; McMillan, N. A. J.; Monteiro, M. J., Self-Catalyzed Degradation of Linear Cationic Poly(2-dimethylaminoethyl acrylate) in Water. *Biomacromolecules* **2011,** *12* (5), 1876-1882.

13. (a) Aksberg, R.; Wågberg, L., Hydrolysis of cationic polyacrylamides. *Journal of Applied Polymer Science* **1989,** *38* (2), 297-304; (b) van de Wetering, P.; Moret, E. E.; Schuurmans-Nieuwenbroek, N. M. E.; van Steenbergen, M. J.; Hennink, W. E., Structure−Activity Relationships of Water-Soluble Cationic Methacrylate/Methacrylamide Polymers for Nonviral Gene Delivery. *Bioconjugate Chemistry* **1999,** *10* (4), 589-597; (c) van de Wetering, P.; Zuidam, N. J.; van Steenbergen, M. J.; van der Houwen, O. A. G. J.; Underberg, W. J. M.; Hennink, W. E., A Mechanistic Study of the Hydrolytic Stability of Poly(2-(dimethylamino)ethyl methacrylate). *Macromolecules* **1998,** *31* (23), 8063-8068.

14. Moad, G.; Chong, Y.; Postma, A.; Rizzardo, E.; Thang, S. H., Advances in RAFT polymerization: the synthesis of polymers with defined end-groups. *Polymer* **2005,** *46* (19), 8458-8468.

15. (a) Cotanda, P.; Wright, D. B.; Tyler, M.; O'Reilly, R. K., A comparative study of the stimuli-responsive properties of DMAEA and DMAEMA containing polymers. *Journal of Polymer Science Part A: Polymer Chemistry* **2013,** *51* (16), 3333-3338; (b) Lee, H.; Son, S. H.; Sharma, R.; Won, Y.-Y., A Discussion of the pH-Dependent Protonation Behaviors of Poly (2-(dimethylamino) ethyl methacrylate)(PDMAEMA) and Poly (ethylenimine-ran-2-ethyl-2-oxazoline)(P (EI-r-EOz)). *The Journal of Physical Chemistry B* **2011,** *115* (5), 844-860.

16. (a) Fineman, M.; Ross, S. D., Linear method for determining monomer reactivity ratios in copolymerization. *Journal of Polymer Science* **1950,** *5* (2), 259-262; (b) Wang, G.-A.; Wang, C.-C.; Chen, C.-Y., The flame-retardant material – 1. Studies on thermal characteristics and flame retardance behavior of phosphorus-containing copolymer of methyl methacrylate with 2-methacryloxyethyl phenyl phosphate. *Polymer Degradation and Stability* **2006,** *91* (11), 2683-2690.

17. Pitchumani, S.; Reddy, C. R.; Rajadurai, S., Reactivity ratios of ethyl acrylate, n-butyl methacrylate copolymer system by 1H-NMR. *Journal of Polymer Science: Polymer Chemistry Edition* **1982,** *20* (2), 277-282.

18. Crownover, E.; Duvall, C. L.; Convertine, A.; Hoffman, A. S.; Stayton, P. S., RAFT-synthesized graft copolymers that enhance pH-dependent membrane destabilization and protein circulation times. *J. Control. Release* **2011,** *155* (2), 167-174.

19. (a) Wong, C.; Stylianopoulos, T.; Cui, J.; Martin, J.; Chauhan, V. P.; Jiang, W.; Popović, Z.; Jain, R. K.; Bawendi, M. G.; Fukumura, D., Multistage nanoparticle delivery

system for deep penetration into tumor tissue. *Proceedings of the National Academy of Sciences* **2011,** *108* (6), 2426-2431; (b) Yamamoto, Y.; Nagasaki, Y.; Kato, Y.; Sugiyama, Y.; Kataoka, K., Long-circulating poly(ethylene glycol)–poly(d,l-lactide) block copolymer micelles with modulated surface charge. *J. Control. Release* **2001,** *77* (1–2), 27-38.
20. Torchilin, V., Tumor delivery of macromolecular drugs based on the EPR effect. *Advanced Drug Delivery Reviews* **2011,** *63* (3), 131-135.
21. Tran, N. T.; Jia, Z.; Truong Phuoc, N.; Cooper, M. A.; Monteiro, M. J., Fine Tuning the Disassembly Time of Thermoresponsive Polymer Nanoparticles. *Biomacromolecules* **2013**.
22. Tran, N. T. D.; Jia, Z.; Truong, N. P.; Cooper, M. A.; Monteiro, M. J., Fine Tuning the Disassembly Time of Thermoresponsive Polymer Nanoparticles. *Biomacromolecules* **2013**.
23. Papadopoulou, V.; Kosmidis, K.; Vlachou, M.; Macheras, P., On the use of the Weibull function for the discernment of drug release mechanisms. *Int J Pharm* **2006,** *309* (1-2), 44-50.

CHAPTER V

DESIGN AND CHARACTERIZATION OF INJECTABLE, SETTABLE POLYURETHANE BONE GRAFTS FOR POTENTIAL TREATMENT OF CANCER INDUCED BONE DISEASE

Introduction

Injectable biomaterials offer significant advantages over pre-formed implants or autologous grafts, in part due to their ability to be administered using minimally invasive techniques and conform to defects with a complex geometry. In the treatment of bone defects, injectable biomaterials are of interest for a number of clinical indications, including filling of contained defects where the structural bone is intact, as well as defects in trabecular bone at non-weight-bearing sites[1]. Injectable, settable grafts would be ideal for defects caused by cancer induced bone disease, where the majority of defects are untreatable due to the inability to surgically resect and replace damaged bone. If a graft could be developed that would replace the resected bone tissue and result in reformation of new bone it would provide a treatment option to patients suffering from essentially an incurable disease. To ensure any remaining cancer cells are destroyed, a therapeutic could be added to the graft for local delivery.

Since their discovery in 1982[2], calcium phosphate cements (CPCs) have been successfully introduced into the clinic due to their ease of use, osteoconductivity, and fast setting times[3]. However, their poor shear and fatigue properties can lead to brittle fracture when CPCs are subject to physiologically relevant dynamic loads[4]. Hydroxyapatite (HA) cements have been combined with hydrogels (e.g., dextran[5] or sodium hyaluronate[6]) to form osteoconductive injectable bone void fillers (BVFs). Other

BVFs for metaphyseal bone defects include non-setting allograft pastes[7], which are typically delivered using viscous carriers such as hyaluronic acid or glycerol[8]. While injectable pastes promote bone healing, they do not set *in situ*, resulting in weak mechanical properties.

Two-component lysine-derived reactive polyurethanes (PURs) have been investigated as injectable BVFs and cements, and have been shown to elicit a mild and transient inflammatory response[9], support cellular infiltration and new bone formation, and degrade to non-cytotoxic breakdown products in metaphyseal bone defects in rats, rabbits, and sheep[10]. In contrast to non-setting pastes, PURs incorporate a viscous isocyanate (NCO)-terminated prepolymer that reacts with viscous active hydrogen compounds (e.g., water, polyols, or polyamines) to form a polymeric network *in situ* with tough, elastomeric mechanical properties. However, injectable PURs present additional challenges beyond the biocompatibility requirements for biomedical implants, such as the toxicity and ultimate fate of reactive components that are not incorporated in the final cured product[11]. Additionally, the injected PUR may have adverse effects on surrounding host tissue due to the reaction exotherm or the reactivity of the NCO-terminated prepolymer[12]. Diffusion of water from the wound bed into the reactive PUR can result in over-expansion of the scaffold, resulting in large voids[13]. Therefore, it is necessary to fully understand the complex PUR reactions to better predict the biocompatibility of the material *in vivo*.

In this study, we investigated the effects of stoichiometry and catalyst concentration on the reactivity, injectability, settability, and biocompatibility of PUR biocomposites. Bovine mineralized bone particles (B-MBP) were incorporated in the biocomposites to increase their strength, control expansion of the material by absorbing excess moisture from the wound bed, and provide an osteoconductive matrix to enhance new bone formation. The liquid components included a ter-polyester triol, a lysine triisocyanate (LTI)-poly(ethylene glycol) (PEG) prepolymer, a catalyst solution comprising triethylene diamine (TEDA) dissolved in dipropylene glycol (DPG), and water (both present in the reactive mixture and diffusing from the environment). A kinetic model describing the reactivity of the injectable biocomposites using an *in situ* ATR-FTIR technique was developed, which was used to calculate the disappearance of isocyanate (NCO) equivalents at two stoichiometric conditions and catalyst concentrations. To assess the biocompatibility of the reactive components released during cure, the biocomposites were incubated in saline or medium at two time points. The composition of the components leached from the biocomposite was determined by NMR, and the cytotoxicity was assessed by live/dead staining. Finally, the ability of the biocomposites to remodel and support new bone formation was evaluated in a rabbit femoral condyle plug defect model.

Experimental

Materials

A lysine triisocyanate-poly(ethylene glycol) (LTI-PEG) prepolymer (21.7% NCO) and a polyester triol (900 g/mol) were obtained from Ricerca Biosciences (Concord, OH). The backbone of the polyester triol comprised 60% caprolactone, 30% glycolide, and 10% lactide. Triethylene diamine (TEDA) and dipropylene glycol (DPG) were purchased from Aldrich (St. Louis, MO). Bovine mineralized bone particles (B-

MBP) were obtained from Medtronic, Inc (Minneapolis, MN). All other reagents were purchased from Aldrich. DPG was dried over 4 Å sieves before use. TEDA, a well-known tertiary amine polyurethane catalyst with low toxicity[14], was dissolved in a 10% (w/v) solution with dry DPG. Excess organic material (e.g. fat) was removed from B-MBPs with a chloroform/acetone solution and the bone was lyophilized before use. The B-MBPs were then sieved to include only 105-500 µm particles.

Characterization of reactive PUR components

The hydroxyl (OH) number of the polyester triol was measured by titration according to ASTM D4274-99 Method C, and the molecular weight was determined by gel permeation chromatography (GPC, Waters Breeze). Prior to use, the polyester triol was washed with hexane and dried under vacuum at 80^{o} C for 24 h. The %NCO of the prepolymer was measured by titration according to ASTM D2572-97. The prepolymer was maintained at 4^{o} C under argon prior to use. Water content for all liquid components was determined by Karl Fischer (KF) titration with a 798 MPT Titrino with a 10 mL burette (Metrohm). Briefly, 0.5-5.0 g of material was dissolved in dry methanol and Hydranal-Composite 2 (Sigma-Aldrich), a stock KF reagent, was used to titrate the samples.

Synthesis of biocomposites

Biocomposites (BCs) were prepared by adding the polyester triol, catalyst solution, and B-MBP (45 wt%) to a mixing cup, in which they were hand-mixed for 30 seconds before adding the prepolymer and hand-mixing for an additional 45 seconds. The BC was then loaded into a syringe. The study design is summarized in Table 1. Two catalyst weight percentages (0.50 and 0.25 wt%) and two index values (108 and

195) were utilized. The index characterizes the stoichiometry and is the ratio of isocyanate (NCO) equivalents in the prepolymer to the sum of the hydroxyl (OH) equivalents in the polyester triol and water[15]:

$$\text{INDEX} = 100 \times \frac{\text{NCO eq}}{\text{OH eq (triol)} + \text{OH eq (water)}} \tag{1}$$

Considering that DPG contains less reactive secondary hydroxyl groups, it was anticipated to have a relatively low reactivity and therefore was not included in the index calculations. Thus at an index of 108, the stoichiometry was expected to be well balanced (e.g., 8% excess NCO). A higher index of 195 was also tested to account for the hydroxyl and amine equivalents from the B-MBP[10a].

Table 5.1. Biocomposite formulations.

	I0-C0	I0-C1	I1-C0	I1-C1
Index	108	108	195	195
B-MBP (wt%)	45.0	45.0	45.0	45.0
Catalyst (wt%)	0.25	0.50	0.25	0.50
Water (wt%, measured)	0.06	0.06	0.05	0.05
Water (wt%, fitted)	0.13	0.23	0.11	0.07
LTI-PEG (wt%)	22.4	21.3	30.2	28.8
T6C3G1L900 (wt%)	30.1	28.8	22.3	21.3
DPG (wt%)	2.3	4.4	2.3	4.4

ATR-FTIR analysis of the reactivity of individual components

Attenuated total reflectance-Fourier transform infrared spectroscopy (ATR-FTIR) measurements were conducted with a Seagull Variable Angle Reflection Accessory

(Harrick Scientific) applied to a Tensor 27 FTIR instrument (Bruker)[16]. A ZnSe hemispherical crystal (Harrick Scientific) was utilized to obtain time-resolved ATR spectra. For each reaction characterized, spectra were taken every 20 to 60 seconds at a resolution of 4 cm^{-1} and 56 scans per spectra. Briefly, to obtain the spectral profiles for the reactions of the biocomposites, a given composite was synthesized and placed on a sample holder in direct contact with the bottom of the ZnSe crystal. To derive the spectral profiles for the individual component reactions of the biocomposites, the components were mixed with the prepolymer and catalyst only. The isocyanate peak (2270 cm^{-1}) was de-convoluted and integrated using a MATLAB program and a calibration curve was used to correlate integrated peak values with known concentrations of isocyanate. The analysis was completed in triplicates (n=3) for each reaction analyzed. In order to obtain meaningful results from ATR-FTIR analysis, excellent contact between the crystal and the sample must be maintained. The evanescent wave generated by the FTIR source reflecting from the crystal surface penetrates 1-2 µm into the sample. While the ATR-FTIR technique is well suited for analysis of PUR reactivity due to the excellent contact maintained between the crystal and the liquid components (Figure 5.1A), its applicability is limited by the assumption that the small analysis volume near the surface of the crystal is well-mixed and representative of the bulk. Also, additional processing of the raw data is required to remove the slight distortion of the isocyanate peak due to the presence of CO_2 generated by the reaction of isocyanate and water (Figure 5.1B). To prevent the distortion, a Gaussian fitting algorithm was utilized (Figure 5.1C), which is applicable for the isocyanate peak due to its symmetry[17]. A separate algorithm was used to integrate the area of the fitted peak, from which the concentration of isocyanate equivalents was calculated using a calibration curve (Figure 5.1D).

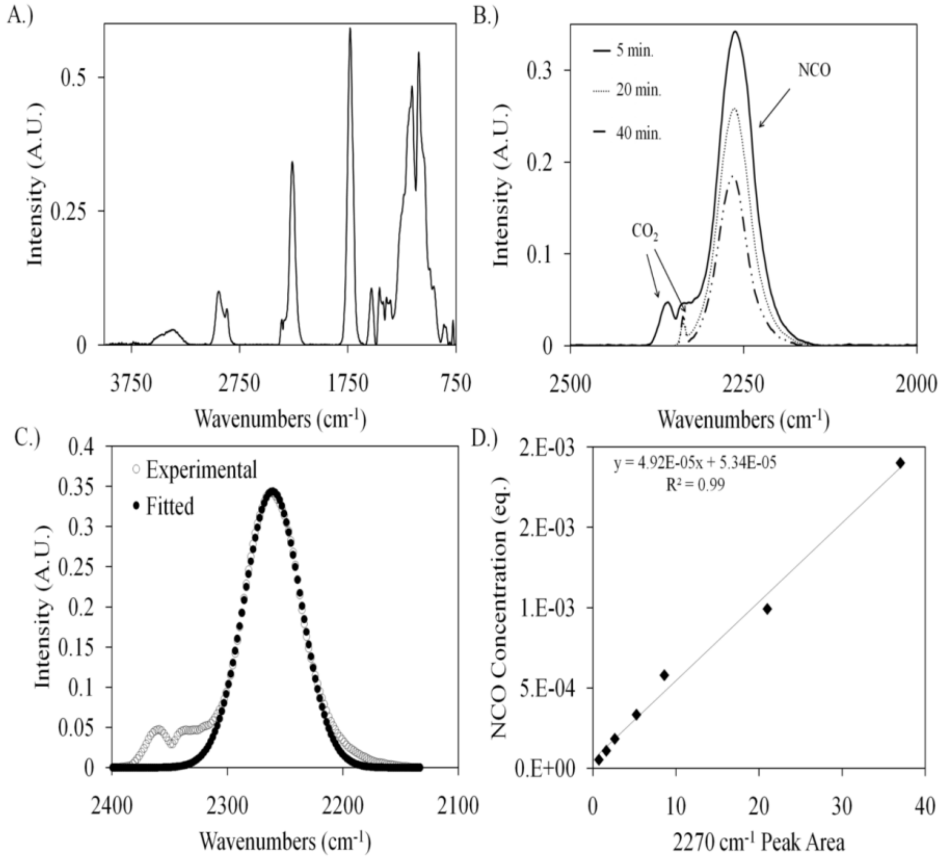

Figure 5.1. Process of determining isocyanate concentration by ATR-FTIR. (A) Typical ATR-FTIR spectra for a given component; (B) Plot of isocyanate peak decreasing with time and the potential influence of CO_2 on the peak shape; (C) Plot of Gaussian fitting algorithm removing the distortion of the CO_2 peaks; (D) Calibration curve to determine the isocyanate concentration in equivalents.

Porosity as a function of water concentration

To determine porosity as a function of water content under dry conditions, biocomposites were prepared with 0 – 1.0 wt% added water and porosity was measured gravimetrically. Briefly, each 0.5 g batch of biocomposites was injected via a straight-bore syringe into cylindrical molds where they were allowed to react overnight at room temperature. Triplicate (n=3) slices of the cylinders were cut from the fully reacted biocomposites and measured with calipers to determine the volume. Scanning electron microscopy (SEM, Hitachi S-4200) micrographs were obtained and analyzed for pore size using MetaMorph 7.1 Image Analysis software (MDS Analytical Technologies). The mass of each slice was used to obtain the density, and the measured density was compared to the theoretical density to calculate the porosity[13], defined as the volume fraction of pores:

$$\boldsymbol{\varepsilon} = 1 - \frac{\underline{\boldsymbol{\rho}}}{\boldsymbol{\rho}_c} \tag{2}$$

where ε is the porosity, $\underline{\rho}$ is the average measured biocomposite density, and ρ_c is the density of the biocomposite assuming there are no pores:

$$\boldsymbol{\rho} = \frac{1}{\frac{x_B}{\boldsymbol{\rho}_B} + \frac{1 - x_B}{\boldsymbol{\rho}_P}} \tag{3}$$

In these equations, $\rho_B = 2100$ kg/m^3 is the density of B-MBP (measured by pycnometry), $\rho_P = 1270$ kg/m^3 is the density of PUR (measured gravimetrically), and x_B is the weight fraction of B-MBP.

In vitro porosity in a simulated wound environment

To simulate the moist curing conditions of the *in vivo* wound environment, biocomposites were injected (immediately after mixing) into 2 mL deionized water and allowed to react overnight in an incubator at 37^o C. Under these wet conditions, porosity measurements were completed for biocomposites with index values of 108 and 195, either 0.50 or 0.25 wt% catalyst, and no added water. At least three cylindrical cores were taken from each sample and analyzed gravimetrically to obtain porosity as described above.

Characterization of components leached from the reactive biocomposites

In order to determine whether cytotoxic reactive components leach from the BC during cure, *in vitro* leaching experiments were performed. Briefly, 2.5 g of each BC were injected into an empty vial and 5 ml PBS was added to the vial 2 min after mixing was started. For the second time point (45 min), 2.5 g of each biocomposite were injected into a sample cup and transferred to a vial filled with 5 mL of PBS after 45 min post-mixing. For the cytotoxicity experiments, samples were incubated in α-minimum essential medium (α-MEM) with 10% (v/v) fetal bovine serum (FBS) and 1% (v/v) penicillin/streptomycin using the procedure described above, and leachates were collected at 2 and 45 min. Samples were maintained at 37^oC for 72 hours, at which time the PBS (or α-MEM) was removed. α-MEM leachates were used for cytotoxicity experiments. The pH of the PBS leachates was measured and the samples subsequently lyophilized and weighed. After reconstitution in PBS, the residue was diluted in deuterated DMSO and characterized by NMR. The spectra were compared to those of the pure components in the biocomposites to determine the presence of individual components in the leachates.

In vitro cytotoxicity of intermediates leached from the reactive biocomposites

The cytotoxicity of the leachates from the biocomposites was measured using MC3T3-E1 embryonic mouse osteoblast precursor cells *in vitro*. Cells were seeded in a 96-well plate with a density of 5×10^3 cells per well and cultured in α-MEM with 10% (v/v) fetal bovine serum (FBS) and 1% (v/v) penicillin/streptomycin in a CO_2 incubator with 5% CO_2 at 37^o C. The concentration of the leachates varied from 6.15% (16X dilution with serum medium) to 100% (1X)[18]. Trypsin-EDTA was used for dissociation of MC3T3-E1 cells. The cells were analyzed for viability using a Live/Dead Viability kit (Invitrogen). The assay was completed as recommended by the manufacturer's instructions. Cells were analyzed after 24 hours exposure to the leachate solution. Triplicates (n=3) for each group were analyzed with control groups treated with blank PBS. All experiments were conducted in accordance with ISO-10993-5.

In vivo biocompatibility and new bone formation in a rabbit femoral condyle plug defect model

Animal experiments were conducted in compliance with the Animal Welfare Act, the implementing Animal Welfare Regulations, and the principles of the Guide for the Care and Use of Laboratory Animals. All surgical and care procedures were carried out under aseptic conditions per the approved IACUC protocol. New Zealand White (NZW) rabbits weighing between 4.0 and 5.4 kg were used in this study. The remodeling process of empty defects (untreated, n=9) was compared to that of defects filled with the I0-C1 biocomposite (n=6) at 8 weeks. The components of the biocomposites were gamma-irradiated using a dose of approximately 25 kGY. Glycopyrrolate was administered at 0.01 mg/kg IM followed by ketamine at 40 mg/kg IM. Bilateral cylindrical defects of approximately 5 mm diameter by 11 mm in depth were drilled in the metaphysis of the distal femurs of each rabbit under copious sterile saline irrigation using a trephine in a MicroAire handpiece. Materials from the I0-C1 group were subsequently injected into each defect using a syringe, made flush with the cortical surface and allowed to harden. Untreated defects were utilized as a control. Closure was attained using a 3-layered approach comprising muscle, fascia, and subcuraneous 3-0 Vicryl sutures. Skin glue was applied topically to maintain closure. Treatment groups for each composite were dispersed randomly among the rabbits. The rabbits were euthanized at 8 weeks using Fatal-plus (1 mL/4.5 kg) intravenously.

μCT analysis

Harvested femoral condyles (n=15) were fixed in 10% neutral buffered formalin at room temperature for one week. During the fixation period, the condyles were scanned with a μCT40 (SCANCO Medical, Basserdorf, Switzerland) while in formalin. Calibration of the μCT40 was completed using the manufacturer's hydroxyapatite (HA) phantom. Scans were performed using an X-ray tube potential of 70 kV, a source current of 114 μA, and a voxel size of 30 μm. The axial images were reconstructed using the software provided by the manufacturer. Attenuation values were converted to Tissue Mineral Density (TMD, in mg HA/cm^3) based on calibration data. After reconstruction, the image stack was rotated such that the depth of the defect was parallel to the z-axis. The volume of interest was defined by centering a 5mm diameter circle on the cross sectional view of the cortical borders of the defect, and extending this cross section to the end of the defect. Segmentation was applied to the resulting cylindrical volume using a threshold of 505 mg HA/cm^3. The threshold value was visually chosen and kept constant for all the samples. Bone volume fraction (BV/TV), Tissue Mineral Density (TMD), connectivity density (Conn.D), and Trabecular number (Tb.N.), thickness (Tb.Th.), and spacing (Tb.Sp.) were quantified in the volume of interest.

Histology

After one week of fixation time in formalin, the samples were decalcified in hydrochloric acid, dehydrated, and embedded in paraffin. The samples were sectioned onto slides 5 μm thick and some were stained using hematoxylin/eosin (H & E stain).

Osteocytes in the interior of new bone as well as the organized structure of the allograft particles were used as parameters to differentiate new bone from allograft bone particles. The remaining sections were stained for the osteoclast marker Tartrate Resistance Acid Phospahatase (TRAP) by treating with a Naphthol AS-BI phosphate substrate solution and a mixture of sodium nitrite and pararosaniline dye followed by a hematoxylin counterstain. Osteoclasts were identified as multinucleated light red cells.

Statistics

One-way ANOVA, performed in JMP 9.0, was used to determine if statistical differences exist between groups. Comparisons of individual sample groups were performed using unpaired Student's t-test. For all experiments, $p < 0.05$ was considered statistically significant.

Results

Reactivity of PUR biocomposites

The five chemical reactions that proceed in parallel during cure of the biocomposite are shown in Figure 5.2. The individual components of the biocomposite (polyester triol, DPG, B-MBP, and water) were analyzed for their reactivity with the NCO-terminated prepolymer. The conversion of NCO equivalents in the prepolymer was monitored *in situ* by ATR-FTIR, which was analyzed to obtain the second-order rate constants for each reaction at each catalyst level.

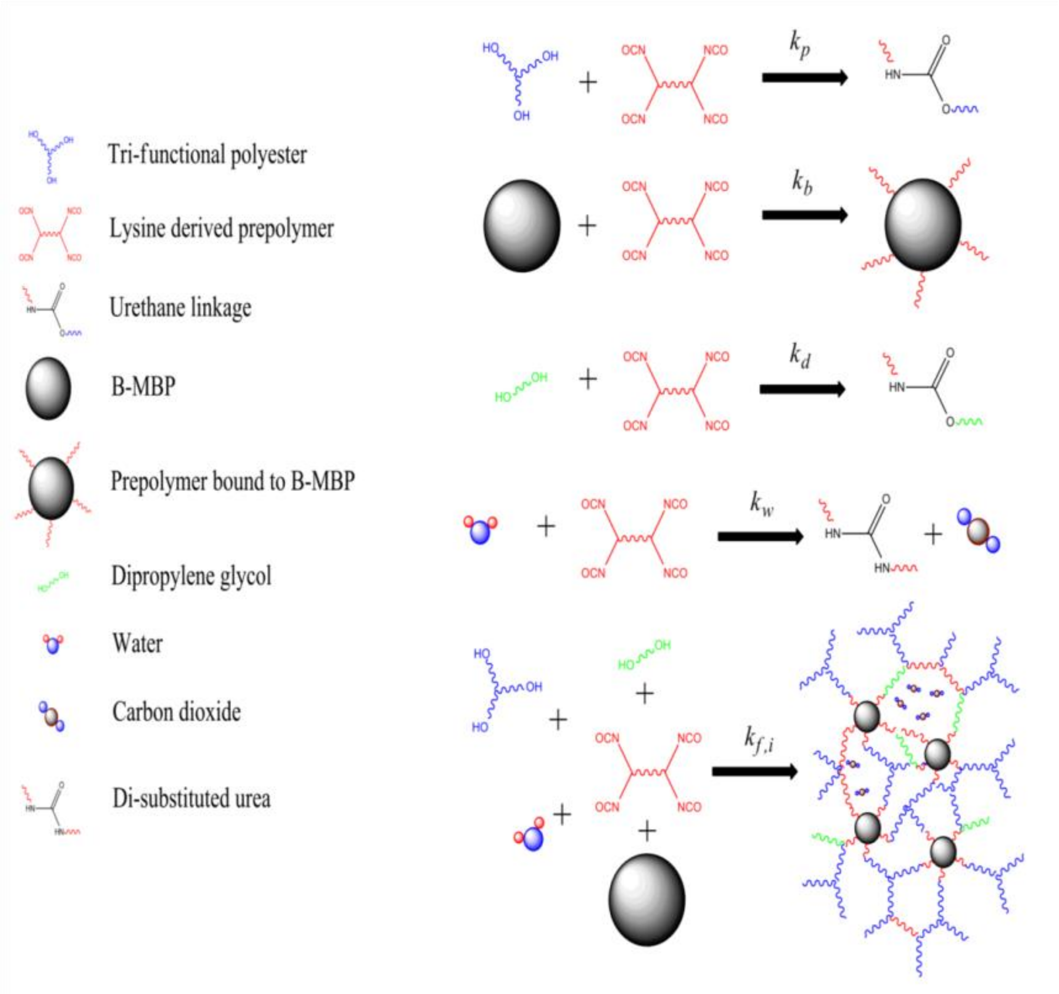

Figure 5.2. Chemical reactions present in the injectable PUR biocomposite.

The same technique was applied for the overall reaction of the biocomposite at two different indices and catalyst levels. The rate law for the assumed second order reaction is given in Eq (4)[19]:

$$rate = k_i \left[\mathrm{OH}\right]\left[\mathrm{NCO}\right] \tag{4}$$

where k_i, [OH] and [NCO] represent the rate constant for component i and the concentrations of hydroxyl and isocyanate equivalents, respectively. The rate equation can be integrated, assuming equal initial concentration (C_0) of [OH] and [NCO], to obtain the following equation:

$$\frac{1}{C} = k_i t + \frac{1}{C_0} \tag{5}$$

where the slope of the inverse concentration of [NCO] equivalents (C) measured by ATR-FTIR plotted versus time represents the second order rate constants for the reaction.

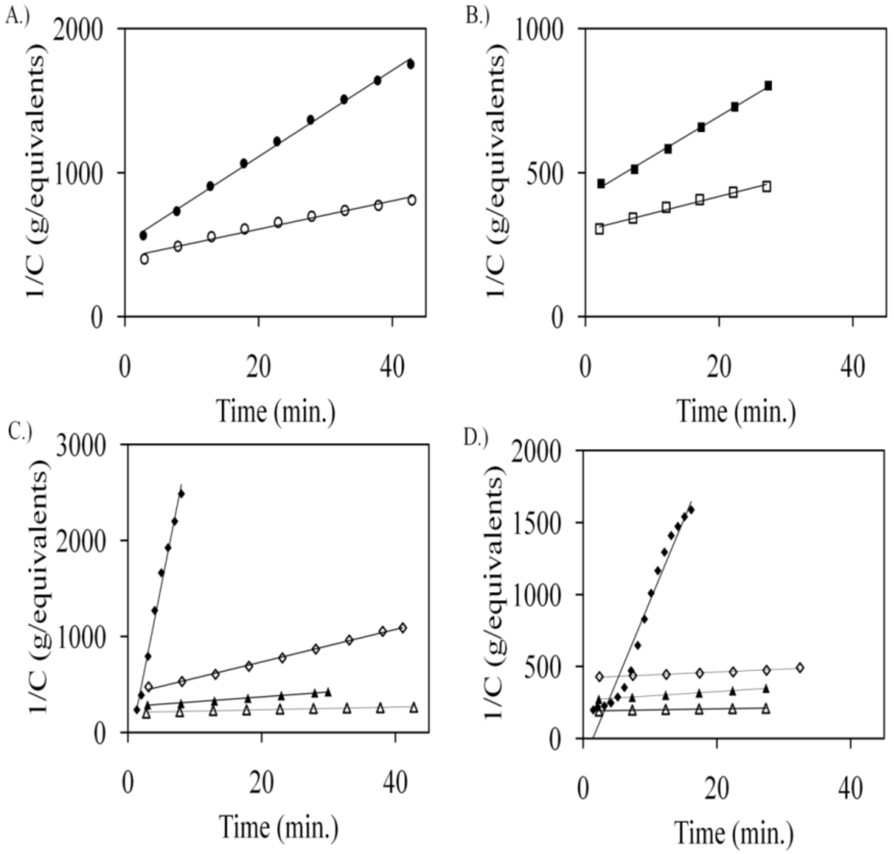

Figure 5.3. Isocyanate (NCO) reactions follow second-order chemical reaction kinetics. The specific reaction rate was calculated by fitting (represented by the straight line) the experimental data to equation 5. Inverse NCO concentration plots for the overall biocomposite reaction at (A) high (0.50 wt%) and (B) low (0.25 wt%) catalyst concentrations. Filled symbols correspond to low (108) index, while open symbols represent high (195) index formulations. Inverse NCO concentration plots for the reaction of the prepolymer with each component shown in Scheme 1 at (C) high (0.50 wt%) and (D) low (0.25 wt%) catalyst concentrations. Key to symbols: water (♦), polyester triol (◊), DPG (▲), and B-MBP (Δ).

Figure 5.3A-B displays plots of inverse concentration of NCO equivalents versus time for the overall biocomposite reaction at high (0.50 wt%) and low (0.25 wt%) catalyst concentrations, respectively. Similarly, inverse NCO concentration plots measured for the reaction of the prepolymer with water, polyester triol, DPG, or B-MBPs are shown in Figure 5.3C-D at high and low catalyst concentrations. The linearity of the inverse concentration plots verifies that each of the reactions follows a second-order mechanism as anticipated[20], and thus the slope of line is equivalent to the rate constant for each of the reactions (Eq. (5)). The second-order rate constants calculated from the data in Figure 5.2 are listed in Table 5.2. Water has the highest reactivity compared to the other reactions, regardless of catalyst concentration. The polyester triol is approximately 20 times less reactive than water for the higher catalyst level, while the DPG is approximately 3 times less reactive than the polyester triol. The reactivity of the B-MBPs is the lowest of all the components at both catalyst levels

Table 5.2. Second-order specific reaction rates for the reaction of each hardener component with the NCO-terminated prepolymer.

		Rate constant (g eq^{-1} min^{-1})	
	Description	C1	C0
k_w	Prepolymer + water reaction	783 ± 140	298 ± 51
k_p	Prepolymer + triol reaction	37.2 ± 4.9	17.4 ± 3.1
k_d	Prepolymer + diol reaction	14.5 ± 0.4	6.16 ± 1.5
k_b	Prepolymer + B-MBP reaction	1.23 ± 0.6*	1.17 ± 0.3*

* There is a statistical significance ($p<0.05$) between all reaction rates except between k_b C1 and k_b C0.

Based on the rate constants measured for the individual components, a kinetic model was developed to predict the overall reactivity of the biocomposites. First, the net rate of reaction r_i is defined for each component i by the following series of equations:

$$\begin{aligned} r_P &= -k_P C_P C_I \\ r_D &= -k_D C_D C_I \\ r_W &= -k_W C_W C_I \\ r_B &= -k_B C_B C_I \\ r_I &= r_P + r_D + r_W + r_B \end{aligned} \tag{7}$$

where k_i is the second-order rate constant measured for component i (g eq^{-1} min^{-1}) and C_i is the concentration of component i (eq g^{-1}). The equivalent balance equations were then solved to calculate the concentration profiles of each component as a function of time:

$$\begin{aligned}\frac{dC_I}{dt} &= -r_I M\\ \frac{dC_P}{dt} &= -r_P M\\ \frac{dC_D}{dt} &= -r_D M\\ \frac{dC_W}{dt} &= -r_W M\\ \frac{dC_B}{dt} &= -r_B M\end{aligned} \tag{8}$$

where M is the mass of the biocomposite in grams. The equivalent weight for polyester triol, DPG and water were calculated from the mass of the sample, molecular weight and functionality (equation 9). The equivalent weights for each of the components are shown in Table 5.3.

$$q_i = m_i/(M_{ni}/f) \tag{9}$$

where q_i is the equivalent weight (in units of g/eq.), m_i is the mass of component i, M_{ni} is the molecular weight of species i, and f is the functionality.

Table 5.3. Kinetic model parameters.

Component	Eq wt (q)	Initial number of equivalents, eq			
	g eq^{-1}	I0-C0	I0-C1	I1-C0	I1-C1
B-MBP	429	0.0021	0.0021	0.0021	0.0021
Water (meas.)	9.01	0.0007	0.0006	0.0005	0.0005
Water (fitted)	9.01	0.0014	0.0025	0.0012	0.00075
LTI-PEG	194	0.0116	0.0110	0.0156	0.0149
T6C3G1L900	300	0.0100	0.0096	0.0074	0.0071
DPG	67	0.0034	0.0066	0.0034	0.0066

The equivalent weight for the B-MBPs cannot be determined directly by equation 1, due to the unknown functionality. We assumed that B-MBPs could be compared to the composition of human bone, which comprises ~23 wt% Type I collagen[21] and the remainder unreactive mineral content. Type I collagen has 210 reactive hydrogen equivalents per 1000 residues resulting from hydroxylysine, lysine, arginine, serine, threonine, glutamine, and cysteine residues in the backbone[22]. Assuming the average molecular weight of an amino acid residue in collagen is 90,000 g/mol, the equivalent weight of the B-MBP was calculated to be 429 g/eq.

From the equivalent weights, the number of equivalents for each component was calculated for a given batch size. The batch size utilized in modeling each individual biocomposite reaction is 10 g, which is clinically relevant for craniofacial clinical applications[23]. The equivalents for each component and each BC composition are tabulated in Table 5.4. The measured value of water was determined by columbic Karl

Fischer titration (ASTM E-1064). However, considering that the measured water concentration did not yield a good fit due to absorption of moisture from the humid air into the hygroscopic catalyst solution and polyester triol, the water concentration was used as a fitting parameter. The initial concentrations of each of the components (shown in Table 5.4) were used to solve the set of equations relating the change in concentration with time and the observed kinetic rate constants. A non-linear R^2 algorithm was chosen to determine goodness of fit with the experimental data and the initial concentration of water was iterated until the R^2 was maximized (R^2 ranged from 0.95-0.99). The value of water that was determined to provide the best fit is displayed in Table 5.1 and 5.4.

Using the fitted rate constants and the initial concentration of equivalents, the overall conversion of NCO equivalents in the biocomposite was plotted and compared to the experimental values in Figure 5.4A and B. Due to difficulties associated with accurately measuring the concentration of water in the polyester triol, catalyst solution, and prepolymer, the initial water concentration was used as a fitting parameter. As shown in Table 5.1, the water concentrations measured by titration varied from 26 to 71% of the fitted values. Figure 5.4C and D show the conversion of OH (or NH_2) equivalents after 24 hours for water, polyester triol, DPG, and B-MBPs calculated from the kinetic model. While the water conversion approaches 100% after approximately 10 – 20 minutes, the conversions of the other active hydrogen components are less than 100%, and decrease with decreasing index.

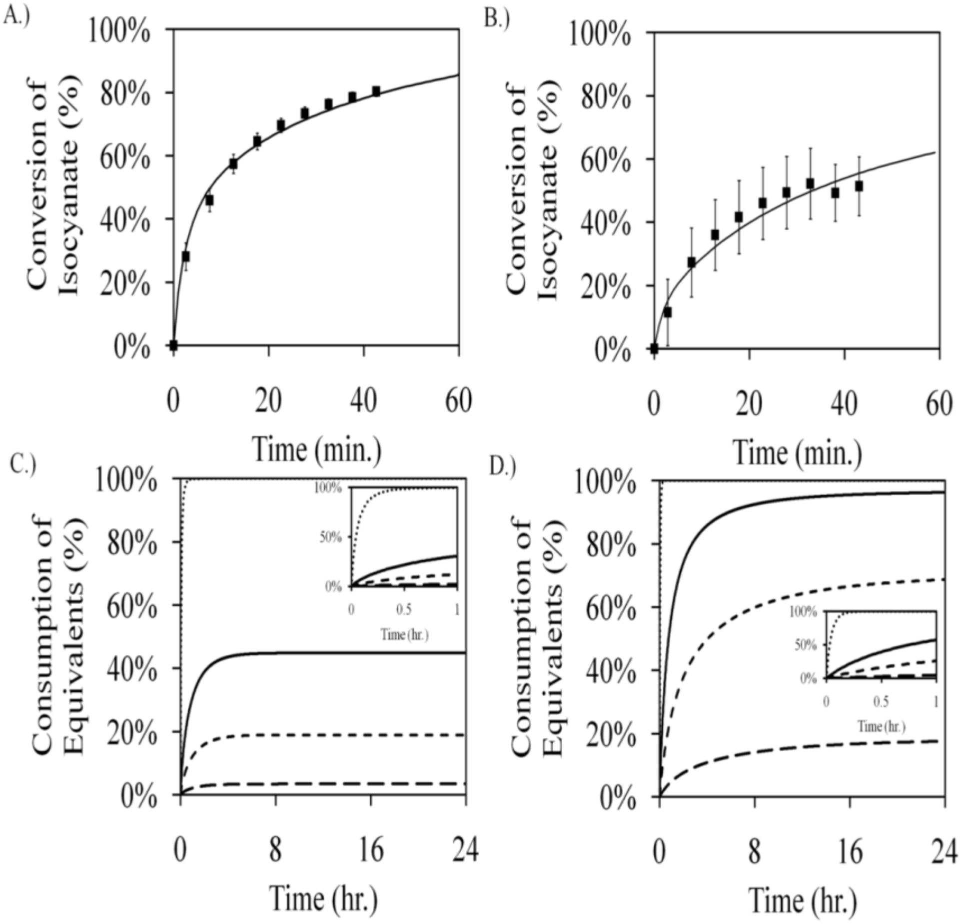

Figure 5.4. Validation of the kinetic model for characterizing the reactivity of the injectable biocomposites. Comparison of experimental and predicted (from the kinetic model) conversions for the overall biocomposite at 0.50 wt% catalyst and (A) low (108) and (B) high (195) indices, showing good agreement between the experimental and predicted values ($R^2 > 0.99$ and 0.97). Due to the difficulty of measuring water concentration at low concentrations (<0.4 wt%) by KF titration, water concentration was used as a fitting parameter. The conversion of OH (or NH_2) equivalents for water, polyester triol, DPG, and B-MBPs particles calculated from the kinetic model at 0.50 wt% catalyst are shown for (C) low (108) and (D) high (195) indices.

Rheology of curing biocomposites

A representative plot of the rheological properties of the I0-C1 biocomposite are shown in Figure 5.5, in which the values of storage modulus G’, loss modulus G”, and the viscosity η are plotted versus time; with the initial viscosities, η'_i and working times (gel points), τ_w, highlighted.

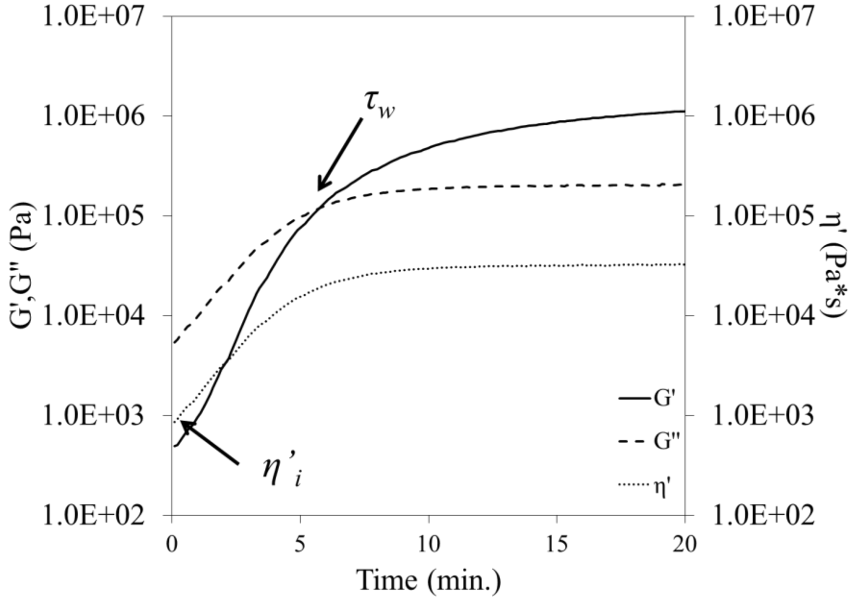

Figure 5.5. Rheological properties of PUR biocomposites. Representative plots for G’, G”, and η as a function of time for I0-C1 BC under wet conditions.

In clinical applications the rheological behavior of an injectable material is important, considering that a settable material must be tack-free within minutes after mixing and injection to avoid excessive times before the wound can be closed. The rheological profiles during cure were measured for each biocomposite *in situ* with an AR 2000ex rheometer with a Rheology Advantage AR Controller (TA Instruments). Continuous oscillation measurements were conducted at 1 Hz and 1% strain with 25 mm disposable parallel plates and a 1 mm gap. Measurements for each configuration of biocomposites were taken with either dry conditions or submerged in water via a submersion assembly kit (TA Instruments). Initial viscosities (η'_i) and working times (gel points, τ_w) were tabulated. Values of these rheological parameters are tabulated in

Table 5.4 for both dry and wet conditions for each biocomposite composition and catalyst level.

Table 5.4. Rheological properties of injectable biocomposites, including τ_w (working time), η'_i (initial viscosity), and ξ_{gp} (isocyanate conversion at the gel point) for each formulation under dry and aqueous conditions. The isocyanate conversions for each formulation at 2 and 45 minutes (i.e., the time points at which leaching experiments were performed) are also listed.

	I0-C0	I0-C1	I1-C0	I1-C1
$\tau_{w,dry}$ (min.)	29.3 ± 0.8*	14.3 ± 0.2*	19.7 ± 0.2*	7.1 ± 1.0
$\tau_{w,wet}$ (min.)	27.3 ± 0.8*	10.2 ± 0.9*	18.5 ± 0.8*	7.2 ± 0.1
$\eta'_{i,dry}$ (Pa*s)	101.9 ± 30.6	510.9 ± 20.7	149.1 ± 12.7	972.9 ± 140.1
$\eta'_{i,wet}$ (Pa*s)	90.8 ± 1.4	507.9 ± 2.1	178.1 ± 17.4	858 ± 96
$\xi_{gp,dry}$	48.7%	61.3%	28.5%	27.7%
$\xi_{gp,wet}$	47.5%	55.5%	28.4%	27.9%
$\xi_{2\ min}$	8.9%	24.7%	6.6%	14.2%
$\xi_{45\ min}$	55.0%	79.4%	36.0%	54.6%

* Signifies significant differences ($p<0.05$).

** For working time and initial viscosity (in both wet and dry), all index and catalysts groupings are statistically significant from each other.

Working times varied from 7 – 29 min, defined by the G'-G" crossover point, and decreased with increasing catalyst concentration and index. Similarly, initial viscosities ranged from 90 – 900 Pa*s, and increased with increasing catalyst concentration and index. For all but the I1-C1 biocomposite, working times measured under wet conditions were significantly shorter than under dry conditions, although the differences were modest. Working time and initial viscosity measured under wet conditions were generally within 15% of values measured for dry conditions.

Effect of water on biocomposite porosity

Reaction of the NCO-terminated prepolymer with water yields carbon dioxide gas, which acts as a blowing agent resulting in the formation of pores [24]. The porosity of the biocomposites as a function of total water (Figure 5.6A) increases with water concentration up to a plateau value of 60 vol% independent of the catalyst level or index.

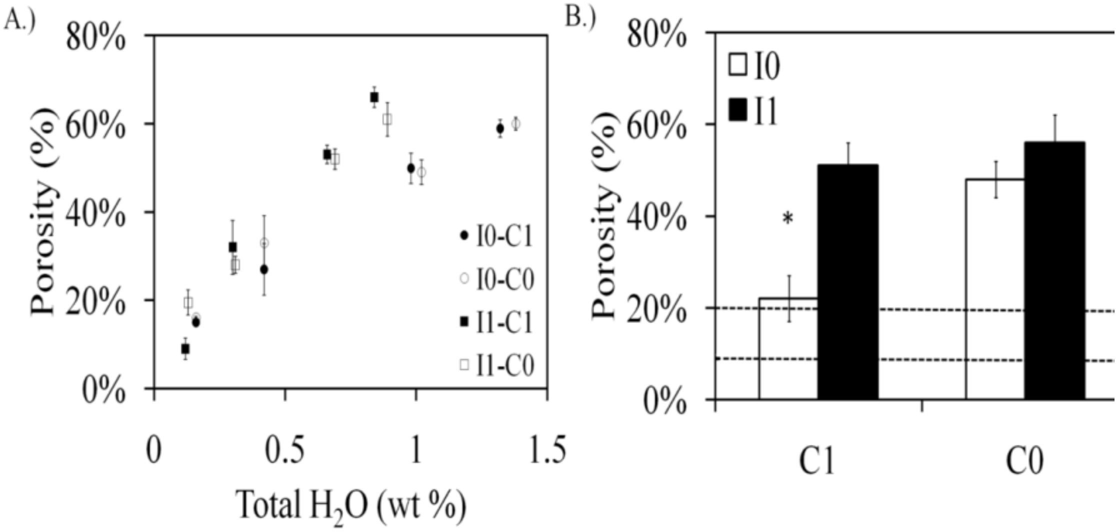

Figure 5.6. Effects of water concentration, index, and catalyst concentration on porosity of biocomposites. (A) Under dry conditions, porosity increases with total water concentration asymptotically up to ~60 vol% independent of index or catalyst concentration. (B) Under wet conditions, I1-C1, I1-C0, and I0-C0 biocomposites expanded to >50% porosity, despite the fact that no water was added the material. In contrast, the I0-C1 biocomposite showed porosity under wet conditions comparable to the range of porosities measured under dry conditions for all biocomposites in the absence of added water (shown in Panel B by the dotted lines). Thus, diffusion of water into the reactive biocomposite can result in higher porosity at a high index. * *$p<0.05$.*

Representative SEM images (Figure 5.7A-C) of biocomposites at 0.2, 0.4, and 1.0 total wt% water reveal that pore diameter, porosity, and interconnectivity increase with water concentration. While the pores are predominantly closed at the lower water concentrations, they appear to be more interconnected at 1.0 wt% water. As shown in Figure 5.7D, pore diameter is independent of index and catalyst concentration and increases with total water concentration over the range of 50 – 100 μm, but the differences are not significant.

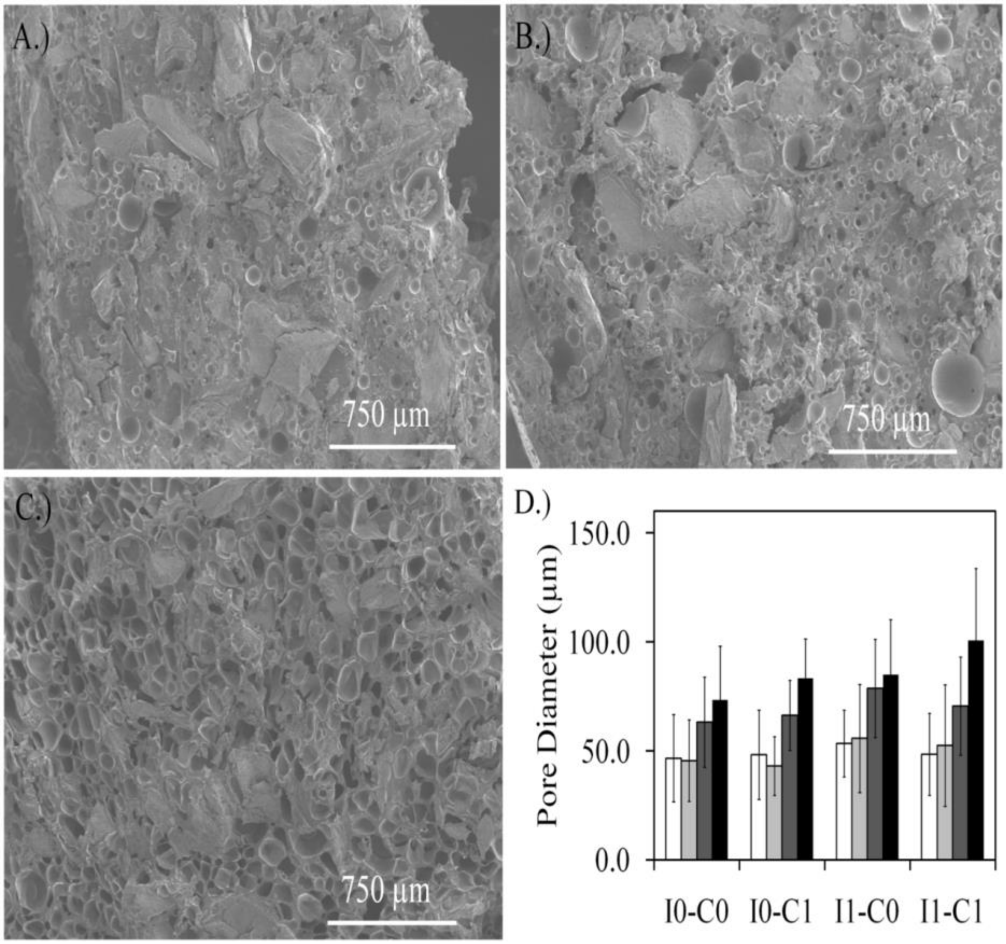

Figure 5.7. SEM images of I0-C1 biocomposites with (A) 0.2, (B) 0.4, and (C) 1.0 wt% total water. (D) Average pore diameter as a function of water concentration for I0-C1 biocomposites (error bars represent SEM). There is no significant difference between pore diameter.

Under *in vivo* conditions, water from the wound bed can diffuse into the biocomposite, resulting in increased expansion and porosity [25]. The effects of water diffusion were simulated in an *in vitro* test where the biocomposites were cured in a fully submerged aqueous environment. The *in vitro* porosity data measured under both dry (Panel A) and wet (Panel B) conditions for both catalyst concentrations are compared in Figure 5.6. At the lower catalyst concentration, both indices yield biocomposites with porosities of 48 – 55%, and at the higher catalyst level the index 195 biocomposite results in 50% porosity under wet conditions with no added water. Thus the porosities obtained under wet cure exceed those obtained from dry cure (Figure 5.6A) with no added water (9 – 20%, note that in the absence of added water, it is still present at 0.1 – 0.2 wt% as measured by KF titration under dry conditions). In contrast, the index I0-C1 biocomposite has a porosity of 22% under wet conditions, which is comparable to the 17% porosity measured for the I0-C1 biocomposite cured under dry conditions with no added water (Figure 5.6A). These observations suggest that diffusion of water from the wound bed can increase expansion, particularly at the low catalyst concentration and high index.

Characterization and cytotoxicity of leachates in vitro

NMR spectra for the leachates from the I0-C1 biocomposite injected into PBS at 2 and 45 minutes after mixing are shown in Figure 5.8D-E and compared to spectra for the individual components (Figure 5.8A-C) to determine which components were leaching from the reactive polymer at time points corresponding to the cream (2 min) and tack-free (45 min) stages of cure. The other biocomposites had nearly identical spectral profiles to that of I0-C1 (data not shown).

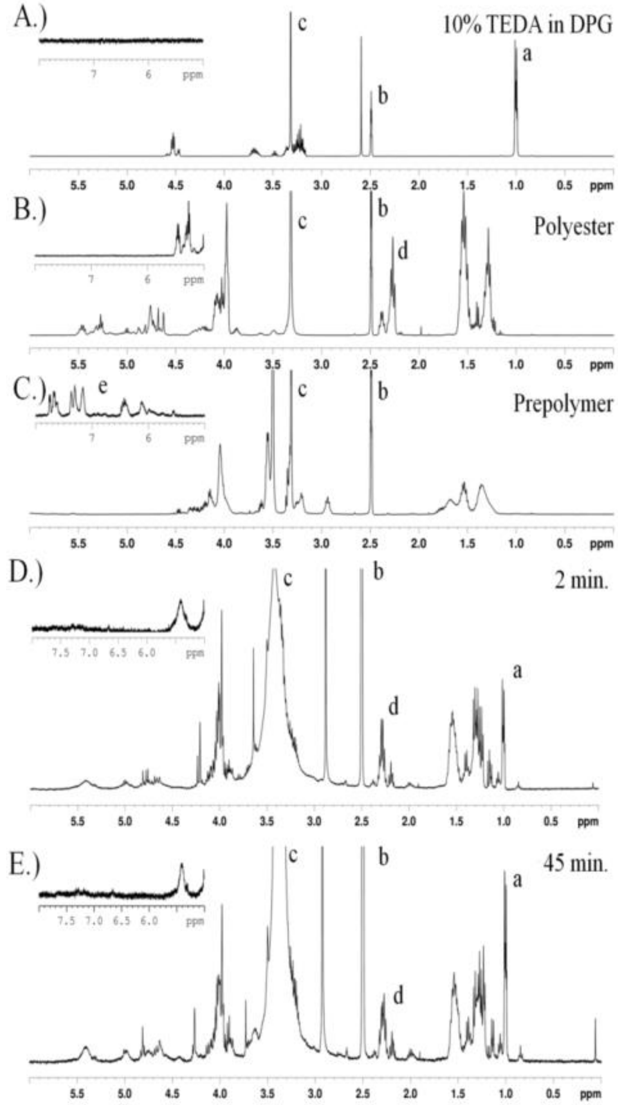

Figure 5.8. Reactive PUR biocomposites do not release potentially cytotoxic NCO-terminated prepolymer molecules during cure. NMR spectra of (A) 10% TEDA in DPG, (B) tri-functional polyester, (C) NCO-terminated prepolymer, (D) leachates collected at the early (2 min) time point, and (E) leachates collected at the late (45 min) time point for I0-C1 BC. Insets show the area where peaks unique to the prepolymer would appear. Key to symbols: a = methyl protons in DPG, b = DMSO-d, c = water from DMSO, d = polyester triol proton closest to carbonyl, and e = prepolymer protons closest to urethane and NCO groups.

The peak at 2.3 ppm associated with the proton adjacent to the carbonyl group in the polyester appears in the spectra of the leachates collected at 2 and 45 min, suggesting that unreacted polyester triol had leached into the medium. Similarly, the peak at 1.0 ppm associated with the protons on the methyl carbon group in DPG also appear in the leachates at both time points, indicating that unreacted DPG had diffused into the medium. While the protons on the methylene carbon appear at 2.8 in the TEDA pure-component spectrum, they shift to 2.6 ppm in the 10% TEDA in DPG spectrum (Panel A). Thus, the peaks at 2.8 ppm in the leachate spectra (Panels D and E) are associated with TEDA. In contrast, the prepolymer was uniquely distinguished by a series of peaks above 6 ppm, none of which appeared in the spectra for any of the leachates, suggesting that the prepolymer did not leach into the medium. Gravimetric analysis of the leached biocomposites revealed a 0.1 – 1.2% mass loss due to diffusion of individual components from the biocomposites into the buffer (Figure 5.9C). The pH of the leachates recovered at 2 and 45 minutes varied from 6.6 to 6.8 compared to the initial value of 7.35.

MC3T3-E1 murine osteoprogenitor cells were treated with leachates from the biocomposites collected at 2 and 45 min and diluted with serum medium such that the final concentration of leachates ranged from 6.25% (16X dilution) to 100% (1X dilution). Cells were cultured for 24 h. Leachate dose-response curves measured for leachates collected at 2 (Figure 5.9A) and 45 (Figure 5.9B) min reveal the anticipated sigmoidal shape. The cytotoxic response is quantified in Figure 5.9C. Three of the eight treatment groups showed cytotoxicity, which is defined as <70% viability, when not diluted (1X dilution). A statistically significant improvement in viability is seen for each of the cytotoxic groups after only a 2X dilution. For the three treatment groups showing cytotoxicity, the dilution factors required to render the culture medium non-cytotoxic varied from 1.36 – 1.66X. For a specific biocomposite composition and dilution factor, the percentage of viable cells was generally higher for leachates collected at 45 min (except for the 1X dilution for I1-C1), which is consistent with the notion that the concentration of leachates was lower at 45 min due to the higher conversion.

The morphology of live MC3T3 cells cultured in 8X diluted medium is shown in Figure 5.9D-F (since all treatment groups showed <1% cytotoxicity at this dilution, no dead cells are present in the field of view). Representative images of cells cultured on tissue culture polystyrene stained with calcein reveal a well-spread phenotype when treated with leachates from biocomposite I0-C1 collected at 2 min (Figure 5.9D) and 45 min (Figure 5.9E) and diluted 8X with serum medium. No substantial differences in size or morphology of the cells were observed between the treated and untreated (control) groups.

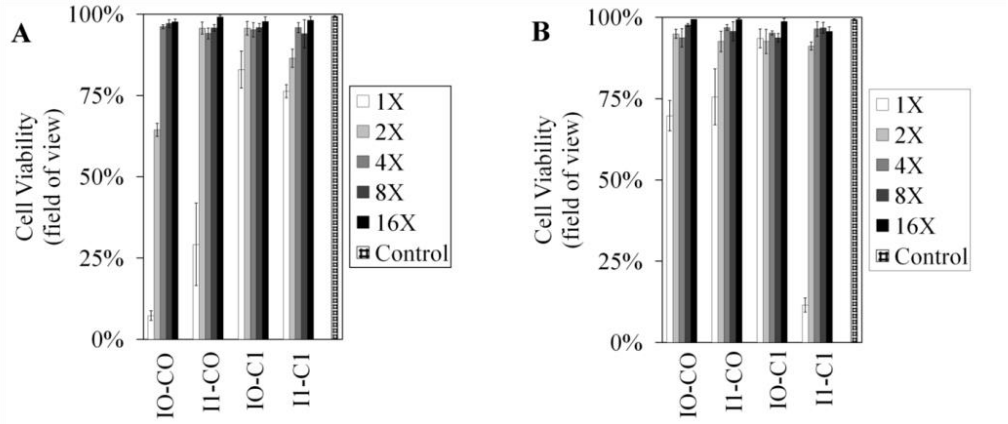

C

Leachate Group	Cytotoxic Response	Lc 50	Leached Mass (wt%)
I0-C0, 2 min.	+	1.66	0.5
I0-C1, 2 min.	+	1.23	0.2
I1-C0, 2 min.	-	-	1.2
I1-C1, 2 min.	-	-	0.34
I0-C0, 45 min.	-	-	0.34
I0-C1, 45 min.	-	-	0.1
I1-C0, 45 min.	-	-	0.68
I1-C1, 45 min.	+	1.36	0.1

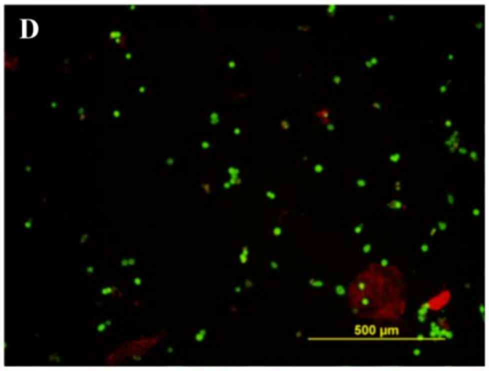

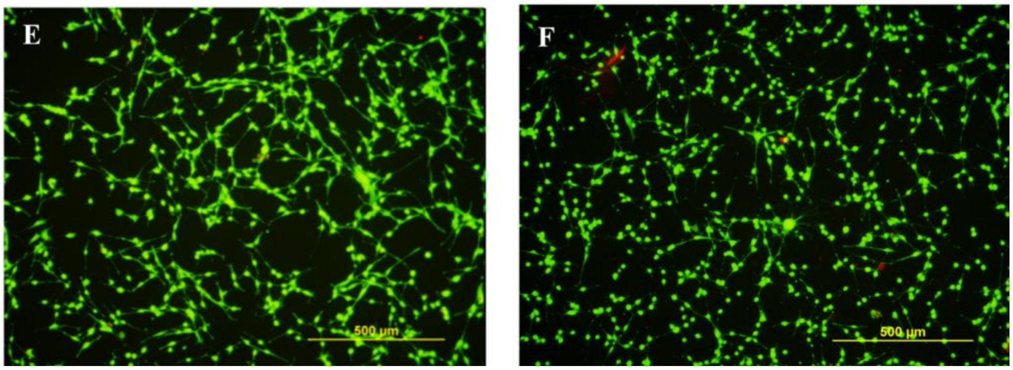

Figure 5.9. Viability of MC3T3-E1 osteoprogenitor cells treated with leachates from PUR biocomposites diluted 1X to 16X with serum medium. (A) – (C) Percent cell viability as assessed by live/dead staining for cells treated with leachates collected at (A) 2 min and (B) 45 min. The cytotoxic response is quantified in Panel (C) for each set of conditions tested as well as the percent mass loss due to leached intermediates. (D) – (F) Images of cells cultured on tissue culture polystyrene stained with calcein when treated with leachates taken from biocomposite I0-C1 after 2 minutes of reaction; diluted (D) 1X with serum medium and (E) 2X with serum medium. Control cells treated with PBS are shown in Panel (F).

Table 5.5. Morphological parameters determined by μCT for the I0-C1 biocomposite not implanted in the defects (non-implanted, n=3), the I0-C1 biocomposite (n=6) and control specimens (n=9) 8 weeks after injection.

Parameter	**I0-C1**		**Empty Defect**
	Non-implanted	**8 weeks**	**8 weeks**
Bone Volume Fraction (BV/TV, %)	14 ± 1 $^{(*)}$	22 ± 4 $^{(**)}$	11 ± 6
Tissue Mineral Density (TMD, mg HA/cm^3)	991 ± 9 $^{(*)}$	802 ± 39	777 ± 38 $^{(***)}$
Trabecular number (Tb.N., 1/mm)	3.7 ± 0.1 $^{(*)}$	2.4 ± 0.5 $^{(**)}$	0.5 ± 0.4
Trabecular thickness (Tb.Th, mm)	0.104 ± 0.005 $^{(*)}$	0.153 ± 0.007 $^{(**)}$	0.207 ± 0.035
Trabecular separation (Tb.Sp, mm)	0.26 ± 0.01 $^{(*)}$	0.46 ± 0.08 $^{(**)}$	2.83 ± 1.07
Connectivity Density (Conn.D, 1/mm^3)	0.036 ± 0.013 $^{(*)}$	24.0 ± 6.8 $^{(**)}$	7.3 ± 6.5

$^{(*)}$ Significantly different than I0-C1 8 weeks ($p<0.05$)

$^{(**)}$ Significantly different than the control ($p<0.05$)

$^{(***)}$ Significantly lower than the surrounding density ($p=0.0008$)

In vivo remodeling in a rabbit femoral plug model

In a previous study, we reported that biocomposites with porosity approaching 60 vol% were friable and had weak mechanical properties[13]. Considering that all formulations except I0-C1 expanded to >50% porosity in the simulated *in vivo* foaming test compared to dry *in vitro* conditions (Figure 5.5B), we evaluated the biocompatibility and remodeling of formulation I0-C1 in a rabbit femoral condyle plug defect model[13]. According to μCT images, the location of the defects in the femur varied and the effective depth of the defects ranged between 6 and 10 mm. Representative μCT images are shown in Figure 5.10, and morphological parameters are reported in Table 5.5 for I0-C1 biocomposites prepared in the laboratory (I0-C1 non-implanted) and at 8 weeks post-injection. Compared to the non-implanted material, the biocomposite showed significantly higher BV/TV and Conn.D at 8 weeks post-injection in femoral defects, as well as lower TMD, Tb.N, and Tb.Th, suggesting that the biocomposite remodeled *in vivo*. While the control (empty) defects showed formation of new cortex but minimal new trabecular bone, the biocomposite group showed significantly greater new bone formation throughout the volume of the defect.

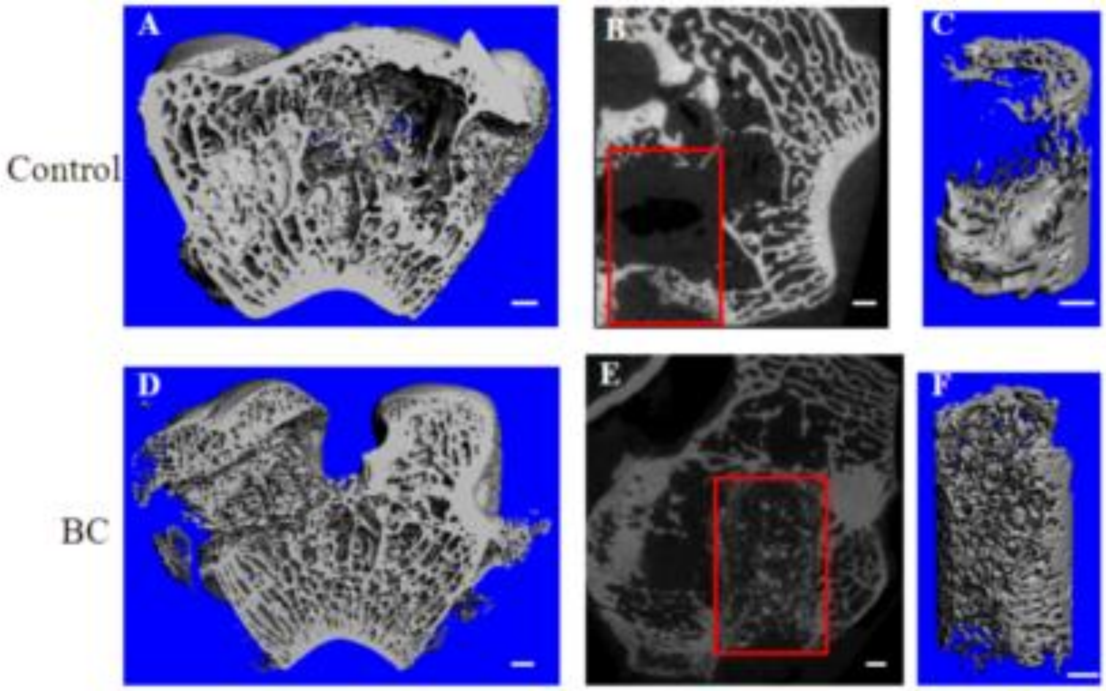

Figure 5.10. Representative μCT images of mean empty (Control) and I0-C1 biocomposite-treated (BC) defects at 8 weeks. (A,D) 3-dimensional images. (B,E) Rotated 2-dimensional images. Red boxes indicate the location of the defect. (C,F) 3-dimensional view of the defect volume. Scale bars represent 1 mm.

The bone in the biocomposite at 8 weeks also had higher Tb.N, and Conn.D, and lower Tb.Th, and Tb.Sp than the bone in the control defects. There were no significant differences in TMD between the biocomposite and empty defect at 8 weeks. Considering that TMD distribution provides information about the mechanical properties of bone matrix [26], similar values of TMD between the control and the treated defects suggest that the ossified tissue has similar quality, although the volume fraction of bone differs between the two defects. Representative thin sections (5 μm) stained with H&E at 8 weeks are presented in Figure 5.11. The defects in the control (empty defect) treatment group were identified by a central area of fat and hematopoietic elements surrounded by a variably vague circle of bone and trabeculae. There appeared to be no new bone and very little inflammation within the center of these defects.

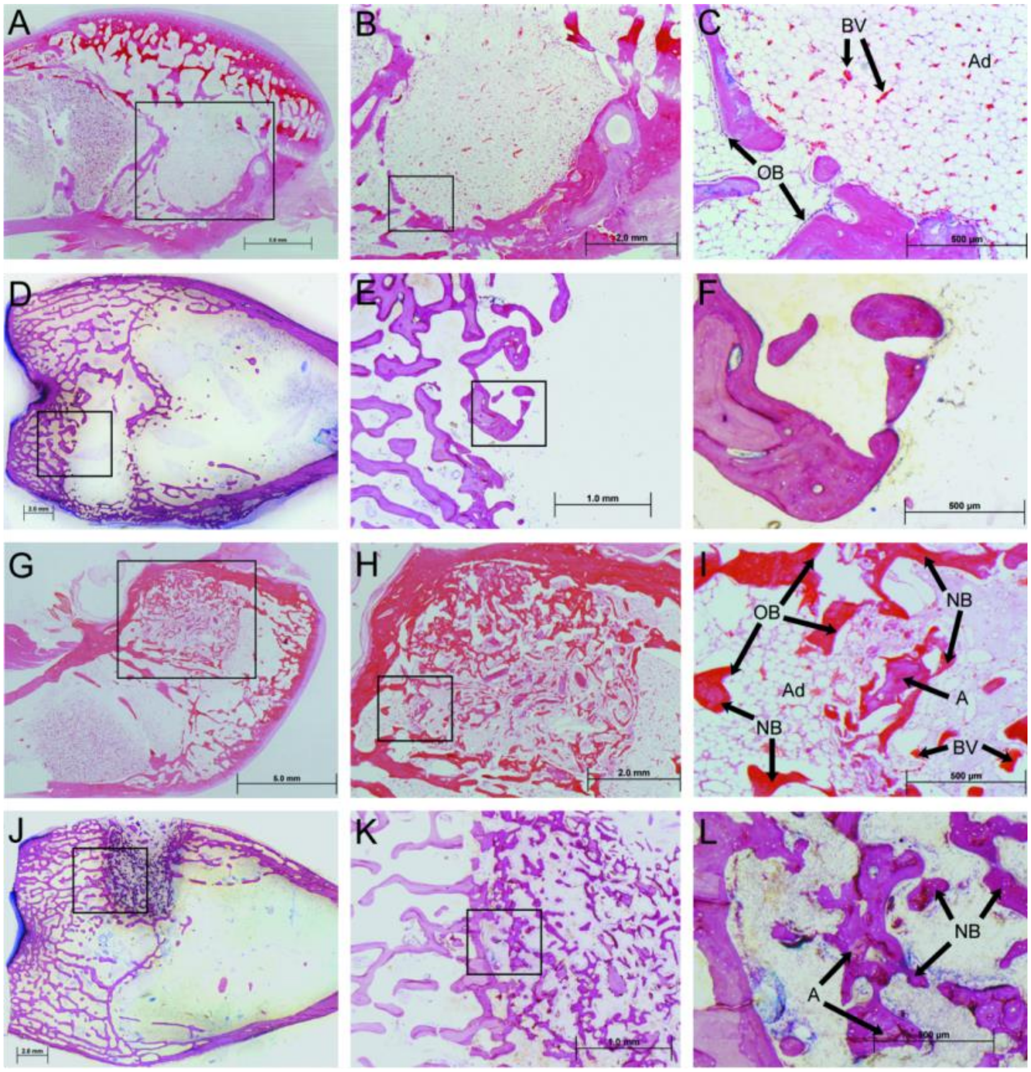

Figure 5.11. Representative images of histological sections at 8 weeks stained for H&E. (A,B) Low and high magnification images of empty (control) defects. (C,D) Low and high magnification images of defects treated with the I0-C1 biocomposite. Labels: (→) Point to osteoblasts lining the surface of new bone. (>) New bone. (A) Allograft particles. (Ad) Adipose tissue.

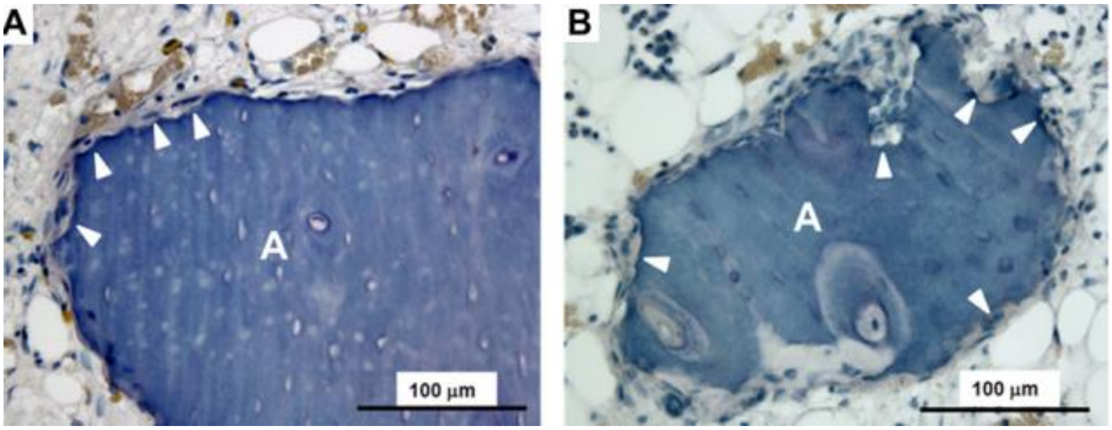

Figure 5.12. Representative images of histological sections of the I0-C1 biocomposite at 8 weeks stained for TRAP. (a,b) Allograft bone particles (A) in representative samples surrounded by resorbing osteoclasts (multinucleated, light red cells). Arrowheads point to resorption pits on the surface of the allograft bone particles.

Defects treated with the I0-C1 biocomposite exhibited mild to moderate inflammation with non-viable bone fragments (allograft) surrounded by osteoclasts generating resorption pits (Figure 5.12, white arrows), osteoblasts, new trabeculae, and marrow elements. The stained sections showed extensive cellular infiltration and remodeling throughout the volume of the defect, as well as new bone formation near the host bone interface, and some non-viable allograft bone particles remained in the interior of the defect. There was minimal to no evidence of residual polymer, suggesting that the polymer had undergone extensive degradation by 8 weeks.

Discussion

Injectable lysine-derived poly(ester urethane) networks have been shown to support tissue remodeling in preclinical models[25, 27]. This class of biomaterials undergoes hydrolytic and oxidative degradation to lysine, α-hydroxy acids, and soluble low-molecular weight urethane adducts[9b, 28]. Furthermore, neither the cured polymers nor the degradation products induce a severe inflammatory response *in vivo*[9b, 15, 27a]. However, the effects of reactive components in the PUR leaching into the surrounding tissue prior to cure, resulting in a potentially adverse tissue response [11], has not been investigated. Curing of the material *in vivo* may also differ from *in vitro* conditions, resulting in unpredictable *in vivo* performance[10a, 25, 29]. In this study, we investigated the effects of stoichiometry and catalyst concentration on the reactivity, biocompatibility, and injectability of PUR biocomposites comprising a lysine-derived prepolymer, polyester triol, water, and a tertiary amine catalyst.

The polyester triol, water, DPG, and B-MBPs had significantly different second-order rate constants, resulting in differences in the conversion of each component (Figure 2). DPG was 3 times less reactive than the polyester triol at the higher catalyst levels, but not at the lower catalyst levels, which could be due to the isomeric structure (i.e., characterized by both primary and secondary hydroxyl groups) of DPG[14a]. The reaction between the NCO-terminated prepolymer and the B-MBPs is more complex due to its particulate state. B-MBPs are composed of ~30% organic compounds, of which >90% is collagen I that contains reactive amines (76% of total active hydrogen equivalents) and hydroxyls (24% of total active hydrogen equivalents)[22]. While primary amines have a rate of reaction with isocyanates approximately 10 times higher than primary hydroxyl groups[30], the reaction between B-MBPs and prepolymer is limited by the diffusion of the prepolymer to the surface of the particles. Furthermore, most of the collagen is embedded in the interior of the bone particles and only a small fraction is available at the surface to react with the prepolymer. Thus, the solid-liquid reaction between the B-MBPs and prepolymer showed the lowest conversion at both catalyst levels.

For all formulations, water was the most reactive component. When the initial water concentration was treated as a fitting parameter, the agreement between the experimental and calculated overall rates was good ($R^2 = 0.95 – 0.99$, Fig. 5.4A and C). As shown in Table 5.1, the fitted initial water concentrations were on average 2.5 times greater than the measured values. Measurement of trace water concentrations by KF titration is limited by factors such as oxidizing and reducing agents (e.g., residual catalysts) present in the test sample[31]. In addition, allograft bone contains a small fraction (up to 2 – 3% as measured by TGA) of surface-bound water[32] that cannot be detected by KF titration. Polyurethanes can also react with moisture in the air under humid conditions[20], and allograft bone can absorb up to 10 wt% water when exposed to humid air, which are not accounted for in the KF titration.

Since the water reaction produces carbon dioxide gas[30b], it can be exploited to generate >50 μm pores (Fig. 5.7) that accelerate cellular infiltration[10b, 13, 29, 33]. The porosity can be tuned to targeted values by controlling the water content under dry *in vitro* conditions (Figure 5.6A)[13]. As water is increased from 0.15 to 0.7 wt%, the porosity increases from 10% to 50%, resulting in a decrease in compressive strength from 9.5 MPa to 5 MPa as we have reported previously[27b]. The maximum porosity that can be attained in the biocomposites is 60 – 65% (water concentrations exceeding 0.7 wt%), at which point the compressive strength drops to <0.3 MPa and the materials become friable[27b]. Thus, to balance the requirements for both mechanical strength and cellular infiltration, expansion of the biocomposites must be controlled such that $\varepsilon < 60$ vol%. As shown in Fig. 5.6B, the porosity of the I0-C0, I1-C0, and I1-C1 biocomposites with no added water increased from 8 – 20% under dry conditions to 50 – 55% under wet conditions. Since the wet reaction conditions are more indicative of the *in vivo* wound environment, these observations suggest that formulations I0-C0, I1-C0, and I1-C1 would undergo unpredictable expansion *in vivo*[13, 25].

The instantaneous selectivity $S_{w/(p+d)}$ of the water reaction relative to the polyester and DPG reactions provides insight into the sensitivity of the overall conversion to the concentrations of the individual components:

$$S_{w/(p+d)} = \frac{r_w}{r_p + r_d} = \frac{k_w C_w}{k_p C_p + k_d C_d} \qquad (10)$$

The water selectivity initially exceeds unity (since $k_w >> k_p, k_d$) and scales with C_w. As the reaction progresses, $S_{w/(p+d)}$ decreases due to the reaction of water, but diffusion of water into the reactive scaffold from an external source results in increased water concentration and selectivity. Thus, curing in a moist environment is predicted to promote over-expansion, which is consistent with the porosity data in Figure 5.6. To prevent potential release of low molecular weight NCO groups, it is desirable to control the value of C_I such that the NCO conversion approaches 100% after final cure (typically ~24 hours). However, the high sensitivity to initial water concentration, as well as diffusion of environmental water into the wound bed, can result in reduced conversion of polyester triol conversion and weak mechanical properties. In contrast, photopolymerizable polymers, including PEG acrylate derivatives [34] and poly(propylene fumarate) (PPF)[35], cure *in situ* upon activation of the initiator using ultraviolet light. Thus, photopolymerization offers the advantages of curing rates on the order of seconds to minutes [36] that are independent of conditions in the wound bed. We anticipate that the adverse effects of environmental water on PUR reactions could be mitigated by using catalysts with low toxicity that selectively catalyze the gelling relative to the blowing reaction. Despite the previously reported strong gelling selectivity of TEDA[14b], $k_w >> k_p$, k_d for both catalyst levels in the present study. The toxicity of heavy metal catalysts (e.g., tin and bismuth) likely precludes their use in injectable formulations[14b], but a lower toxicity gelling catalyst with $k_w << k_p$, k_d, such as ferric acetylacetonate[37], is anticipated to reduce the sensitivity to environmental water.

While formulation I0-C1 minimized the effects of external water on expansion, the lower index resulted in a lower conversion of polyester and DPG (Fig. 5.4C, D). Incomplete conversion is anticipated to reduce the crosslink density and introduce network defects that reduce the mechanical properties of the cured polymer[38]. The time scale required for crosslinking can be estimated from the measured working times of the composites listed in Table 5.4. The working time, which is determined experimentally as the time at which the storage modulus G' equals the loss modulus G", approximates the gel point, or the time at which the reactive polymer forms a non-flowable crosslinked network. Prior to the gel point, the low yield stress (2.1 Pa) and initial viscosity (170 Pa*s) render the biocomposites both injectable and flowable[39]. At the gel point, the biocomposite transitions to a non-flowable gel that can no longer be injected. The isocyanate conversions ξ_{gp} at the gel point (approximated by the working time) measured under dry and wet conditions were calculated from the kinetic model and are also listed in Table 5.4. For the high index conditions, $27\% < \xi_{gp} < 29\%$, while for the low index conditions, $48\% < \xi_{gp} < 61\%$.

At the early stages of the curing process prior to the gel point, the NCO conversion is lower than the conversion at the gel point for each formulation (e.g., 6.6 – 24.7% at 2 min, see Table 5.4), and thus leaching of reactive components may occur. However, prepolymer was not identified in the NMR spectra of the leachates at any conditions, and only a small amount of polyester and DPG (0.2 – 1.2%) leached from the biocomposites at 2 min. At 45 min, the NCO conversion exceeds that at the gel point (36.0 – 79.4%, see Table 5.4). Consequently, the fraction of leachable components decreased for all groups, ranging from 0.1 – 0.68% of the total mass, due to the increased crosslinking at 45 min. As anticipated, the measured concentration of leachables decreased with the conversion of NCO groups calculated from the kinetic model (Figure 5.13).

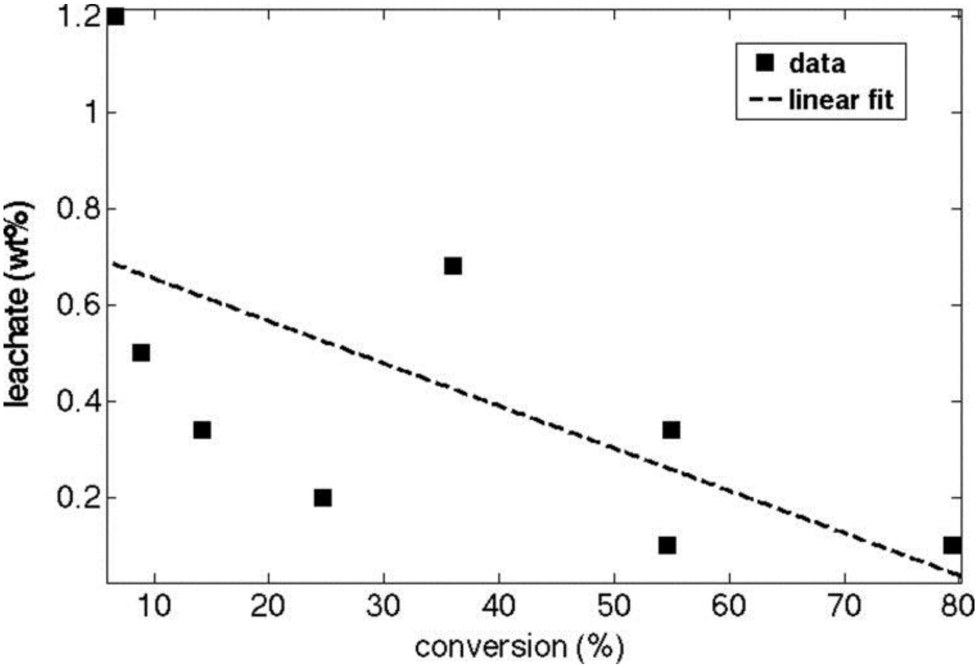

Figure 5.13. Plot of the measured concentration of leachable components versus isocyanate conversion calculated from the kinetic model.

The NMR spectra revealed that a significant amount of TEDA leached from the reactive biocomposite at both 2 and 45 min. However, with an oral LD50 in rats of 1,700 mg/kg (MSDS, sigmaaldrich.com), even rapid leaching of TEDA from the reactive biocomposite is not anticipated to adversely affect cells. When diluted with fresh medium[40], the leachates had no adverse effect on cell viability, which is consistent with previous studies investigating the cytotoxicity of the degradation products from PUR elastomers[41] and networks[42]. Previous studies have also reported that the reaction exotherm is <15°C[15]. These observations suggest that reactive PUR networks do not release unreacted cytotoxic components or large amounts of thermal energy that are harmful to cells and host tissue, as has been reported for other reactive thermosetting polymers (e.g., cyanoacrylate glues[43]) or for some photopolymerizable systems[35a].

When injected into excisional wounds in rats, lysine-derived PUR scaffolds supported proliferation of Ki67+ cells and formation of procollagen I, and the extent of cell apoptosis (as assessed by TUNEL staining) was comparable to the empty defect control[9a]. Macrophages infiltrated the defect and accelerated the degradation of the scaffold by oxidation of lysine residues in the polymer, as evidenced by positive staining for anti-PGP9.5 and myeloperoxidase [9b]. Thus, the inflammatory response was transient and localized to residual PUR remnants. To more specifically assess the host tissue response in the bone environment, the extent of osseointegration and remodeling of the I0-C1 biocomposite were evaluated at 8 weeks in a rabbit femoral condyle plug defect model in the present study. At 8 weeks, residual allograft bone particles were surrounded by functional osteoclasts and showed visual evidence of surface resorption (resorption pits) as well as a lower TMD. Moreover, the biocomposites supported the recruitment and differentiation of osteoblasts that deposited new bone as evidenced by the increase in BV/TV and Conn.D after 8 weeks implantation time. Minimal evidence of residual polymer existed at this time point, suggesting that no adverse responses associated with the cured polymer, the unreacted components, or the breakdown products resulting from degradation of the polymer was evident. These observations are consistent with the data in Figure 6 reporting low cytotoxicity of the unreacted leachates from the polymer prior to cure, as well as previous studies reporting that lysine-derived PURs release degradation products with low toxicity[9b, 15, 44] and support new bone formation in bone defects in rats, rabbits, and sheep[27a-c, 45].

Conclusions

In this study, we measured the chemical reaction rate constants of the active hydrogen components with the isocyanate-terminated prepolymer in an injectable lysine-derived polyurethane biocomposite using an *in situ* ATR-FTIR technique. The rate constants were used to build a kinetic model describing the reactivity of the injectable biocomposite. The tertiary amine catalyst TEDA preferentially catalyzes the blowing reaction with water relative to the gelling reactions with polyester triol, DPG, and allograft bone particles, despite the fact that TEDA has been reported as one of the strongest amine gelling catalysts[14b]. Thus, the conversions of polyisocyanate and water were nearly complete, while the conversions of polyester triol and DPG were incomplete (<70%). These predictions of the kinetic model were in agreement with leaching experiments showing that polyester triol, DPG, and TEDA were released from the reactive PUR, which were shown to be non-cytotoxic *in vitro*. When injected into plug defects in the femoral condyles of NZW rabbits, the PUR biocomposite supported cellular infiltration and remodeling at 8 weeks with no evidence of an adverse inflammatory response induced by the polymer degradation products. Thus, the kinetic model is a potentially useful approach for predicting the biocompatibility of reactive biomaterials.

References

1. Khan, Y.; Yaszemski, M. J.; Mikos, A. G.; Laurencin, C. T., Tissue engineering of bone: Material and matrix considerations. *J. Bone Joint Surg.-Am. Vol.* **2008,** *90A*, 36-42.

2. Legeros, R. Z.; Chohayeb, A.; Schulman, A., APATITIC CALCIUM PHOSPHATES POSSIBLE DENTAL RESTORATIVE MATERIALS. *Journal of Dental Research* **1982,** *61* (SPEC. ISSUE), 343.

3. (a) Chim, H.; Gosain, A. K., Biomaterials in Craniofacial Surgery Experimental Studies and Clinical Application. *J. Craniofac. Surg.* **2009,** *20* (1), 29-33; (b) Moreira-Gonzalez, A.; Jackson, I. T.; Miyawaki, T.; Barakat, K.; DiNick, V., Clinical outcome in cranioplasty: Critical review in long-term follow-up. *J. Craniofac. Surg.* **2003,** *14* (2), 144-153; (c) Friedman, C. D.; Costantino, P. D.; Takagi, S.; Chow, L. C., BoneSource (TM) hydroxyapatite cement: A novel biomaterial for craniofacial skeletal tissue engineering and reconstruction. *Journal of Biomedical Materials Research* **1998,** *43* (4), 428-432; (d) Gasparini, G.; Boniello, R.; Moro, A.; Tamburrini, G.; Di Rocco, C.; Pelo, S., Cranial Reshaping Using Methyl Methacrylate: Technical Note. *J. Craniofac. Surg.* **2009,** *20* (1), 184-190.

4. (a) Bohner, M., Designing ceramics for injectable bone graft substitutes. In *Injectable Biomaterials: Science and Applications*, Vernon, B. L., Ed. Woodhead Publishing: Philadelphia, 2011; (b) Wagoner Johnson, A. J.; Herschler, B. A., A review of the mechanical behavior of CaP and CaP/polymer composites for applications in bone replacement and repair. *Acta Biomaterialia* **2011,** *7* (1), 16-30.

5. Chan, C.; Thompson, I.; Robinson, P.; Wilson, J.; Hench, L., Evaluation of Bioglass/dextran composite as a bone graft substitute. *Int. J. Oral Maxillofac. Surg.* **2002,** *31* (1), 73-77.

6. Chazono, M.; Tanaka, T.; Komaki, H.; Fujii, K., Bone formation and bioresorption after implantation of injectable beta-tricalcium phosphate granules-hyaluronate complex in rabbit bone defects. *Journal of Biomedical Materials Research Part A* **2004,** *70A* (4), 542-549.

7. Schwartz, Z.; Goldstein, M.; Raviv, E.; Hirsch, A.; Ranly, D. M.; Boyan, B. D., Clinical evaluation of demineralized bone allograft in a hyaluronic acid carrier for sinus lift augmentation in humans: a computed tomography and histomorphometric study. *Clinical Oral Implants Research* **2007,** *18* (2), 204-211.

8. Cammisa, F. P.; Lowery, G.; Garfin, S. R.; Geisler, F. H.; Klara, P. M.; McGuire, R. A.; Sassard, W. R.; Stubbs, H.; Block, J. E., Two-year fusion rate equivalency between Grafton (R) DBM gel and autograft in posterolateral spine fusion. *Spine* **2004,** *29* (6), 660-666.

9. (a) Adolph, E. J.; Hafeman, A. E.; Davidson, J. M.; Nanney, L. B.; Guelcher, S. A., Injectable polyurethane composite scaffolds delay wound contraction and support cellular infiltration and remodeling in rat excisional wounds. *J Biomed Mater Res A* **2011**; (b) Hafeman, A. E.; Zienkiewicz, K. J.; Zachman, A. L.; Sung, H. J.; Nanney, L. B.; Davidson, J. M.; Guelcher, S. A., Characterization of the degradation mechanisms of lysine-derived aliphatic poly(ester urethane) scaffolds. *Biomaterials* **2011,** *32* (2), 419-429.

10. (a) Dumas, J. E.; Davis, T.; Holt, G. E.; Yoshii, T.; Perrien, D. S.; Nyman, J. S.; Boyce, T.; Guelcher, S. A., Synthesis, characterization, and remodeling of weight-bearing allograft bone/polyurethane composites in the rabbit. *Acta Biomaterialia* **2010,** *6* (7), 2394-2406; (b) Bennett, S.; Connolly, K.; Lee, D. R.; Jiang, Y.; Buck, D.; Hollinger, J. O.; Gruskin, E. A., Initial biocompatibility studies of a novel degradable polymeric bone substitute that hardens in situ. *Bone* **1996,** *19* (1), S101-S107; (c) Bonzani, I. C.; Adhikari, R.; Houshyar, S.; Mayadunne, R.; Gunatillake, P.; Stevens, M. M., Synthesis of two-component injectable polyurethanes for bone tissue engineering. *Biomaterials* **2007,** *28* (3), 423-433.
11. Ertel, S. I.; Ratner, B. D.; Kaul, A.; Schway, M. B.; Horbett, T. A., IN-VITRO STUDY OF THE INTRINSIC TOXICITY OF SYNTHETIC SURFACES TO CELLS. *Journal of Biomedical Materials Research* **1994,** *28* (6), 667-675.
12. (a) Pons, F.; Fischer, A.; Frossard, N.; Lugnier, A., Effect of toluene diisocyanate and its corresponding amines on viability and growth of human lung fibroblasts in culture. *Cell Biology and Toxicology* **1999,** *15* (5), 333-340; (b) Mishra, P. K.; Panwar, H.; Bhargava, A.; Gorantla, V. R.; Jain, S. K.; Banerjee, S.; Maudar, K. K., Isocyanates induces DNA damage, apoptosis, oxidative stress, and inflammation in cultured human lymphocytes. *Journal of Biochemical and Molecular Toxicology* **2008,** *22* (6), 429-440.
13. Dumas, J. E.; Zienkiewicz, K.; Tanner, S. A.; Prieto, E. M.; Bhattacharyya, S.; Guelcher, S. A., Synthesis and Characterization of an Injectable Allograft Bone/Polymer Composite Bone Void Filler with Tunable Mechanical Properties. *Tissue Eng. Part A* **2010,** *16* (8), 2505-2518.
14. (a) Hinrichsen, G., Polyurethane handbook (2nd ed.). Edited by G. Oertel, Hanser Publishers, Munich 1993, 770 pp., DM 358, ISBN 3-446-17198-3. *Acta Polymerica* **1994,** *45* (5), 398-398; (b) Silva, A. L.; Bordado, J. C., Recent developments in polyurethane catalysis: Catalytic mechanisms review. *Catalysis Reviews-Science and Engineering* **2004,** *46* (1), 31-51.
15. Hafeman, A.; Li, B.; Yoshii, T.; Zienkiewicz, K.; Davidson, J.; Guelcher, S., Injectable biodegradable polyurethane scaffolds with release of platelet-derived growth factor for tissue repair and regeneration. *Pharm Res* **2008,** *25* (10), 2387-99.
16. (a) Hoven, V. P.; Tangpasuthadol, V.; Angkitpaiboon, Y.; Vallapa, N.; Kiatkamjornwong, S., Surface-charged chitosan: Preparation and protein adsorption. *Carbohydrate Polymers* **2007,** *68* (1), 44-53; (b) Li, S.; Vatanparast, R.; Lemmetyinen, H., Cross-linking kinetics and swelling behaviour of aliphatic polyurethane. *Polymer* **2000,** *41*, 5571-5576.
17. (a) Romero, R. R.; Grigsby, R. A.; Rister, E. L.; Pratt, J. K.; Ridgway, D., A Study of the Reaction Kinetics of Polyisocyanurate Foam Formulations using Real-time FTIR. *J. Cell. Plast.* **2005,** *41* (4), 339-359; (b) Thomson, M. A., Melling, P.J., and Slepski, A.M., Real time monitoring of isocyanate chemistry using a fiber-optic FTIR probe. *Polymer Preprints* **2001,** *42* (1), 310-311.
18. Guan, J. J.; Sacks, M. S.; Beckman, E. J.; Wagner, W. R., Biodegradable poly(ether ester urethane)urea elastomers based on poly(ether ester) triblock copolymers and putrescine: synthesis, characterization and cytocompatibility. *Biomaterials* **2004,** *25* (1), 85-96.
19. Parnell, S.; Min, K.; Cakmak, M., Kinetic studies of polyurethane polymerization with Raman spectroscopy. *Polymer* **2003,** *44*, 5137-5144.

20. Ortel, G., *Polyurethane Handbook*. Hanser Gardner Publications: 1994.

21. Dequeker, J.; Merlevede, W., Collagen content and collagen extractability pattern of adult human trabecular bone according to age, sex and amount of bone mass. *Biochimica et Biophysica Acta (BBA) - General Subjects* **1971,** *244* (2), 410-420.

22. Steven, F. S. J., D. S., Purification and amino acid composition of monomeric and polymeric collagens. . *Biochem. J.* **1967,** *104*, 534-536.

23. (a) Siemionow, M. Z. a. E.-K., M., *Plastic and Reconstructive Surgery*. Springer: London, England, 2010; (b) Wong, R. K.; Gandolfi, B. M.; St-Hilaire, H.; Wise, M. W.; Moses, M., Complications of Hydroxyapatite Bone Cement in Secondary Pediatric Craniofacial Reconstruction. *J. Craniofac. Surg.* **2011,** *22* (1), 247-251 10.1097/SCS.0b013e3181f7b7db.

24. Guelcher, S. A.; Patel, V.; Gallagher, K. M.; Connolly, S.; Didier, J. E.; Doctor, J. S.; Hollinger, J. O., Synthesis and in vitro biocompatibility of injectable polyurethane foam scaffolds. *Tissue Engineering* **2006,** *12* (5), 1247-1259.

25. Adolph, E. J.; Hafeman, A. E.; Zienkiewicz, K. L.; Davidson, J. M.; Nanney, L. B.; Guelcher, S. A., Injectable biodegradable polyurethane scaffolds for wound healing. *Submitted* **2011**.

26. Kim, D. G.; Shertok, D.; Ching Tee, B.; Yeni, Y. N., Variability of tissue mineral density can determine physiological creep of human vertebral cancellous bone. *J Biomech* **2011,** *44* (9), 1660-5.

27. (a) Adhikari, R.; Gunatillake, P. A.; Griffiths, I.; Tatai, L.; Wickramaratna, M.; Houshyar, S.; Moore, T.; Mayadunne, R. T.; Field, J.; McGee, M.; Carbone, T., Biodegradable injectable polyurethanes: synthesis and evaluation for orthopaedic applications. *Biomaterials* **2008,** *29* (28), 3762-70; (b) Dumas, J. E.; Zienkiewicz, K.; Tanner, S. A.; Prieto, E. M.; Bhattacharyya, S.; Guelcher, S., Synthesis and Characterization of an Injectable Allograft Bone/polymer Composite Bone Void Filler with Tunable Mechanical Properties. *Tissue Eng Part A* **2010,** *16* (8), 2505-18; (c) Bennett, S.; Connolly, K.; Lee, D. R.; Jiang, Y.; Buck, D.; Hollinger, J. O.; Gruskin, E. A., Initial biocompatibility studies of a novel degradable polymeric bone substitute that hardens in situ. *Bone* **1996,** *19* (1, Supplement), 101S-107S; (d) Buckley, M. J.; Beckman, E. J., Adhesive Use in Oral and Maxillofacial Surgery. *Oral and Maxillofacial Surgery Clinics of North America* **2010,** *22* (1), 195-199.

28. (a) Zhang, J.-Y.; Beckman, E. J.; Piesco, N. J.; Agarwal, S., A new peptide-based urethane polymer: synthesis, biodegradation, and potential to support cell growth in vitro. *Biomaterials* **2000,** *21*, 1247-1258; (b) Elliott, S. L.; Fromstein, J. D.; Santerre, J. P.; Woodhouse, K. A., Identification of biodegradation products formed by L-phenylalanine based segmented polyurethaneureas. *Journal of Biomaterials Science Polymer Edition* **2002,** *13* (6), 691-711; (c) Bonzani, I. C.; Adhikari, R.; Houshyar, S.; Mayadunne, R. T. A.; Gunatillake, P. A.; Stevens, M. M., Synthesis of two-component injectable polyurethanes for bone tissue engineering. *Biomaterials* **2007,** *28*, 423-433.

29. Adhikari, R.; Gunatillake, P. A.; Griffiths, I.; Tatai, L.; Wickramaratna, M.; Houshyar, S.; Moore, T.; Mayadunne, R. T. M.; Field, J.; McGee, M.; Carbone, T., Biodegradable injectable polyurethanes: Synthesis and evaluation for orthopaedic applications. *Biomaterials* **2008,** *29* (28), 3762-3770.

30. (a) Lu, Q.-W.; Hoye, T. R.; Macosko, C. W., Reactivity of common functional groups with urethanes: Models for reactive compatibilization of thermoplastic

polyurethane blends. *Journal of Polymer Science Part A: Polymer Chemistry* **2002,** *40* (14), 2310-2328; (b) Szycher, M., *Szycher's Handbook of Polyurethanes*. CRC Press LLC: Boca Raton, 1999.
31. Kar, A., *Pharmaceutical Drug Analysis*. 2nd ed.; New Age International Limited: Daryaganj, New Delhi, 2005.
32. Neuman, W. F.; Toribara, T. Y.; Mulryan, B. J., The surface chemistry of bone. VII. The hydration shell. *J. Am. Chem. Soc.* **1953,** *75* (17), 4239-4242.
33. Zhang, J. Y.; Beckman, E. J.; Piesco, N. P.; Agarwal, S., A new peptide-based urethane polymer: synthesis, biodegradation, and potential to support cell growth in vitro. *Biomaterials* **2000,** *21* (12), 1247-1258.
34. (a) Mann, B. K.; Gobin, A. S.; Tsai, A. T.; Schmedlen, R. H.; West, J. L., Smooth muscle cell growth in photopolymerized hydrogels with cell adhesive and proteolytically degradable domains: synthetic ECM analogs for tissue engineering. *Biomaterials* **2001,** *22* (22), 3045-51; (b) Bryant, S. J.; Nuttelman, C. R.; Anseth, K. S., Cytocompatibility of UV and visible light photoinitiating systems on cultured NIH/3T3 fibroblasts in vitro. *J Biomater Sci Polym Ed* **2000,** *11* (5), 439-57; (c) Kim, I. S.; Jeong, Y. I.; Kim, S. H., Self-assembled hydrogel nanoparticles composed of dextran and poly(ethylene glycol) macromer. *Int J Pharm* **2000,** *205* (1-2), 109-16.
35. (a) Timmer, M. D.; Shin, H.; Horch, R. A.; Ambrose, C. G.; Mikos, A. G., In vitro cytotoxicity of injectable and biodegradable poly(propylene fumarate)-based networks: Unreacted macromers, cross-linked networks, and degradation products. *Biomacromolecules* **2003,** *4* (4), 1026-1033; (b) Fisher, J. P.; Dean, D.; Mikos, A. G., Photocrosslinking characteristics and mechanical properties of diethyl fumarate/poly(propylene fumarate) biomaterials. *Biomaterials* **2002,** *23* (22), 4333-43; (c) Kim, C. W.; Talac, R.; Lu, L.; Moore, M. J.; Currier, B. L.; Yaszemski, M. J., Characterization of porous injectable poly-(propylene fumarate)-based bone graft substitute. *J Biomed Mater Res A* **2008,** *85* (4), 1114-9.
36. Nguyen, K. T.; West, J. L., Photopolymerizable hydrogels for tissue engineering applications. *Biomaterials* **2002,** *23* (22), 4307-14.
37. (a) Semsarzadeh, M. A.; Navarchian, A. H., Effects of NCO/OH ratio and catalyst concentration on structure, thermal stability, and crosslink density of poly(urethane-isocyanurate). *Journal of Applied Polymer Science* **2003,** *90* (4), 963-972; (b) Gorna, K.; Gogolewski, S., Preparation, degradation, and calcification of biodegradable polyurethane foams for bone graft substitutes. *Journal of Biomedical Materials Research Part A* **2003,** *67A* (3), 813-827.
38. Storey, R. F.; Wiggins, J. S.; Puckett, A. D., Hydrolyzable poly(ester-urethane) networks from L-lysine diisocyanate and D,L-lactide/ϵ-caprolactone homo- and copolyester triols. *Journal of Polymer Science Part A: Polymer Chemistry* **1994,** *32* (12), 2345-2363.
39. Dumas, J. E.; Brownbaer, P. B.; Prieto, E. M.; Guda, T.; Hale, R. G.; Wenke, J. C.; Guelcher, S. A., Injectable reactive biocomposites for bone healing in critical-size rabbit calvarial defects. *Biomed Mater* **2012,** *7* (2), 024112.
40. (a) Loh, X. J.; Colin Sng, K. B.; Li, J., Synthesis and water-swelling of thermo-responsive poly(ester urethane)s containing poly(ε-caprolactone), poly(ethylene glycol) and poly(propylene glycol). *Biomaterials* **2008,** *29* (22), 3185-3194; (b) ISO, Biological

evaluations of medical devices. In *Tests for in vitro cytotoxicity*, ISO: Geneva, Switzerland, 2009(E); Vol. 10993-5.

41. Guan, J.; Sacks, M. S.; Beckman, E. J.; Wagner, W. R., Biodegradable poly(ether ester urethane)urea elastomers based on poly(ether ester) triblock copolymers and putrescine: synthesis, characterization and cytocompatibility. *Biomaterials* **2004,** *25* (1), 85-96.

42. Hafeman, A.; Li, B.; Yoshii, T.; Zienkiewicz, K.; Davidson, J.; Guelcher, S., Injectable Biodegradable Polyurethane Scaffolds with Release of Platelet-derived Growth Factor for Tissue Repair and Regeneration. *Pharm. Res.* **2008,** *25* (10), 2387-2399.

43. (a) Kerber, C. W.; Wong, W., Liquid acrylic adhesive agents in interventional neuroradiology. *Neurosurg Clin N Am* **2000,** *11* (1), 85-99, viii-ix; (b) Vinters, H. V.; Galil, K. A.; Lundie, M. J.; Kaufmann, J. C., The histotoxicity of cyanoacrylates. A selective review. *Neuroradiology* **1985,** *27* (4), 279-91.

44. Zhang, J.-Y.; Beckman, E. J.; Hu, J.; Yuang, G.-G.; Agarwal, S.; Hollinger, J. O., Synthesis, biodegradability, and biocompatibility of lysine diisocyanate-glucose polymers. *Tissue Eng* **2002,** *8* (5), 771-785.

45. Dumas, J. E.; Davis, T. E.; Yoshii, T.; Nyman, J.; Holt, G. E.; Perrien, D. S.; Boyce, T. M.; Guelcher , S. A., Synthesis of Allograft Bone/Polymer Composites and Evaluation of Remodeling in a Rabbit Femoral Condyle Model. *Acta Biomaterialia* **2010,** *6*, 2394–2406.

CHAPTER VI

NOVEL CHEMISTRIES FOR CELL SPECIFIC DEGRADATION OF POLYURETHANE BIOMATERIALS

Introduction

Biodegradable scaffolds made from synthetic polymers have been extensively investigated for use in tissue engineering and regenerative medicine. Examples include poly(lactic-*co*-glycolic acid) (PLGA)[1], poly(ε-caprolactone) (PCL)[2], polyanhydrides (PAA)[3], and polyurethanes[4], all of which have a history of use in products approved by the FDA[5]. These materials are applicable for a diverse range of regenerative applications because they offer a high degree of tunability, generate a minimal host inflammatory response, and degrade into non-cytotoxic components[6] that are resorbed and cleared from the body[7].

In situ curing, injectable scaffolds such as poly(ester urethanes) (PEURs) that support cellular infiltration and degrade into non-toxic breakdown products represent a particularly promising class of biomaterial[8]. Porous PEUR scaffolds are formed by mixing hydroxyl-functionalized polyols (*e.g.*, 900 g mol^{-1} triols comprised of caprolactone, glycolide, and D,L-lactide)[6a] with isocyanate-functional precursors to form a crosslinked network. Water can be added as a blowing agent to create an inter-connected pore structure, and the mechanical, chemical, and degradation properties of the scaffold can be modified through the selection of the polyol and isocyanate precursors[9]. Unlike many other methods used for fabrication of porous scaffolds, this approach does not require a porogen leaching step. This *in situ* foaming approach, combined with the relatively short working time of the reactive liquid mixture[10], renders PEURs useful as injectable and settable scaffolds suitable for minimally invasive procedures in the clinic.

PEUR scaffolds are primarily degraded by acid-catalyzed hydrolysis of ester bonds in the amorphous soft segment, resulting in chain scission and formation of hydroxyl and carboxylic acid end groups. Residual carboxylic acids in the polymer reduce the local pH at later stages of degradation[11], thereby catalyzing accelerated hydrolysis of the polymer[12]. As the polymers degrade, low molecular weight and soluble α-hydroxy acids diffuse from the scaffold into the medium, resulting in mass loss. Although α-hydroxy acids are non-toxic and can be cleared from the body[6a, 13], autocatalytic degradation of the PEUR network driven by residual carboxylic acid groups can result in a mismatch in the rates of scaffold degradation and tissue in-growth that leads to resorption gaps and compromised tissue regeneration[14].

Environmentally-responsive polymers have been heavily investigated for the development of smart materials that respond to specific biological stimuli[15]. In particular, biomaterials that degrade by cell-mediated mechanisms, such as materials with protease-cleavable peptides, have been successfully utilized to synthesize environmentally-sensitive nanoparticles[16], hydrogels[17], and polymeric scaffolds[18]. Development of degradable polymers that can be cheaply synthesized in large scales, similar to polyesters, but that target a ubiquitous cell-mediated signal for scaffold degradation may provide a more generalizable and better-performing biomaterial. Scaffolds degraded by cell-generated reactive oxygen species (ROS) are a promising candidate because ROS serve as important biological mediators in many normal biological processes[19], and elevated ROS, or “oxidative stress”, is a hallmark of inflammation and the pathogenesis of myriad diseases, such as cancer and during wound healing[20]. Polymeric biomaterial implants have also been shown to elicit a stable three-fold increase in ROS production at surgery sites over a four week timeframe[21], highlighting the potential utility of this cell-generated signal for triggering material degradation. Additionally, in the bone microenvironment, osteoclasts are known to secrete ROS during resorption[22]. This has motivated the recent emergence of new classes of ROS-responsive polymer-based nanoparticles[23] and development of salt-leached, porous scaffolds composed of a combination of the polyester PCL and ROS-sensitive, proline-based peptides[24].

Here we sought to develop a generalizable, cell-degradable polyurethane scaffold formulated from polyols exhibiting ROS-dependent degradation. To do so, we synthesized a new class of polyols based on ROS-degradable poly(thioketals). Poly(thioketals) (PTKs) were recently applied for development of orally-delivered nanoparticles that remain stable in transit through the stomach and specifically release their cargo "on demand" at sites of ulcerative colitis[23b]. To date, however, this unique polymer chemistry has solely been utilized in targeted nanoparticle drug delivery applications[23b, 23f]. Herein, we report the development and testing of a new class of PTK macrodiols amenable to synthesis of injectable, porous poly(thioketal)-urethane (PTK-UR) tissue engineering scaffolds that are selectively degraded by cell-generated ROS. These fully synthetic scaffolds have been developed to further explore utilization of an ROS-dependent degradation mechanism in order to yield scaffolds with better matched rates of cellular infiltration and degradation.

Experimental

Materials

All chemicals were purchased from Sigma-Aldrich (Milwaukee, WI, USA) except the following. 2-mercaptoethyl ether (MEE), glutaraldehyde, and cobalt chloride were purchased from Fisher Scientific (Pittsburgh, PA), and the tertiary amine catalyst (TEGOAMIN33) was obtained from Goldschmidt (Hopewell, VA). Glycolide and D,L-lactide were obtained from Polysciences (Warrington, PA). Coscat83, an organobismuth urethane catalyst, was supplied by ChasChem, Inc. (Rutherford, NJ). Hexamethylene diisocyanate trimer (HDIt, Desmodur N3300A) was received as a gift from Bayer Material Science (Pittsburgh, PA). Cell culture reagents, including Dulbecco's Modified Eagle Medium (DMEM), fetal bovine serum (FBS), and penicillin/streptomycin were supplied by Gibco Cell Culture (Carlsbad, CA). All materials were used as received unless otherwise indicated.

PTK dithiol synthesis

The condensation polymerization protocol for PTK prepolymer synthesis was adapted from Wilson et al. [23b]. Briefly, p-toluenesulphonic acid monohydrate (PTSA) was added to a tri-necked boiling flask equipped with an attached addition funnel. The vessels were placed under vacuum for 15 min before being purged with nitrogen. The boiling flask was charged with anhydrous acetonitrile and batch-specific amounts of MEE (x molar eq) and 1,4 butanedithiol (BDT) (1-x molar eq) where x = 1, 0.75, 0.5, 0.25, and 0 for the different synthesized PTKs. The addition funnel was also charged with anhydrous acetonitrile and 2,2-dimethoxypropane (DMP) (0.83 molar eq). A molar excess of dithiol monomers was utilized relative to DMP to ensure the formation of polymers with free terminal thiols. Both the addition funnel and boiling flask's solutions were purged with flowing nitrogen for 30 min before submerging the boiling flask into an oil bath at 80°C. After 15 min of temperature equilibration, the addition funnel stopcock was set so that the acetonitrile-DMP solution was added drop-wise into the continuously stirring boiling flask over a period of 16 h. Post synthesis, the acetonitrile was removed by rotary evaporation and the resultant PTKs were isolated by precipitation into cold ethanol and dried under vacuum. To evaluate polymer compositions, samples of the respective PTKs were dissolved in deuterated chloroform ($CDCl_3$) and analyzed with ^1H nuclear magnetic resonance spectroscopy (NMR, Bruker 400 MHz Spectrometer). ^1H NMR chemical shifts were reported as δ values in ppm relative to the deuterated $CDCl_3$ ($\delta = 7.26$). Multiplicities are reported as follows: s (singlet), d (doublet), t (triplet), q (quartet), and m (multiplet). The number of protons (n) for a given resonance is indicated as nH and is based on integration values. ^1H NMR (400 MHz, $CDCl_3$): $\delta = 3.67\text{-}3.61$ (m, 4H), $\delta = 2.83$ (t, 4H), $\delta = 2.63$ (t, 4H), $\delta = 1.72$ (t, 4H), $\delta = 1.60$ (s, 6H).

Polyester polyol synthesis

Trifunctional or bifunctional polyester polyols were synthesized as previously documented [6a]. To synthesize the trifunctional polyol, glycerol was vacuum dried for 48 hours at 80^oC and then added to a 100 mL three neck flask. By molar amount, 60% ε-caprolactone, 30% glycolide, and 10% D,L-lactide were added to the glycerol starter along with a stannous octoate catalyst to yield a 900 g mol^{-1} triol, a 1000 g mol^{-1} diol, and a 1500 g mol^{-1} triol.

PTK hydroxyl functionalization

The hydroxyl-functionalization of the PTK dithiols was completed [25] in order to generate polyols compatible with standard polyurethane synthesis. Briefly, PTK dithiol polymers were transferred to a boiling flask, placed under vacuum, and then exposed to a nitrogen atmosphere. The flask was charged with dichloromethane (DCM) before adding a 10x molar excess of β-mercaptoethanol to the solution. This solution was stirred continuously at room temperature to reduce any disulfide bonds and recover the reactive thiol end groups. After 3 h of stirring, the DCM was evaporated and the residue was washed three times in cold ethanol to remove residual β-mercaptoethanol. The reduced PTK polymers were dissolved in anhydrous tetrahydrofuran (THF) before adding a 10x molar excess of cesium carbonate ($CsCO_3$) under nitrogen and stirring for 30 min at room temperature. A 5x molar excess of 2-bromoethanol was next added to the solution and stirred for 18 hours under nitrogen at room temperature. After stirring, the solution was added to a separation funnel with an excess of deionized water to effectively separate the PTK-solubilizing THF layer from the water-soluble $CsCO_3$ catalyst. The hydroxyl-functionalized PTKs were extracted in THF before removing the solvent by rotary evaporation, followed by precipitation three times in cold ethanol before vacuum drying for 24 h. Molecular weights and polydispersities of the five synthesized PTK diols were analyzed by gel permeation chromatography (GPC, Agilent Technologies, Santa Clara, CA) using a mobile phase of *N*,*N*-dimethylformamide (DMF) with 100mM LiBr. Polymer molecular weights were quantified using a calibration curve generated from poly(ethylene glycol) (PEG) standards (400 – 4000 g mol^{-1}). Hydroxyl-functionalization was confirmed by ^1H NMR (400 MHz, $CDCl_3$): $\delta = 2.74$ (t, 4H) and attenuated total reflectance Fourier transform infrared spectroscopy (ATR-FTIR; Bruker Tensor 27 FTIR, Billerica, MA). For ATR-FTIR, thiol-terminated and hydroxyl-terminated PTK polymers were placed in contact with a ZnSe ATR crystal to quantify absorbance at 2550 cm^{-1} and 3400 cm^{-1}, which correspond to absorbance peaks of free thiol and free hydroxyl groups, respectively. The hydroxyl (OH) numbers of the different PTK diols were determined by titration (Metrohm 798 MPT Titrino) according to ASTM E1899 – 08 [26]. Equation 1 was used to relate the molecular weight to the hydroxyl number of each titrated PTK:

$$\boldsymbol{M_n = \frac{56100f}{OH\ number}} \tag{1}$$

where 56,100 represents the molecular weight of KOH in mg/mol, f represents the hydroxyl functionality of the PTK (assumed to be 2 for the linear homobifunctional polymers in this study), and M_n represents the number-average molecular weight of the polymer. The full synthesis scheme is displayed in Figure 6.1.

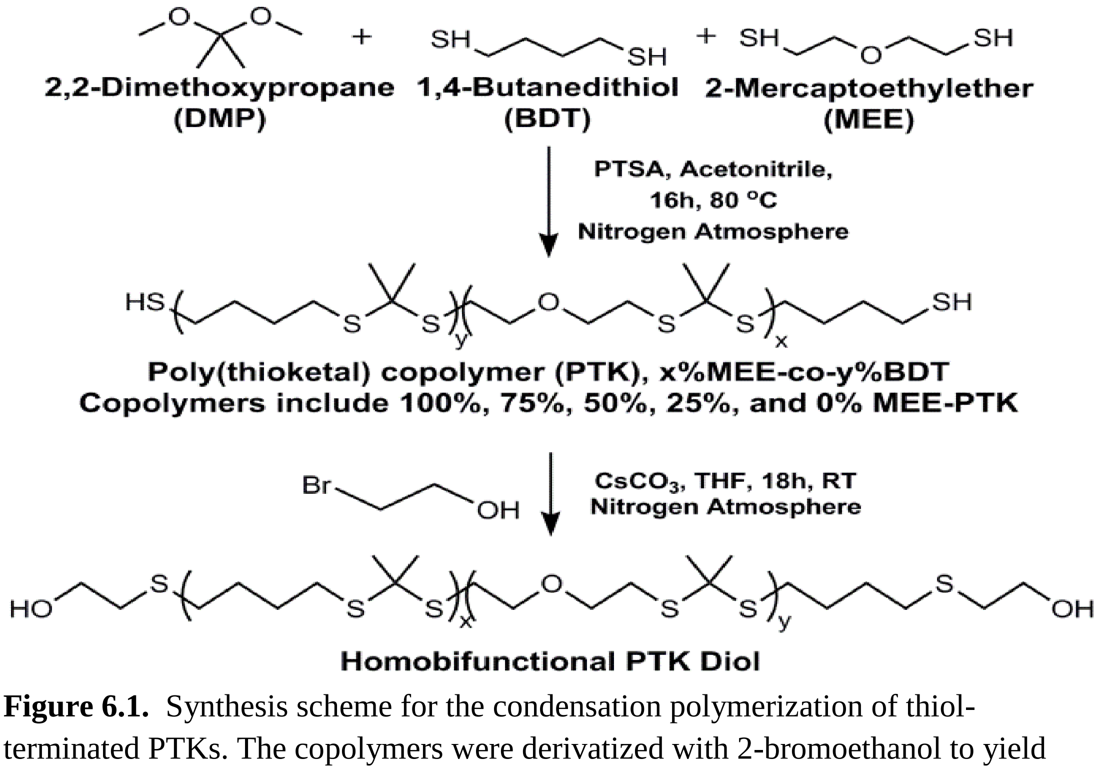

Figure 6.1. Synthesis scheme for the condensation polymerization of thiol-terminated PTKs. The copolymers were derivatized with 2-bromoethanol to yield PTK diols.

PTK-UR and PEUR synthesis

The PTK-UR and PEUR scaffolds were prepared using two-component reactive liquid molding of: (a) hexamethylene diisocyanate trimer (HDIt), and (b) a hardener component comprising the PTK diol, 0.5 – 1.5 parts per hundred parts polyol (pphp) water, 10.0 pphp TEGOAMIN33 catalyst, 0.5 – 3.0 pphp sulfated castor oil stabilizer, and 4.0 pphp calcium stearate pore opener [6a]. The makeup of the hardener components for the different respective PTK diols was individually optimized to yield scaffolds with mechanical integrity and an intact porous structure. PEUR scaffolds were respectively designated by their polyester precursor as 900t-PEUR, 1000d-PEUR, and 1500t-PEUR and served as hydrolytically-degradable controls. The hardener component elements were first mixed for 30 s at 3300 rpm in a Hauschild DAC 150 FVZ-K SpeedMixer (FlackTek, Inc., Landrum, SC) before adding the HDIt and mixing for an additional 30 s. This reactive liquid mixture was allowed to rise freely for 10-20 min for complete setting and hardening. The targeted index (ratio of NCO to OH equivalents times 100) was 115, where the number of OH equivalents is calculated from the experimentally measured OH number for the relevant PTK diol.

Characterization of scaffold physical properties

The core densities of PTK-UR and PEUR scaffolds were determined by measuring the mass and volume of cylindrical porous scaffold core samples, with the core porosities being subsequently calculated from these density values [6a]. The porous morphologies of the different PTK-UR scaffolds were qualitatively assessed by scanning electron microscopy (Hitachi S-4200 SEM, Finchampstead, UK). The amount of unreacted components (sol fraction) in the cross-linked network was measured from the mass loss of dried scaffold cylinders (25 mm × 12 mm) previously incubated in DCM for 24 h. To measure the molecular weight between crosslinks (M_c), scaffold samples (n = 3) were weighed dry and then incubated in DCM for 24 h. After incubation, samples were gently blotted to remove excess DCM and then the samples' swollen mass was measured. These values, along with the solvent parameters, were used in the Flory-Rhener equation to determine M_c. For measuring scaffold hydrophilicity, PTK-UR films of 100%, 50%, and 0% MEE-PTK diols were synthesized using an index of 105 and the gelling catalyst Coscat83 at 1000 ppm. After mixing the catalyst and PTK diol for 30 s at 3300 rpm, HDIt was added and mixed for an additional 30 s. The mixtures were cast into Teflon compression molds and allowed to cure for 18 h at 60°C. The contact angle of water on these PTK-UR films was measured using a Rame-Hart (Mountain Lakes, NJ) Model A-100 contact angle goniometer. A 4 μL water drop was added to the film surface, and after 10 min, an equilibrium contact angle was measured to account for molecular surface reorganization which increased the hydrophilicity at the contact site[27].

Thermal and mechanical properties

Thermal transitions were measured by a TA Instruments (New Castle, DE) Q200 DSC and Q800 DMA. For DSC analysis, samples ranging in mass from 10-15 mg were heated from -80^{o} C to 200^{o} C at a rate of 10^{o} C min^{-1}, cooled to -80^{o} C at a rate of -20^{o} C min^{-1}, and heated a second time to 200^{o} C at a rate of 10^{o} C min^{-1}. All transitions were obtained from the second heating run. For dynamic mechanical analysis (DMA, Q800 DMA, TA Instruments, New Castle, DE), cylindrical samples (6 × 6 mm) were analyzed from -80^{o} to 55^{o} C at a ramp rate of 1^{o} C min^{-1}. Scaffolds were compressed at a frequency of 1 Hz with 1% strain during the thermal treatment. Glass transitions were obtained at the peak of tan δ.

The mechanical properties of the different PTK-UR and PEUR scaffold formulations were measured in compression at 37°C in a submersion compression clamp using the Q800 DMA. Cylindrical 6 × 6 mm scaffold samples were tested after incubation in phosphate buffered saline (PBS) for 7 days at 37°C. Using a preload force of 0.1 N, samples were compressed along the longitudinal axis at a strain rate of 10% per min until 60% compressive strain was achieved. The Young's modulus for each sample was calculated from the slope of the initial linear region of each respective stress-strain curve after toe-in.

In vitro degradation of PTK-UR and PEUR scaffolds

Long-term hydrolytic stability of PTK-UR and PEUR scaffolds was determined by incubating 10 mg samples in PBS at 37°C on a shaker and measuring the mass loss at each time point (n = 3). Before beginning the experiment, scaffolds were soaked in an excess of DCM for 24 h to remove any unreacted components before vacuum drying for 24 h. Scaffold samples were removed from the buffer at each time point, rinsed in deionized water, vacuum dried for 48 h, and weighed. The buffer medium was not changed between time points. Short term oxidative degradation rates of PTK-UR scaffolds were similarly assessed using an oxidative degradation medium that simulates *in vivo* oxidative degradation at an accelerated rate[28]. This oxidative medium comprised 20 wt% hydrogen peroxide (H_2O_2) in 0.1 M cobalt chloride ($CoCl_2$), with the H_2O_2 and cobalt ion reacting to stimulate oxidative radical formation[28a]. As with the long-term study, triplicate samples were pre-soaked in DCM for 24 h before vacuum drying and incubated at 37°C in the oxidative medium on a shaker. At specified time points over 10 d, samples were removed, rinsed with deionized water, vacuum dried, and weighed. The oxidative medium was replaced every 3 days, and the morphology of both PBS-incubated and H_2O_2-incubated scaffolds was qualitatively assessed with SEM.

The effect of radical concentration on PTK-UR scaffold degradation kinetics was also explored. The original 20% H_2O_2 in 0.1 M $CoCl_2$ degradation medium was diluted ten and one hundred fold to yield a 2% H_2O_2 in 0.01 M $CoCl_2$ solution and a 0.2% H_2O_2 in 0.001 M $CoCl_2$ solution. These three degradation media were used to incubate 100%, 50%, and 0% MEE-PTK-UR scaffolds along with 900t-PEUR control samples, with material preparation steps and incubation conditions being the same as previously described.

Mathematical modeling of PTK-UR oxidative degradation

The degradation behavior of the PTK-UR scaffold formulations were fit to first-order decay kinetics equation to create a mathematical model of scaffold degradation with respect to H_2O_2 concentration. The first-order degradation model is given in Equation 2.

$$\boldsymbol{M_t / M_0 = e^{-kt}} \tag{2}$$

In this equation, M_t is the scaffold mass remaining at time t, M_0 is the initial scaffold mass, and k is the degradation rate constant. Non-linear regression was used to fit this first-order degradation model to the experimentally determined degradation data. This method was used to determine the degradation rate constant k for the different scaffolds in the different control and oxidative media.

In vitro culture of macrophages on PTK-UR scaffolds

RAW 264.7 macrophages were cultured in DMEM supplemented with 10% FBS and 1% penicillin/streptomycin. 100% and 0% MEE-PTK-UR scaffolds were cut into 6.5 × 1-mm discs, sterilized by UV-radiation for 1 h (30 min per side), placed into 96-well plates, and incubated with culture medium for 30 min. Macrophages were seeded onto the scaffolds at a density of 2.5×10^5 cells/scaffold. The cells were allowed to adhere to the scaffolds for 3 h, at which point the old media were removed and the cells were treated with either fresh culture media or activation media containing 5 μg mL^{-1} lipopolysaccharide (LPS) and 1000 U mL^{-1} interferon gamma (IFN-γ). Cells were incubated on the scaffolds for 3 d with fresh culture media being applied daily. After the 3 d incubation, the scaffolds were fixed in 5% glutaraldehyde for 2 h followed by 2% osmium tetroxide for 1 h. These fixed scaffolds were dehydrated in ascending grades of ethanol before being vacuum dried, sputter-coated, and imaged with SEM to evaluate surface pitting.

Cytotoxicity of PTK-UR and PEUR scaffolds

NIH 3T3 mouse fibroblasts stably transfected with a firefly luciferase reporter gene were cultured in DMEM supplemented with 10% FBS and 1% penicillin/streptomycin. 100% MEE-PTK-UR, 0% MEE-PTK-UR, and 900t-PEUR scaffolds were cut into 6.5 × 1-mm discs, sterilized by UV-radiation for 1 h (30 min per side), placed into a black-walled 96-well plate, and incubated with culture medium for 30 min. Fibroblasts were seeded at a density of 5.0×10^4 cells/scaffold on n=3 scaffolds and allowed to grow for 0, 1, and 3 days in 200 μL of culture media per well (changed every two days). At the endpoint, the cell-seeded scaffolds were treated with culture media containing a luciferin substrate. After 10 min, the scaffolds were imaged with an IVIS 200 (Caliper Life Sciences, Hopkinton, MA) bioluminescence imaging system with an exposure time of 2 min to quantify the luciferase-based bioluminescence signal from each scaffold’s viable cell population. All readings were normalized to day 0 bioluminescence values.

In vivo degradation of PTK-UR scaffolds implanted subcutaneously in rats

All surgical procedures were reviewed and approved by the Institutional Animal Care and Use Committee. 100% MEE-PTK-UR and 900t-PEUR scaffolds were cut into 10 × 2.5 mm discs, sterilized with ethylene oxide prior, and implanted into ventral subcutaneous sites in adult male Sprague-Dawley rats. Scaffolds were excised at weeks 1, 3, 5 and 7 to evaluate new tissue formation in the implants. The tissues were fixed in formalin for 48 h followed by incubation in 70% ethanol for 48 h, embedding in paraffin, sectioning, and staining with hematoxylin & eosin. Histological sections were evaluated with Metamorph Imaging Software (Molecular Devices Inc., Sunnyvale CA) to assess wound size, scaffold degradation, and new tissue growth.

Statistical Analysis

All data are reported as the mean and standard error of the mean. Statistical analysis was performed using single factor analysis of variance (ANOVA) and Tukey post-hoc comparison tests, with *p*-values less than 0.05 considered statistically significant.

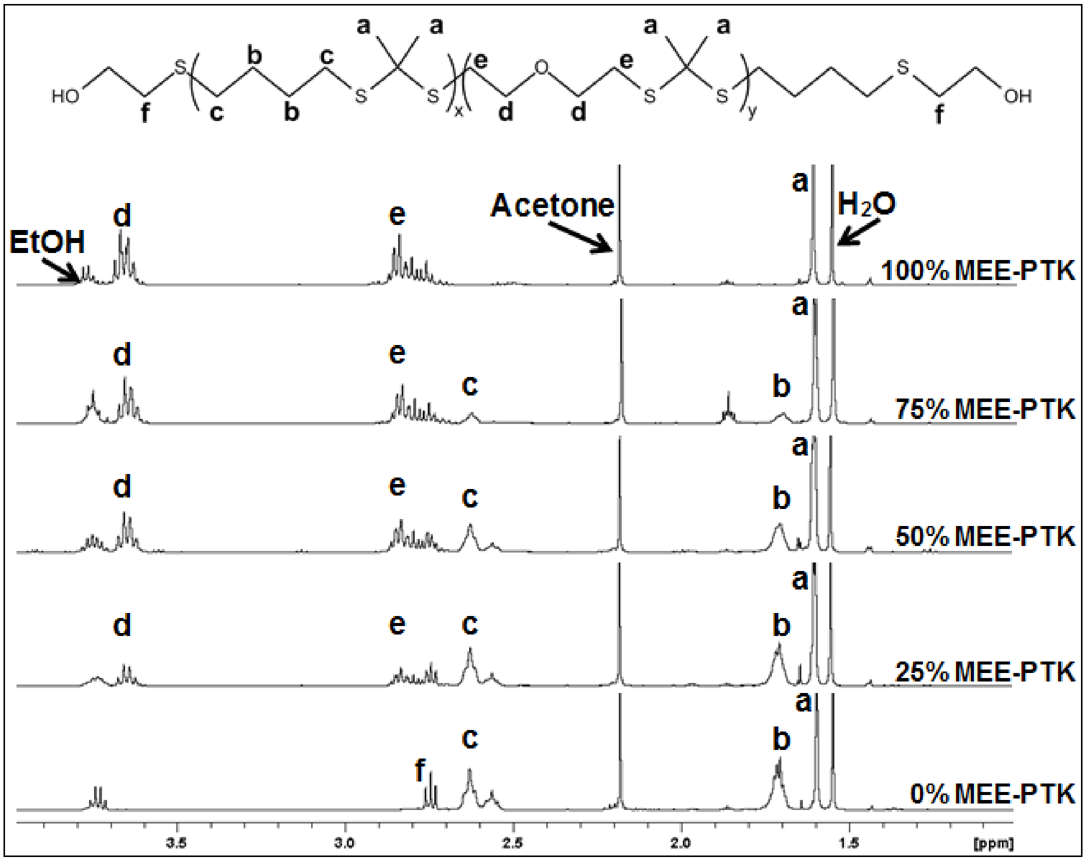

Figure 6.2. ^{1}H-NMR spectra of the synthesized PTK copolymer diols. Peaks associated with MEE and BDT monomers correlated with molar composition used in the polymer feed.

Table 6.1. Characterization of PTK diols.

Copolymer (PTK diol)	**100% MEE**	**75% MEE**	**50% MEE**	**25% MEE**	**0% MEE**
GPC M_n	1027	1005	947	1053	807
PDI	1.38	1.34	1.35	1.36	1.32
Titration M_n	825	850	810	745	680
Theoretical MEE%	100%	75%	50%	25%	0%
Actual MEE%	100%	76%	52%	26%	0%

Results

Thiol-terminated PTK polymers were successfully synthesized from the condensation polymerization of MEE, BDT, and DMP monomers using PTSA as a catalyst. Five copolymers were synthesized with varying percent molar composition of MEE and BDT, and each polymer is designated by its relative mol% MEE. ^{1}H-NMR spectra confirmed that the composition of the synthesized polymers closely matched the monomer ratios in the feed (Figure 6.2, Table 6.1), and gel permeation chromatography (GPC) analysis showed that the polymers had M_n of ~1000 g mol^{-1} with polydispersity index (PDI) values around 1.35.

Efficient conversion of terminal thiols to hydroxyls was demonstrated by ATR-FTIR. The thiol absorbance peak at 2550 cm^{-1} was apparent in the thiol-terminated, parent PTKs but did not appear with the hydroxyl-terminated polymers, which generated a characteristic ATR-FTIR hydroxyl peak at 3400 cm^{-1} (Figure 6.3). OH numbers experimentally measured with titration were utilized to calculate a titration M_n that was used to balance the hydroxyl-isocyanate reaction used to form PTK-URs. Consistent with previous findings, the experimental OH numbers trended higher than theoretical values[9a].

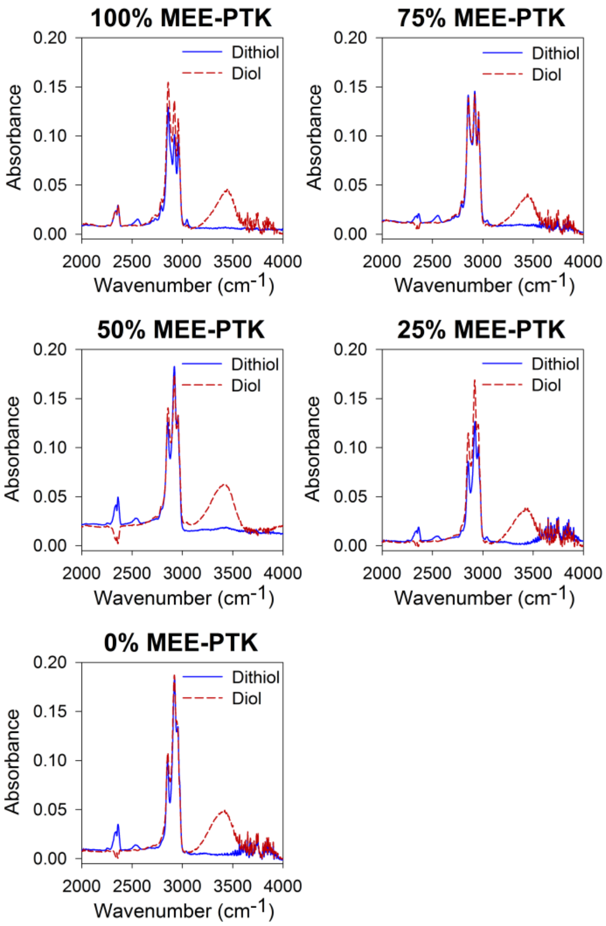

Figure 6.3. ATR-FTIR spectra of thiol- and hydroxyl-terminated PTKs. The thiol absorbance peak is seen at 2550 cm^{-1} and the hydroxyl absorbance peak is seen at 3400 cm^{-1}. These spectra demonstrate efficient conversion of PTK terminal thiols into hydroxyls.

PTK-UR scaffolds were successfully synthesized from the PTK diols and HDIt, yielding porous, mechanically robust 3D scaffolds (Figure 6.4, top row). PEUR control scaffolds were also successfully formed from HDIt and the three different polyester prepolymers (1000d, 1500t, and 900t). The resulting PTK-UR and PEUR scaffolds possessed similar sol fraction and porosity, as seen in Table 6.2. The average molecular weight between crosslinks (M_c) for 1000d- and 1500t-PEUR was statistically equal to all of the PTK-UR scaffolds, while the 900t-PEURs had a significantly lower M_c ($p < 0.05$) relative to all other formulations except for the 100% and 0% MEE-PTK-UR scaffolds

(Table 6.2). The relative surface hydrophilicity of the PTK-UR materials was assessed using contact angle measurements on films, with 100%, 50%, and 0% MEE-PTK-URs having contact angle values of 66°, 77°, and 80°, respectively.

The glass-transition temperature (T_g) of PTK polyols was determined by differential scanning calorimetry (DSC), and the T_g of the PTK-UR scaffolds was measured by DSC and dynamic mechanical analysis (DMA) (Table 6.3). The wet compressive moduli of the PTK-UR scaffolds ranged from 100 - 250 kPa, and the PEUR moduli ranged from 20 – 100 kPa (Figure 6.5). All the PTK-UR formulations had significantly higher modulus values than the 1500t-PEUR and 1000d-PEUR materials, while the lower M_c 900t-PEUR scaffolds possessed stiffness values closer to the PTK-UR samples. However, even this formulation was significantly less stiff than the 100% and 0% MEE-PTK-UR materials.

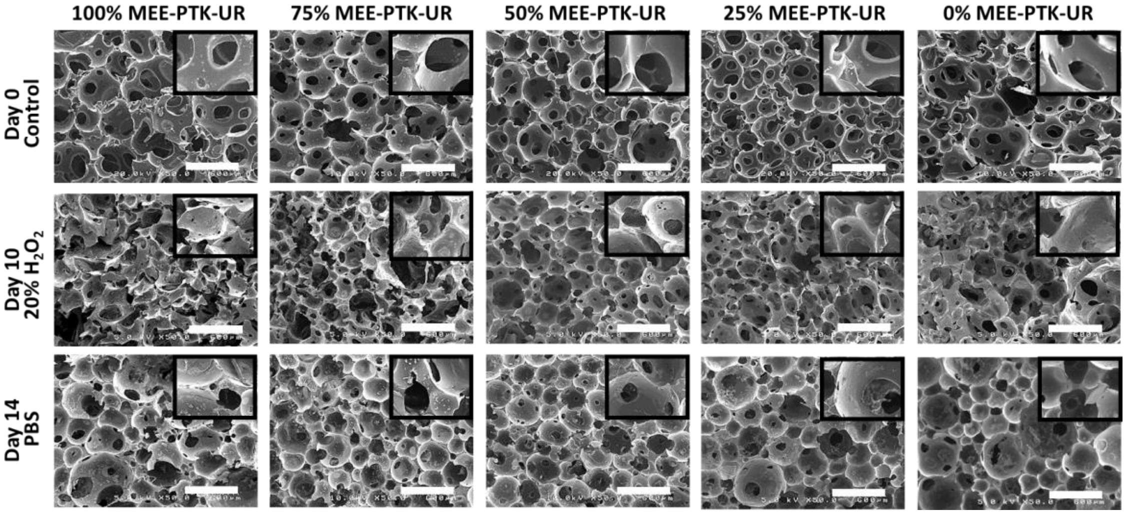

Figure 6.4. SEM images of PTK-UR scaffolds. Day 0 samples (top row) show representative untreated scaffolds. The day 10 degradation samples (middle row) were incubated in 20% H_2O_2 in 0.1M $CoCl_2$ for 10 days at 37°C to demonstrate oxidative degradation of the PTK-URs (note visible changes in structure of "macro-pores" and appearance of "micro-pores" in the struts of the scaffold). Day 14 control samples (bottom row) were incubated in PBS for two weeks at 37°C to demonstrate the resistance of the PTKs to hydrolytic breakdown. White scale bar represents 600 μm, and the inset images display higher magnification views (2.6x magnification of large image).

Table 6.2. Physical properties of PTK-UR and PEUR scaffolds.

Scaffold	Sol Fraction (%)	Core Porosity (vol. %)	M_c (kg mol^{-1})
100% MEE PTK-UR	6.9%±1.6%	90.9%±0.4%	7.6±4.2
75% MEE PTK-UR	8.4%±1.4%	89.0%±1.2%	10.1±4.9
50% MEE PTK-UR	9.7%±6.1%	86.9%±1.4%	13.8±6.5
25% MEE PTK-UR	9.1%±2.7%	90.6%±1.5%	9.0±5.0
0% MEE PTK-UR	8.3%±3.2%	88.8%±1.4%	9.0±5.8
900t PEUR	4.1%±1.6%	89.8%±1.2%	2.5±1.6
1500t PEUR	4.7%±0.1%	91.3%±0.2%	13.2±5.4
1000d PEUR	7.7%±0.1%	92.7%±0.7%	7.7±2.8

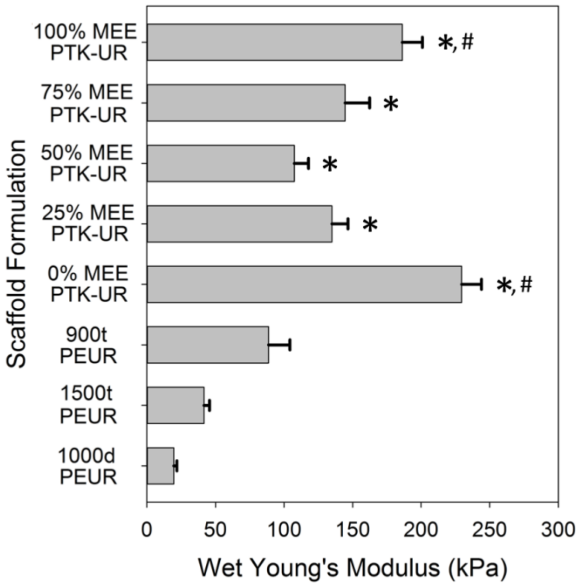

Figure 6.5. Polyurethane scaffold mechanical properties. The compressive moduli of porous scaffolds were determined under wet conditions at 37°C. *$p < 0.05$ compared to 1500t- and 1000d-PEUR. $^{\#}p < 0.05$ compared to 900t-PEUR.

Table 6.3. Thermomechanical properties of PTK-UR and PEUR scaffolds and neat polymers.

	Polymer	*Scaffold*	
	DSC T_g (°C)	**DSC T_g (°C)**	**DMA T_g (°C)**
100%MEE-PTK	-66.1	-25.2	20.7
75%MEE-PTK	-67.7	-36.0	14.9
50%MEE-PTK	-78.5	-11.1	13.9
25%MEE-PTK	-72.9	-27.9	20.3
0%MEE-PTK	-76.8	-19.3	23.1
900 Triol	-47.7	-1.7	34.4
1500 Triol	-56.9	-26.4	24.7
1000 Diol	-43.1	-30.1	18.2

The hypothesized oxidative degradation mechanism of PTK copolymers is seen in Figure 6.6. Qualitative PTK-UR degradation was demonstrated by SEM as scaffolds incubated for 10 d in oxidative media illustrated loss of porous architecture and surface pitting (Figure 6.4, middle row), while these morphological changes in scaffold architecture were not apparent following PTK-UR scaffold incubation in PBS for 14 days (Figure 6.4, bottom row). The PTK-UR scaffolds were stable over a long-term, 25-week study in PBS at 37°C, while the 900t-PEUR scaffolds underwent significant hydrolytic degradation over this time period (Figure 6.7B). Conversely, the PTK-URs rapidly degraded under accelerated oxidative conditions (20% H_2O_2 in 0.1 M $CoCl_2$) as seen in Figure 6.7C. The degradation profiles of all PTK-UR formulations in the 20% H_2O_2 media are seen in Figure 6.7G.

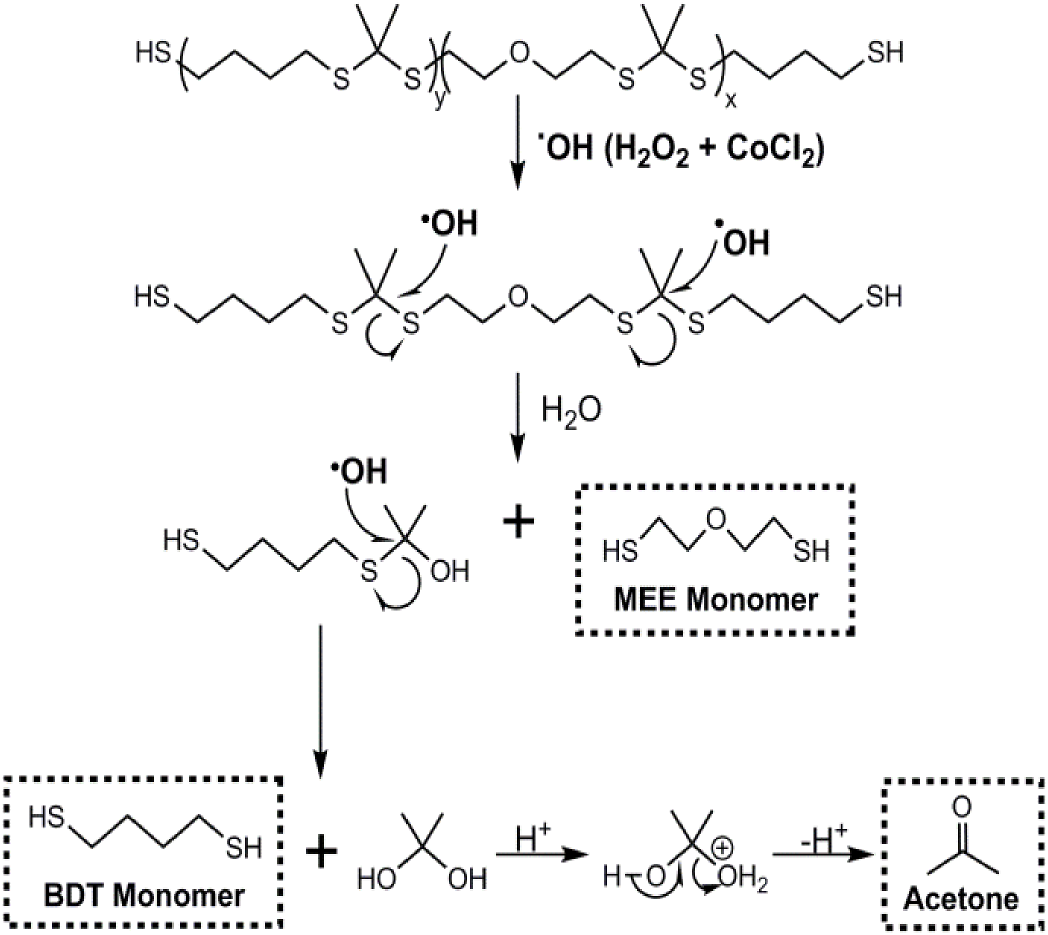

Figure 6.6. Proposed mechanism for hydroxyl radical degradation of PTK polymers. Hydroxyl radicals formed from the breakdown of H_2O_2 react with and break the TK bond, leading to PTK degradation into its original constitutive monomers (BDT and MEE) and acetone.

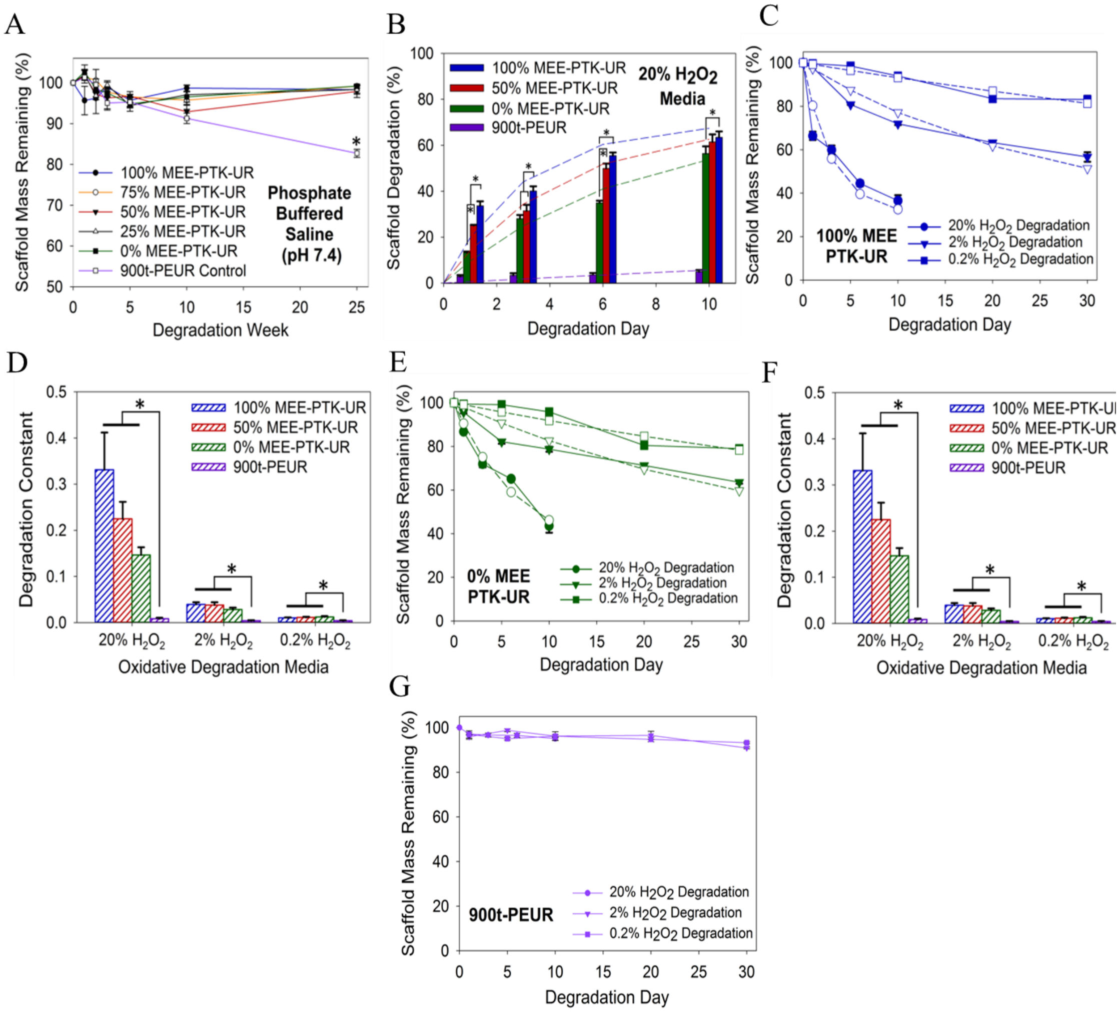

Figure 6.7. *In vitro* degradation of PTK-UR scaffolds. Data are presented as mean ± standard error with n = 3. (A) Long-term stability of PTK-UR scaffolds incubated in PBS. (B) Percent degradation of PTK-UR scaffolds incubated in oxidative medium (20% H_2O_2 in 0.1M $CoCl_2$). Dashed lines represent best-fit curves, $*p < 0.05$. Percent mass remaining of (C) 100% MEE-PTK-UR, (D) 50% MEE-PTK-UR, and (E) 0% MEE-PTK-UR scaffolds incubated in oxidative media containing 20%, 2%, and 0.2% H_2O_2.(F) Degradation constants used to generate the best-fit curves in (B-E), as determined by non-linear regression analysis. (G) The PTK-UR but not the PEUR scaffolds exhibited H_2O_2 dose-dependent degradation.

To further elucidate the relationship between ROS concentration and the degradation rates of the different PTK-UR scaffold formulations, degradation was measured in oxidative media comprising 20%, 2%, and 0.2% H_2O_2 and 0.1, 0.01, and 0.001 M $CoCl_2$, respectively. The degradation rates of PTK-UR scaffolds were dependent on the concentration of H_2O_2 (Figure 6.7C-E). The mass loss profiles of the PTK-UR scaffolds were fit to first-order degradation kinetics (Equation 2) to mathematically model the process of scaffold degradation with respect to H_2O_2 concentration. The model-generated degradation profiles are concurrently shown with the respective experimental data as dotted lines in Figure 6.6B-E, with the derived degradation rate constants being shown in Figure 6.6F. The 900t-PEUR samples incubated in these same oxidative media did not display significant degradation over the same time scale (Figure 6.7G).

100% and 0% MEE-PTK-UR scaffolds were seeded with murine-derived RAW 267.4 macrophages. Seeded cells were treated with either control culture media or macrophage-activating media containing LPS and IFN-γ. SEM imaging of scaffolds after three days illustrated surface pitting by activated macrophages, but cell mediated scaffold degradation was not apparent for the control cells (Figure 6.8).

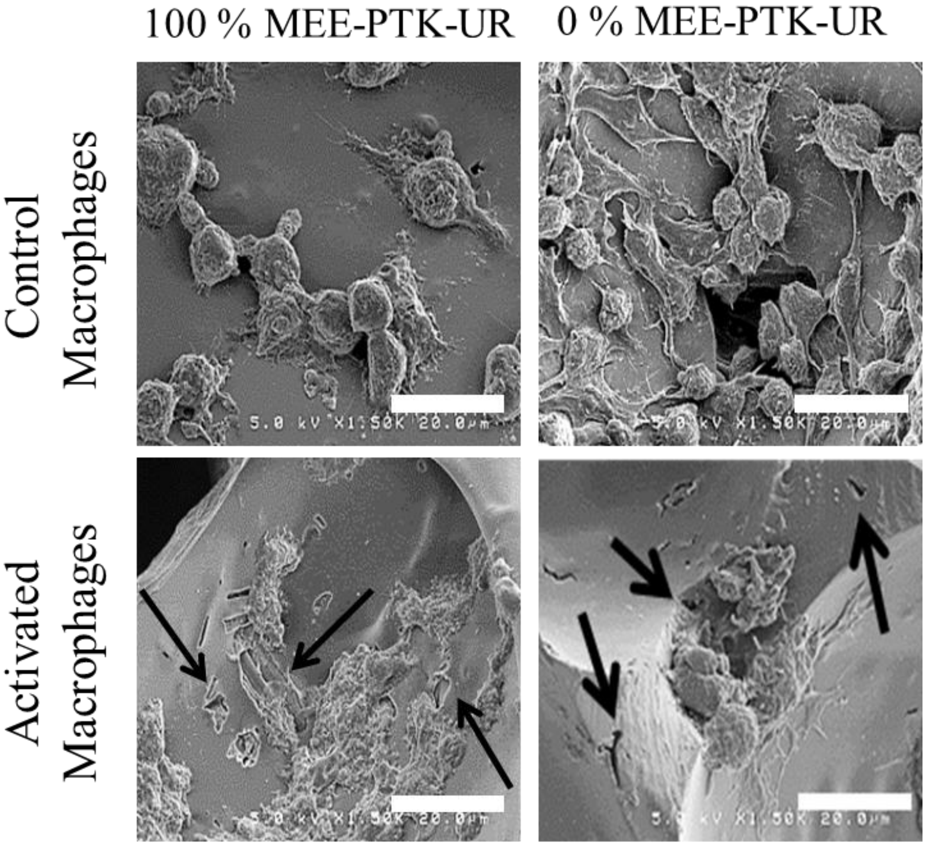

Figure 6.8. Macrophage pitting of PTK-UR scaffolds. PTK-UR scaffolds seeded with RAW 267.4 macrophages and incubated for 3 d in either control or activation media (LPS and IFN-γ). The activated macrophages generated visible pitting on the scaffold surface (black arrows), indicating ROS-mediated scaffold degradation. Scale bar = 20μm.

NIH 3T3 mouse fibroblasts stably transduced to express luciferase were seeded onto 100% MEE-PTK-UR, 0% MEE-PTK-UR, and 900t-PEUR scaffolds, and relative cell number was measured based on luciferase activity over 3 days of culture (Figure 6.9A). Cell-generated bioluminescent signal was steadily maintained over the culture period, and there were no significant differences between the scaffold compositions tested.

100% MEE-PTK-UR and 900t-PEUR scaffolds subcutaneously implanted into male Sprague-Dawley rats demonstrated robust cellular infiltration and granulation tissue formation by 3 weeks post implantation, while the 0% MEE-PTK-UR materials supported visibly less tissue in-growth (Figure 6.9B). Both the 100% MEE-PTK-UR and 900t-PEUR materials displayed significant degradation over 7 weeks. However, the 100% MEE-PTK-UR implants degraded gradually over 7 weeks to reach 40% degradation, whereas at their end point the 900t-PEUR scaffolds were 75% degraded compared to week 1 values and experienced all their degradation between weeks 3 and 7. The 900t-PEUR scaffolds were also significantly more compressed than the PTK-UR materials, which stented the implant site significantly more than the PEUR scaffolds (Figure 6.9C). Wound lengths were relatively consistent between PTK-UR and PEUR implant sites over time, while wound area measurements followed trends similar to the scaffold thickness values.

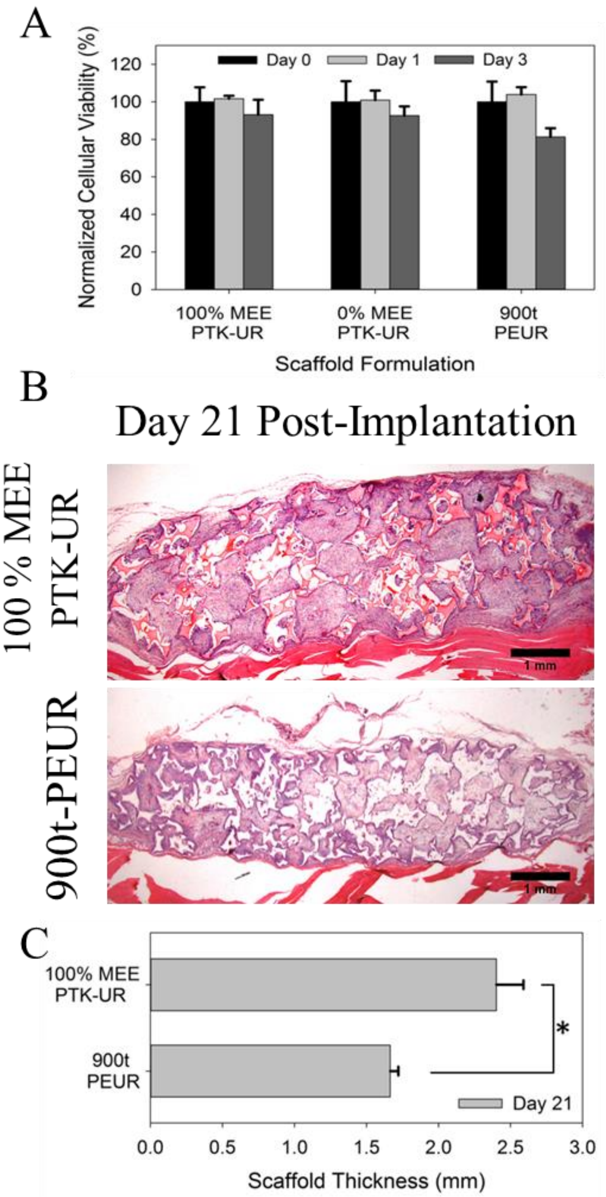

Figure 6.9. *In vitro* and *in vivo* biocompatibility of PTK-UR scaffolds. (A) *In vitro* biocompatibility of porous 3D PTK-UR scaffolds. (B) *In vivo* cellular infiltration into PTK-UR and control PEUR scaffolds 21 d post-implantation in Sprague-Dawley rats. The PTK-UR polymer is stained orange while the PEUR is unstained and appears white. (C) Wound thickness of PTK-UR vs. PEUR scaffolds. The PTK-UR scaffolds better maintain their mechanical integrity and provide a stenting effect relative to the PEUR scaffolds.

Discussion

Most currently utilized tissue engineering scaffolds feature hydrolytically degradable ester bonds which non-specifically break down in the presence of water. Cleavage of ester bonds produces free carboxylic acids which can acidify the local environment and cause autocatalytic degradation of the polyester-based material[12], leading to reduced tissue regeneration[14]. Here, a novel PTK-based scaffold technology is presented that is specifically degraded by cell-generated ROS while remaining insensitive to hydrolysis[23b]. Because these PTK-UR materials selectively degrade by cell-mediated activity, they avoid autocatalytic degradation and are predicted to yield better matched rates of cellular infiltration and scaffold degradation. To this end, PTK copolymers were successfully synthesized with varying chain compositions but similar M_n and PDI values. The resulting dithiol-terminated MEE-PTK polymers were converted into diols to generate telechelic end groups compatible with standard polyurethane synthesis and to provide PTK polyols amenable to direct comparison with polyesters used in PEUR scaffold formation.

The PTK-UR scaffolds were fabricated using HDIt and compared to PEUR scaffolds made from 900t, 1000d, and 1500t polyester-based PEUR scaffolds. While the 900t-PEUR represented a biological control that has been successfully used for *in vivo* applications[9b, 29], the 1000d-PEUR and 1500t-PEUR were synthesized for a more direct material comparison to the PTK-URs since they yield PEUR scaffolds with similar crosslink densities to the PTK-UR scaffolds. The PTK-UR scaffolds produced from the PTK macrodiols were approximately 90% porous and were morphologically similar to more conventional PEUR 3D porous scaffolds. This level of porosity is optimal for promoting cellular in-growth, nutrient exchange, and neo-vascularization in tissue engineering applications[30]. The PTK-URs also featured relatively low sol fraction values, indicating that the isocyanates and diols were well matched and efficiently reacted during scaffold formation. As expected, the scaffolds' relative hydrophilicity was influenced by the composition of the PTK polyol, and the contact angle was inversely correlated with the mol% of the more hydrophilic MEE monomer in the PTK copolymer. These data suggest that the 100% MEE-PTK-UR and the 66° contact angle may be optimal for cellular adhesion and tissue formation *in vivo* because relatively hydrophobic surfaces with contact angles > 76° (such as the 50% and 0% MEE-PTK-UR formulations) preferentially adsorb hydrophobic serum proteins such as albumin over cellular adhesion proteins like fibronectin and vitronectin[31].

Thermal analysis of PTK-UR and PEUR scaffolds, along with their polymeric precursors, indicated that the scaffolds are phase-mixed materials since the 3D materials all possessed a T_g exceeding that of the polyol precursor soft segment[9a]. The scaffold T_g values determined by DMA also exceeded those measured by DSC by 30 – 50°C, as has been previously reported for similar 3D polyurethane materials[6a]. Wet compression testing of these materials indicated that although the 1500t-PEUR, 1000d-PEUR, and PTK-UR scaffolds had similar M_c values, all of the PTK-UR formulations had significantly higher modulus values than the 1500t-PEUR and 1000d-PEUR materials. However, there was no consistent trend between PTK-UR scaffold composition and modulus. Due to its higher crosslink density, the 900t-PEUR achieved stiffness values closer to the PTK-UR samples, though even this formulation was significantly less stiff than the 100% and 0% MEE-PTK-UR materials. Because of the more closely matched mechanical properties and the established precedent for their use[6a, 9b], the 900t-PEUR scaffolds were used as a control for comparison to PTK-UR scaffolds in subsequent *in vitro* and *in vivo* studies.

The PTK-UR scaffolds were formulated with HDIt because it is stable relative to other isocyanates[8, 9b, 29a], allowing more specific study of the degradation behavior of the polyol component. Degradation of PTK-UR and 900t-PEUR scaffolds was tested in an oxidative degradation medium comprising H_2O_2 and $CoCl_2$ that produces hydroxyl radicals [28a]. These radicals destabilize the thioketal bond, leading to chain scission and breakdown into the original constitutive monomers (MEE and BDT) and acetone. It is predicted that these small byproducts will be rapidly cleared in an *in vivo* environment. Furthermore, these thiolated monomers have been shown to cause limited *in vitro* cytotoxicity[32] and a minimal host inflammatory response *in vivo*[33] when incorporated into a similar polyurethane system.

The long-term stability of PTK-UR scaffolds over 25 weeks in PBS is significantly different than these materials' rapid degradation under accelerated oxidative conditions as seen in, highlighting the ROS-specific degradation mechanism of the PTK-UR scaffolds. Furthermore, there was a relationship between the PTK composition and degradation rate, as the scaffolds with higher MEE content in the PTK polyol degraded faster. It has been previously reported that ethers are stable in aqueous media but that oxidative radicals can degrade them *in vitro* and *in vivo*[28a]. Thus, it is hypothesized that the faster ROS-dependent degradation seen in both the 100% and 50% MEE-PTK-UR materials may result from a combination of oxidative degradation of both thioketals and ethers, while the 0% MEE-PTK-UR scaffolds are degraded solely by thioketal scission.

These results indicate that ROS-dependent scaffold degradation rates can be tuned by the composition of the PTK polyol.

For all PTK-UR compositions tested, the degradation rate was dependent on ROS concentrations. This dose-dependent relationship between ROS levels and degradation rate coupled with the agreement between the model and experimental data confirm that the PTK-UR scaffolds degrade by first-order kinetics with respect to ROS concentration. The degradation rate constants derived from the non-linear regression fitting of the experimental data gathered in 20% H_2O_2 media also illustrate the relationship between degradation rate and the %MEE-PTK polyol used in PTK-UR scaffold fabrication, though this trend was decreased under lower H_2O_2 concentrations. In contrast, the 900t-PEUR samples incubated in these same oxidative media did not display H_2O_2 dose-dependent degradation, highlighting the unique degradation mechanism of the PTK-UR relative to PEUR scaffolds. These collective data confirm that PTK-based polyols are selectively cleaved by ROS and that their rate of degradation is first-order with respect to the concentration of radical species in the local environment.

PTK-UR scaffolds were shown to display a high level of *in vitro* cytocompatibility with both RAW 267.4 macrophages and NIH 3T3 fibroblasts. Seeded macrophages were treated with either control culture media or media containing LPS and IFN-γ to activate the macrophages through the classical pathway[34], which is known to lead to ROS production[9b, 24]. Scaffolds with activated macrophages displayed enhanced surface pitting while cell-mediated remodeling of the scaffold surface was less evident for the control cells, indicating that the PTK-UR scaffolds were degraded by physiologically-relevant concentrations of ROS. Further highlighting these materials’ cytocompatibility, luciferase-expressing fibroblasts seeded on PTK-UR and PEUR scaffolds steadily maintained their bioluminescent signal over the culture period, similar to viability profiles seen in other biocompatible 3D scaffolds[35]. Similar cell lines stably transduced to express luciferase have been previously used to reliably measure *in vitro* cellular viability, as their constitutive luciferase activity directly correlates with cell number[16a]. Furthermore, none of the scaffold formulations displayed a significant difference in bioluminescence over time or relative to each other, indicating that PTK-UR scaffolds possessed biocompatibility levels analogous to PEUR scaffolds that are cytocompatible and have been successfully utilized *in vivo*[9b]

This *in vivo* cytocompatibility was confirmed by histological analysis of subcutaneous implants, which showed that neither the 100% nor 0% MEE-PTK-UR formulations elicited an inflammatory response from the native tissue that was obviously different from the conventional PEUR scaffolds. However, the 0% MEE-PTK-UR scaffolds supported less robust tissue infiltration into the scaffold interior relative to the 100% MEE-PTK-UR or 900t-PEUR scaffolds. On possible explanation for this result is that the relative hydrophobicity of the 0% MEE-PTK-UR scaffolds (80° contact angle) did not allow cells to properly adhere and migrate into the scaffold interior. As such, only the 100% MEE-PTK-UR and 900t-PEUR histology samples were quantitatively analyzed. Both these formulations supported new tissue growth into the scaffold interior 3 weeks after implantation and displayed significant biodegradation over 7 weeks. The 900t-PEURs experienced a steep increase in degradation after 3 weeks as expected from previous work with these materials[9b], while the 100% MEE-PTK-UR scaffolds displayed gradual, first-order degradation over time. This confirms the initial hypothesis that PTK-

UR scaffolds degrade in a more controlled, cell-mediated mechanism than more conventional PEUR materials which have been recently shown to undergo to autocatalytic degradation *in vivo* resulting in a reduced wound healing response[14]. Furthermore, the PTK-UR samples were more mechanically resilient and more effectively stented subcutaneous pockets. Though all scaffolds possessed 90% porosity and were cut to the same thickness pre-implantation, the PEUR materials were significantly more compressed than the PTK-UR scaffolds at all time points. This *in vivo* compression of PEUR scaffolds can be potentially attributed to both the significantly higher modulus of the 100% MEE-PTK-UR samples relative to the 900t-PEUR formulation, and also to the 900t-PEUR T_g value (34.4 °C) which is close to body temperature. This relatively high T_g is predicted to make this PEUR scaffold less mechanically resilient at body temperature because it will be in its glassy transition viscoelastic region. The stenting effect seen in these PTK-UR scaffolds is advantageous because it ensures that the scaffold pores remain open, maximizing cell infiltration and new tissue formation and potentially decreasing scarring in clinical applications.

Conclusion

ROS are key mediators of cell function in both health and disease, especially at sites of inflammation and tissue healing. Utilizing these cell-generated species as triggers for selective polymer degradation represents a promising methodology for creating a tissue engineering scaffolds with well-matched rates of tissue in-growth and cell-mediated scaffold degradation. Here, novel poly(thioketal) polymers featuring tunable reactive end-chemistries, chain compositions, and ROS-mediated degradation rates have been developed towards this end. These PTK polymers were successfully incorporated into 3D porous tissue engineering scaffolds with more robust mechanical properties than similar constructs fabricated from standard polyesters. These PTK-UR scaffolds were selectively degraded by ROS but were stable under aqueous conditions, indicating that their biodegradation would be exclusively cell-mediated, as opposed to PEURs that hydrolytically degrade independent of cellular activity. Moreover, the oxidative degradation rates of the PTK-URs followed first-order degradation kinetics and displayed dose-dependent degradation with respect to ROS levels. PTK scaffolds exhibited cytocompatibility *in vitro* and were shown to be degraded by activated, ROS-secreting macrophages. The PTK-UR scaffolds also supported cell infiltration and granulation tissue formation *in vivo,* and their superior mechanical properties lead to significantly greater stenting of subcutaneous “wounds” compared to more standard PEUR scaffolds. Furthermore, the PTK-URs experienced controlled first-order *in vivo* biodegradation in contrast to the PEUR scaffolds which experienced dramatic increases in degradation at later time points. These collective data indicate that PTK-URs represent a useful new class of biomaterials that provide a robust, cell-degradable substrate for guiding new tissue formation.

Additionally, the simple synthesis chemistry for PTKs allows for a large level of customization. Nearly any low molecular weight thiol should be able to be utilized as a starting material, including low molecular weight, thiol functionalized peptides. These peptides can be specifically designed to impart enzymatic functionality to the degradation of the resulting polymer. More information regarding the potential uses of enzymatically degradable PTK materials can be found in Chapter VIII.

References

CHAPTER VII

CONCLUSIONS

The culmination of this dissertation is a roadmap for a three pronged approach to analyze and treat cancer induced bone disease. The studies conducted in the previous chapters outline the foundational work to the generation of an ambitious combination of degradable polyurethane graft systems with anti-cancer releasing nano-particles for treatment of metastatic bone disease and regeneration of healthy tissue.

Chapter III discusses the use of a polyurethane film with tunable rigidity for studying metastatic cancers in bone *in vitro*[36]. Specifically, the 2D polyurethane film culture system can accurately match the rigidity associated with soft and hard tissues in the body. This allows for advanced investigation into the effects that rigidity has on the underlying molecular causes of cancers that metastasize to bone. The primary analysis showed that osteolytic gene expression and integrin expression is upregulated on films that have bone like mechanical properties. Previous studies utilizing the polyurethane cell culture system pointed to Rho associated kinase (ROCK), as a main target for potential therapeutic targets[37], but when we inhibited ROCK in tumor cells and implanted the cells intratibially in mice, osteolysis was not reduced. We looked to another cell mechanism known to be highly relevant in carcinogenesis, the epithelial to mesenchymal (EMT) pathway[38], for inspiration into the possible underlying causes of rigidity induced changes in tumor cells. It was found that associations between the TGF-β signaling pathway and integrin $\alpha_v\beta_3$ were stimulated on rigid materials by a novel FRET study. The associations caused upregulation of osteolytic factors that could be inhibited by targeting the activation of integrins. While integrins have long been associated with increased metastatic potential[39], this is one of the first times that integrins have been associated with increased osteolysis after tumor establishment in the bone microenvironment. Inhibition of integrins with a tumor cell line stably transfected against producing integrin β_3 limited ostelysis upon intratibial implantation *in vivo*. The elucidation of an underlying mechanism of solid state signaling (integrins) cross-talking with soluble receptor (TGF-β) signaling pathways allows for therapeutic targeting of the full range of both signaling cascades.

With the potential molecular targets identified, compounds that are known to inhibit various sections of the signaling cascade were identified. These drugs are commonly hydrophobic small molecules with limited solubility in aqueous environments. The known limitations of traditional drug delivery methods, poor solubility, pharmacokinetics and intracellular uptake, have resulted in the need for novel delivery systems that can be tailored for specific applications. One of the methods to overcome these challenges is with cationic polymers that utilize pH responsive protonation to release therapeutics into the cytoplasm of cells. However, many cationic polymers are also cytotoxic due to the membrane disruptive potential of the charged species. Chapter IV describes the development of a library of self-assembling polymers micelles with pH responsive drug release and hydrolytic degradation for encapsulation and release of hydrophobic small molecule drugs[40]. Twelve polymers were synthesized via reversible-addition fragmentation chain-transfer (RAFT) polymerization with a poly(ethylene glycol) (PEG) corona and a cationic and hydrophobic core. The cationic monomers were either non-degradable or degradable branches that would hydrolyze over time. While many of the polymers appeared to be non-cytotoxic and resulted in encapsulation and release of a model hydrophobic drug, the 60% diethylamino ethyl acrylate (DEAEA) polymer seemed to provide the most pH responsive release and was selected as the most promising candidate for future analysis. Similar polymers have been combined with polyurethane materials developed in our lab to generate nanoparticle releasing combination grafts[41]. The 60% DEAEA polymer is currently undergoing testing to release hydrophobic drugs from polyurethane grafts.

Our lab has a long history of utilizing lysine derived isocyanates for the synthesis of non-toxic, degradable polyurethane materials for tissue engineering[10, 29a, 42], however, there were no mechanistic studies into the reaction kinetics of the complex reactive mixtures. Chapter V describes the detailed study of lysine based injectable, degradable polyurethane bone grafts[29b]. A novel *in situ* technique to analyze the individual reaction kinetics of each component of the grafts was developed using attenuated-total reflectance infrared spectroscopy. Interestingly, the amine catalyst utilized for a majority of the materials developed in our lab was found to preferentially catalyze the reaction of isocyanates and water. This is contradictory to the industrial uses for amine based catalysts and most likely is due to the unique structure of the lysine based isocyanates. From the bulk kinetic data a model of the reacting material could be attained. This model predicted conversion percentage of each component. The predictions were matched with leached materials during various stages of curing. The materials found via NMR analysis of the leachates correlated with the components that showed the lowest percentage of conversion. These major components of the leached materials were the polyester polyol and dipropylene glycol (the carrier for the amine catalyst), both of which are non-cytotoxic. The overall results of this study were the development of an *in situ* monitoring system for reactive polyurethane materials that allowed for a detailed understanding of a complex kinetic phenomenon.

The polyurethane biomaterials developed previously in our lab have primarily focused on the use of a polyester polyol hardener. The polyesters are hydrolytically degradable and it has been shown that the degradation mechanism is autocatalytic[12, 43]. This autocatalytic degradation can result in a resorption gap between the regeneration of new tissue and residual graft material[42b]. Chapter VI describes the synthesis and characterization of poly(thioketals) (PTKs) a novel cell degradable chemistry[44]. PTKs were found to be highly sensitive to reactive oxygen species and resulted in near first order degradation kinetics. The PTK based polyurethane materials outperformed similar polyesters based polyurethanes in terms of mechanical strength and thermal properties. The 100% mercapto ethyl ether (MEE) PTK was the most biocompatible, showing the least cytotoxicity *in vitro* and similar cell infiltration compared to the polyester polyurethanes *in vivo*. PTKs represent a viable alternative to polyester based polyurethanes and shift the focus of future grafts to more cell responsive materials. The simple chemistry also opens possibilities of highly specific degradation mechanisms by the addition of enzymatic sensitivity.

References

1. (a) Whang, K.; Thomas, C. H.; Healy, K. E.; Nuber, G., A novel method to fabricate bioabsorbable scaffolds. *Polymer* **1995,** *36* (4), 837-842; (b) Ishaug-Riley, S. L.; Crane-Kruger, G. M.; Yaszemski, M. J.; Mikos, A. G., Three-dimensional culture of rat calvarial osteoblasts in porous biodegradable polymers. *Biomaterials* **1998,** *19* (15), 1405-1412.
2. (a) Lowry, K. J.; Hamson, K. R.; Bear, L.; Peng, Y. B.; Calaluce, R.; Evans, M. L.; Anglen, J. O.; Allen, W. C., Polycaprolactone/glass bioabsorbable implant in a rabbit humerus fracture model. *Journal of Biomedical Materials Research* **1997,** *36* (4), 536-541; (b) Ciapetti, G.; Ambrosio, L.; Savarino, L.; Granchi, D.; Cenni, E.; Baldini, N.; Pagani, S.; Guizzardi, S.; Causa, F.; Giunti, A., Osteoblast growth and function in porous poly ε-caprolactone matrices for bone repair: a preliminary study. *Biomaterials* **2003,** *24* (21), 3815-3824.
3. (a) Leong, K. W.; Simonte, V.; Langer, R. S., Synthesis of polyanhydrides: melt-polycondensation, dehydrochlorination, and dehydrative coupling. *Macromolecules* **1987,** *20* (4), 705-712; (b) Ibim, S. E. M.; Uhrich, K. E.; Attawia, M.; Shastri, V. R.; El-Amin, S. F.; Bronson, R.; Langer, R.; Laurencin, C. T., Preliminary in vivo report on the osteocompatibility of poly(anhydride-co-imides) evaluated in a tibial model. *Journal of Biomedical Materials Research* **1998,** *43* (4), 374-379.
4. (a) Nilsson, A.; Liljensten, E.; Bergström, C.; Sollerman, C., Results from a degradable TMC joint Spacer (Artelon) compared with tendon arthroplasty. *The Journal of Hand Surgery* **2005,** *30* (2), 380-389; (b) Gogolewski, S.; Gorna, K.; Turner, A. S., Regeneration of bicortical defects in the iliac crest of estrogen-deficient sheep, using new biodegradable polyurethane bone graft substitutes. *Journal of Biomedical Materials Research Part A* **2006,** *77A* (4), 802-810.
5. (a) Lü, J.-M.; Wang, X.; Marin-Muller, C.; Wang, H.; Lin, P. H.; Yao, Q.; Chen, C., Current advances in research and clinical applications of PLGA-based nanotechnology. *Expert Review of Molecular Diagnostics* **2009,** *9* (4), 325-341; (b) Bezwada, R. S.; Jamiolkowski, D. D.; Lee, I.-Y.; Agarwal, V.; Persivale, J.; Trenka-Benthin, S.; Erneta, M.; Suryadevara, J.; Yang, A.; Liu, S., Monocryl® suture, a new ultra-pliable absorbable monofilament suture. *Biomaterials* **1995,** *16* (15), 1141-1148; (c) Dang, W.; Daviau, T.; Brem, H., Morphological Characterization of Polyanhydride Biodegradable Implant Gliadel® During in Vitro and in Vivo Erosion Using Scanning Electron Microscopy. *Pharm Res* **1996,** *13* (5), 683-691; (d) Chen, J.; Xu, J.; Wang, A.; Zheng, M., Scaffolds for tendon and ligament repair: review of the efficacy of commercial products. *Expert Review of Medical Devices* **2009,** *6* (1), 61-73.
6. (a) Hafeman, A. E.; Li, B.; Yoshii, T.; Zienkiewicz, K.; Davidson, J. M.; Guelcher, S. A., Injectable biodegradable polyurethane scaffolds with release of platelet-derived growth factor for tissue repair and regeneration. *Pharm. Res.* **2008,** *25* (10), 2387-2399; (b) Ignatius, A. A.; Claes, L. E., In vitro biocompatibility of bioresorbable polymers: poly(L, DL-lactide) and poly(L-lactide-co-glycolide). *Biomaterials* **1996,** *17* (8), 831-839.
7. (a) Hua, N.; Sun, J., Body distribution of poly(d,l-lactide-co-glycolide) copolymer degradation products in rats. *J Mater Sci: Mater Med* **2008,** *19* (10), 3243-3248; (b) Visscher, G. E.; Robison, R. L.; Maulding, H. V.; Fong, J. W.; Pearson, J. E.; Argentieri,

G. J., Biodegradation of and tissue reaction to 50:50 poly(DL-lactide-co-glycolide) microcapsules. *Journal of Biomedical Materials Research* **1985,** *19* (3), 349-365.

8. Guelcher, S. A., Biodegradable Polyurethanes: Synthesis and Applications in Regenerative Medicine. *Tissue Engineering: Part B* **2008,** *14* (1), 3-17.

9. (a) Guelcher, S. A.; Srinivasan, A.; Hafeman, A.; Gallagher, K. M.; Doctor, J. S.; Khetan, S.; McBride, S.; Hollinger, J. O., Synthesis, In Vitro Degradation, and Mechanical Properties of Two-Component Poly(Ester Urethane)Urea Scaffolds: Effects of Water and Polyol Composition *Tissue Engineering* **2007,** *13* (9), 2321-2333; (b) Hafeman, A. E.; Zienkiewicz, K. J.; Zachman, A. L.; Sung, H.-J.; Nanney, L. B.; Davidson, J. M.; Guelcher, S. A., Characterization of the degradation mechanisms of lysine-derived aliphatic poly(ester urethane) scaffolds. *Biomaterials* **2011,** *32* (2), 419-429.

10. Dumas, J. E.; BrownBaer, P. B.; Prieto, E. M.; Guda, T.; Hale, R. G.; Wenke, J. C.; Guelcher, S. A., Injectable reactive biocomposites for bone healing in critical-size rabbit calvarial defects. *Biomedical Materials* **2012,** *7* (2), 024112.

11. (a) Fu, K.; Pack, D. W.; Klibanov, A. M.; Langer, R., Visual Evidence of Acidic Environment Within Degrading Poly(lactic-co-glycolic acid) (PLGA) Microspheres. *Pharm Res* **2000,** *17* (1), 100-106; (b) Lu, L.; Peter, S. J.; D. Lyman, M.; Lai, H.-L.; Leite, S. M.; Tamada, J. A.; Uyama, S.; Vacanti, J. P.; Langer, R. S.; Mikos, A. G., In vitro and in vivo degradation of porous poly(dl-lactic-co-glycolic acid) foams. *Biomaterials* **2000,** *21* (18), 1837-1845.

12. Antheunis, H.; van der Meer, J.-C.; de Geus, M.; Heise, A.; Koning, C. E., Autocatalytic Equation Describing the Change in Molecular Weight during Hydrolytic Degradation of Aliphatic Polyesters. *Biomacromolecules* **2010,** *11* (4), 1118-1124.

13. An, Y. H.; Woolf, S. K.; Friedman, R. J., Pre-clinical in vivo evaluation of orthopaedic bioabsorbable devices. *Biomaterials* **2000,** *21* (24), 2635-2652.

14. Dumas, J. E.; Prieto, E. M.; Zienkiewicz, K. J.; Guda, T.; Wenke, J. C.; Bible, J. E.; Holt, G. E.; Guelcher, S. A., Balancing the Rates of New Bone formation and Polymer Degradation Enhances Healing of Weight-Bearing Allograft/Polyurethane Composites in Rabbit Femoral Defects. *Tissue Engineering Part A* **2013**.

15. Roy, D.; Cambre, J. N.; Sumerlin, B. S., Future perspectives and recent advances in stimuli-responsive materials. *Progress in Polymer Science* **2010,** *35* (1–2), 278-301.

16. (a) Li, H.; Yu, S. S.; Miteva, M.; Nelson, C. E.; Werfel, T.; Giorgio, T. D.; Duvall, C. L., Matrix Metalloproteinase Responsive, Proximity-Activated Polymeric Nanoparticles for siRNA Delivery. *Advanced Functional Materials* **2013,** *23* (24), 3040-3052; (b) Ku, T.-H.; Chien, M.-P.; Thompson, M. P.; Sinkovits, R. S.; Olson, N. H.; Baker, T. S.; Gianneschi, N. C., Controlling and Switching the Morphology of Micellar Nanoparticles with Enzymes. *Journal of the American Chemical Society* **2011,** *133* (22), 8392-8395.

17. (a) West, J. L.; Hubbell, J. A., Polymeric Biomaterials with Degradation Sites for Proteases Involved in Cell Migration. *Macromolecules* **1998,** *32* (1), 241-244; (b) Lutolf, M. P.; Weber, F. E.; Schmoekel, H. G.; Schense, J. C.; Kohler, T.; Muller, R.; Hubbell, J. A., Repair of bone defects using synthetic mimetics of collagenous extracellular matrices. *Nat Biotech* **2003,** *21* (5), 513-518.

18. (a) Dey, J.; Xu, H.; Shen, J.; Thevenot, P.; Gondi, S. R.; Nguyen, K. T.; Sumerlin, B. S.; Tang, L.; Yang, J., Development of biodegradable crosslinked urethane-doped

polyester elastomers. *Biomaterials* **2008,** *29* (35), 4637-4649; (b) Stakleff, K. S.; Lin, F.; Smith Callahan, L. A.; Wade, M. B.; Esterle, A.; Miller, J.; Graham, M.; Becker, M. L., Resorbable, amino acid-based poly(ester urea)s crosslinked with osteogenic growth peptide with enhanced mechanical properties and bioactivity. *Acta Biomaterialia* **2013,** *9* (2), 5132-5142.

19. Hensley, K.; Robinson, K. A.; Gabbita, S. P.; Salsman, S.; Floyd, R. A., Reactive oxygen species, cell signaling, and cell injury. *Free Radical Biology and Medicine* **2000,** *28* (10), 1456-1462.

20. Pacher, P.; Beckman, J. S.; Liaudet, L., Nitric Oxide and Peroxynitrite in Health and Disease. *Physiological Reviews* **2007,** *87* (1), 315-424.

21. Liu, W. F.; Ma, M.; Bratlie, K. M.; Dang, T. T.; Langer, R.; Anderson, D. G., Real-time in vivo detection of biomaterial-induced reactive oxygen species. *Biomaterials* **2011,** *32* (7), 1796-1801.

22. Halleen, J. M.; Räisänen, S.; Salo, J. J.; Reddy, S. V.; Roodman, G. D.; Hentunen, T. A.; Lehenkari, P. P.; Kaija, H.; Vihko, P.; Väänänen, H. K., Intracellular fragmentation of bone resorption products by reactive oxygen species generated by osteoclastic tartrate-resistant acid phosphatase. *Journal of Biological Chemistry* **1999,** *274* (33), 22907-22910.

23. (a) Napoli, A.; Valentini, M.; Tirelli, N.; Muller, M.; Hubbell, J. A., Oxidation-responsive polymeric vesicles. *Nat Mater* **2004,** *3* (3), 183-189; (b) Wilson, D. S.; Dalmasso, G.; Wang, L.; Sitaraman, S. V.; Merlin, D.; Murthy, N., Orally delivered thioketal nanoparticles loaded with TNF-α–siRNA target inflammation and inhibit gene expression in the intestines. *Nat Mater* **2010,** *9* (11), 923-928; (c) de Gracia Lux, C.; Joshi-Barr, S.; Nguyen, T.; Mahmoud, E.; Schopf, E.; Fomina, N.; Almutairi, A., Biocompatible Polymeric Nanoparticles Degrade and Release Cargo in Response to Biologically Relevant Levels of Hydrogen Peroxide. *Journal of the American Chemical Society* **2012,** *134* (38), 15758-15764; (d) Gupta, M. K.; Meyer, T. A.; Nelson, C. E.; Duvall, C. L., Poly(PS-b-DMA) micelles for reactive oxygen species triggered drug release. *J. Control. Release* **2012,** *162* (3), 591-598; (e) Broaders, K. E.; Grandhe, S.; Fréchet, J. M. J., A Biocompatible Oxidation-Triggered Carrier Polymer with Potential in Therapeutics. *Journal of the American Chemical Society* **2010,** *133* (4), 756-758; (f) Shim, M. S.; Xia, Y., A Reactive Oxygen Species (ROS)-Responsive Polymer for Safe, Efficient, and Targeted Gene Delivery in Cancer Cells. *Angewandte Chemie International Edition* **2013,** *52* (27), 6926-6929.

24. Yu, S. S.; Koblin, R. L.; Zachman, A. L.; Perrien, D. S.; Hofmeister, L. H.; Giorgio, T. D.; Sung, H.-J., Physiologically Relevant Oxidative Degradation of Oligo(proline) Cross-Linked Polymeric Scaffolds. *Biomacromolecules* **2011,** *12* (12), 4357-4366.

25. Salvatore, R. N.; Smith, R. A.; Nischwitz, A. K.; Gavin, T., A mild and highly convenient chemoselective alkylation of thiols using Cs2CO3–TBAI. *Tetrahedron Letters* **2005,** *46* (51), 8931-8935.

26. ASTM-International, E1899 - 08. Standard Test Method for Hydroxyl Groups Using Reaction with p-Toluenesulfonyl Isocyanate (TSI) and Potentiometric Titration with Tetrabutylammonium Hydroxide. 2008.

27. Pike, J. K.; Ho, T.; Wynne, K. J., Water-Induced Surface Rearrangements of Poly(dimethylsiloxane−urea−urethane) Segmented Block Copolymers. *Chemistry of Materials* **1996,** *8* (4), 856-860.

28. (a) Schubert, M. A.; Wiggins, M. J.; Anderson, J. M.; Hiltner, A., Role of oxygen in biodegradation of poly(etherurethane urea) elastomers. *Journal of Biomedical Materials Research* **1997,** *34* (4), 519-530; (b) Christenson, E. M.; Anderson, J. M.; Hiltner, A., Oxidative mechanisms of poly(carbonate urethane) and poly(ether urethane) biodegradation: In vivo and in vitro correlations. *Journal of Biomedical Materials Research Part A* **2004,** *70A* (2), 245-255.

29. (a) Adolph, E. J.; Hafeman, A. E.; Davidson, J. M.; Nanney, L. B.; Guelcher, S. A., Injectable polyurethane composite scaffolds delay wound contraction and support cellular infiltration and remodeling in rat excisional wounds. *Journal of Biomedical Materials Research Part A* **2012,** *100A* (2), 450-461; (b) Page, J. M.; Prieto, E. M.; Dumas, J. E.; Zienkiewicz, K. J.; Wenke, J. C.; Brown-Baer, P.; Guelcher, S. A., Biocompatibility and chemical reaction kinetics of injectable, settable polyurethane/allograft bone biocomposites. *Acta Biomaterialia* **2012,** *8* (12), 4405-4416.

30. (a) Hu, Y.; Grainger, D. W.; Winn, S. R.; Hollinger, J. O., Fabrication of poly(α-hydroxy acid) foam scaffolds using multiple solvent systems. *Journal of Biomedical Materials Research* **2002,** *59* (3), 563-572; (b) Karageorgiou, V.; Kaplan, D., Porosity of 3D biomaterial scaffolds and osteogenesis. *Biomaterials* **2005,** *26* (27), 5474-5491; (c) Mikos, A. G.; Temenoff, J. S., Formation of highly porous biodegradable scaffolds for tissue engineering. *Electronic Journal of Biotechnology* **2000,** *3* (2), 114-119.

31. (a) Harbers, G. M.; Grainger, D. W., Cell-Material Interactions: Fundamental Design Issues for Tissue Engineering and Clinical Considerations. In *An Introduction to Biomaterials*, Guelcher, S. A.; Hollinger, J. O., Eds. CRC Press, Taylor & Francic Group: 2006; (b) Arima, Y.; Iwata, H., Effect of wettability and surface functional groups on protein adsorption and cell adhesion using well-defined mixed self-assembled monolayers. *Biomaterials* **2007,** *28* (20), 3074-3082.

32. Eglin, D.; Griffon, S.; Alini, M., Thiol-Containing Degradable Poly(thiourethane-urethane)s for Tissue Engineering. *Journal of Biomaterials Science, Polymer Edition* **2010,** *21* (4), 477-491.

33. Laschke, M. W.; Strohe, A.; Scheuer, C.; Eglin, D.; Verrier, S.; Alini, M.; Pohlemann, T.; Menger, M. D., In vivo biocompatibility and vascularization of biodegradable porous polyurethane scaffolds for tissue engineering. *Acta Biomaterialia* **2009,** *5* (6), 1991-2001.

34. (a) Aste-Amezaga, M.; Ma, X.; Sartori, A.; Trinchieri, G., Molecular Mechanisms of the Induction of IL-12 and Its Inhibition by IL-10. *The Journal of Immunology* **1998,** *160* (12), 5936-5944; (b) Jayakumar, A.; Widenmaier, R.; Ma, X.; McDowell, M. A., Transcriptional Inhibition of Interleukin-12 Promoter Activity in Leishmania Spp.–Infected Macrophages. *Journal of Parasitology* **2008,** *94* (1), 84-93.

35. (a) Oh, S. H.; Ward, C. L.; Atala, A.; Yoo, J. J.; Harrison, B. S., Oxygen generating scaffolds for enhancing engineered tissue survival. *Biomaterials* **2009,** *30* (5), 757-762; (b) Rockwood, D. N.; Akins Jr, R. E.; Parrag, I. C.; Woodhouse, K. A.; Rabolt, J. F., Culture on electrospun polyurethane scaffolds decreases atrial natriuretic peptide expression by cardiomyocytes in vitro. *Biomaterials* **2008,** *29* (36), 4783-4791.

36. Page, J. M.; Merkel, A. R.; N.S., R.; Cannonier, S.; Dadwal, U.; Guelcher, S. A.; Sterling, J. A., Complexation of TGF-β Receptor Type II and β3 Integrins Facilitate Induction of Osteolytic Gene Expression in Highly Invasive Tumor Cells. *In Preparation.* **2014**.

37. Ruppender, N. S.; Merkel, A. R.; Martin, T. J.; Mundy, G. R.; Sterling, J. A.; Guelcher, S. A., Matrix Rigidity Induces Osteolytic Gene Expression of Metastatic Breast Cancer Cells. *Plos One* **2010,** *5* (11).

38. Huang, S.; Ingber, D. E., Cell tension, matrix mechanics, and cancer development. *Cancer cell* **2005,** *8* (3), 175-176.

39. Wong, N.; Mueller, B.; Barbas, C.; Ruminski, P.; Quaranta, V.; Lin, E. K.; Smith, J., αv Integrins mediate adhesion and migration of breast carcinoma cell lines. *Clin Exp Metastasis* **1998,** *16* (1), 50-61.

40. Page, J. M.; Evans, B. C.; Gupta, M. K.; Nelson, C. M.; Guelcher, S. A.; Duvall, C. L., Hydrophobic Drug Loading and Release from Micelles based on Hydrolytically Degradable, pH-Responsive Monomers. *In Preparation.* **2014**.

41. (a) Nelson, C. E.; Gupta, M. K.; Adolph, E. J.; Guelcher, S. A.; Duvall, C. L., siRNA Delivery from an Injectable Scaffold for Wound Therapy. *Advances in Wound Care* **2013,** *2* (3), 93-99; (b) Nelson, C. E.; Gupta, M. K.; Adolph, E. J.; Shannon, J. M.; Guelcher, S. A.; Duvall, C. L., Sustained local delivery of siRNA from an injectable scaffold. *Biomaterials* **2012,** *33* (4), 1154-1161.

42. (a) Dumas, J. E.; Davis, T.; Holt, G. E.; Yoshii, T.; Perrien, D. S.; Nyman, J. S.; Boyce, T.; Guelcher, S. A., Synthesis, characterization, and remodeling of weight-bearing allograft bone/polyurethane composites in the rabbit. *Acta Biomaterialia* **2010,** *6* (7), 2394-2406; (b) Dumas, J. E.; Prieto, E. M.; Zienkiewicz, K. J.; Guda, T.; Wenke, J. C.; Bible, J. E.; Holt, G. E.; Guelcher, S., Balancing the Rates of New Bone formation and Polymer Degradation Enhances Healing of Weight-Bearing Allograft/Polyurethane Composites in Rabbit Femoral Defects. *Tissue Engineering* **2013,** (ja); (c) Guelcher, S.; Srinivasan, A.; Hafeman, A.; Gallagher, K.; Doctor, J.; Khetan, S.; McBride, S.; Hollinger, J., Synthesis, In vitro degradation, and mechanical properties of two-component poly(ester urethane)urea scaffolds: Effects of water and polyol composition. *Tissue Engineering* **2007,** *13*, 2321-2333; (d) Guelcher, S. A.; Brown, K. V.; Li, B.; Guda, T.; Lee, B.-H.; Wenke, J. C., Dual-Purpose Bone Grafts Improve Healing and Reduce Infection. *Journal of Orthopaedic Trauma* **2011,** *25* (8), 477-482 10.1097/BOT.0b013e31821f624c; (e) Guelcher, S. A.; Gallagher, K. M.; Didier, J. E.; Klinedinst, D. B.; Doctor, J. S.; Goldstein, A. S.; Wilkes, G. L.; Beckman, E. J.; Hollinger, J. O., Synthesis of biocompatible segmented polyurethanes from aliphatic diisocyanates and diurea diol chain extenders. *Acta Biomaterialia* **2005,** *1* (4), 471-484; (f) Guelcher, S. A.; Patel, V.; Gallagher, K. M.; Connolly, S.; Didier, J. E.; Doctor, J. S.; Hollinger, J. O., Synthesis and in vitro biocompatibility of injectable polyurethane foam scaffolds. *Tissue Engineering* **2006,** *12* (5), 1247-1259; (g) Guelcher, S. A.; Srinivasan, A.; Dumas, J. E.; Didier, J. E.; McBride, S.; Hollinger, J. O., Synthesis, mechanical properties, biocompatibility, and biodegradation of polyurethane networks from lysine polyisocyanates. *Biomaterials* **2008,** *29* (12), 1762-1775; (h) Li, B.; Brown, K. V.; Wenke, J. C.; Guelcher, S. A., Sustained release of vancomycin from polyurethane scaffolds inhibits infection of bone wounds in a rat femoral segmental defect model. *J. Control. Release* **2010,** *145* (3), 221-230; (i) Li, B.; Davidson, J. M.; Guelcher, S. A., The

effect of the local delivery of platelet-derived growth factor from reactive two-component polyurethane scaffolds on the healing in rat skin excisional wounds. *Biomaterials* **2009,** *30* (20), 3486-3494; (j) Li, B.; Yoshii, T.; Hafeman, A. E.; Nyman, J. S.; Wenke, J. C.; Guelcher, S. A., The effects of rhBMP-2 released from biodegradable polyurethane/microsphere composite scaffolds on new bone formation in rat femora. *Biomaterials* **2009,** *30* (35), 6768-6779; (k) Hafeman, A.; Li, B.; Yoshii, T.; Zienkiewicz, K.; Davidson, J.; Guelcher, S., Injectable Biodegradable Polyurethane Scaffolds with Release of Platelet-derived Growth Factor for Tissue Repair and Regeneration. *Pharm. Res.* **2008,** *25* (10), 2387-2399; (l) Hafeman, A. E.; Li, B.; Davidson, J. M.; Guelcher, S. A., INJECTABLE, BIODEGRADABLE, POLYURETHANE SCAFFOLDS FOR TISSUE RESTORATION. *Wound Repair Regen.* **2009,** *17* (4), A68-A68; (m) Hafeman, A. E.; Zienkiewicz, K. J.; Carney, E.; Litzner, B.; Stratton, C.; Wenke, J. C.; Guelcher, S. A., Local delivery of tobramycin from injectable biodegradable polyurethane scaffolds. *Journal of Biomaterials Science, Polymer Edition* **2010,** *21* (1), 95-112; (n) Hafeman, A. E.; Zienkiewicz, K. J.; Zachman, A. L.; Sung, H. J.; Nanney, L. B.; Davidson, J. M.; Guelcher, S. A., Characterization of the degradation mechanisms of lysine-derived aliphatic poly(ester urethane) scaffolds. *Biomaterials* **2011,** *32* (2), 419-429.

43. Pitt, C. G.; Chasalow, F. I.; Hibionada, Y. M.; Klimas, D. M.; Schindler, A., Aliphatic polyesters. I. The degradation of poly(ϵ-caprolactone) in vivo. *Journal of Applied Polymer Science* **1981,** *26* (11), 3779-3787.

44. Martin, J. R.; Gupta, M. K.; Page, J. M.; Yu, F.; Davidson, J. M.; Guelcher, S. A.; Duvall, C. L., A porous tissue engineering scaffold selectively degraded by cell-generated reactive oxygen species. *Biomaterials* **2014,** *35* (12), 3766-3776.

CHAPTER VIII

SUGGESTIONS FOR FUTURE WORK

This dissertation addresses the usefulness of polyurethanes to both study and potentially treat cancer induced bone disease (CIBD). The main conclusions of this work have created many intriguing research questions. The following section discusses suggestions for future studies that will lead to advanced analysis of CIBD and therapeutic interventions for tumor induced bone destruction.

Three Dimensional (3D) Printed Bone-Mimetic Scaffolds for Bioreactor Studies

While the 2D films covered in Chapter III are a significant advancement to studying bone specific cell populations, the limitations of 2D culture are well known[1]. Traditional 2D cell culture has provided an untold amount of insight into the world of cell and molecular biology, however 3D cell culture has significant advantages. There is certainly no argument to the cost effectiveness and ease of use of 2D cell culture, but there are significant drawbacks that still have yet to be fully addressed. There are two main issues, which are abundantly clear, with typical 2D culture: (1) Physiological conditions *in vivo* are not 2D and (2) Cellular microenvironments cannot be mimicked with rigid polystyrene or glass. 2D cell culture forces cells to adapt and survive on substrates that are not native. The ultimate goal of *in vitro* culture systems should be to study cellular aspects in environments that can be closely translated to *in vivo* systems.

Researchers have been interested in analyzing cells in environments that better mimic physiological conditions for nearly three decades, though the task is not without challenges. The knowledge gained from 2D cultures seemed to overshadow the importance of utilizing 3D systems. However, research in the early 1980's started the rise of 3D culture techniques. Collagen gels and ECM components derived from mouse tumor cells (termed Matrigel) were utilized to study cells in a 3D environment[2]. Even after the development of these techniques some researchers felt that 3D culture was too expensive, difficult and unnecessary[3]. It was not widely accepted that 3D culture systems were able to discern very useful information until Weaver et al. showed the inherently different behavior of cancer cells in 3D cell culture[4]. In their culture system, cancerous breast cells grown in 3D culture matching normal breast tissue became quiescent and returned to a native epithelial phenotype , a result never seen in 2D[4]. Since this initial discovery, a large group of research has focused on developing materials that better match the native ECM environment. However, with most of these 3D cell culture systems the range of mechanical properties is only relevant for soft tissue applications. To date, there has been little work on 3D cell culture systems that mimic the rigidity of hard tissue.

Transitioning to 3D *in vitro* systems has generated a large number of significant findings that are more closely related to *in vivo* pathologies[5]. The 2D polyurethane (PUR) film system is generated by casting a reactive liquid. The polyurethane is simply cast into a well plate or mold. This technique can be directly translated to a 3D system if the proper mold is created. Preliminary studies on 3D-printed poly-l-lactic acid (PLA) molds were completed. The molds were printed as layers of fibers with a known fiber diameter (FD) and fiber spacing (FS). The liquid reactive PUR was then cast around the PLA molds and allowed to cure overnight at 60^{o} C. After curing the excess PUR is removed and the PLA is leached with the following solvents acetone:dichloromethane:acetone:ethanol over a period of three days. The PUR swells significantly in the dichlormethane wash, so care must be taken to immediately place in the secondary acetone wash to prevent cracking or crumbling of the scaffold. A diagram of the molding process and SEM images of a leached PUR mold are shown in Figure 7.1. The resulting PUR scaffold is 100% interconnected, due to the overlapping PLA fibers, and has a pore size that is equal to the FD.

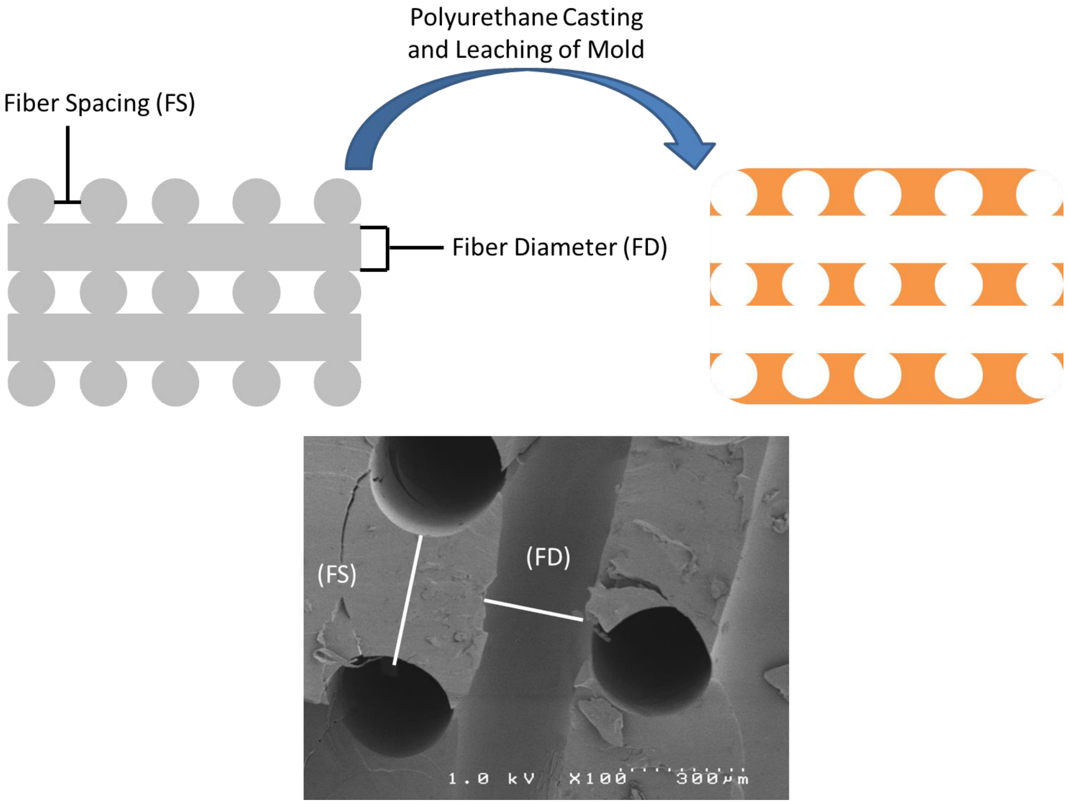

Figure 7.1. Schematic diagram of the generation of PUR 3D scaffolds.

The 3D-PUR scaffolds can be tuned to various rigidity just as the 2D PUR films. Cells can be directly seeding onto the scaffolds via capillary uptake of the cell suspension. Additionally, the surface area is much larger than traditional 2D culture systems so much larger populations of cells can be analyzed at one time. The mechanical properties of the 3D-PUR scaffolds were assessed by nanoindentation and compared to the 2D films (Table 7.1).

Table 7.1. Mechanical properties of 2D and 3D PUR materials obtained by nano-indentation.

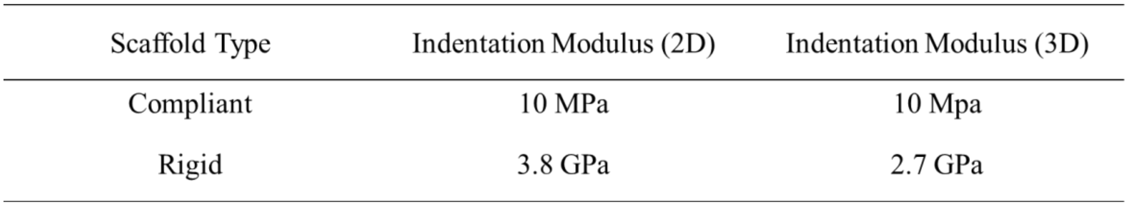

Scaffold Type	Indentation Modulus (2D)	Indentation Modulus (3D)
Compliant	10 MPa	10 Mpa
Rigid	3.8 GPa	2.7 GPa

Preliminary studies with cell seeding were conducted with 3D PUR scaffolds with a pore size of 300 μm. The scaffolds were coated overnight in a fibronectin solution to aid cell adhesion. Green fluorescent protein (GFP) transfected MDA-MB-231 cells were seeded into the 3D scaffolds and imaged with fluorescent and electron microscopy (Figure 7.2A-C). The cells attached readily and after 48 hours of static culture the cells were harvested with a modified TRIzol extraction method. Expression of PTHrP was conducted and found to match 2D experiments (Figure 7.2D).

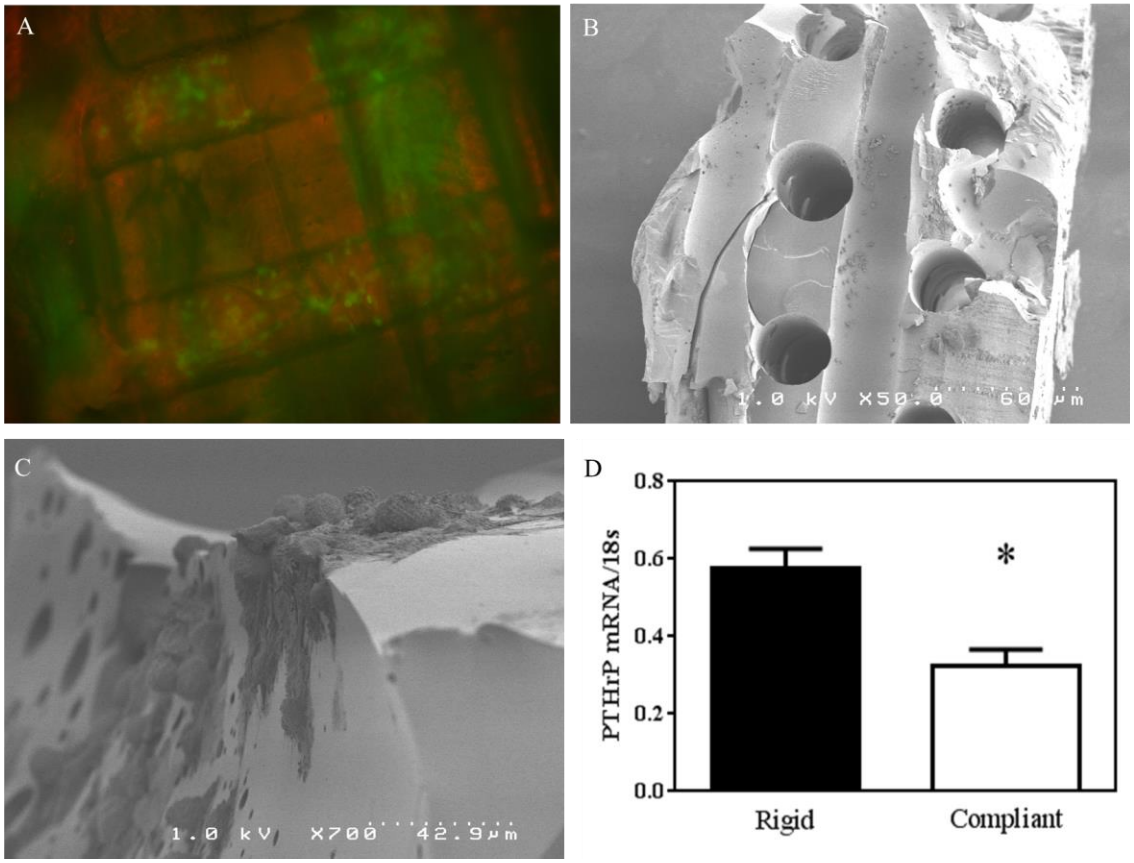

Figure 7.2. Attachment and gene expression of MDA-MB-231cells seeded within 3D PUR scaffolds. (A) Fluorescent microscopy of GFP labeled MDA-MB-231 cells; (B&C) Electron microscopy of MDA-MB-231 cells showing adhesion and morphology; (D) Expression of PTHrP on rigid and compliant 3D scaffolds.

A pilot *in vivo* experiment was conducted with MDA-MB-231 seeded 3D-PURS implanted subcutaneously in the backs of mice. Tumors were observed after 21 days by *in situ* fluorescence imaging, however in many scaffolds the tumors had died, possibly due to lack of nutrients after implantation. The 3D-PURS that expressed tumors were excised, imaged fluorescently, shown in Figure 7.3A, and RNA was harvested from the scaffold using TRIzol. Quantitative PCR data showed a larger difference, Figure 7.3B, in PTHrP expression between soft and rigid scaffolds with 300 µm pores. Furthermore, both soft and rigid scaffolds with 500 µm pores had significantly lower expression of

PTHrP than the rigid 300 µm scaffolds. The changes in PTHrP expression with differences in rigidity and pore size point to an active response to environmental cues by osteolytic cancer cells. This model is ideal for studies of the microenvironmental effects on tumor cells. Specifically, this model will allow for molecular signaling studies and testing of potential inhibitors of the mechanotransduction pathway that can be clinically translated.

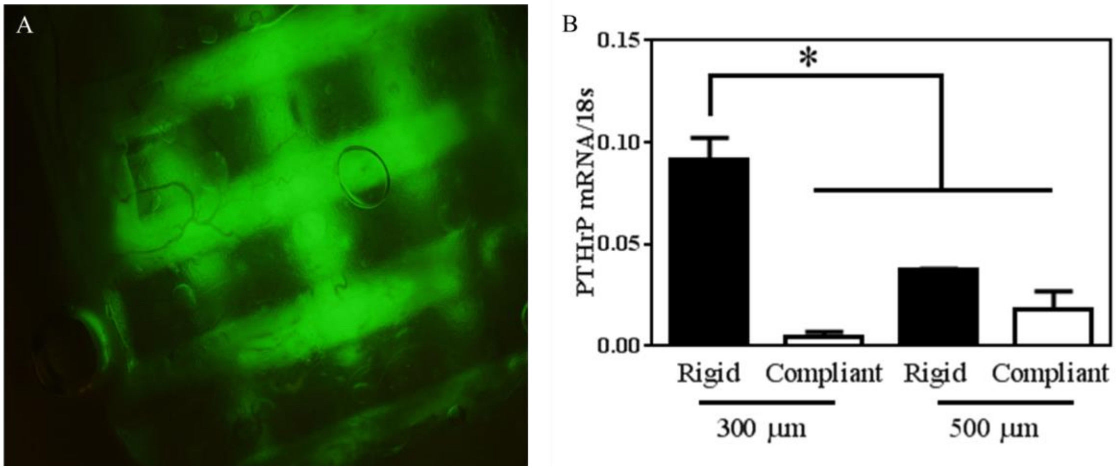

Figure 7.3. *Ex vivo* analysis of metastatic cancer cells in 3D polyurethane scaffolds. (A) *Ex-vivo* fluorescent images of MDA-MB-231 cells in 3D PUR scaffolds after 21 days *in vivo*. (B) PTHrP expression of MDA-231 cells culture on 3D PUR scaffolds after 21 days.

To further add to the utility of the 3D scaffolds, a commercially available perfusion flow bioreactor was purchased from 3D Biotek (Figure 7.4A). This bioreactor allows for up to 4 simultaneous experiments at a designated flow rate. The flow rates are adjustable and the range of circulating volume is 7 mL-500 mL. The 3D PUR scaffolds are printed to the exact diameter of the sample tubes for the bioreactor and up to 10 (0.5”) scaffolds can fit per tube. Pilot studies testing MDA-MB-231 cells seeded on rigid and compliant 3D PUR scaffolds were conducted at a flow rate of 2.1 rpm. Gene expression was analyzed after 48 hours of culture (Figure 7.4D-F). For all genes analyzed the expression matched that of experiments performed in 2D films.

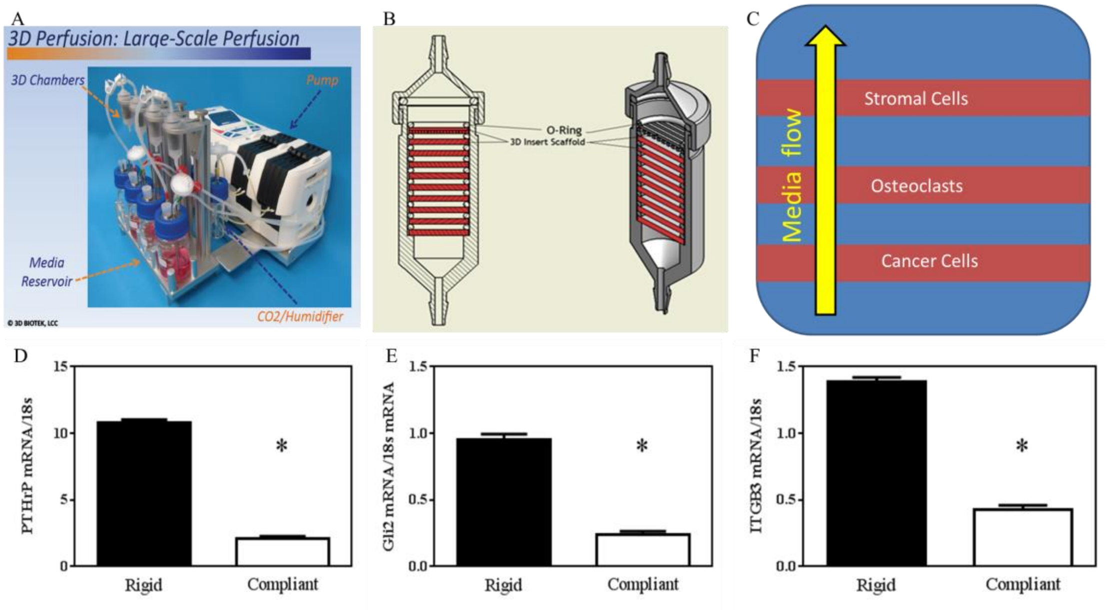

Figure 7.4. Perfusion bioreactor preliminary analysis. (A&B) Images of 3D Bioteks' bioreactor and sample tube; (C) Potential study of multiple cell types on different 3D PUR scaffolds within the same tube (bone-in-a-tube study); (D-F) Gene expression for PTHrP, Gli2 and ITGβ3 for MDA-MB-231 cells cultured over 48 hours of perfusion flow.

These preliminary studies show the potential utility of 3D printed molds, 3D PUR scaffolds and the perfusion bioreactor. Complex analysis can be conducted *in vitro* and then directly applied *in vivo* to match outcomes. Future studies should look to adding multiple cell populations to generate a bone-in-a-tube study (Figure 7.4C). The combination of adding a cell degradable scaffold (discussed below) seeded with osteoclasts creates another primary outcome to test the interplay of tumor cells and the bone microenvironment. Finally, the only limitation is the resolution of the 3D printer that generates the mold. As the technology improves it is easy to conceive of printing a mold of human trabecular bone from a CT scan and directly making exact replicas of bone. This would be a truly biomimetic architecture that could be tuned to fully examine the mechanotransduction effects at play in the bone microenvironment.

Targeted Nanoparticles for Bone Applications and Cell Specific Drug Release

The nanoparticles studied in Chapter IV are an interesting type of polymer system that has the benefits of cationic branches to ensure drug delivery within the cytosol of the cell; however, there are no current targeting ligands to direct nanoparticle delivery and the degradation mechanism is hydrolytic which is difficult to control *in vivo*. The self-assembly method of generating nanoparticles allows for the doping of a small percentage of functionalized polymers. This would generate a mixed micelle, displayed in Figure 7.5. The functionalization can be customized *post hoc* with a targeting agent that matches the desired pathology.

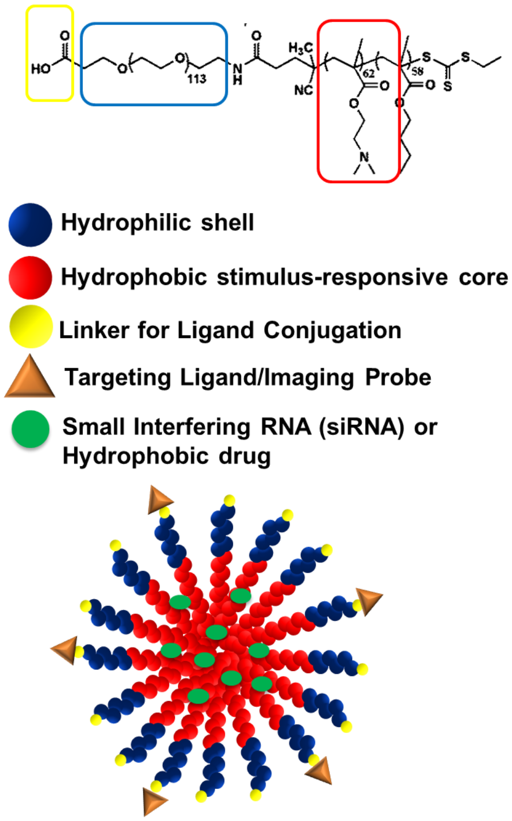

Figure 7.5. Diagram of the potential functionalization of self-assembled nanoparticles through the incorporation of a small number of functionalized polymers.

Efficient targeted drug delivery can be accomplished with a wide range of chemistries and would theoretically eliminate many of the pharmacokinetic challenges associated with systemic or local therapeutics[6]. Specifically, directing therapeutics to the bone microenvironment has been achieved with a variety of targeting molecules. The bone microenvironment is unique target due to the large amount of mineralized matrix. The mineralized hydroxyapatite can be easily bound to negatively charged species, such as bisphosphonates, acidic peptides, or acrylic acid based polymers[7]. In order to address both the targeting and degradation limitations of the cationic polymers a new class of cell degradable polymers was developed based on a ROS degradable poly(propylene sulfide) (PPS) chemistry.

Non-functionalized PPS polymers were recently tested for loading and release of a small molecule hydrophobic drug *in vitro*[8]. The PPS polymer were well tolerated by cells *in vitro* and were highly sensitive to ROS, showing an almost switch like degradation at physiologically relevant ROS levels. Degradation occurs by ROS mediated oxidation of the sulfide to sulfones which adjusts the solubility parameter enough that it is no longer hydrophobic. This shift in hydrophobicity drives micelle destabilization. Additionally, the more hydrophilic polymers would then easily be cleared from the body *in vivo* due to the high aqueous solubility and small size.

Two types of PPS polymers were functionalized with either a hydrophilic corona of PEG (PPS-b-PEG) or a bone targeting sequence of 8-10 acrylic acid monomers (PPS-b-PAA) via RAFT polymerization (Figure 7.6). A range of 0-100% PPS-b-PAA polymers were tested for hydrodynamic volume, surface charge and the ability to bind to hydroxyl apatite crystals *in vitro* (Figure 7.7).

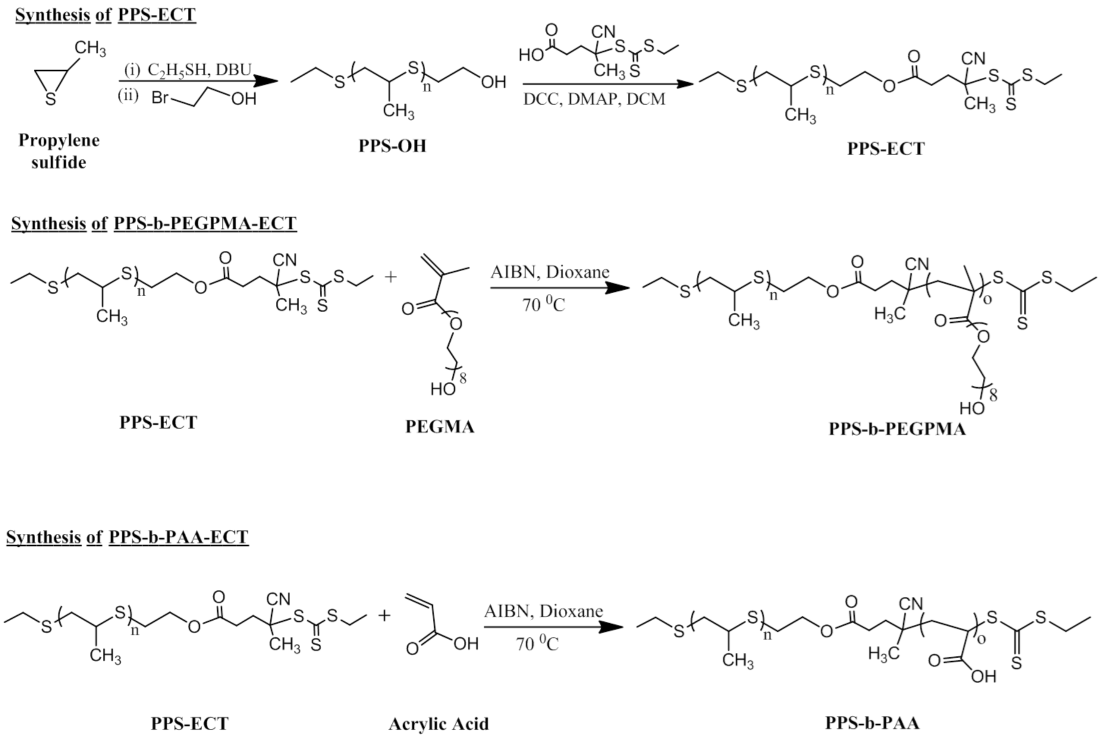

Figure 7.6. Diagram of PPS polymer synthesis.

The mixed micelles showed a decreasing trend of surface charge with increasing amounts of PPS-b-PAA. Surprisingly, the DLS profile showed little change upon incorporating more PPS-b-PAA into the micelle. The size ranged from 87-166 nm at 0 and 100% PPS-b-PAA incorporation, respectively. The increase in size is likely due to the electrostatic repulsion caused by the close proximity of the PAA in the corona. *In vitro* binding was obtained incubating the mixed micelles at a concentration of 1 mg/mL in 0.5 mL of PBS with 0.1 g of dispersed HA powder at 37^{o} C overnight on a shaking tray. The suspension was centrifuged down at <1000 rpm to prevent any nanoparticle sedimentation and the supernatant was read on a plate reader. The trithiocarbonate chain transfer agent (ECT) has an absorbance at 310 nm and could be used as a marker for the micelles. A standard curve was obtained with concentrations ranging from 1-0.03 mg/mL of the various mixed micelles. The residual polymer was subtracted from the initial amount in the solution and a percentage of bound micelles were obtained. It was found that the micelles with 100% PPS-b-PAA bound the highest to the HA powder, at nearly 50% binding efficiency. There was some residual binding with the PPS-b-PEG control group at ~12% binding, but this could simply be an artifact of the centrifugation step. These experiments show that the potential for generating a bone targeted, cell specific drug delivery platform is well within reach of the current technology. In the future studies the mixed micelles should be analyzed for drug loading capacity and tested *in vivo* to ascertain any toxicities, although based on previous studies, none are expected.

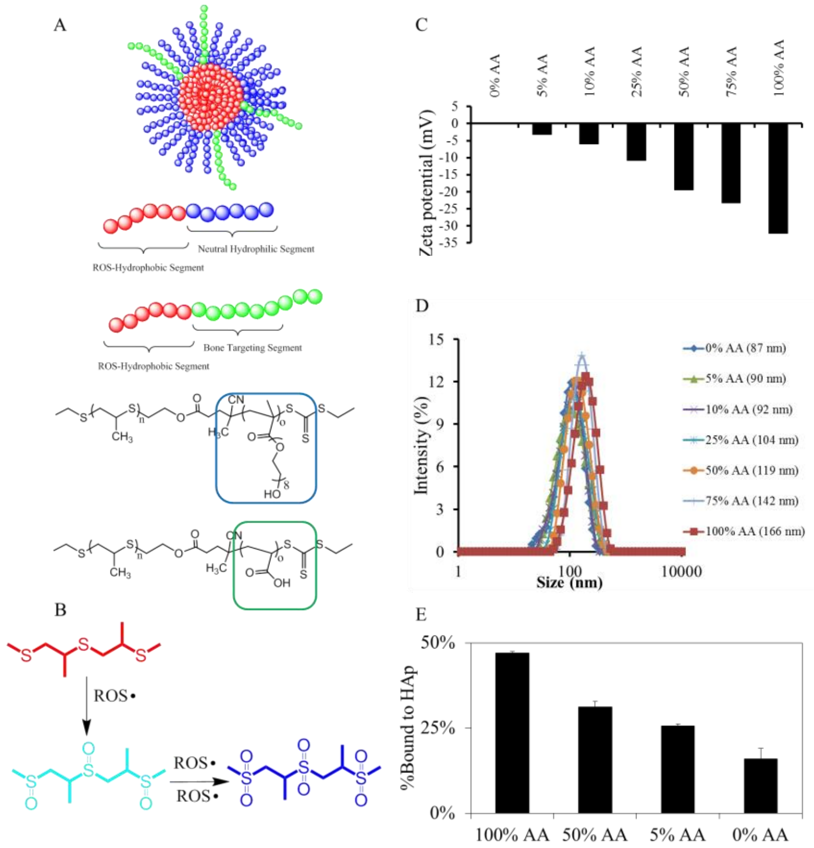

Figure 7.7. Description and characterization of PPS mixed micelles. (A) Diagram of the formation of PPS mixed micelles; (B) Degradation mechanism of ROS mediated sulfide to sulfone transition; (C) Zeta potential and (D) DLS of 0-100% PPS-b-PAA micelles; (E) Binding of mixed micelles to hydroxy apatite powder in an aqeuous environment *in vitro*.

Combination Product: PUR Bone Graft Releasing Localized Nanoparticle Therapeutics

As mentioned several times throughout this dissertation, metastatic tumors that establish in the bone are effectively incurable. The damages associated with cancer induced bone disease are extremely devastating to patients' quality of life (Figure 7.8). Often when the tumors become large enough, or when a tumor induced fracture occurs, the surgical intervention results in catastrophic loss of tissue and little hope for regeneration of new healthy bone. Ideally, if there was a way to surgically resect the tumor infected bone and replace the lost tissue with a synthetic graft that would allow for regeneration of new tissue this would give the surgeons a tool to combat the tumor induced bone destruction. In order to ensure the tumor does not simply colonize the implant, a therapeutic can be added to target any residual tumor cells at the margins of resection.

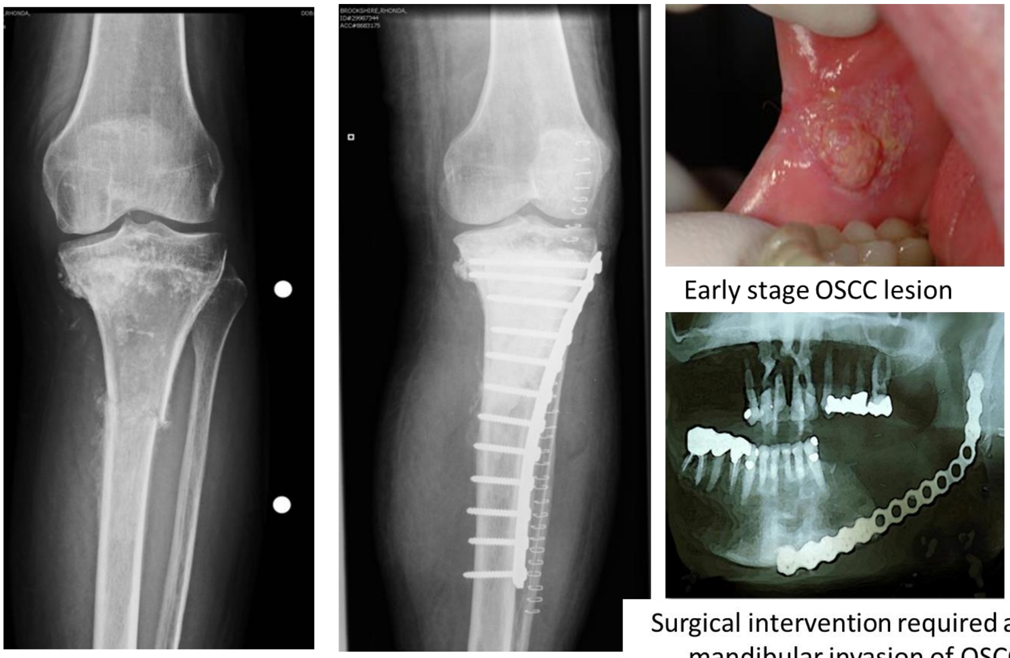
Early stage OSCC lesion

Surgical intervention required after mandibular invasion of OSCC

Courtesy Ginger Holt, M.D.

Figure 7.8. Clinical images of cancer induced bon disease and the limited surgical interventions that can be completed.

The bone grafts developed in Chapter V and the nanoparticles discussed in Chapter IV (or in the above section) could be theoretically loaded with anti-cancer therapeutics and combined into an injectable bone regenerating graft that releases tumor killing agents locally. The current limitations to this technology is the development of more stable nanoparticles that can be loaded into the liquid reactive polyurethane without destabilization. Previous iterations of the cationic nanoparticles were loaded with siRNA which induced an electrostatic stability to the particles. Without this electrostatic stability the nanoparticles are held together by simple hydrophobic interactions, which are easily destabilized upon introduction to the relatively hydrophobic liquid polyurethane.

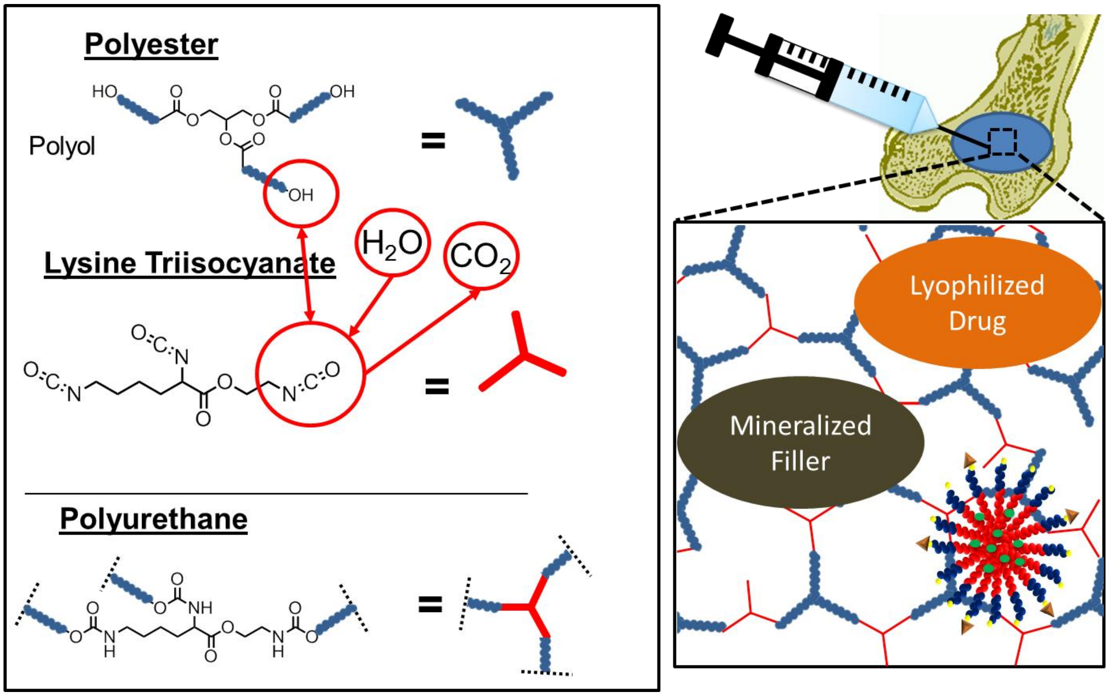

Figure 7.9. Diagram of a potential combination graft that targets both regeneration of new bone and destruction of residual tumor cells.

There are several potential solutions to this issue that can and should be addressed in future studies. The easiest solution is to simply utilize anti-cancer siRNA as the therapeutic. This could be immediately implemented in pilot studies. An alternative solution, if hydrophobic small molecule drugs are the required therapeutic, is to utilize alginate beads as a filler for the polyurethane graft. The alginate beads can are formed in an aqueous environment and can be prepared with drug loaded nanoparticles (Figure 7.10). The alginate can be processed to degrade quickly releasing a burst of nanoparticles to the local environment surrounding the graft. This method would have some limitations due to the increased porosity and resulting lack of mechanical strength upon degradation of the alginate filler.

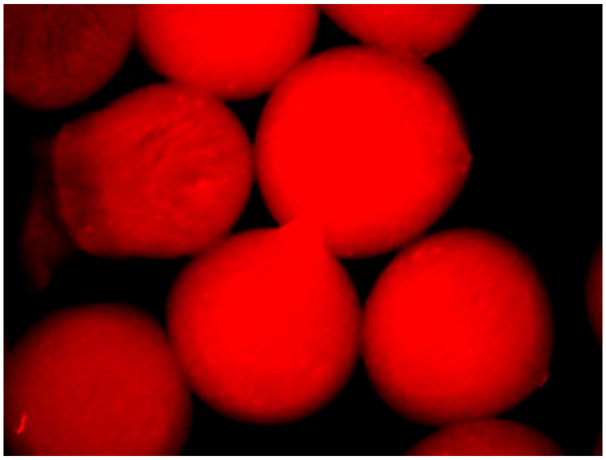

Figure 7.10. Fluorescent image of alginate beads prepared with Nile Red loaded nanoparticles.

Another alternative method could be the development of dual charged "electrostatic zipper" polymers. These can either be random block copolymers or a simple mixed micelle of positive and negatively monomers with a hydrophobic block to induce initial formation. Upon formation at the correct pH, the electrostatic interactions should induce a zipper-like stability inside the core of the micelle. This zipper can then be undone as the pH shifts out of the range of dual protonation/deprotonation or in the case of DEAEA polymers, when the cationic branch degrades. The potential of this type of novel therapy for treating an uncurable disease would be hugely important to afflicted patients.

Cell Specific Degradable PUR Products

Passive biodegradation, such as hydrolysis, is difficult to control *in vivo*. Novel polymers and amino acid sequences have been synthesized with oxidative and enzymatic degradable sequences to produce a cell specific degradation mechanism. Initial studies discussed in Chapter VI show that poly(thioketals) (PTKs) can be synthesized via an acid catalyzed step polymerization of 2,2-dimethoxypropane and dimercapto-precursors. PTKs are known to be acid, base and enzymatically resistant, but oxidatively degrade to the dimercapto-precursor and acetone[9]. Oxidative degradation is physiologically relevant with the release of oxidative species during the natural wound healing response. To further aid the cell specific degradation of PTKs, enzymatically cleavable amino acids, with dithiol functionality, have been synthesized and will be incorporated into the polymer backbone. Specific amino acid substrates have been synthesized for enzymes relevant to bone regeneration, such as cathepsin K and matrix metalloprotease 9 (MMP-9) which are secreted by osteoclasts during bone remodeling. The dimercapto-PTK-amino acid copolymers exhibit “click” reactivity with isocyanates resulting in facile incorporation into PURs[10].

Amino acid sequences with known sensitivity to cathepsin K are taken from literature as well as the MEROPS database for enzyme substrate specificity[11]. Care was taken to ensure that amino acids with no reactive side groups (such as amines or hydroxyls) are used to limit protection chemistry and possible side reactions with isocyanates. The sequence that was chosen to test is a tetramer composed of Gly-Gly-Pro-nLeu (Figure 7.11). Solid phase peptide synthesis with Wang resins was utilized to generate the amino acid sequences. Di-thiol functionalization was completed by utilizing a thiol coupled amino acid starting resin. Individual acids were added with Fmoc protection/deprotection chemistry. The addition of the final acid was followed by capping with mercapto-proponic acid. Removal from the resin will be completed with acid cleavage. NMR was utilized to assess structural purity.

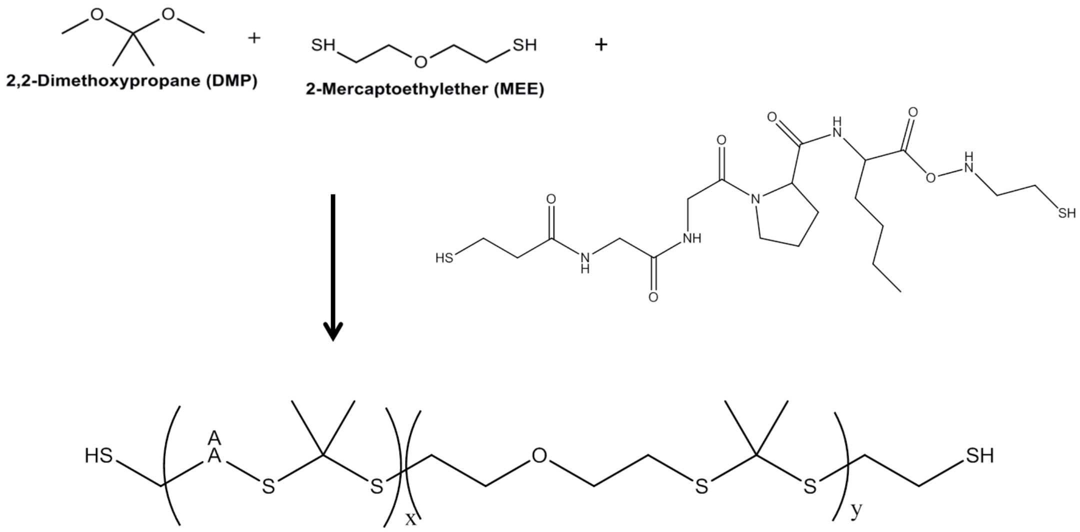

Figure 7.11. Chemical diagram of PTK-AA synthesis.

The dimercapto-amino acid sequence was incorporated into the PTK backbone along with dimercapto diethyl ether in the exact synthesis scheme described in Chapter VI. The only additional step was a redissolution in dichloromethane after polymerization and a wash with brine to remove any unreacted monomers. The addition of di-thiol amino acids was completed at ratios of 0, 2.5, and10%, with the 10% PTK-AA approaching a solid. The molecular weight of the step polymerization can be adjusted based on stoichiometry and reaction times. Target molecular weight was set for 1 kDa (degree of polymerization ~3-10 depending on the percentage of amino acid incorporation). Molecular weight and structural purity was analyzed with gel permeation chromatography (GPC) (Table 7.2). The resulting polymers were utilized to derive polythiourethane foams (PUR-PTK-AA-X), where X is the percentage of amino acid incorporated into the PTK backbone.

Table 7.2. Table of characterizations of PTK-AA polymers.

Polymer	%AA	Targeted Mw	Experimental Mw (GPC)	PDI	Tg C° (DSC)
PTK-10	10	1167	1000	1.6	-76
PTK-2.5	2.5	1167	1090	1.7	-78

The PTK-AA-0, 2.5 and 10 were utilized to generate PUR foams, however, due to the thiol termination the polymers had roughly a 10 fold higher reactivity with the isocyanate. Amine catalysts utilized in the normal hydroxyl foaming reaction are utilized in literature to catalyze the click reaction of thiols and isocyanates. This resulted in a highly balance reaction with the water reactivity being closely matched to the thiol reactivity. Therefore the polyurethane would not foam with the amine based catalyst. Attempts were made with the most powerful blowing catalyst in our lab (DMAEE), yet no foams were generated. The only method that would allow even small amounts of foaming was to overindex (>200) and add a large excess of water to the formulation. The foams were tested for degradation and compared to polyester controls in water, ROS media, and a solution of cathepsin K (Figure 7.12). None of the materials showed significant degradation upon incubation in water, however, the PUR-PTK-AA materials displayed some mass loss initially. This is likely due to the unbalanced reaction that results in ~10% mass loss of unreacted monomers. The ROS treatment equally degraded all of the PUR-PTK materials over 4 weeks with no discernable difference between the incorporation of AA. The cathepsin K treatment only degraded the PUR-PTK-AA-2.5 and 10, although there was no difference between the two materials.

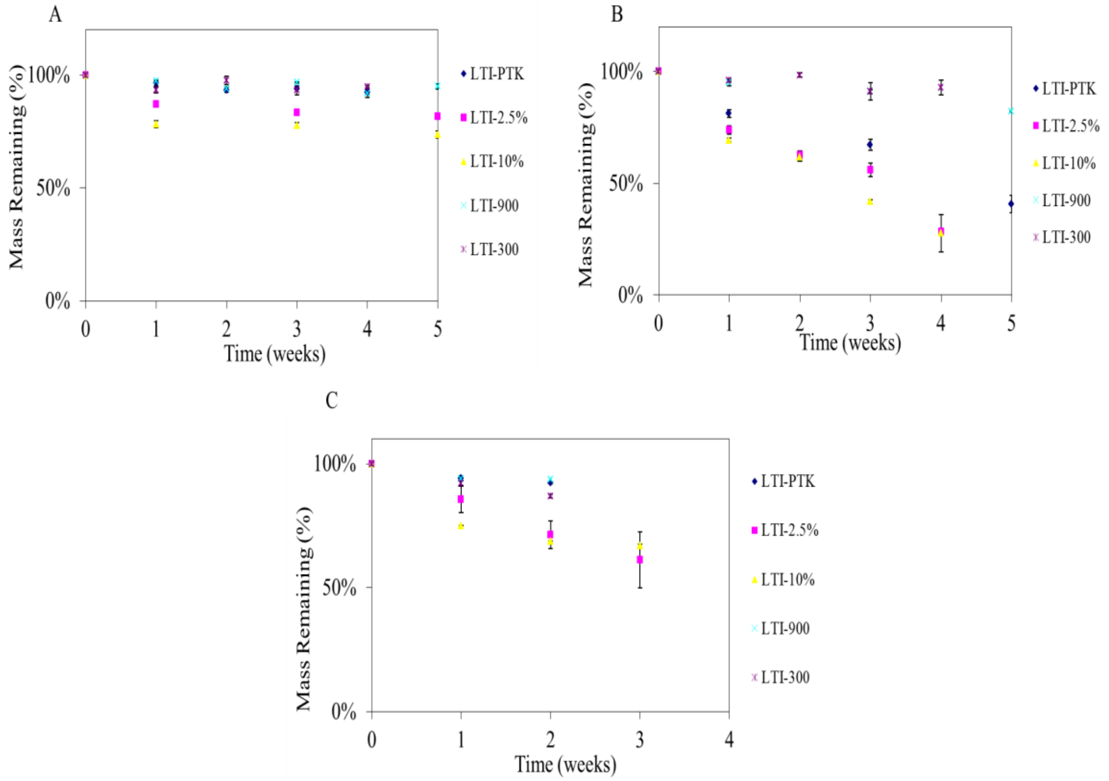

Figure 7.12. Degradation profiles of PTK-AA polymers and polyester controls at physiological temperatures. Mass loss as a function of time for foams incubated in (A) water, (B) ROS media, (C) cathepsin K.

These pilot studies point to the fact that enzymatically cleavable amino acids can be incorporated into the PTK backbone, which induces a further layer of specificity to the cell degradable mechanism. Additionally, there seems to be little benefit to adding more than 2.5% of the amino acid which should result in reduced cost and difficulty during synthesis. For future studies, the PTK-AA polymers should be end-functionalized to hydroxyls to reduce the foaming difficulties. The polymers should be tested *in vivo* in bone to see if there is any benefit to the added specificity of degradation. Alternatively, the PTK-AA-2.5 could be utilized to generate an osteoclast degradable 3D PUR scaffold for bioreactor studies. This cell degradable scaffold could be seeded with osteoclasts and then measured for resorption, by either observing the thiol degradation products in the media or in mass loss over time. This would provide for an additional primary outcome of bone-in-a-tube experiments looking at the effects of multiple cell populations in a single tube of the bioreactor.

References

1. (a) Schindler, M.; Nur-E-Kamal, A.; Ahmed, I.; Kamal, J.; Liu, H. Y.; Amor, N.; Ponery, A. S.; Crockett, D. P.; Grafe, T. H.; Chung, H. Y.; Weik, T.; Jones, E.; Meiners, S., Living in three dimensions - 3D nanostructured environments for cell culture and regenerative medicine. *Cell Biochemistry and Biophysics* **2006,** *45* (2), 215-227; (b) Smalley, K. S. M.; Lioni, M.; Herlyn, M., Life isn't flat: Taking cancer biology to the next dimension. *In Vitro Cellular & Developmental Biology-Animal* **2006,** *42* (8-9), 242-247.

2. (a) Kleinman, H. K.; McGarvey, M. L.; Hassell, J. R.; Star, V. L.; Cannon, F. B.; Laurie, G. W.; Martin, G. R., BASEMENT-MEMBRANE COMPLEXES WITH BIOLOGICAL-ACTIVITY. *Biochemistry* **1986,** *25* (2), 312-318; (b) Kleinman, H. K.; McGarvey, M. L.; Liotta, L. A.; Robey, P. G.; Tryggvason, K.; Martin, G. R., ISOLATION AND CHARACTERIZATION OF TYPE-IV PROCOLLAGEN, LAMININ, AND HEPARAN-SULFATE PROTEOGLYCAN FROM THE EHS SARCOMA. *Biochemistry* **1982,** *21* (24), 6188-6193.

3. Abbott, A., Cell culture: Biology's new dimension. *Nature* **2003,** *424* (6951), 870-872.

4. Weaver, V. M.; Petersen, O. W.; Wang, F.; Larabell, C. A.; Briand, P.; Damsky, C.; Bissell, M. J., Reversion of the malignant phenotype of human breast cells in three-dimensional culture and in vivo by integrin blocking antibodies. *Journal of Cell Biology* **1997,** *137* (1), 231-245.

5. (a) Seunarine, K.; Gadegaard, N.; Tormen, M.; Meredith, D. O.; Riehle, M. O.; Wilkinson, C. D. W., 3D polymer scaffolds for tissue engineering. *Nanomedicine* **2006,** *1* (3), 281-96; (b) Stegemann, J. P.; Nerem, R. M., Altered response of vascular smooth muscle cells to exogenous biochemical stimulation in two- and three-dimensional culture. *Experimental Cell Research* **2003,** *283* (2), 146-155; (c) Sun, T.; Jackson, S.; Haycock, J. W.; MacNeil, S., Culture of skin cells in 3D rather than 2D improves their ability to survive exposure to cytotoxic agents. *J. Biotechnol.* **2006,** *122* (3), 372-381; (d) Sun, T.; Norton, D.; McKean, R. J.; Haycock, J. W.; Ryan, A. J.; MacNeil, S., Development of a 3D cell culture system for investigating cell interactions with electrospun fibers. *Biotechnol. Bioeng.* **2007,** *97* (5), 1318-1328.

6. Brannon-Peppas, L.; Blanchette, J. O., Nanoparticle and targeted systems for cancer therapy. *Advanced Drug Delivery Reviews* **2012,** *64, Supplement* (0), 206-212.

7. (a) Hirabayashi, H.; Fujisaki, J., Bone-Specific Drug Delivery Systems: Approaches via Chemical Modification of Bone-Seeking Agents. *Clinical Pharmacokinetics* **2003,** *42* (15), 1319-1330; (b) Hirabayashi, H.; Takahashi, T.; Fujisaki, J.; Masunaga, T.; Sato, S.; Hiroi, J.; Tokunaga, Y.; Kimura, S.; Hata, T., Bone-specific delivery and sustained release of diclofenac, a non-steroidal anti-inflammatory drug, via bisphosphonic prodrug based on the Osteotropic Drug Delivery System (ODDS). *J. Control. Release* **2001,** *70* (1–2), 183-191; (c) Low, S. A.; Kopeček, J., Targeting polymer therapeutics to bone. *Advanced Drug Delivery Reviews* **2012,** *64* (12), 1189-1204; (d) Ouyang, L.; Huang, W.; He, G.; Guo, L., Bone Targeting Prodrugs Based on Peptide Dendrimers, Synthesis and Hydroxyapatite Binding In Vitro. *Letters in Organic Chemistry* **2009,** *6* (4), 272-277; (e) Ouyang, L.; Pan, J.; Zhang, Y.; Guo, L., Synthesis of Second- and Third-Generation Asp Oligopeptide Conjugated Dendrimers for Bone-

Targeting Drug Delivery. *Synthetic Communications* **2009,** *39* (22), 4039-4052; (f) Pan, H.; Kopeckova, P.; Wang, D.; Yang, J.; Miller, S.; Kopecek, J., Water-soluble HPMA copolymer--prostaglandin E1 conjugates containing a cathepsin K sensitive spacer. *J Drug Target* **2006,** *14* (6), 425-35; (g) Pan, H.; Liu, J.; Dong, Y.; Sima, M.; Kopečková, P.; Brandi, M. L.; Kopeček, J., Release of Prostaglandin E1 from N-(2-Hydroxypropyl)methacrylamide Copolymer Conjugates by Bone Cells. *Macromolecular Bioscience* **2008,** *8* (7), 599-605; (h) Uludag, H., Bisphosphonates as a Foundation of Drug Delivery to Bone. *Current Pharmaceutical Design* **2002,** *8* (21), 1929-1944.

8. Gupta, M. K.; Meyer, T. A.; Nelson, C. E.; Duvall, C. L., Poly(PS-b-DMA) micelles for reactive oxygen species triggered drug release. *J. Control. Release* **2012,** *162* (3), 591-598.

9. Wilson, D. S.; Dalmasso, G.; Wang, L.; Sitaraman, S. V.; Merlin, D.; Murthy, N., Orally delivered thioketal nanoparticles loaded with TNF-α–siRNA target inflammation and inhibit gene expression in the intestines. *Nature materials* **2010,** *9* (11), 923-928.

10. (a) Li, H.; Yu, B.; Matsushima, H.; Hoyle, C. E.; Lowe, A. B., The Thiol−Isocyanate Click Reaction: Facile and Quantitative Access to ω-End-Functional Poly (N, N-diethylacrylamide) Synthesized by RAFT Radical Polymerization. *Macromolecules* **2009,** *42* (17), 6537-6542; (b) Shin, J.; Matsushima, H.; Chan, J. W.; Hoyle, C. E., Segmented Polythiourethane Elastomers through Sequential Thiol−Ene and Thiol−Isocyanate Reactions. *Macromolecules* **2009,** *42* (9), 3294-3301.

11. Rawlings, N. D.; Morton, F. R.; Kok, C. Y.; Kong, J.; Barrett, A. J., MEROPS: the peptidase database. *Nucl. Acids Res.* **2008,** *36* (suppl_1), D320-325.

APPENDIX A

EXPERIMENTAL PROTOCOLS

Polyurethane Precursor Synthesis and Solvent Film Casting

Materials

1. 10X PBS stock composed of 0.011 M KH_2PO_4 (EMD Millipore, catalog number PX1565), 1.54 M NaCl (Research Products International, catalog number S23020), and 0.056 Na_2HPO_4 (EMD Millipore, catalog number SX0720) in ultrapure water. Dilute with ultrapure water to make a 1X PBS solution.
2. Methyl 2,6-diisocyanatohexane (lysine methyl ester diisocyanate, LDI, Adamas Reagent Co.,Ltd., catalog number 13010).
3. Hexamethylene diisocyanate trimer (HDIt, Bayer Material Science, Desmodur N3300 A).
4. ε-caprolactone monomer (99%, Acros Organics, catalog number AC17344-2500).
5. dl-lactide (Polysciences, catalog number 17085).
6. Glycolide (Polysciences, catalog number 16640).
7. Stannous octoate (Nusil, catalog number 00002CAT0000AX).
8. Glycerol (99.5%+, Sigma Aldrich, catalog number 191612-1L).
9. Phthalic anhydride (99%+, Sigma Aldrich, catalog number 320064).
10. Sodium hydroxide, pellets (98%, Sigma Aldrich, catalog number S5881).
11. Potassium hydrogen phthalate (99.9%+, Sigma Aldrich, catalog number P1088).
12. Pyridine, anhydrous (99.8%, Sigma Aldrich, catalog number 270970).
13. Sodium hydroxide (1 N in water, Sigma Aldrich, catalog number 38215).
14. Dipropylene glycol (Sigma Aldrich, catalog number D215554-500G).
15. 1,4 Diazabicyclo[2.2.2] octane (triethylene diamine (TEDA), Sigma Aldrich, catalog number D27802-100G).
16. Polycaprolactone triol (300 Mn, Sigma Aldrich, catalog number 200387-250G).
17. Magnesium sulfate, anhydrous (>99.5%, Sigma Aldrich, catalog number M7506-500G).
18. Di-n-butylamine (>99.5%, Sigma Aldrich, catalog number 471232).
19. Hydrochloric acid (37%, Sigma Aldrich, catalog number 320331).
20. Potassium hydroxide in methanol (0.995-1.005N, Fisher, catalog number SP220-1).
21. Methanol (99.9%, Fisher, catalog number A454-4).
22. Hexanes (Fisher Scientific, catalog number H303-1).
23. Coscat 83 (Vertellus, catalog number CAT83).
24. 1,2 Dichloroethane, anhydrous (99.8%, Sigma Aldrich, 284505-1L).

25. Fibronectin (Life Technologies, catalog number 33016015).
26. Ethanol (PHARMCO-AAPER, catalog number 111000190). Prepare a 70% ethanol solution in ultrapure water.
27. Sterile PBS (Cellgro, catalog number 21-040-CV).
28. Paraformaldehyde (Fisher, catalog number 30525-89-4). Prepare a 3.7% paraformaldehyde solution in 1X PBS. NaOH can be used to aid in dissolution, but the solution must be pH'ed back to 7.4.
29. Triton X-100 (Research Products International, catalog number 111036). Prepare a 0.1% Triton X-100 solution in 1X PBS.
30. Bovine serum albumin (EMD Millipore, catalog number 2960).
31. Aqua Poly/Mount (Polysciences, catalog number 18606).
32. 22x22 coverslips (Fisher, catalog number 12-541-B).
33. CellCrowns for 24 well-plate (Scaffdex, catalog number C00001N).
34. 24 well plates (Corning, catalog number 3513).
35. 12 well plates (Corning, catalog number 3524).
36. Glass slides (Fisher, catalog number 12-545-C).
37. Alexa Fluor 546 phalloidin (Life Technologies, catalog number A22283).
38. Kimwipes, glass pipettes, pipette box lid, fine tip tweezers, surgical scissors, filter paper, Erlenmeyer flasks, funnels, magnetic stirrer, magnetic stir bars, overhead stirrer, 100 mL 3-neck flasks, heating sleeves for 3-neck flask, vacuum oven (with liquid nitrogen trap), oil bath, assorted glassware and standard polymer characterization equipment (gel permeation chromatography and automatic titrator).

Polyurethane Precursor Preparation (See Note 1 for additional information)

1. Dry 5 g glycerol at 80^{o} C under vacuum (750 torr) for 24 hours. Store under desiccant until use.
2. Dry 75 g ε-caprolactone monomer with 1-5 g anhydrous magnesium sulfate (see Note 2), then pour through filter paper into 100 mL beaker.
3. Add 0.1 g stannous octoate to a clean, dry 100 mL 3-neck flask.
4. Add 3.07 g of the dried glycerol to the 3-neck flask.
5. Add 9.69 g of dl-lactide to the 3-neck flask.
6. Add 19.39 g of glycolide to the 3-neck flask.
7. Add 67.85 g of the dry, filtered ε-caprolactone monomer to the 3-neck flask.
8. Place 3-neck flask in heating sleeve and stir with overhead stirring apparatus at medium speed.
9. Flush reactor with constant stream of dry argon.
10. Slowly bring temperature up to 140^{o} C and allow reaction to occur for 48 hours.

11. After 48 hours of reaction time, the polymer should be a highly viscous, slightly milky white color liquid.
12. Pour polymer into a 250 mL beaker and add 100 mL of hexane. Stir with a magnetic stirrer and stir bar. If the polymer is too viscous to stir, apply heat up to 100^{o} C.
13. Carefully remove excess hexane and repeat the wash three times.
14. After final wash, place beaker on hot plate at 100^{o} C for 8 hours to remove excess solvent.
15. Dry remaining polymer at 80^{o} C under vacuum (750 torr) for 24 hours. Store under desiccant until use.

Characterization of Polyester Triol (OH# See Note 3)

1. Dissolve 148.12 g of phthalic anhydride in 500 mL of anhydrous pyridine and bring total volume to 1 L with excess anhydrous pyridine. Stir overnight in dark bottle with closed cap. Prepare fresh daily as required.
2. Dissolve 40 g of sodium hydroxide pellets in 500 mL of water and bring total volume to 1 L with excess water.
3. Weight 2-3 g of potassium hydrogen phthalate into a beaker and add 150 mL of water with stirring until dissolved.
4. Titrate until end point with sodium hydroxide solution to calculate the solutions normality.
5. Accurately weigh 1-5 g of polyester triol in 125 mL Erlenmeyer flask and dissolve in 10 mL of phthalic anhydride/pyridine solution. Attach condenser and reflux at 170^{o} C for 30 minutes.
6. After cooling, rinse condenser with 15 mL of anhydrous pyridine and 15 mL water.
7. Titrate to endpoint with 1 N sodium hydroxide solution.
8. Complete steps 5-7 without the addition of polyester for blank runs.
9. If the titrant volume required for the polyester samples is less than 75% of the volume required for the blank, the sample was too large and steps 5-7 will need to be repeated with smaller samples of polyester.
10. The final OH# can be calculated from the following equation:

$$OH\# = \frac{[(B - A) * N * 56.11]}{W}$$

Where:

B = Average mL of NaOH solution consumed by the blanks.

A = NaOH solution consumbed by the sample in mL.

N = Normality of the NaOH solution.

W = Grams of sample.

Isocyanate Prepolymer Preparation

1. Add 0.025 g of Coscat 83 to a dry, clean 100 mL 3-neck flask.
2. Add 44.07 g of lysine methyl ester diisocyanate (LDI) to the 3-neck flask.
3. Heat oil bath to 90^{o} C over magnetic stir plate.
4. Place 3-neck flask securely in oil bath and apply medium stirring. Flush with a constant stream of dry argon.
5. Allow up to 1 hour for temperature to equilibrate, then add 5.94 g of polycaprolactone triol (300 Mn) dropwise to the 3-neck flask.
6. Allow the reaction to proceed for 3 hours.
7. After the reaction is complete, the prepolymer should be a low viscosity, light yellow color liquid.
8. Pour the prepolymer into a container for storage and keep under nitrogen at 4^{o} C until use.

Characterization of the Prepolymer (NCO# see Note 4 for more details)

1. Prepare 1 mol/L solution of dibutylamine in toluene (example 170 mL dibutylamine diluted up to 1 L with toluene).
2. Prepare a 1 mol/L solution of HCl in methanol (example 83.3 mL of 37% HCl diluted up to 1 L with methanol).
3. Add 25 mL of 1N KOH in methanol into a 100 mL beaker diluted with 50 mL water.
4. Titrate to end point with HCl in methanol and calculate HCl solution normality from the following equation:

$$N_{HCl} = \frac{N_{KOH} * V_{KOH}}{V_{HCl}}$$

Where:

N_{KOH} = Normality of KOH solution in methanol.

V_{KOH} = Volume of KOH in methanol (mL).

V_{HCl} = Titrant consumption (mL).

5. For sample analysis weight out 0.5-1 g of isocyanate prepolymer into 125 mL Erlenmeyer flask.

6. Add 30 mL of toluene and stir until dissolution.
7. Add 20 mL of 1 mol/L dibutylamine solution and stir for 10 minutes.
8. Add 30 mL methanol and titrate excess dibutylamine with 1 mol/L HCl in methanol.
9. Repeat steps 5-8 without the addition of samples to obtain the blank values.
10. Calculate the NCO# from the following equation:

$$NCO\# = \frac{[(B - V) * N * 0.042]}{W}$$

Where:

B = Volume of HCl for titration of the blank (mL).

V = Volume of HCl for titration of sample (mL).

N = Normality of HCl.

W = Weight of sample in grams.

Polyurethane Film Preparation (See Note 5)

1. Add 1 mg (0.2 wt%) of Coscat 83 to a 5 mL glass vial (#1).
2. Add 64 mg of LDI prepolymer to the glass vial (#1).
3. Add 435 mg of 3000 g/mol polyester triol to a new glass vial (#2). See Notes 6 and 7 for description of polyurethane reaction and additional comments on use of different molecular weight triols or isocyanates with different NCO#'s.
4. Add 1.75 mL of anhydrous dichloroethane to each of the vials (#1 & #2).
5. Shake or vortex until dissolution of components.
6. Carefully transfer the solution in vial #2 to vial #1. The final concentration will be 10 wt% polymer.
7. Shake or vortex for 30 seconds to homogenize solutions.
8. Pipette 75 µl of solution to glass portion of treated MatTek dishes (see Note 8).
9. Carefully transfer dishes to an oven flushed with a steady stream of dry argon and cure overnight at room temperature.
10. Increase temperature in the oven to 60^{o} C for an additional 24 hours to ensure complete cure. MatTek dishes can be stored in a desiccator until use.
11. Incubate polyurethane films with 300 µl of 0.1 mg/ml poly-d-lysine in ultrapure water for 1 hour at 37°C on a rack in a water bath such that the water makes contact with the bottom of the dishes.

12. Polyurethanes and polyesters have been known to autofluoresce causing some difficulty with sensitive fluorescent analysis. See Note 9 for a discussion on reducing this phenomenon.

Notes

1. For the synthesis of a 900 g/mol polyester triol the following changes need to be made to steps 4-7 in section 3.3.1: 4. Add 10.23 g of dry glycerol. 5. Add 8.98 g of dl-lactide. 6. Add 17.95 g of glycolide. 7. Add 62.84 g of dry, filtered ε-caprolactone monomer. The remaining steps are kept the same. The final polyester triol is clear instead of milky white. The polycaprolactone triol (Sigma Aldrich, catalog number 200387-250G) is utilized as the 300 g/mol precursor so no additional steps are required for synthesis.
2. The drying of ε-caprolactone monomer with $MgSO_4$ is convenient, but there is some loss upon filtration. Therefore it is required to add 10-15 g of additional ε-caprolactone monomer to ensure enough material for the reaction. Alternative drying procedures, such as vacuum drying can be completed.
3. Characterizations of OH# are required to obtain the exact amount of hydroxyls per mole of polyester triol. The OH# instructions were specified for a 789 MPT Titrino (Metrohm) although the instructions can be applied with most automated titration equipment. The procedure works by esterification of the hydroxyl with the phthalic anhydride. The excess phthalic anhydride is hydrolyzed with water to form phthalic acid. The acid is then titrated with the standard sodium hydroxide solution. The OH# is calculated from the difference in titration of the blank and sample solutions. For more information see ASTM D 4662-93. Additional characterization via GPC should show broad peaks (depending on extent of washing) centered on the target molecular weight.
4. Characterization of the NCO# is required to accurately account for the isocyanate per mole of material. The NCO# instructions were specified for a 789 MPT Titrino (Metrohm) although the instructions can be applied with most automated titration equipment. The procedure works by the reaction of isocyanate with the dibutylamine. The excess dibutylamine is titrated with standard hydrochloric acid. For more information see ASTM D 4662-93.
5. The 4 mL batch is the smallest batch with which to easily measure out the catalyst. It should produce up to 50 films.
6. The polyurethane reaction is balanced by the amount of isocyanate and hydroxyl equivalents. The ratio of these equivalents multiplied by 100 is known as the index. For the films utilized in this study an index of 105 is utilized. In order to keep this index value constant the amount of triol and prepolymer is adjusted when a different molecular weight triol is utilized. Since the mechanical

properties of the polyurethane film are directly related to the molecular weight of the polyester triol, it is essential to utilize the correct concentration of materials. More information can be found in the following publications [1]. Steps 2 and 3 in section 3.5 need to be changed accordingly. For 900 g/mol polyester triol: 2. Add 164 mg of LDI prepolymer to vial #1. 3. Add 331 mg of 900 g/mol polyester triol to vial #2. For 300 g/mol polycaprolactone triol: 2. Add 297 mg of LDI prepolymer to vial #1. 3. Add 202 mg of 300 g/mol polycaprolactone triol to vial #2. The remaining steps are the same.

7. Similar to the OH# The NCO# is a measure of the isocyanate per mole of material. This number varies for each isocyanate and new batch of the prepolymer. When accounting for different NCO#, generally, the higher the value the less isocyanate is required to keep the index constant. For instance, the NCO# for the LDI prepolymer is around 29.9 and HDI trimer has an NCO# of 21.8. To incorporate HDI trimer instead of the LDI prepolymer in the polyurethane films steps 2 and 3 in section 3.5 need to be changed accordingly. For a 3000 g/mol polyester triol: 2. Add 84 mg of HDI trimer to vial #1. 3. Add 415 mg of 3000 g/mol polyester triol to vial #2. For a 900 g/mol polyester triol: 2. Add 201 mg HDI trimer to vial #2. 3. Add 298 mg of 900 g/mol polyester triol to vial #2. Finally, for a 300 g/mol polycaprolactone triol: 2. Add 334 mg of HDI trimer to vial #2 . 3. Add 165 mg of polycaprolactone triol to vial #2. The remaining steps are the same.
8. Dichloroethane is a good solvent for polystyrene, therefore care should be taken when applying the polyurethane solution to the MatTek dishes.
9. Autofluorescence is a common occurrence with many types of polymers. This can occur from conjugated bonds, cyclic moieties and hydrogen bonding [2]. Due to the large amount of carbonyl moieties and hydrogen bonding that can be present in polyester based polyurethanes, it is not atypical to observe autofluorescence in red, green and blue channels. In order to mitigate the effect, a method of quenching background autofluorescence in polyesters and polyurethanes using Sudan Black B (SB) was recently published [2b]. The authors were able to show that SB does not interfere with imunnofluorescent imaging of cells cultured on materials that autofluoresce.

Synthesis of Melt Cast Polyurethane Films

Principle:

Generate a melt cast 2D polyurethane film.

Before starting:

- Read and understand the MSDS of the reagents listed below
- Personal Protective and Safety Equipment required:
  - Disposable nitrile gloves
  - Appropriate attire according to the Chemical Hygiene Plan (shoes, labcoat, goggles, etc.)

Reagents:

- Polyester polyol (various Mw)
- Hexamethylene diisocyanate trimer (HDIt; DN3300A) or alternative isocyanate
- Iron(III) Acetylacetonate (5 weight percent solution in dry epsilon-caprolactone)
- Ethanol

Materials and Equipment:

- Speed mixer
- Balance
- Well plates
- Mixing cups
- Mixing cup holder for speed mixer
- Disposable syringes
- Kim wipes
- Glass vials
- Fume hood

Procedure:

1. Add appropriate amounts of diisocyanate, polyol, and catalyst with disposable syringes into mixing cup
2. Speed mix at full speed for 30 seconds
3. Add enough of reactive liquid polyurethane mixture to cover bottom of well plates
4. Allow to cure overnight, at 60^o C
5. Sterilize films with ethanol before use

Film Coating with Adhesion Proteins

Principle:

Coating of PUR films with adhesion molecules for cell culture.

Before starting:

- Read and understand the MSDS of the reagents listed below
- Personal Protective and Safety Equipment required:
    - Disposable nitrile gloves
    - Appropriate attire according to the Chemical Hygiene Plan (shoes, labcoat, goggles, etc.)

Reagents:

- PUR films
- Adhesion molecule (Fn, Vn, Col, etc.)
- Sterile PBS
- Ethanol

Materials and Equipment:

- Kim wipes
- Cell Culture hood

Procedure:

6. Sterilize PUR films before use with either ethanol or UV in a sterile cell culture hood
7. Add 4 μg/mL of adhesion molecule solution to PUR wells with enough volume to cover the surface
8. Allow to adsorb at 4^{o} C overnight
9. Remove solution and directly plate cells

Notes:

1. If the goal is irreversible adhesion, the desired concentration of adhesion molecules should be calculated from the surface area of the well plate and the volume of the solution
2. The volume of concentrated adhesion molecules should be added as noted in the procedure above, however the step 3 should be replaced with drying in the cell culture hood for 2-3 hours (or until evaporation is complete).

Synthesis of 3D PUR Scaffolds from 3D Printed Molds

Principle:

Generate a 3D scaffolds based around a 3D printed mold

Before starting:

- Train on proper use of 3D printer
- Reserve balance on Google Calendar
- Read and understand the MSDS of the reagents listed below
- Personal Protective and Safety Equipment required:
    - Disposable nitrile gloves
    - Appropriate attire according to the Chemical Hygiene Plan (shoes, labcoat, goggles, etc.)

Reagents:

- Polyester polyol (various Mw)
- Hexamethylene diisocyanate trimer (HDIt; DN3300A)
- Iron(III) Acetylacetonate (in 5% solution in epsilon-caprolactone)
- 3D printed scaffolds
- Acetone
- Dichloromethane
- Ethanol

Materials and Equipment:

- Speed mixer
- Balance
- Teflon mold/casting dish
- Mixing cups
- Mixing cup holder for speed mixer
- Disposable syringes
- Kim wipes
- Glass vials
- Razor blades
- Wire cutters
- No. 7 biopsy punch
- Fume hood

Procedure:

10. Print out 3D scaffolds with the Makerbot printer
    a. Open Makerware software
    b. Add .stl file to build plate
    c. Press the Make it button
    d. Use either 300 micron or 500 micron print settings

    e. After printing cut scaffold into appropriate size

11. Add appropriate amounts of diisocyanate, polyol, and catalyst with disposable syringes into mixing cup
12. Speed mix at full speed for 30 seconds
13. Place 3D printed scaffolds in Teflon mold/casting dish
14. Add enough drops of reactive liquid polyurethane mixture to cover the top of the scaffolds and apply slight pressure with Teflon plunger
15. Allow to cure overnight hours at 60^{o} C then remove from mold (cure time can be cut down to 3-4 hours if slight excess of catalyst is used)
16. Remove excess cured polyurethane from around 3D scaffold with razor blade or wire cutter
17. Fill glass beaker with acetone in fume hood
18. Place polyurethane coated scaffold in vial of acetone and allow scaffold to leach overnight
19. Pour acetone out (keep scaffolds in the beaker) and replace with dichloromethane in fume hood and allow to leach for at least 3 hours (preferably overnight)
20. Place polyurethane coated scaffold in vial of acetone and allow scaffold to leach for at least 3 hours
21. Remove scaffolds from acetone and place directly in ethanol for at least 3 hours
22. After the ethanol treatment, place scaffolds directly into media for cell culture

Clean-up:

1. Collect all glass waste (pipettes, vials, or broken glass) and dispose in the broken glass container (box)
2. Collect all sharps and dispose in the sharps waste container (red box)
3. Collect all solid waste and dispose in the solid waste container
4. Collect all liquid waste and dispose in the appropriate liquid waste container (acetone or halogenated)

Cell Harvesting from 3D Scaffolds

Principle:

Culturing cells in the 3D-PUR scaffolds discussed in Chapter VIII allows for novel analysis, but first the cells must be isolated from the scaffolds. This protocol discusses methods for obtaining useful quantities of RNA from cells within the 3D-PUR scaffolds.

Before starting:

- Read and understand the MSDS of the reagents listed below
- Personal Protective and Safety Equipment required:
    - Disposable nitrile gloves
    - Appropriate attire according to the Chemical Hygiene Plan (shoes, labcoat, goggles, etc.)

Reagents:

- 3D-Scaffolds seeded with cells
- Qiagen RNA extraction kit
- RNAse free water
- Ethanol

Materials and Equipment:

- Kim wipes
- Cell Culture hood
- Centrifuge

Procedure:

1. Wash the scaffolds gently with PBS at least 3 times
2. Using a fresh razor blade (rinsed with ethanol and dried) cut the 3D-PUR scaffolds into small pieces and place them in a 15 mL conical tube
3. Add Qiagen lysis buffer (with added mercapto-ethanol to stabilize the RNA)
4. Pipette vigorously ensuring all the pieces of the scaffold are mixed well within the lysis buffer
5. Add the lysis buffer and the scaffold pieces to the Qiagen filter tube and centrifuge
6. Follow manufacturer protocol for the remainder of the process to extract RNA

Notes:

1. The MDA-MB-231 cells adhere very well to the hard scaffolds so ensure that the lysis buffer is very well mixed and fully covers the pieces of scaffold
2. It may be necessary to use more than the 350 μL of lysis buffer recommended to fully cover the scaffolds. If this is the case just run multiple filtration steps until all the lysis buffer has been used

Micelle Generation and Drug Loading

Principle:

Generate a stock solution of ROS degradable nanoparticles. The nanoparticles are synthesized from a poly(propylene) sulphide (PPS) and branched polyethylene glycol (PEG). The particles can be loaded with any hydrophobic compound. The particles are soluble in hydrophobic organic solvents and spontaneously form nanostructured micelles upon introduction to aqueous media.

Before starting:

- Read and understand the MSDS of the reagents listed below
- Personal Protective and Safety Equipment required:
    - Disposable nitrile gloves
    - Appropriate attire according to the Chemical Hygiene Plan (shoes, labcoat, goggles, etc.)

Reagents:

- PEG-PPS polymer
- Organic solvent, miscible with water (THF, MeOH, EtOH)
- Hydrophobic drug or compound (if loading nanoparticles)
- DI Water or PBS -/-

Materials and Equipment:

- Balance
- Syringe pump
- Tubes
- Disposable syringes
- 0.2 µm filters
- Kim wipes

Procedure:

1. Dissolve PEG-PPS polymer in the organic solvent (10 µL/mg) in small tube
2. Add hydrophobic compound to solution of polymer at therapeutic dose
3. Setup and place syringe pump to add water or PBS -/-
4. Begin adding water at a rate of 8 mL/min
5. Leave solution exposed to allow evaporation of the majority of the organic solvent
6. Vortex and filter new solution before use

Notes:

- If the polymer makes a cloudy solution upon adding the full amount of water try additional vortexing to dissolve the remaining polymer. If this still does not work increase the initial amount of organic solvent to 20 µL/mg.
- The exact concentration of the hydrophobic drug loaded into the nanoparticles is difficult to ascertain directly. However you can assume nearly complete loading at small ratios of drug/polymer (>6 µg/mg). Additionally, if the organic solvent is fully evaporated any un-encapsulated drug should form particles that would be filtered out before use.
- This protocol can be completed with any of the self-assembly nanoparticle systems

Clean-up:

5. Collect all glass waste (pipettes, vials, or broken glass) and dispose in the broken glass container (box)
6. Collect all sharps and dispose in the sharps waste container (red sharps box)
7. Collect all solid waste and dispose in the solid waste container
8. Collect all liquid waste and dispose in the appropriate liquid waste container (acetone or halogenated)

Reactivity Analysis

Principle:

Obtain the reactivity of a given isocyanate and polyol or water at a specific catalysts concentration. The FTIR spectra of a given isocyanate yields a unique and intense peak around ~2260. This peak is concentration dependent with ATR-FTIR. In traditional FTIR Beers-Lamberts Law would make this measurement difficult due to the thickness dependence, however, in ATR the penetration depth of the IR beam is a function of refractive index and the angle of incidence (which can be kept relatively constant if measuring similar materials). In this way this SOP (and the related files) are designed to obtain the calibration curve for a given isocyanate and then measure the reactivity of the isocyanate with a polyol or water. The main.m file is a customizable Matlab code designed to read in .csv files from excel and fit a Gaussian curve (generated by the function mygaussfit.m) to the isocyanate peak and then integrate this peak with a trapezoidal integration function. The Gaussian fitting is used to eliminate any non-isocyanate peaks such as CO_2 from the integrated value. The peak areas are then plugged into Calibration Curve.xls and the linear slope fit to the concentration of isocyanate is used in Samples.xls to obtain the rate constant from the reactive mixture.

Before starting:

- Read and understand the MSDS of the reagents listed below
- Personal Protective and Safety Equipment required:
    - Disposable nitrile gloves
    - Appropriate attire according to the Chemical Hygiene Plan (shoes, labcoat, goggles, etc.)

Reagents:

- Polyester polyol (various Mw)
- Isocyanate (LTI, LTI-PEG, HDIt, etc.)
- Catalyst (iron(III) acetylacetonate (in 5% solution in epsilon-caprolactone), TEDA in solution, etc.)
- DI Water
- Inert non-volitile solvent, vacuum dried (dipropylene glycol, ε-caprolactone, propylene glycol, etc.)
- ZnSe ATR crystal
- Crystal/Sample holder kit
- Methanol/acetone bottle (for rinsing crystal between runs)
- Spatula
- Mixing cups

Materials and Equipment:

- Balance
- Crystal/Sample holder kit
- Seagull ATR assembly

- Bruker FTIR (VINSE chemistry lab)
- Methanol/acetone bottle (for rinsing crystal between runs)
- Spatula
- Mixing cups
- Disposable syringes
- Kim wipes
- Timer

Software/Documents:

- OPUS
- Matlab
- Excel
- Calibration Curve.xls
- Sample.xls
- Mygaussfit.m
- Main.m

Procedure:

Equipment startup

7. Turn on nitrogen gas (in sequential order: Tank, regulator valve, valve above tank and valve behind FTIR)
8. Turn on FTIR (Tensor 27) unit
9. Remove pellet sample holder and install Seagull kit
    a. Seagull kit is located directly below the Tensor 27 unit in a wooden box
    b. Make sure the angle is 45^o on the Seagull kit
    c. Locate small silver sample tray (usually in pockets and always should stay with the Seagull kit)
10. Turn on computer and open OPUS software
11. Login with user name (no password)

Collecting background spectra

1. Place ATR crystal in sample holder
    a. Check crystal for clean surface
    b. If dirty wash with water then methanol or acetone
2. Place sample holder in Seagull kit
3. Create a new folder before starting experiments (OPUS does not allow creation of folders)
4. In OPUS software go to measurements tab and select either Advanced Measurements for one scan or repeated measurements for repeated scans

5. The only tabs needed to be adjusted are the Basic and Advanced tab
6. Under the Basic tab, make sure the Experiment is set to Tensor 27.XPM
    a. If not, click Load and the folder that opens should have Tensor 27.XPM
7. Under the Advanced tab, ensure that you measure the file name you want, resolution of 4 and 56 sample scan time with 56 background scan time, the data should be saved from 4000 to 750 cm^{-1}
8. Under the Basic tab once the crystal is placed in the holder and in the Seagull box select Background Single Channel, this will begin the background collection
9. The Active Task Bar at the bottom of the screen will count up to 100%, after it is finished you can begin collecting samples
10. Leave the ATR crystal in the sample holder, but remove the sample pan (this will save time when adding the first sample)

Preparing isocyanate concentration curve

1. Prepare dilutions of your chosen isocyanate with your chosen unreactive, non-volatile solvent (0.1 g batch sizes are sufficient)
2. The dilutions should start with 0.1 g pure isocyanate then dilute down to 0.07, 0.05, 0.02, 0.002 g isocyante with the remaining mass solvent
3. Add each dilution to the sample pan is succession and in OPUS click Measure -> Advanced Measurement
4. In the Advanced Measurement window the Basic tab allows you to change the sample name, file name and pathway to save
5. In the Advanced tab, make sure you are measuring absorbance and the following data blocks are checked to be saved: Absorbance, signal channel, and background
6. Additionally ensure that the Resolution is set to 4, the sample scan is set to 56 scans and the background scan is set to 56 scans; save data from 4000 to 750 wavenumbers (cm^{-1})
7. In the Basic tab select Sample Single Channel to obtain a spectra
8. Be sure to clean the crystal and sample holder with methanol or acetone between each run
9. Save your files and export the data via File -> Save File As
10. The Save File As window has three tabs, in the Select File tab change the name and pathway; in the Mode tab select Data point table as the file extension
11. Data point table files (.DPT) can be opened in excel
12. Open the .DPT files in excel as tab delimited files and then save as .csv files (these can be read by Matlab) Do not make any changes to the files other than saving them as .csv

13. Open Mygaussfit.m and main.m in Matlab and move them to the active workspace along with all of the .csv files generated from the calibration curve data
14. Edit the variable “t” in main.m to the names of the .csv files in the active workspace
15. Run main.m and use column output in the variable “value” this is the peak area for the isocyanate vibration (~2260 cm^{-1}) in the FTIR spectra
16. Plug this column into G5:G9 in Calibration Curves.xls
17. Ensure that the NCO# is correct for your isocyanate
18. The resulting plot should be linear and the linear fit is utilized in the Samples.xls file to obtain the concentration of isocyanate and thusly the reactivity

Taking reactivity measurements

1. Prepare the crystal and equipment to begin taking measurements directly after mixing
2. Click Measure -> Repeated Measurements to open a dialog window
3. In this window the Basic tab will allow you to change the sample name, file name and pathway
4. In the Advanced Tab set the resolution to 4, sample scans to 56 scans, background scans to 56 scans, and save the data from 4000 to 750 wavenumbers
5. Back in the Basic tab select to repeat the measurement 20-60 times with a delay of 60 seconds between measurements
6. Usually a 0.25-0.5 g batch is fully sufficient for measurements without making a quantity difficult to weigh out
7. Add catalyst, then polyol (or water if measuring blowing reaction) and mix for 10 seconds and move mixture to one side of the mixing cup
8. Add isocyanate to the empty side of the mixing cup
9. Once the addition is complete start the timer and begin mixing isocyanate and polyol/catalyst, continue mixing for 30 seconds
10. Apply roughly 0.1-0.2 g onto the sample hold and make good contact with ATR crystal (when measuring the blowing reaction the mixture may begin to foam immediately)
11. Begin taking repeated measurements by clicking Repeated Sample Single Channel in the Basic tab under Measure -> Repeated Measurements
12. Depending on how many repeats you have the sample may take from 20 to 60 minutes
13. Be sure to write down the time upon the end of the first set of 56 scans as this will be your first timepoint (Generally if everything is prepared to run immediately after 30 seconds of mixing you can obtain a 2 minute first timepoint)

14. Be sure to clean the crystal and sample holder with methanol or acetone between each run
15. To save time and data space, every 5th sample is saved as a .csv file starting with your first sample (It is best to save the time point of each run in the .csv file to keep track of the data e.g if you're your first timepoint finished scanning at 2'24" after mixing started then the file name could look like this: LTI-PEG_Polyol_2.4.csv)
16. Save your files and export the data via File -> Save File As
17. The Save File As window has three tabs, in the Select File tab change the name and pathway; in the Mode tab select Data point table as the file extension
18. Data point table files (.DPT) can be opened in excel
19. Open the .DPT files in excel as tab delimited files and then save as .csv files (these can be read by Matlab) Do not make any changes to the files other than saving them as .csv
20. Open Mygaussfit.m and main.m in Matlab and move them to the active workspace along with all of the .csv files generated from the calibration curve data
21. Edit the variable "t" in main.m to the names of the .csv files in the active workspace
22. Run main.m and use column output in the variable "value" this is the peak area for the isocyanate vibration (~2260 cm^{-1}) in the FTIR spectra
23. As of now main.m is set up to run 5 samples with spacing for an additional 4 samples after comments (%) are removed, if additional spaces are required copy and plate this section of code at the end:

    ```
    %% data

    t=dlmread('FileName.csv');% FileName needs to be exactly the same as the .csv

    file

    x=t(868:967,1);

    y=t(868:967,2);

    z=t(1:25,2);

    %z_avg=mean(z);

    %y_adj=y+abs(z_avg);

    subplot(521)

    plot(x,y,'^k');
    ```

```
%% fitting

[sigmaNew,muNew,Anew]=mygaussfit(x,y);

ynew=Anew*exp(-(x-muNew).^2/(2*sigmaNew^2));

subplot(521)

hold on; plot(x,ynew,'+k');

%% Integrating

value(1,1)=abs(trapz(x,ynew));
```

24. The subplot function will need to be adjusted for all sections of the code if 10 or more samples samples are analyzed at once; see http://www.mathworks.com/help/matlab/ref/subplot.html for more information
25. After main.m finished running, the variable “value” will output a column of peak areas for the isocyanate
26. These can be plugged into columns B3:B15, E3:E15, or H3:H15 in Samples.xls
27. The equations used in columns A3:A15, D3:D15, and G3:G15 in Samples.xls are derived from Calibration Curves.xls
28. The time columns can be unique for each run of each sample
29. The generated plot should be linear and the slope of the line is the rate constant for the given sample and run
30. Generally, each mixture should be run in triplicate to ensure uniform data acquisition

Notes:

- If the spectra increases in intensity for the first few minutes of a run it could be caused by continued wetting of the crystal surface; begin your first timepoint after the spectra begins to decrease
- If the peak does not look centered or is not fitting properly in the plot after running main.m you may need to adjust the range in this set of code for each sample:

```
x=t(868:967,1);  % These are the row numbers for the FTIR spectra that usually

                    corresponds to the 2260 wavenumber peak of isocyante,
```

however they may need to be adjusted manually to fit the peak correctly . If you adjust x you need to equally adjust y

```
y=t(868:967,2);
```

Clean-up:

9. Collect all glass waste (pipettes, vials, or broken glass) and dispose in the broken glass container (box)
10. Collect all sharps and dispose in the sharps waste container (red sharps box)
11. Collect all solid waste and dispose in the solid waste container
12. Collect all liquid waste and dispose in the appropriate liquid waste container (acetone or halogenated)

Rheology for Working Time and Viscosity

Principle:

The working time of a reactive, curing liquid is key to understanding the amount of time that physical manipulation will not begin to cause plastic deformation. The viscosity is also important in terms of determining the injectability of the material during the working time. The point where the storage modulus (G') crosses the loss modulus (G") is known as the crossover point. This is significant in terms of network formation because beyond the crossover point the material is no longer a liquid, it is a cross-linked gel. The storage modulus will continue to rise beyond the crossover point as the material hardens and will eventually plateau. The time from mixing until the crossover point is the working time of the material.

Before starting:

- Read and understand the MSDS of the reagents listed below
- Personal Protective and Safety Equipment required:
    - Disposable nitrile gloves
    - Appropriate attire according to the Chemical Hygiene Plan (shoes, labcoat, goggles, etc.)

Reagents:

- Polyester polyol (various Mw)
- Isocyanate (LTI, LTI-PEG, HDIt, etc.)
- Catalyst (iron(III) acetylacetonate (in 5% solution in epsilon-caprolactone), TEDA in solution, etc.)
- DI Water
- Methanol/acetone bottle (for rinsing crystal between runs)
- Spatula
- Mixing cups

Materials and Equipment:

- Balance
- 25 mm disposable plates geometry
- 40 mm non-disposable plate geometry
- AR2000ex Rheomety
- Methanol/acetone bottle (for rinsing crystal between runs)
- Spatula
- Mixing cups
- Disposable syringes
- Kim wipes
- Timer

Software/Documents:

- TA Rheology Advantage

- TA Rheology Manual
- TA Rheology Analysis

Procedure:

Working time measurement

- Open the rheology software
- Install the proper peltier plate (the staged disposable or the flat for non-disposable geometries)
- Install the proper geometries
- Perform calibrations (oscillation, inertia and zeroing gap)
- Prepare run before mixing sample
    - Check the conditioning step and set the temperature for the experiment
    - Prepare the experiment for a time sweep of 1 hour with 1 Hz frequency and 1% strain
    - Check the post experiment step and set the temperature back to room temperature
    - Name your sample before you begin mixing to avoid wasting excess time before the test begins
- Prepare sample (at least 1 g of material is usually enough for a 500-1000 μm gap)
- Start timer directly upon mixing
- Carefully place sample between peltier plate and upper geometry ensuring that enough material is used to fully cover the space between the two plates
- Lower gap to a predetermine position (500-1000 μm gap)
- Carefully clear away excess material
- Begin the test and stop the timer
- The crossover point is automatically calculated in the TA Rheology Analysis software
    - Open your file and click send to graph
    - Using the dropdown menu in the analysis panel select G'. G" crossover and set the limits before and after the crossover event
    - Add the time on during mixing and adding the sample to the rheometer to the calculated time from the software to obtain the working time

Viscosity measurements

- Open the rheology software
- Install the proper peltier plate (the staged disposable or the flat for non-disposable geometries)
- Install the proper geometries
- Perform calibrations (oscillation, inertia and zeroing gap)
- Check the conditioning step and set the temperature for the experiment
- Prepare the experiment for a frequency sweep of 0.1 - 100 Hz frequency and 1% strain
- Prepare the materials without catalyst to avoid curing

- Begin the test and upon completion the viscosity is automatically calculated with the TA Rheology Analysis software

Notes:

- Consistent gap distances is important when trying to compare multiple unique samples
- The strain and frequency parameters can be adjusted, however, utilize literature values for comparison (1 Hz and 1% strain is widely used for most normal materials)
- The larger diameter geometry can reduce noise in the data, however, it requires the use of more material

Clean-up:

1. Collect all glass waste (pipettes, vials, or broken glass) and dispose in the broken glass container (box)
2. Collect all sharps and dispose in the sharps waste container (red sharps box)
3. Collect all solid waste and dispose in the solid waste container
4. Collect all liquid waste and dispose in the appropriate liquid waste container (acetone or halogenated)

<u>*In vitro* Wet Test for Porosity</u>

Principle:

Injectable, settable polyurethane materials designed for implantation *in vivo* need to be assessed for the capacity of over foaming due to biological fluids interacting with the reactive polyurethane mixture. This protocol allows for the *in vitro* test of a "worst case" exposure to a wound bed with high amounts of liquids.

Before starting:

- Read and understand the MSDS of the reagents listed below
- Personal Protective and Safety Equipment required:
  - Disposable nitrile gloves
  - Appropriate attire according to the Chemical Hygiene Plan (shoes, labcoat, goggles, etc.)

Reagents:

- Isocyanate
- Polyester
- Filler
- Water
- Catalyst Solution

Materials and Equipment:

- Speed mixer
- Balance
- Mixing cups
- Mixing cup holder for speed mixer
- Disposable syringes
- Kim wipes

Procedure:

23. Determine sample size:
    Size can be varied based on applications, however, smaller samples (2.5 g or less)

    produce more uniform porosities through the whole composite

24. Based on sample size fill appropriate mixing cup with 2-5 mL DI water and warm in incubator for ~1 hour, be sure to leave enough room for the potential expansion of the polyurethane, but ensure that the water completely envelopes the material during the curing process
25. Prepare reactive polyurethane mixture by adding appropriate amounts of isocyanate, polyol, filler, and catalyst with disposable syringes into mixing cup
26. Speed mix at full speed for 30 seconds

27. Inject directly into warmed water, ensuring that the water is covering the composite, try to avoid folding the composite onto itself. This creates erroneous porosity when coring or cutting the sample to measure gravimetric porosity. Try to keep the injected material as cylindrical as possible.
28. Place sample in incubator for 24 hours
29. After 24 hours in the incubator dry samples for an additional 24 hours
30. Core or cut the sample into easily measured pieces and gravimetrically test the porosity
31. Additional analysis can be conducted through SEM imaging and ImageJ or Metamorph pore size analysis

Notes:

Clean-up:

5. Collect all glass waste (pipettes, vials, or broken glass) and dispose in the broken glass container (box)
6. Collect all sharps and dispose in the sharps waste container (red box)
7. Collect all solid waste and dispose in the solid waste container
8. Collect all liquid waste and dispose in the appropriate liquid waste container (acetone or halogenated)

Leached Material Cytotoxicity Testing

Principle:

Injectable, reactive materials have the potential to extravasate during implantation. Extravasation of reactive material could induce local toxicity. This protocol aims to analyze and test the leached materials from injectable, reactive PURs. PBS is used for NMR analysis, cell culture media is used for cytotoxicity analysis.

Before starting:

- Read and understand the MSDS of the reagents listed below
- Personal Protective and Safety Equipment required:
  - Disposable nitrile gloves
  - Appropriate attire according to the Chemical Hygiene Plan (shoes, labcoat, goggles, etc.)

Reagents:

- Isocyanate
- Polyester
- Filler
- Water
- Catalyst Solution
- PBS
- Cell culture media
- Appropriate cell line

Materials and Equipment:

- Speed mixer
- Balance
- Mixing cups
- Mixing cup holder for speed mixer
- Disposable syringes
- Cell culture hood and incubator
- Kim wipes

Procedure:

Preparing samples

1. Prepare 4 2.5 g batches of a desired formulation
2. After mixing and loading into a syringe wait 2 minutes before injecting one of the batches into PBS or cell culture media in a conical tube
3. Allow to leach overnight at 37 C

4. For the remaining two batches mix and load into a syringe and inject into a 12 mm tube
5. Allow to react for 45 minutes and then cut out of tube and place into PBS or culture media
6. Allow to leach overnight for 37 C
7. Remove solid samples from media after 24 hours

Chemical Analysis of leachates

1. Lyophilize the PBS and weigh the residue
2. Subtract the known value of salt in the PBS to obtain the amount of leached mass from the PUR
3. Re-suspend in deuterated solvents to prepare NMR solution
4. Use individual components as a reference to determine leached materials

Cytotoxicity of leachates

1. Measure pH of cell culture media to determine acidity of leachates
2. Use pure leachates for a serial dilution up to 16X with sterile media (keep enough pure leachates to use as a 1X group)
3. Plate NIH3T3 cells in a 96 well plate in triplicate for each of your dilutions and one set for positive (blank culture media) and negative controls (PBS)
4. After 24 hours of culture remove media and add treatment groups
5. Culture for an additional 24 hours and then test viability with either live/dead stain or similar assay
6. Plot cell viability (cell viability less than 70% is considered cytotoxic
7. In the case of a cytotoxic response use a fitting algorithm (PCHIP in matlab works well) to obtain the LC50 (the concentration of leachates that causes 50% toxicity)

Notes:

Clean-up:

9. Collect all glass waste (pipettes, vials, or broken glass) and dispose in the broken glass container (box)
10. Collect all sharps and dispose in the sharps waste container (red box)
11. Collect all solid waste and dispose in the solid waste container
12. Collect all liquid waste and dispose in the appropriate liquid waste container (acetone or halogenated)

Metamorph Thresholding Image Analysis

Principle:

This protocol describes the steps to perform specific thresholding in Metamorph for histomorphometry analysis.

Materials and Equipment:

- Microscope
- Histology slides (stained)
- Metamorph

Procedure:

- Image the stained histology slides at an acceptable magnification
- Open image in metamorph
- Open the data log through the Log dropdown menu
- Open the dynamic data exchange and an excel file will open automatically (this file will hold your sample data)
- If you need accurate measurements of length, width, area etc. then open the calibrate distances box under the Measure dropdown menu and select the magnification of the image and press apply
- Use the free draw tools to outline an area of interest and make the desired area measurements
- To view the measurements open the Region Measurements in the Measurements drop down menu (this dialog box allows you to log the data to the open excel file; you must manually log the data for each analysis)
- Open the Threshold Image and Set Color Threshold dialog boxes under the Measure drop down menu
- In the Threshold Image dialog box select Add to Threshold and then click Clear Threshold (this prepares the software for the manual thresholding in the next step)
- Select the Set by Example button in the Set Color Threshold dialog box and begin clicking on the image
- Every pixel you click in the image will be added to the color threshold
- Log the data after you are comfortable with the threshold specificity and the area and %threshold value will be copied into the open excel file

Notes:

- This technique works extremely well when there is a difference between colors in the area of interest and the surrounding tissue (Example shown below)
- The value for %Threshold is only given for the area of interest draw

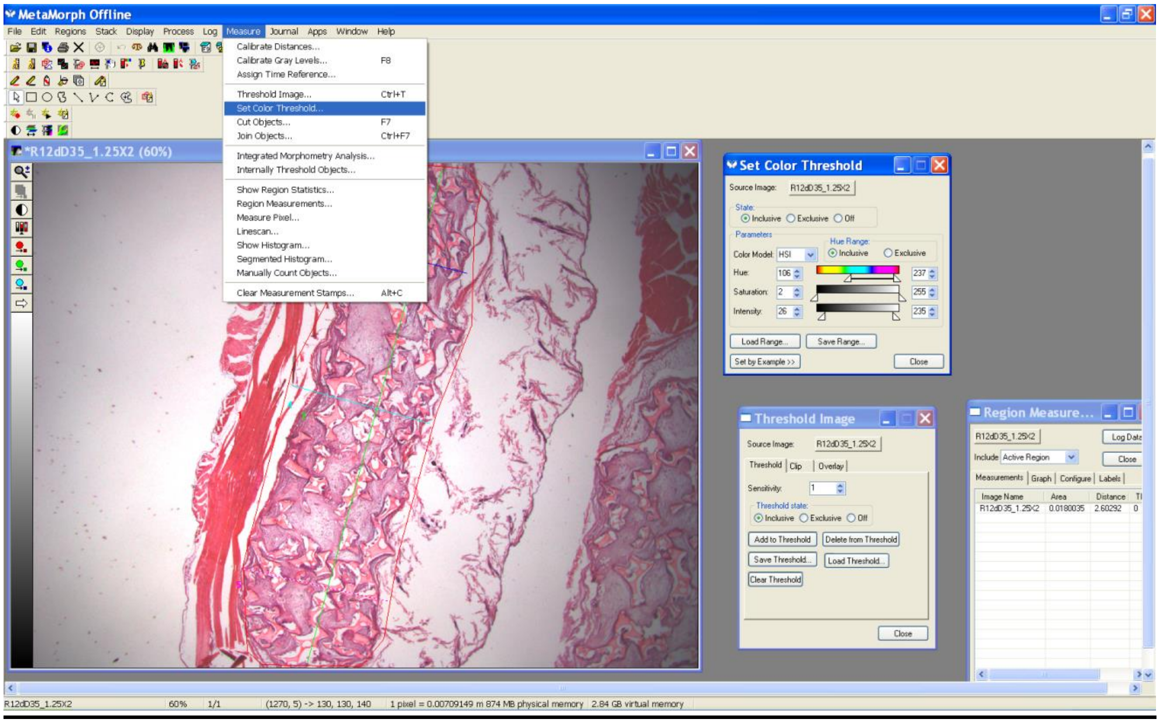

Set Color Threshold

Source Image: R12dD35_1.25X2

State: ● Inclusive ○ Exclusive ○ Off

Parameters

Color Model: HSI

Hue Range: ● Inclusive ○ Exclusive

Hue: 106 – 237

Saturation: 2 – 255

Intensity: 26 – 235

Threshold Image

Source Image: R12dD35_1.25X2

Threshold | Clip | Overlay

Sensitivity: 1

Threshold state: ● Inclusive ○ Exclusive ○ Off

Region Measure...

R12dD35_1.25X2

Include: Active Region

Measurements | Graph | Configure | Labels

Image Name	Area	Distance	Tl
R12dD35_1.25X2	0.0180035	2.60292	0

R12dD35_1.25X2 60% 1/1 (1270, 5) -> 130, 130, 140 1 pixel = 0.00709149 m 874 MB physical memory 2.84 GB virtual memory

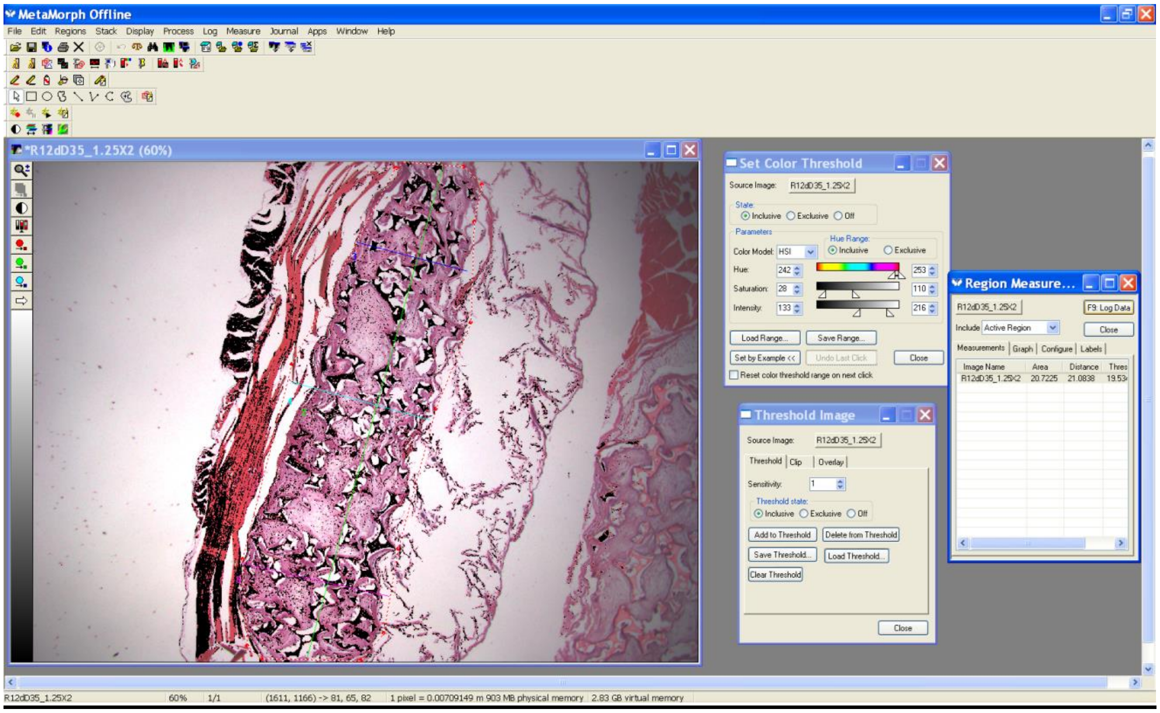

Set Color Threshold

Source Image: R12dD35_1.25X2

State: ● Inclusive ○ Exclusive ○ Off

Parameters

Color Model: HSI

Hue Range: ● Inclusive ○ Exclusive

Hue: 242 – 253

Saturation: 28 – 110

Intensity: 133 – 216

☐ Reset color threshold range on next click

Threshold Image

Source Image: R12dD35_1.25X2

Threshold | Clip | Overlay

Sensitivity: 1

Threshold state: ● Inclusive ○ Exclusive ○ Off

Region Measure...

R12dD35_1.25X2

Include: Active Region

Measurements | Graph | Configure | Labels

Image Name	Area	Distance	Thres
R12dD35_1.25X2	20.7225	21.0838	19.53

R12dD35_1.25X2 60% 1/1 (1611, 1166) -> 81, 65, 82 1 pixel = 0.00709149 m 903 MB physical memory 2.83 GB virtual memory

Figure A1. Example of Metamorph thresholding for histomorpometric analysis.

References

1. (a) Guelcher, S. A.; Srinivasan, A.; Dumas, J. E.; Didier, J. E.; McBride, S.; Hollinger, J. O., Synthesis, mechanical properties, biocompatibility, and biodegradation of polyurethane networks from lysine polyisocyanates. *Biomaterials* **2008,** *29* (12), 1762-1775; (b) Ruppender, N. S.; Merkel, A. R.; Martin, T. J.; Mundy, G. R.; Sterling, J. A.; Guelcher, S. A., Matrix Rigidity Induces Osteolytic Gene Expression of Metastatic Breast Cancer Cells. *Plos One* **2010,** *5* (11).
2. (a) Gachkovskii, V. F., Universal fluorescence of polymers. *Journal of Structural Chemistry* **1967,** *8* (2), 318-320; (b) Jaafar, I. H.; LeBlon, C. E.; Wei, M.-T.; Ou-Yang, D.; Coulter, J. P.; Jedlicka, S. S., Improving fluorescence imaging of biological cells on biomedical polymers. *Acta Biomaterialia* **2011,** *7* (4), 1588-1598.